Internal Sensing and Actuation Topologies for Active Rotors

Jimenez, Samuel

Award date:
2017

Awarding institution:
University of Bath

Internal Sensing and Actuation Topologies for Active Rotors

submitted by

Samuel Jiménez

for the degree of Doctor of Philosophy

of the

University of Bath

Deparment of Mechanical Engineering

October 2016

Contents

Acknowledgements 4
Publications 5
Abstract 6

1 Introduction **7**
1.1 Motivation and goals 7
1.2 Active rotor concept 9
1.3 Scope of the research 11
1.4 Structure of the thesis 12

2 Background, aims and objectives **13**
2.1 Introduction 13
2.2 State of the art 13
2.3 Discussion and research gaps 36
2.4 Aims and objectives 38
2.5 Summary 39

3 Active rotor model **45**
3.1 Introduction 45
3.2 Finite element model 45
3.3 Equations of motion 47
3.4 Dynamic model 51
3.5 Model validation 54
3.6 Model prototype predictions 55
3.7 Conclusions 57
3.8 Summary 59

4 Active rotor prototype **60**
4.1 Introduction 60
4.2 Design overview 60
4.3 Mechanical design 62

4.4 Electronic design . . . 78
4.5 Software design . . . 85
4.6 Conclusions . . . 92
4.7 Summary . . . 94

5 Sensing of rotordynamics with internal MEMS accelerometers 96
5.1 Introduction . . . 96
5.2 Operating principles of MEMS accelerometers . . . 97
5.3 Output of MEMS accelerometers located in a rotating frame . . . 101
5.4 Orbit characteristics as measured by internal accelerometers . . . 107
5.5 Transient vibration as measured by internal accelerometers . . . 115
5.6 Extracting displacement information from internal accelerometers 122
5.7 Estimation of rotational speed with internal accelerometers . . . 126
5.8 Sources of measurement error and mitigation techniques . . . 130
5.9 Experimental results: effect of rotor unbalance . . . 136
5.10 Conclusions . . . 140
5.11 Summary . . . 141

6 Vibration control with active rotors 144
6.1 Introduction . . . 144
6.2 Control problem formulation . . . 145
6.3 Model-based control . . . 148
6.4 *Non a priori* control . . . 153
6.5 Conclusions . . . 177
6.6 Summary . . . 178

7 Active rotors combined with AMBs 180
7.1 Introduction . . . 180
7.2 Tackling non-collocation with active rotors . . . 181
7.3 AMB control by accelerometer-derived position . . . 182
7.4 Mitigation of frame conversion errors . . . 185
7.5 Simulated levitation . . . 190
7.6 Conclusions . . . 192
7.7 Summary . . . 193

8 Conclusions and further work 194
8.1 Conclusions . . . 194
8.2 Further work . . . 196

A Element matrices **204**
A.1 Element stiffness matrix 205
A.2 Element mass matrix 205
A.3 Element gyroscopic matrix 207

B Stationary points of the objective function **208**

Acknowledgements

I would like to express my heartfelt thanks to my principal supervisor, Prof. Patrick Keogh. His knowledge, experience, patience, support and encouragement have been constant throughout these four years, and without him I would not be where I find myself today. His approach to research and his concern for the development of his students have been inspirational, and I am extremely grateful for having had the privilege of working with such an outstanding professional.

I would also like to thank Dr. Necip Sahinkaya and Dr. Matthew Cole, who both acted as supervisors at different stages of my PhD. Their knowledge and, more importantly, their willingness to share it with me, have had a profound impact on my work.

Many thanks to the technical staff in the Department of Mechanical Engineering who have helped me throughout the PhD with their skills and experience. In particular, I am indebted to Guy Brace and Alan Jefferis, without whose wisdom the prototype could never have been built.

I am thankful to all the anonymous contributors of the Open Source movement, in particular the Arduino and Latex communities. Whoever you are, wherever you are, thank you for sharing your genius.

A very special thanks is due to Lucía, who has been at my side every step of the journey, enduring my grumbling and celebrating the victories. She is a perpetual source of encouragement, joy and affection. Mil gracias, compañerilla.

Lastly, I thank my parents. At every turn, they have given me the freedom to make my own choices, the wisdom I needed to do my best and their unconditional support when things went awry. I owe them everything that I am, and everything that I ever will be.

Publications

- S. Jiménez and P. S. Keogh, "A self-sensing and self-actuating active rotor with an algorithmic direct search controller", *IEEE/ASME Transactions on Mechatronics*, 2016. Submitted.
- S. Jiménez and P. S. Keogh, "Active control of rotor dynamics using on-board sensing and actuation", in *11th International Conference on Vibrations in Rotating Machinery*, (Manchester, United Kingdom), 2016.
- S. Jiménez and P. S. Keogh, "Control of magnetic bearings with rotor-mounted MEMS accelerometers", in *15th International Symposium on Magnetic Bearings*, (Kitakyushu, Japan), 2016.
- S. Jiménez, M. Cole, and P. S. Keogh, "Vibration sensing in smart machine rotors using internal MEMS accelerometers", *Journal of Sound and Vibration*, vol. 377, pp. 58–75, 2016.
- S. Jiménez, P. S. Keogh, and M. Cole, "Internal Sensing and Actuation Strategies for Smart Machine Rotors", in *Proceedings of the 9th IFToMM International Conference on Rotor Dynamics* (P. Pennacchi, ed.), (Milan, Italy), pp. 1527–1537, Springer International Publishing, 2014.
- M. Cole, S. Jiménez, and P. S. Keogh, "Feedback control of a magnetic bearing using fusion of rotor acceleration and position measurements", in *14th International Symposium on Magnetic Bearings*, (Linz, Austria), 2014.

Abstract

Active control constitutes the state of the art in vibration management in rotating machines. However, existing designs are impractical and costly, and hence not yet widely applied. The goal of the research reported here was to develop a design which would allow the implementation of active technology in a wider range of rotating machine applications. Thus, this study focuses on a novel active rotor topology, consisting of a hollow rotor with internally mounted sensors and actuators. This layout provides greater freedom to select the sensor and actuator positions along the rotor, and naturally protects the devices from harsh working environments.

The research was structured according to four themes. Firstly, the concept feasibility was explored by constructing a fully functioning prototype. MEMS accelerometers and mass balancer actuators were mounted in an assembled rotor, together with a microcontroller and radio unit to enable wireless transmission of data. Secondly, the behaviour of MEMS accelerometers in a rotating frame of reference was studied. An output model was derived and applied to the study of whirl orbits and transient vibration. Further, techniques were developed to extract mean displacement and angular velocity information from the sensor signals. An analysis of potential sources of measurement error was conducted, and methods for their mitigation devised. The third theme focused on developing active vibration control techniques suitable for use with active rotors. The core of this work is the development and successful implementation of a *non a priori* method, Algorithmic Direct Search Control. This technique enables vibration to be minimised without knowledge of the system characteristics, by applying a direct search optimisation technique as a control law. Finally, the combination of active rotors and Active Magnetic Bearings was considered to tackle the problem of sensor/actuator non-collocation. The challenge of levitating a rotor on AMBs using only internal accelerometers was approached via integration-based displacement information extraction, to exploit existing PID controllers. This method proved unfeasible in practice, but valuable lessons were derived from the study.

The key finding of this work is that active rotor technology is versatile, cost-effective, powerful and feasible. As such, it offers great potential as a route to achieving a more practical and generalised implementation of active control technology in rotating machinery.

Chapter 1

Introduction

1.1 Motivation and goals

Rotating machines form an integral part of the history of human ingenuity, making possible some of the greatest technological advancements of mankind. Inventions such as the watermill, the spinning jenny or the jet engine, to name but a few, have all had a profound impact on our shared history, shaping the modern world one revolution at a time. Humanity's natural inquisitiveness has underpinned this continued technological evolution, leading us to constantly tinker, modify and improve. In the context of rotating machines, this desire to push the boundaries of technology has driven engineers to strive for higher operating speeds, increased power density, longer lifetime and reduced vibration.

Various authors have predicted the future of rotating machinery to lie in smart rotor technology. Maslen and Schweitzer [1] define a machine as smart if "*it uses its internally measured signals to optimise its state*". According to Lees [2], the concept involves machines which can sense their condition, diagnose faults if they arise and, critically, make corrections to address them. A truly smart machine, in essence, should operate with minimum human interaction. Although some basic capabilities of smart rotors are achievable with existing state of the art technology, the required functionality extends much beyond current capabilities, as discussed by Burrows and his colleagues [3]. Further development is therefore required.

The platform from which to develop smart rotor technology further is active vibration control. Although still in its infancy in terms of its widespread implementation, it constitutes the most significant advancement of rotating machine technology in the last century. Active vibration control equips a rotating machine with basic sensing, diagnosis and control capabilities. It allows operators to monitor the health of a rotating machine and then, crucially, modify

its dynamic behaviour to enable improved performance. This improvement can materialise in a number of ways. For example, reducing vibration at steady operating conditions can reduce bearing wear or permit smaller gap clearances between rotor and stator. The greatest advantage of active systems is their ability to make adjustments during operation and adapt to uncertainty and changing conditions. This provides rotating machines with a degree of robustness which cannot be achieved through other means. In some cases, active control can even enable altogether new types of rotating machines, such as rotors levitated by Active Magnetic Bearings (AMBs).

In order for active control capability to evolve into smart rotor technology, various limitations need to be addressed. One aspect which demands particular attention is the difficulty of implementation. Currently, active control systems are designed for specific applications, and often require rotating machines to be designed around them. The associated complexity, cost and required expertise preclude a generalised implementation of active control in rotating machines. Further, the number and location of sensors and actuators is often restricted by working components such as seals, bearings or turbine blades, which limits the performance of the technology. For instance, Friswell and He [4] indicate that the most significant barrier to condition monitoring of cracked rotors is the poor quantity and quality of vibration measurement information available during operation.

It would therefore be desirable to provide any and all rotating machines with active control capability. In a recent publication, Hahn [5] also states that "*There remains a need in industry, for a health monitoring system that covers the complete rotating unit in its entirety, covering bores, shafts, discs and blades*". Given the prevalence of rotating machines in almost all aspects of industry and engineering, providing even small performance boosts to simple machines could have an immense impact on a global scale. For instance, if active control could be generally implemented in power generation turbines to achieve a small improvement in efficiency, vast energy savings could be attained globally. Improved machining tolerances might be derived if manufacturing equipment such as lathes or mills could be easily fitted with active control. Another example would be improving the evacuation time of rotary vacuum pumps by reducing the clearances between rotor and stator. This could have a significant impact on industries which rely on vacuum processes.

The goal of this research, therefore, was to study active control system designs which could be more easily implementable in any general rotating machine. By necessity, this implies considering solutions which can provide ver-

satile, robust and cost-effective systems, requiring minimum adaptation for different applications. The result was the introduction of a new rotor topology, referred to as an “active rotor” design.

1.2 Active rotor concept

An active rotor topology is one in which the complete active system, including sensing, control and actuation, is entirely located within a hollow rotor. Its naming distinguishes it from more conventional “passive rotor” systems, in which the components of the active control system are usually distributed throughout the stator and the rotor shaft is a passive element.

Figure 1.1 shows an example of a rotating machine with an active control system which uses a passive rotor design. The machine is an aeration blower for use in a wastewater treatment facility. The rotor is suspended on AMBs, with its position being measured by displacement sensors. As the sensors, actuators and electric motor all require space in the stator, the active control and mechanical functionality of the machine are inextricably linked, leading to a complex design. Further, no sensors can be located in the central section because of the presence of the motor windings, so that any observation of vibration behaviour is limited to the two external sensor positions. For a flexible rotor, it would be desirable, for example, to monitor the clearance between the motor magnets and windings, but this would not be possible with the passive rotor design.

An active rotor design is depicted in Fig. 1.2. In this case, the rotor is hollow and the sensors and actuators are housed within it. In this way, the mechanical functionality of the rotor becomes independent of the active system aspect, greatly simplifying the design considerations. As the sensors and actuators no longer require space in the stator, large numbers of them can be used, and their location can be chosen freely to improve observability and controllability. This topology also introduces the compelling notion of being able to retrofit existing machines with active control systems by replacing only the passive rotor with an active one. As the outer surface of such a rotor would remain unchanged, the mechanical operation of the machine would not be affected, but capabilities such as condition monitoring or vibration reduction could be provided.

The physical realisation of active rotors is not without challenges. Containing a complete active control system inside a shaft evidently produces a compact arrangement, but also greatly increases the design and manufacturing complexity of the rotor. The type of sensor and actuator used must be such that the active system can function independently of the stator, which limits

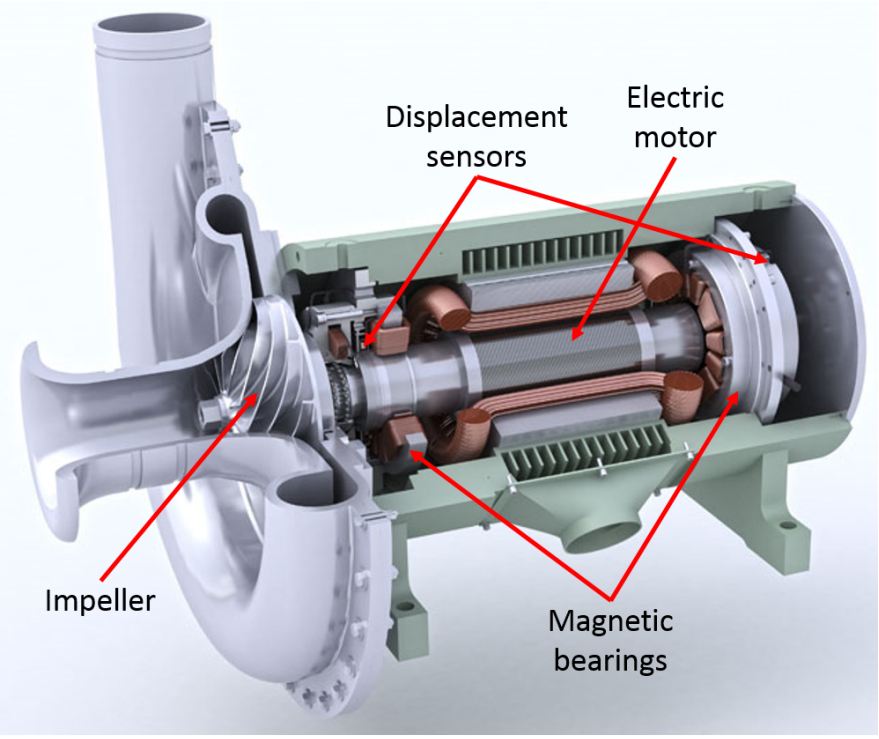

Figure 1.1: Rotating machine with active control system of the passive rotor type. Adapted from original image courtesy of SKF.

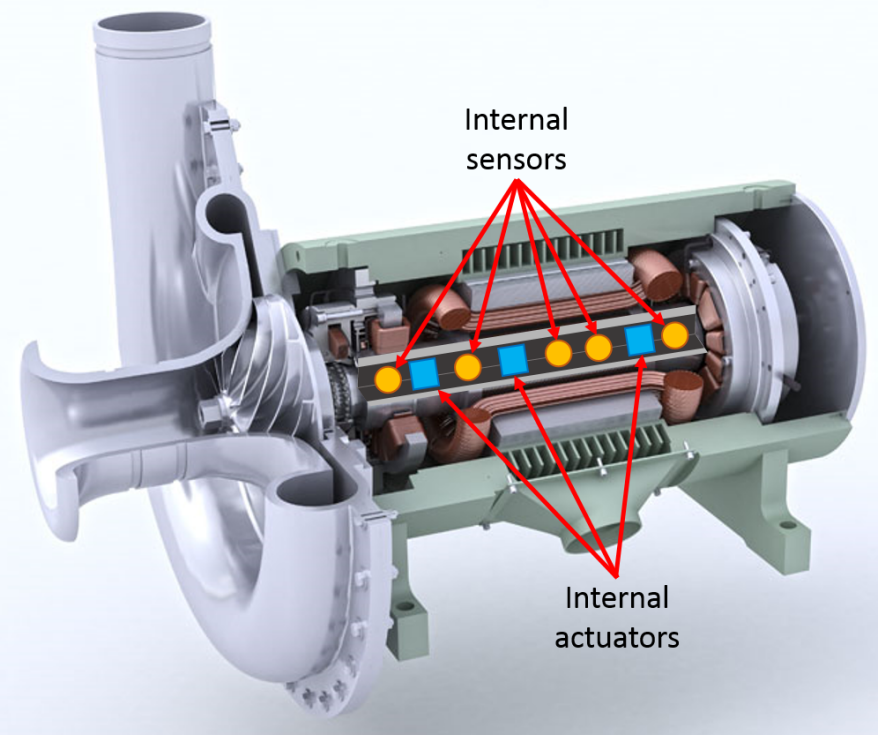

Figure 1.2: Rotating machine with active control system of the active rotor type. Adapted from original image courtesy of SKF.

the choice of suitable devices. Further, all internal components must be small, permit practical installation within a shaft and be strong enough to withstand potentially large centrifugal forces. Another aspect which requires consideration is how to transmit data and power to and from the active rotor.

The research work presented in this thesis considers, therefore, the possibilities and challenges afforded by active rotor topologies. Such a technology may open a route towards a generalised implementation of active vibration control in rotating machines, and consequently lead to performance improvements in a vast range of applications and industries.

1.3 Scope of the research

This thesis describes the design, development and study of the active rotor topology. The scope of the research can be broadly classified into four themes: feasibility of internal topologies, vibration sensing with internal accelerometers, control methods for active rotors and application of active rotors to specific rotordynamic challenges.

The first theme explores the difficulties and benefits of installing sensing and actuation within a rotor. The product of this work was the design and construction of a fully functional active rotor prototype, which also served as an experimental test bed for further studies.

The prototype uses internally-mounted MEMS accelerometers to measure rotor vibration, and so the second theme involves understanding how these devices operate when located within a rotating frame of reference. The research studied the output of these sensors, the limitations associated with various measurement error sources and also methods of extracting useful information from the devices. Particular attention was given to methods for inferring rotor displacement and angular velocity from the accelerometer signals.

The third theme focused on the control and actuation aspect of active rotors. Most advanced control techniques applied to rotating machines involve model-based methods. However, a weakness of these is that their performance is conditioned by the accuracy of the model used. Given the general uncertainty present in many rotordynamic applications, this was identified as a potentially limiting characteristic when considering the widespread implementation of active control systems. Thus, the core of the control-related research consists of the development of a model-free, *non a priori* control technique, referred to as Algorithmic Direct Search Control (ADSC), suitable for use in active rotors.

Finally, the fourth theme centred on studying specific rotordynamic chal-

lenges which active rotor technology might be well suited to tackle. In particular, the problem of sensor and actuator non-collocation in Active Magnetic Bearing (AMB) systems was identified as one which might be addressed by active rotors. An inherent characteristic of active rotors is that of allowing sensors and actuators to be freely positioned along the rotor shaft. Thus, by using internally-mounted sensing systems, users would be able to locate the sensors at the same axial position as the AMBs, preventing non-collocation.

1.4 Structure of the thesis

The thesis is broadly structured around the research themes. Chapter 1 explains the motivation behind the research and scope of the work. The background of active rotors, as well as the aims and objectives derived from identified research gaps are discussed in Chapter 2. Chapter 3 describes the techniques used to model and simulate the active rotor. Chapter 4 details the design and construction process of the active rotor prototype. Considerations related to the mechanical, electrical and software design are highlighted. Chapter 5 discusses the use of MEMS accelerometers as sensors and Chapter 6 is focused on control methods for active rotors. Chapter 7 discusses the uses of active rotors as a means to prevent non-collocation issues in AMB systems. Chapter 8 provides closing remarks and outlines suggestions for further work.

References

[1] E. H. Maslen and G. Schweitzer, *Magnetic Bearings: Theory, Design, and Application to Rotating Machinery*. Springer, 2009.

[2] A. W. Lees, "Smart machines with flexible rotors," *Mechanical Systems and Signal Processing*, vol. 25, no. 1, pp. 373–382, 2011.

[3] C. R. Burrows, P. S. Keogh, and M. Sahinkaya, "Progress towards smart rotating machinery through the use of active bearings," *Proceedings of the Institution of Mechanical Engineers, Part C: Journal of Mechanical Engineering Science*, vol. 223, no. 12, pp. 2849–2859, 2009.

[4] M. I. Friswell and Y. Y. He, "Smart rotating machines for condition monitoring," in *Damage Assessment of Structures VIII*, vol. 413 of *Key Engineering Materials*, pp. 423–430, Trans Tech Publications, 11 2009.

[5] W. Hahn, "Managing life extension for large rotating plant in power stations," in *Proceedings of 10th International Conference on Vibration Engineering and Technology of Machinery VETOMAC X* (K. J. Sinha, ed.), (Manchester, UK), pp. 39–49, Springer International Publishing, 2014.

Chapter 2

Background, aims and objectives

2.1 Introduction

The fundamental goal of the research was to develop new active vibration control systems which could lends themselves to a generalised implementation in rotating machines. In order to achieve this, it was important to understand the limitations of current systems, and identify ways in which these could be overcome. A review of the state of the art in rotordynamic vibration management was therefore conducted, and is discussed in this Chapter. The conclusions derived from this exercise allowed the identification of research gaps which should be addressed. The chosen route to achieve this was to explore the possibility of mounting active systems solely within hollow rotors to enable "active rotor" topologies. A set of aims and objectives for the necessary research were then determined, and are also outlined here.

2.2 State of the art

Active vibration control constitutes the most advanced vibration management technology currently available to rotating machines. As such, it serves as the basic frame around which smart rotor technology can be developed. In order to better understand its potential and limitations, a review of current literature was conducted, and is presented in this section. Zhou and Shi's [1] survey provided an excellent starting point.

Firstly, precursor technologies are discussed, consisting of off-line balancing and passive balancing devices. This is followed by a full analysis of the various types of active control systems, which is subdivided into their three principal constituent elements: sensing, actuation and control.

Figure 2.1: Off-line balancing of a helical gear set by material removal. The rotor is mounted on a special support rather than its stator. Photograph courtesy of Schenck RoTec GmbH.

2.2.1 Precursor technologies

Off-line balancing The earliest forms of vibration control targeted unbalance-induced vibration, which is typically the most prevalent and significant. Off-line balancing was the first technique developed and consists of reducing rotor unbalance by adding or removing mass at specific rotor locations, before operation. Figure 2.1 shows, for instance, an operator balancing a helical gear set by removing material with a hand-held drill.

For a rigid rotor, only two balance planes are needed to correct any unbalance distribution, as demonstrated by Wowk [2]. However, the rigid rotor assumption does not hold for rotors operating at high speed and so two different methods were developed to balance flexible rotors. The first, called the Modal Balancing (MB) technique, was introduced in 1953 [3] and aims to balance each mode of vibration of the rotor. Masses are placed in such a way as to correct the unbalance at a given mode without affecting any of the previously balanced modes. Typically, the method requires an accurate dynamic model of the rotor, something which is not always readily available. The second method is known as the Influence Coefficient (IC) technique, and was devised by Goodman [4]. This is an experimental procedure where the vibration of the rotor in response to known, discreet unbalances is measured at various points along the shaft. The measured data can be collected in an influence coefficient ma-

trix, which matches the vibration measured at each sensor station to a certain amount of unbalance at each balancing plane. The superposition of these unbalances gives an indication of the overall rotor unbalance distribution. As the influence coefficients change with operating speed, the procedure must be repeated for each speed of interest, a process which can be time-consuming. The Unified Balancing Approach was developed by Darlow [5] in an attempt to combine the advantages of MB and IC and avoid their drawbacks. The resulting method calculates modal balancing mass sets taking as a reference measurements obtained through an influence coefficients process. In general the method can achieve balancing in fewer runs than IC but without the prior knowledge required for MB. The principal disadvantage of Unified Balancing is its complexity, as operators require a good understanding of both MB and IC.

Off-line balancing is still widely used in industrial applications. For mass produced components, such as automotive crankshafts, it can provide a suitable, low-cost solution. However, off-line balancing methods struggle to achieve desired results when very low levels of unbalance are required, such as with high speed operation. In addition, the balancing process is usually performed with the rotor housed in a specialised machine and not in the stator where it will operate. In Fig. 2.1, for example, the rotor is supported on a specialised rig. When balancing in this way, any vibration which is caused by imperfections in rotor-stator interaction (for example, bearing wear or misalignment) cannot usually be accounted for.

On-line passive balancing On-line techniques are defined as those which enable vibration control during operation. This allows them to overcome some of the limitations of off-line methods. The principal disadvantage of on-line systems is their added complexity.

On-line passive balancing, sometimes referred to as automatic balancing, relies on devices which are attached to the rotor and typically consist of an enclosed race containing a fluid and free-moving ball bearings. During operation, the ball bearings naturally change their position to reach a state of minimal unbalance, reducing vibration. Since their first embodiment in a patent by Leblanc [6] and early research by Thearle [7], they have been used successfully in a range of configurations, including using pendulums instead of ballbearings [8]. Typical applications are balancing hand-held machine tools [9] and optical disc drives [10, 11]. An example of the latter is given in Fig. 2.2.

In general, passive balancing methods are regarded to be less effective than active ones [12]. This is often attributed to tribological effects caused at high

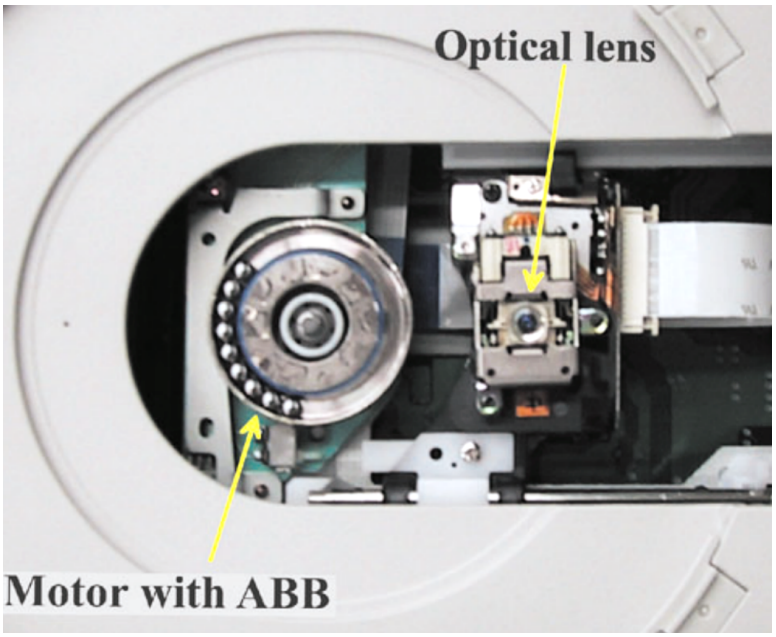

Figure 2.2: Automatic ball balancer (ABB) on a DVD drive, showing the ball bearings contained in the race [11].

speeds as well as the sensitivity to imperfections in the manufacture of the devices themselves. In fact, various authors [13, 14] have concluded through different methodologies that it is not possible to obtain perfect balancing of the rotor if an imperfect passive balancing device is used. Further, passive systems are often designed to tackle a specific mode of vibration under normal operating conditions. Thus, in cases where operating conditions may vary (for instance, if thermal warping occurs), passive systems may prove unsuitable.

2.2.2 Active vibration control

Active vibration control methods are forms of on-line techniques, and as such are operational while the rotating machine is functioning. Their active nature enables them to react to changing operating conditions, which provides them with the capability to tackle sources of vibration other than unbalance. This improved functionality comes at the cost of added design complexity. These techniques find themselves at the forefront of vibration control technology and have garnered considerable research interest. The first examples of active control systems applied to rotating machines began appearing in the second half of the 20^{th} century, although they have not yet been widely used in industrial applications.

In order to manage vibration, active control systems must be able to sense a rotor's vibration state, determine an adjustment which can modify it to achieve

a target state and then execute said adjustment. Thus, the main constituent elements are sensors, actuators and controllers. A separate review of these aspects is provided in this section.

Sensing methods for active vibration control

Sensing technology was first applied to rotating machinery to provide a degree of condition monitoring capability. This is the process of measuring parameters which can determine the health of a system, and hence give early warning of faults. In rotating machines the most common parameter measured is vibration, although others such as, stator temperature, lubrication degradation or acoustic emissions may also be monitored [15].

Although condition monitoring is fundamentally a passive technique, which cannot directly reduce rotor vibration, its implementation serves to prevent some of the more damaging consequences of undesirable vibration. As a vast, active field of research, a detailed analysis of condition monitoring falls beyond the scope of this research (see [16] or [17] for further references). However, its relevance to active vibration control lies in the fact that, as a simpler, less intrusive addition to rotating machines, it has seen much wider implementation. Hence, many of the developments in sensing technology driven by condition monitoring have been used in active control systems. A review of sensing technologies applicable to active vibration control is provided in this section.

Accelerometers Some of the most widely used vibration sensing transducers are accelerometers. The most common type uses the piezoelectric effect, whereby certain materials produce an electric charge when subjected to strain. A portion of piezoelectric material is fitted with a seismic mass and packaged in a housing, which is attached to the surface whose vibration is to be measured. As the machine vibrates, the motion of the seismic mass relative to the housing causes the piezoelectric material to produce a charge, which can be translated into a measurable voltage. Figure 2.3 shows two common examples of piezoelectric accelerometer.

In recent times, MEMS (microelectromechanical system) accelerometers have emerged as a compact, low-cost alternative to traditional piezoelectric designs. These consist of a seismic mass suspended on a sprung structure and surrounded by capacitor plates, as shown in Fig. 2.4. The complete system is micromachined from polysilicon, producing a very compact system with thicknesses in the $10-20$ μm range [18]. Under acceleration, the motion of the proof mass can be inferred by measuring the capacitance change across the plates.

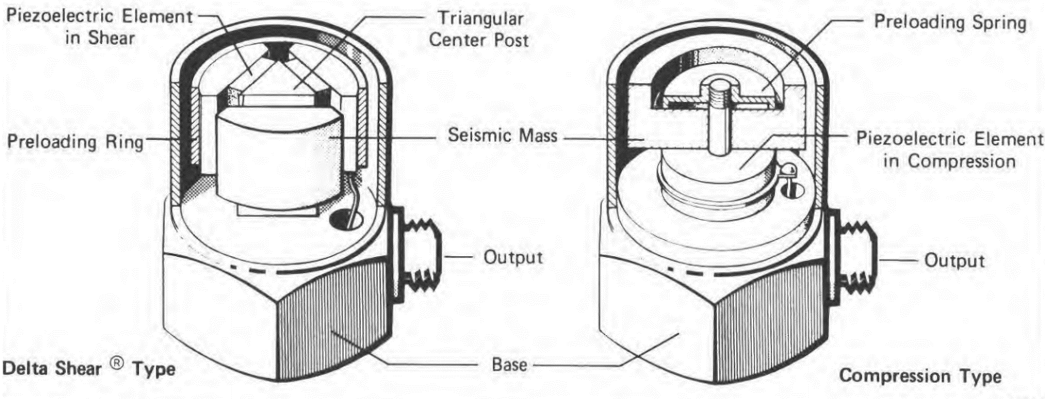

Figure 2.3: Cutaways of two common types of piezoelectric accelerometer [22].

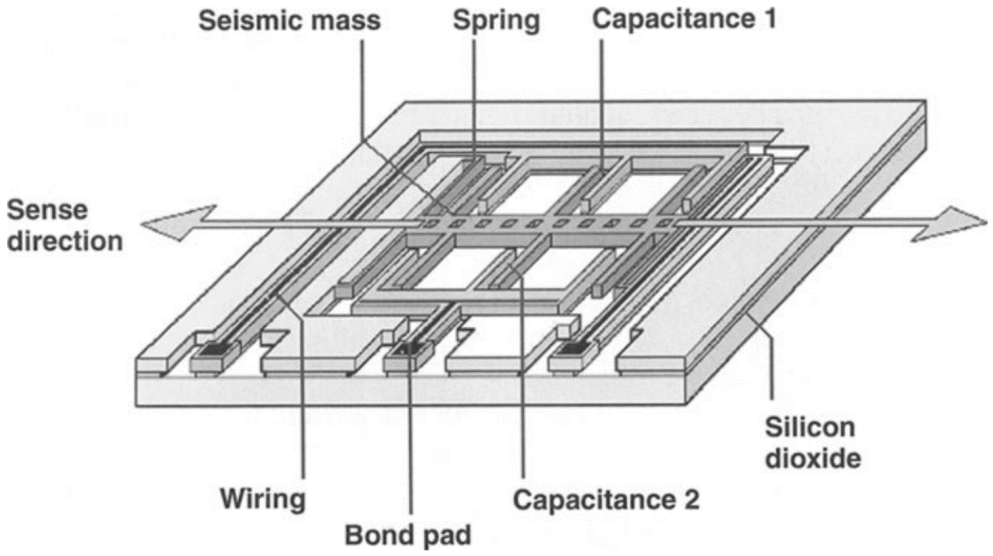

Figure 2.4: Schematic of a MEMS accelerometer [18].

For condition monitoring of machinery, accelerometers are typically attached to the stator casing, usually at the bearing locations (see for instance [19, 20]). This is a simple and inexpensive technique, which, with appropriate processing of the resulting signals, can detect machine faults. However, Muszynska [21] explains that, in practice, accelerometers mounted on the stator casing can only give an idea of whether the vibration of a rotor is over or below an acceptable threshold, but cannot provide detailed insight into the exact nature of the vibration. In essence, the source of the vibration is the rotor itself and so any measurements taken elsewhere on the machine will only give an indirect vibration signal, useful only as a basic or cost-effective means of vibration monitoring.

With the appearance of MEMS accelerometers, it became possible to design much more compact sensing systems, thanks to their small size and direct integration into electronic circuits. Thus, the possibility of mounting accelerometers on the rotor emerged, which could provide much more detailed results than the

more conventional stator-mounting. MEMS accelerometer systems have been used by Arebi *et al.* [23] to detect misalignment of rotating coupled shafts. They located a wireless accelerometer on the rotor shaft, with the measurement axis aligned tangentially. Their results showed that the rotor-mounted accelerometer performed better than both bearing-mounted accelerometers and the encoder-measured Instantaneous Angular Speed [24]. Baghli *et al.* [25] used two MEMS accelerometers, located at a certain distance from the rotor centre and with 180° phase difference so as to average out the gravitational component. The system was powered using rotor-mounted batteries and trialled both Bluetooth and Nordic radio protocols for wireless transmission. The sensing device was successfully applied to measure the instantaneous torque produced by an induction motor coupled to a shaft. Elnady *et al.* [26] focused on using MEMS accelerometers for condition monitoring. They identified the split of the resonance peak in the response spectrum into two peaks, shifted by the addition and subtraction, respectively, of the operating speed frequency. In [27], Elnady and his colleagues also attempted to produce a simple model to predict their output, although errors were made in the derivation.

The literature therefore shows that MEMS accelerometers can be rotor-mounted to provide detailed vibration measurement of rotors. Their small size and low-cost are desirable characteristics for any rotating machine. In addition, and the evolution of electronics in recent years and the fact that MEMS accelerometers can output digital information means that providing the accelerometers with fast and reliable wireless data transmission is simple and cost-effective. However, sensors installed on the rotor would require power to be transmitted to the rotating shaft, either by sliprings or contactless transmission, which leads to a more complex design. Further, all of the uses reported in the literature have simply attached the MEMS accelerometers and wireless transmission systems to the outer surface of the rotor. If these sensors are to be used within widely implementable active control systems, their placement must not interfere with the machine's working components, and so further development would be required to find a topology which provides a less intrusive installation.

Eddy current displacement sensors Displacement transducers gained popularity over casing-mounted accelerometers as demand for ever more accurate vibration sensing increased. Contactless displacement sensors must be installed within the stator itself, which can be a complex procedure when dealing with fully enclosed rotating machines. However, they provide a direct measurement

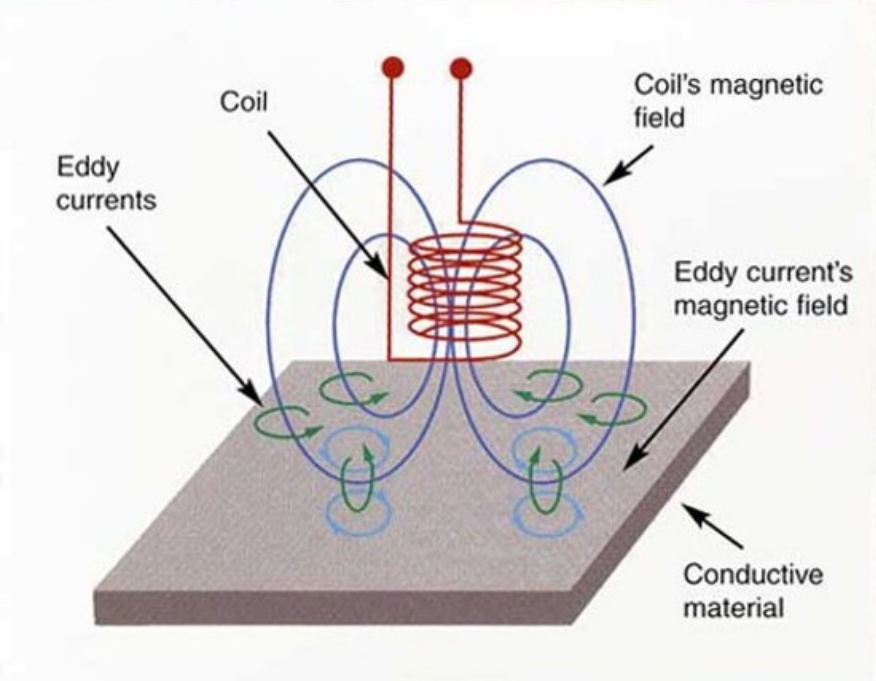

Figure 2.5: Principle of operation of eddy current displacement sensors. Image courtesy of the NDT Education Resource Centre of the Iowa State University.

of the rotor vibration, and hence the data obtained through them is much less dependent on the signal extraction method used. They have been applied to a wide range of rotating machines, typically as part of a condition monitoring systems [16, 28], and have become ubiquitous in Active Magnetic Bearing systems [29].

The most common form of displacement transducers are eddy current sensors. These use a probe which produces a changing magnetic field through a coil, and is placed close to the conductor whose displacement is to be measured. The changing magnetic field generates eddy currents in the target, which in turn change the impedance of the probe coil. This principle is illustrated in Fig. 2.5. The variation in impedance can be measured with a bridge circuit and will be proportional to the separation between the probe and the conductor. In this way, the distance of a conducting target can be measured. The voltage output of the bridge circuit will typically be small, and so will often require amplification. Thus, an eddy current sensor measurement system will usually consist of a probe, a power supply and an amplifier.

Eddy current sensors are contactless, display high bandwidth and resolution, and can be relatively cost-effective. Another benefit is that of being able to measure displacement directly, which can be very valuable when monitoring gap clearances. On the other hand, Pfister *et al.* [30] discussed some of their drawbacks. For instance, the fact that the sensors require a conductive target

means they are unsuitable for use with non-metallic rotors, which have been considered as a potential future development in rotating machinery [31, 32]. Eddy current sensor measurements will also be influenced by the outer shape of the rotor, which can cause out-of-roundness to be misinterpreted as vibrational motion. This error source is known as mechanical runout, and its mitigation typically requires the use of an auxiliary sensor such as an encoder. In addition, local variations in material properties of the rotor produce changes in conductivity which lead to a similar type of error: electrical runout. This phenomenon is much more significant in materials with high permeability, such as steel.

When considered specifically as part of a generally implementable active control system, eddy current sensors have the principal drawback of interfering with the location of working components. The probes require clear access to a reference surface, which must be metallic and sufficiently smooth. Hence, even if the probes and amplifiers could be miniaturised and mounted on the spinning shaft, they could not be placed at the same locations as magnets, turbine blades or seals.

Strain gauges The measurement of strain is a commonly used vibration sensing technique. Strain gauges consist of a metallic foil which is bonded onto the measurement surface. As the surface deforms under vibration-induced cyclical straining, the area of the foil changes, and, consequently, so does electrical resistance. This is illustrated in Fig. 2.6. A Wheatstone bridge is used to measure this change, and thus infer the straining of the surface. As the change in electrical resistance is small, strain measurement requires signal amplification.

In rotating machines, strain gauges have been used to monitor stresses in turbine blades during development and qualification testing, particularly in the aerospace industry. The strain gauges are placed on the tips of the turbine blades, as shown in Fig. 2.7. This enables the measurement of the strain in the blade during operation, from which the stress can be inferred. Although this technique has been widely used, Knappet and Garcia [33] examined some of its drawbacks, chief amongst which is the fact that the mounting of the gauges is a costly and time consuming process. They also suggest that measurement error is introduced when the gauge is fixed onto the blade, as perfect positioning is not achievable. Additionally, strain gauges are sensitive to thermal expansion caused in the blades by changes in temperature.

Strain gauges were also explored as a sensing technique for an active vibration control system by Sloetjes and de Boer [35]. They bonded strain gauges on the surface of a rotor shaft with a square cross-section, in order to detect the

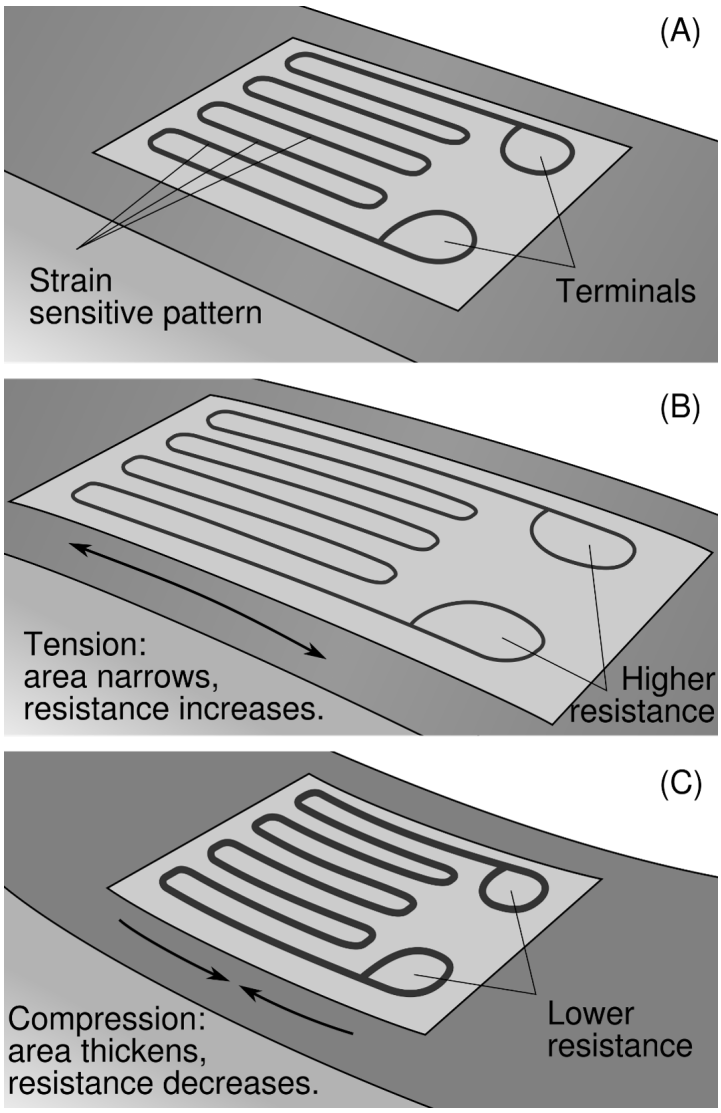

Figure 2.6: Principle of operation of a strain gauge.

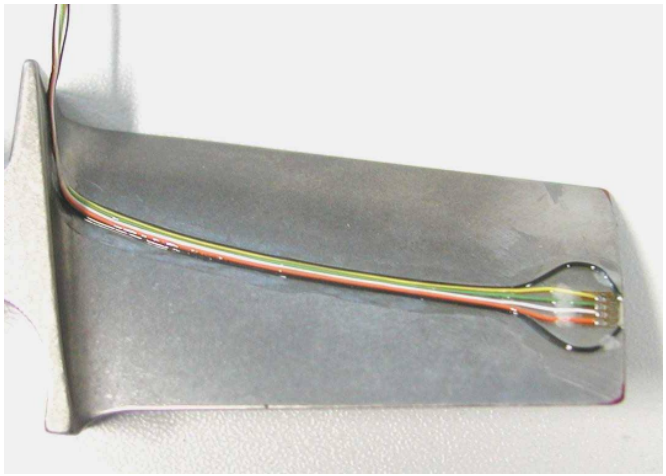

Figure 2.7: Strain gauge instrumented turbine blade. Image courtesy of Polytech [34].

bending of the shaft at critical speeds. Although their research studied the possibility of using harvested energy to enable a self-powered system, the testing rig used a slipring assembly for power and data transmission. They identified a difficulty which may apply to other types of rotor-mounted sensors: that of establishing the zero-output reference accurately. Sensors typically require calibration so that their zero-output state matches the system equilibrium point. In the case of stator-mounted sensor, measurements are given with respect to the stator, which serves as a known, static reference frame. However, the reference point for a rotor-mounted sensor is the idealised zero-vibration equilibrium point, a dynamic state which a rotor in operation may never reach. Thus, establishing an accurate offset can prove challenging. To address this problem, Sloetjes and his colleagues estimated the offset by assuming a zero strain state at low operating speeds.

Strain gauges can provide information on rotor vibration with a considerable degree of accuracy. They are cost effective and widely used in a range of industrial settings. Like other rotor-mounted sensors, strain gauges would require power and data transmission to and from the rotor shaft, but the small voltages and currents involved would make wireless communication a feasible option. However, the use of strain gauges as sensors for generally implementable active control systems has certain drawbacks. Firstly, strain gauges would not be able to detect rigid body modes because the associated mode shapes do not cause the rotor to strain. Secondly, affixing strain gauges on the outer surface of the rotor would interfere with the placement of working components. The gauges could instead be mounted on the inner surface of a hollow rotor, but this presents certain practical challenges due to the difficulty of accessing the space and ensuring the devices are correctly bonded. An alternative option could be to design an inner frame which could be instrumented with strain gauges. If the frame is rigidly connected to the inside of the rotor shaft, a relation between the straining of the shaft and the inner frame can be developed. However, this does not allow a direct measurement of shaft strain, and the dynamics of the frame would have to be considered.

Optical position sensors A recent development in vibration sensing is the use of optical technology. One of the most relevant driving forces behind their development has been the interest in producing non-contact position measurement techniques for gas turbine blades. Two key capabilities have been sought [36]: measurement of blade clearance [37, 38] and Blade Tip Timing (BTT) [39, 40]. The latter, in particular, was developed as an improved blade

stress measurement technique, which could replace the aforementioned strain gauge method. BTT involves measuring the position of the blade tips as they pass an optical sensor fixed to the stator. By comparing the real arrival time of the blade with the static case the deformation of the blade can be inferred and the stresses calculated.

A number of techniques have been developed in order to achieve position measurement with optical sensors. Pfister, Buttner and Czarske [41] provide an overview of some of these, including triangulation [42], focus sensing [43], time-of-flight [44], dual-wavelength interferometry [45] and optical coherence tomography [46]. However, the authors state that most of these techniques are unsuitable for accurate position measurement of fast moving objects. Thus, Pfister and his colleagues [47] introduced the Laser Doppler Distance Sensor (LDDS). The LDDS is an extension of Laser Doppler Velocimetry (LDV), which is a well-established technique used to measure particle velocity in fluid flows and vibration of surfaces [48] and relies on using two intersecting laser beams to produce an interference fringe pattern. Figure 2.8 presents a schematic of a typical application of LDV to measure particle velocity, showing that the fringes are parallel and evenly spaced [49]. When a particle passes through the beam pattern, the frequency of the reflected light will be different from that of the incident light, due to the Doppler effect. By measuring this frequency shift, the velocity of the particle can be inferred. In the LDDS, the laser beams are defocused to produce a fan-shaped interference pattern, making the fringe spacing position dependent. This can be observed in Fig 2.9. Two interference patterns with opposite spacing gradients and produced with beams of different frequency (four beams in total) are superposed. This generates a fringe pattern in which both the velocity and position of a particle can be measured. The complete measurement system is illustrated in Fig. 2.10.

The research team used the LDDS to measure the tip clearance and vibration of a compressor [47]. Further, Gunther *et al.* [50] measured not only the whirling orbit of a rotor, but also its radial expansion, a phenomenon which could be critical for the correct estimation of unbalance of rotors operating at very high speeds.

This new position measurement technique is contactless, boasting very high bandwidths and resolution in the single-digit micron range [50]. Unlike eddy current sensors, they are not dependent on the material of the rotor shaft and, unlike most optical sensors, they are insensitive to surface roughness and the consequent introduction of speckle noise in the measurement signal [41]. As the target of the measurement beams does not need to be smooth, LDDSs can

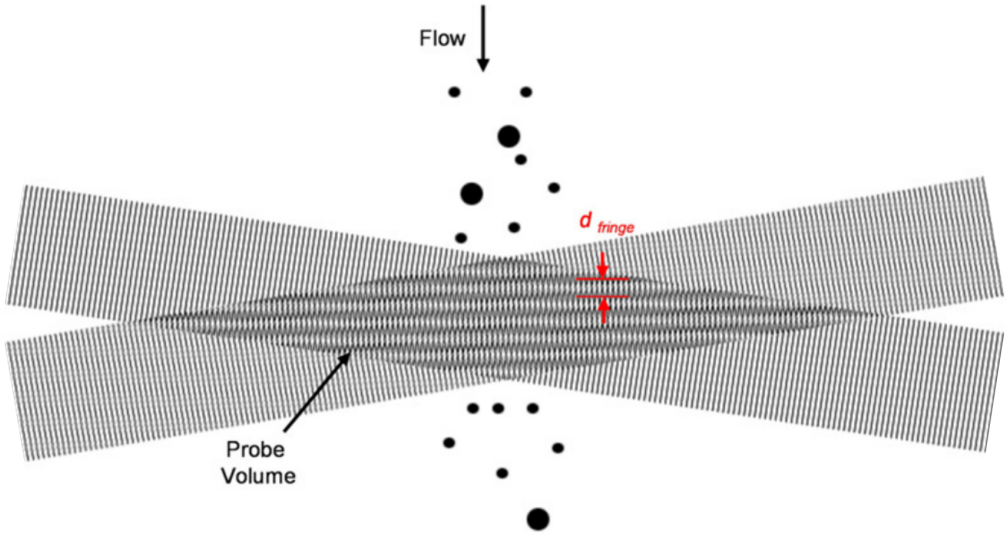

Figure 2.8: Interference patter in Laser Doppler Velocimetry, in which the fringes are parallel and evenly spaced [49].

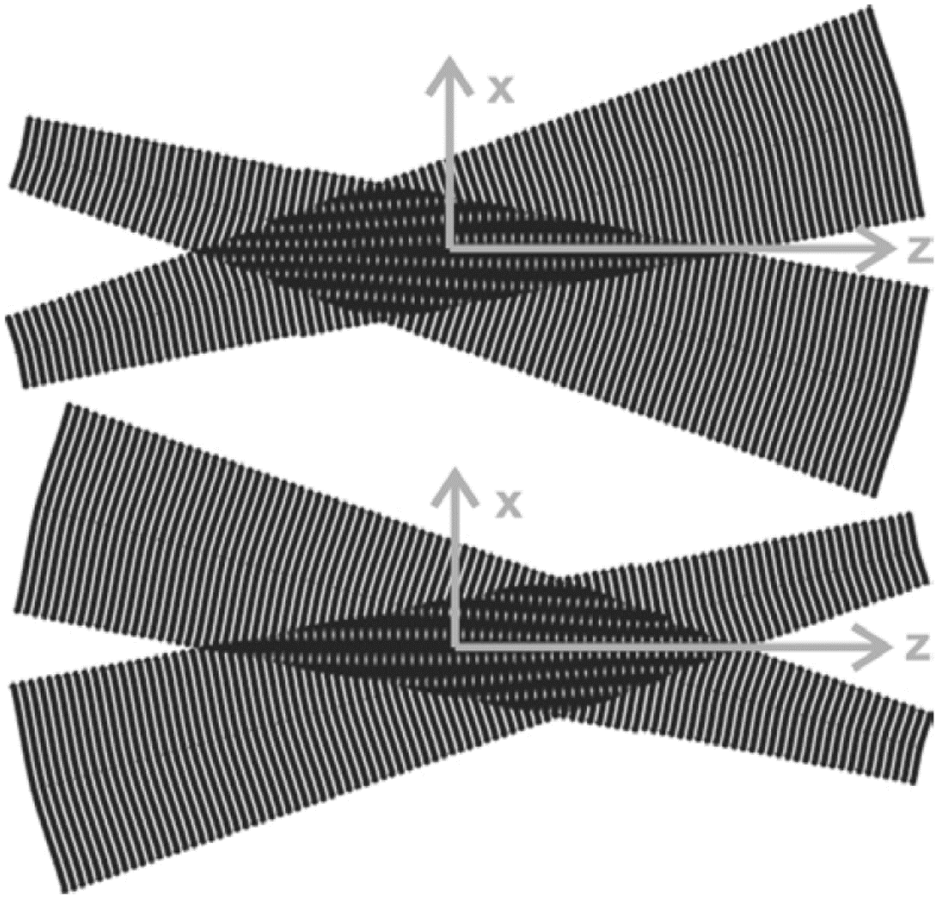

Figure 2.9: Interference patter in Laser Doppler Distance Sensors. Divergent (top) and convergent (bottom) fringe spacing gradients, each having a different light frequency, are superposed to achieve a position-dependent interference pattern [41].

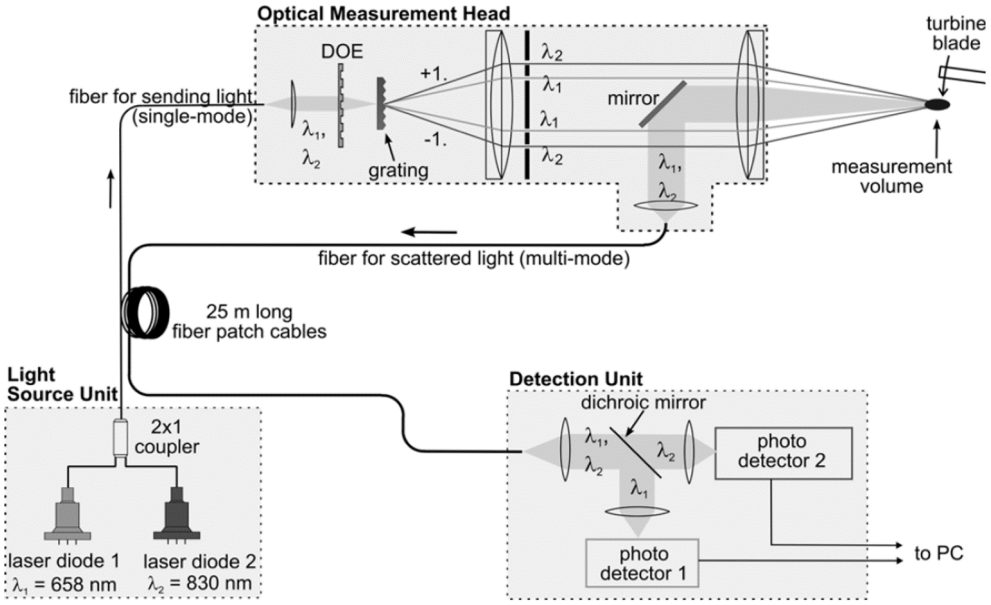

Figure 2.10: Schematic of the Laser Doppler Distance Sensor system [41].

be installed along the length of the stator, even at positions where working components such as turbine blades are located.

Despite these advantageous features, the LDDS is still an experimental technology and hence is costly and highly complex. In an effort to alleviate this, Pfister *et al.* [41] introduced a simpler variant of the LDDS named the Divergent Fringe Sensor (DFS). This uses a single interference fringe pattern and relies on having *a priori* knowledge of the particle velocity to produce a position measurement. In rotating systems, the tangential velocity of the rotor can usually be known with a considerable degree of accuracy, given that the rotational speed and diameter of the shaft are known. Thus, the DFS could prove to be a suitable sensing device for rotating machinery applications. Overall, however, LDDS technology is not currently a feasible option for widely implemented active control systems.

Actuation methods for active vibration control

The development of active control systems has been closely linked to the development of the actuation technology. The reason for this is that actuators can only be used as part of active control systems, whereas sensors have seen a more generalised use in condition monitoring. Thus, actuation serves as an exclusive, enabling technology in active control.

Different techniques for producing control forces have been developed, each with its own strengths and weaknesses. These are discussed in what follows.

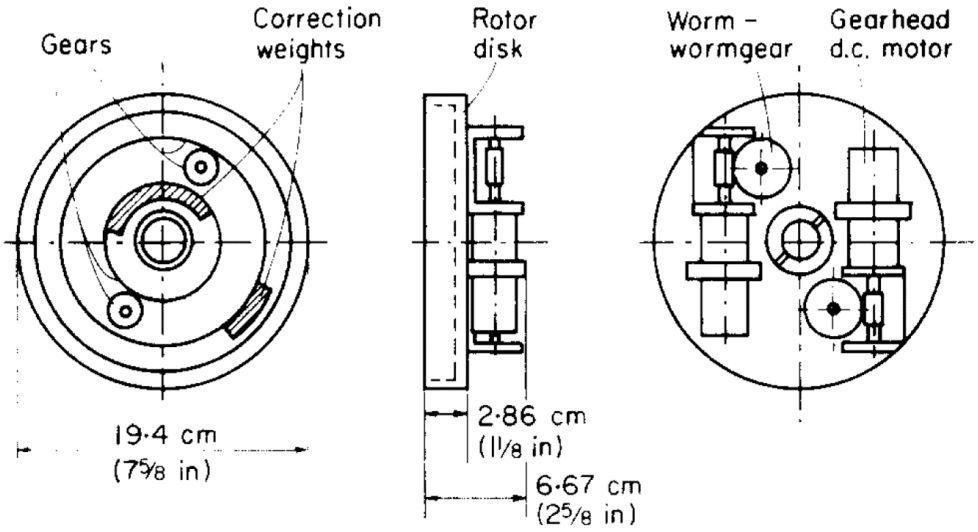

Figure 2.11: Van de Vegte's second mass-balancer design, which used rotating masses to produce a counter-unbalance [52].

Mass balancing The earliest instances of active vibration control methods were developed to tackle unbalance-induced vibration, and so they operated by producing a controllable counter-unbalance. The actuators used were partly conceived as an evolution of passive balancing devices, but in which the balance masses were driven instead of being free-moving. This allowed overcoming some of the limitations of passive balancing devices.

The first such system was proposed by Van de Vegte [51]. He used a single rotor-mounted balancing device, consisting of two motors which could move masses along perpendicular axes on the rotor. This type of device is often referred to as a "mass-balancer". The position of the masses allowed the creation of a counter unbalance. By measuring the vibration at the bearings, a mass position could be determined which would cancel or minimise the overall rotor unbalance. His system was only successful when operating far from critical speeds, but showed that active balancing was feasible. He later introduced a new type of actuator in which two masses could rotate around the rotor centreline [52], shown in Fig. 2.11. The relative position of the masses gives an equivalent heavy spot which can generate any unbalance from 0 g.mm to twice that of a single mass. Lee and Kim [53] provided an evolution of Van de Vegte's system by using wireless transmission of control signals and a rotor-mounted Ni-Cd battery, doing away with the need for sliprings.

Van de Vegte's design had served as the basis for active control technology in the second half of the 20th century, but in 1998 Dyer *et al.* [54] patented a new form of actuator. It consisted of two weighted rings containing permanent magnets which were placed around the spindle. An electromagnet located in the

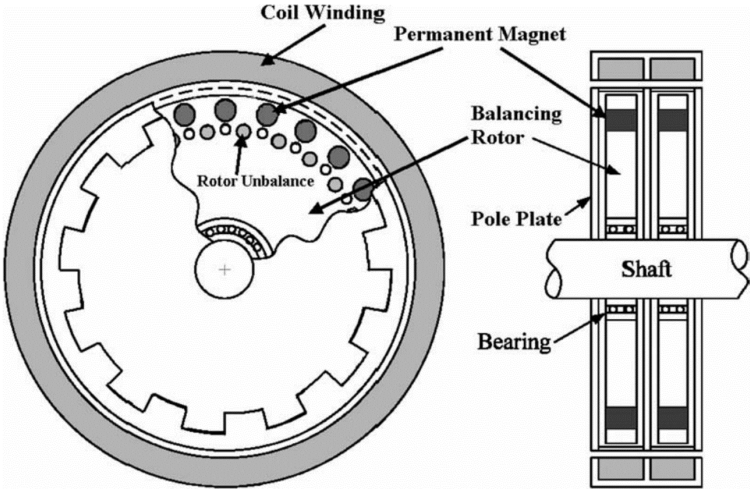

Figure 2.12: Dyer's electromagnetic actuator design, which uses stator-mounted coil windings to control the position of balance discs which contain permanent magnets [56].

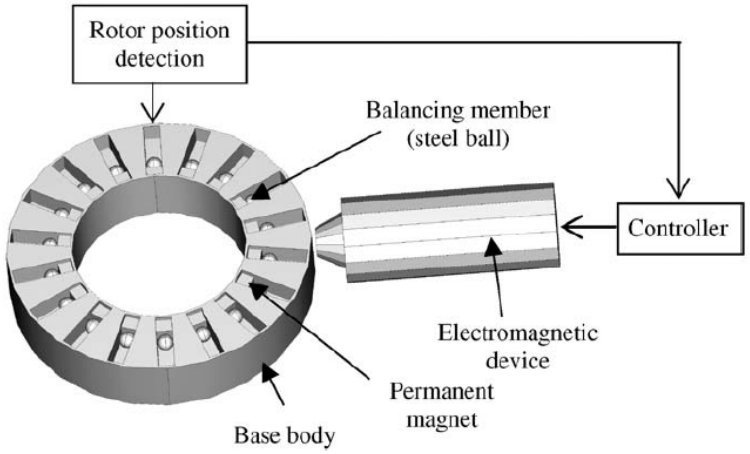

Figure 2.13: Hredzak's ball bearing balancer [57].

stator could be used to change the angular position of the balance rings. The main advantage of this design was that the power and control signals did not have to be transmitted to the rotor, thus avoiding sliprings or wireless transmission systems and reducing the complexity of the rotor. The device has since been made commercially available. Dyer and Ni [55] used it to research technology aimed at reducing vibration of a rotating spindle in high-speed machining, in order to gain higher machining precision.

A more recent innovation in mass-balancer design was proposed by Hredzak and Guo [57]. They developed a balancer based on multiple ball bearings located in radial grooves on a disc, shown in Figure 2.13. Permanent magnets and an electromagnetic actuator enable the balls to be located in one of two radial positions, an inner radius and an outer radius. The distribution of the

balls generates an overall unbalance which can be modified in operation to suit requirements. It was designed for use in balancing hard disk drives, as an alternative to passive balancers. Although innovative, it may prove unsuitable in high speed applications due to the large magnetic forces that would be needed to maintain the balls at the inner location.

The use of piezoelectric ultrasonic motors (PUM) to drive balance masses was proposed by Sloetjes *et al.* [58]. These devices are compact, self-locking and can achieve high speeds, allowing a simple actuator design with many desirable features. Giraud and his colleagues [59] report a positioning resolution of around $0.57°$ at 50 rpm for the same motor used by Sloetjes. These values are comparable to 200-step stepper motors, which suggests that PUMs may be a promising drive technology for compact active balancing systems. Their cost, however, remains high.

In general, mass-balancer actuators prove to be relatively simple, compact and cost-effective solutions. A further positive feature, which has not yet been explored in literature, is the possibility of continuously moving the masses during operation, which could allow these actuators to produce sub- or super-synchronous forces, suitable for tackling vibration sources other than unbalance. However, two distinct drawbacks would require further development. Firstly, having to mount the actuators on the rotating shaft could yield complex rotor designs, and may limit the performance capabilities of the devices. Secondly, the actuators require both power and data, which impose the use of sliprings or contactless transmission. The former is usually undesirable due to the associated maintenance requirements. The latter, however, could prove to be a viable alternative, thanks to the evolution of compact and cost-effective wireless transmission technology used in the consumer electronics industry.

Active Magnetic Bearings The most widely used form of active actuation is Active Magnetic Bearing (AMB) technology. These devices use electromagnetic fields to generate a force with which a rotor can be levitated, enabling contactless support. Despite the complexities associated with implementing AMB systems, they have gained acceptance in a number of industries thanks to their unique characteristics. Their ability to operate with no mechanical wear is a highly desirable trait in applications such as flywheels and blowers. They have also seen use in turbomolecular vacuum pumps due to their lubrication-free design. Because of their principle of operation, AMBs can also provide active vibration control capability, a feature which is gaining importance in industrial settings [29].

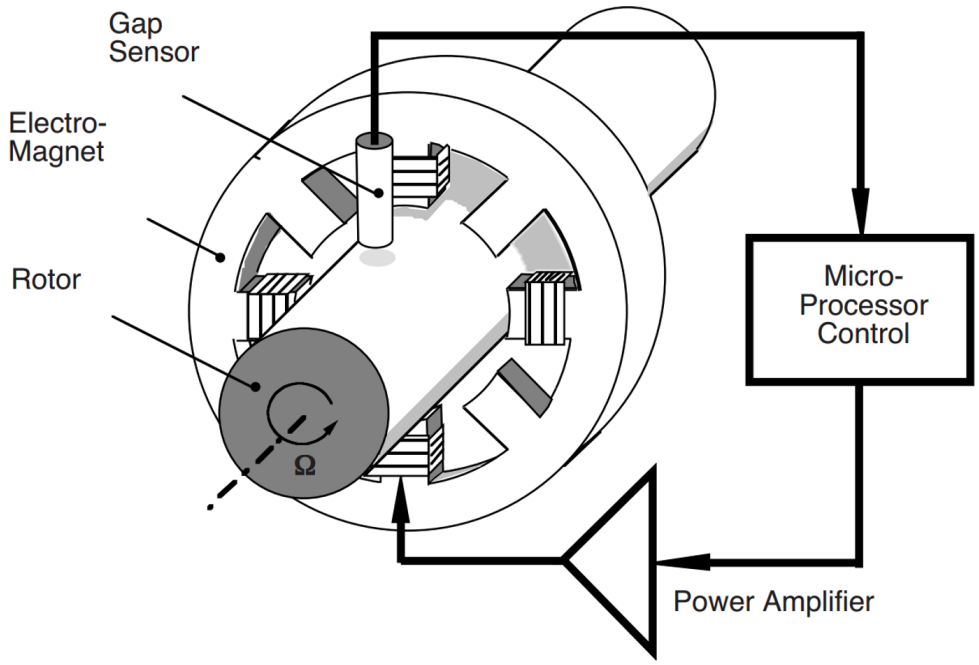

Figure 2.14: Schematic of a magnetic bearing system, with main constituent elements labelled [29].

Figure 2.14 presents a schematic diagram of a magnetic bearing system. It consist of a stator-based electromagnet, which is controlled by a microprocessor and a power amplifier. The rotor, which is either ferromagnetic or may be fitted with a ferromagnetic collar, is suspended on the magnetic field. The magnetic levitation is inherently unstable, and so the rotor's position is continuously measured by a gap sensor so that a stabilising controller may be applied.

The force produced by an AMB is determined by controlling the current in the electromagnet coil windings. Apart from levitating the rotor, this allows the application of a synchronous force which can be used to counteract the effect of unbalance. The ability to vary their stiffness and damping characteristics also permits multi-objective control methodologies, for instance minimising rotor displacement or transmitted bearing force, depending on which objective is most important at a particular speed [60].

The first known application of magnetically supported rotors was in centrifuges used for molecular sedimentation, in the late 1930s [61]. The systems were highly complex, relying on vacuum tubes for electronic control, and so were not used outside of academic environments. The invention of the transistor in the late 1940s would pave the way for more practical designs, which were successfully applied to attitude control systems in spacecraft in the 1980s [62]. The main driver behind their development was the desire for a lubrication- and wear-free bearing design. However, with the evolution of digital control

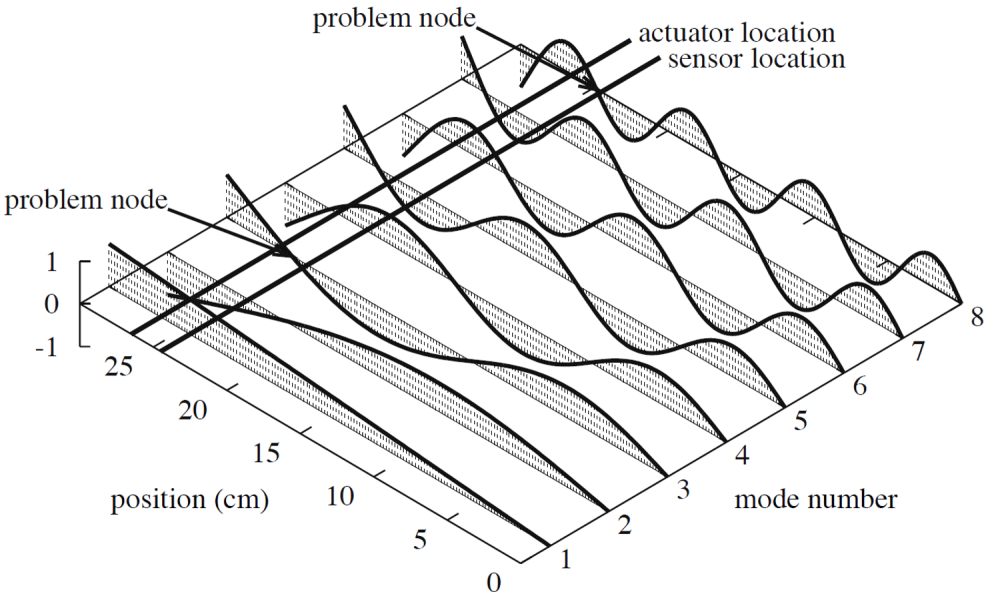

Figure 2.15: Mode shapes of a flexible rotor for a non-collocated AMB setup [29]. Issues can arise if the mode shape node lies between the sensor and actuator positions.

and the possibilities offered by improving computing capability, much of the research focus in the later parts of the 20th century turned to developing new methods that enabled not only levitation of the rotor but also active control of its vibration, for example [63–65]. AMB systems have since remained an active field of study, and a comprehensive analysis of notable opportunities for further development is provided by Schweitzer [66].

Although AMBs are currently the most developed solution to provide active control capability, they display certain drawbacks which can limit their generalised implementation. Firstly, existing AMB systems are bulky and complex, requiring substantial space in the stator for their installation. This limits the practical number of AMB actuators that could be used in compact rotating machines. Due to the physical layout of the AMB system, non-collocation of sensors and actuators is unavoidable at present. When a node of a mode shape of a flexible rotor lies between the sensor and actuator, as depicted in Fig. 2.15, a $180°$ phase error is introduced, which can make control much more difficult [29]. Further, AMBs require a substantial and continuous power supply, which may be impractical in many applications. Finally, AMB systems can be costly to produce, particularly the power amplifiers. Although reduced maintenance requirements could partly offset this, their installation would substantially increase the production costs of most rotating machines.

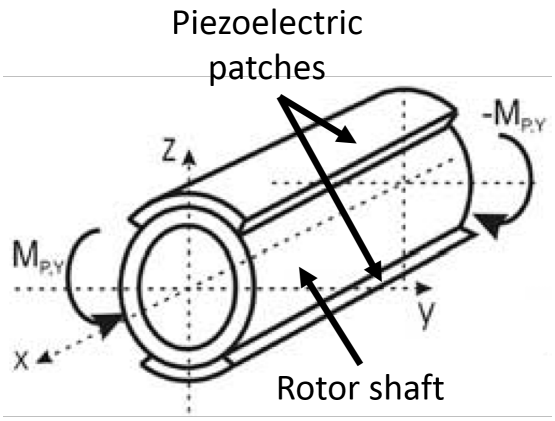

Figure 2.16: Schematic of a typical piezoelectric patch actuation system [67].

Piezoelectric patches In more recent times, researchers have explored the possibilities offered by piezoelectric patches as a form of actuation in active control systems. These are bonded onto the surface of the rotor in pairs placed at $180°$ from each other, as shown in Fig. 2.16. They work by applying strains (tensile on one side, compressive on the other) along the rotor axis, thus generating a bending moment.

Kunze et al. [68] applied the patches to an automotive drive shaft, with the aim of reducing the rotor vibration at the first critical speed. Horst and Wolfel [67] were the first to undertake detailed study into the use of piezoelectric patches for active vibration control in rotating machines. They successfully reduced vibration of the first and second critical speeds in their experimental rig. Sloetjes and De Boer [35] explored using the patches as an active damping device, where the vibration energy was dissipated by harvesting the electric current generated. This electrical charge could be stored in capacitors and then used to power the patches to actively reduce rotor vibration further. Due to the fact that internal damping has a destabilising effect beyond the first critical speed, they developed a low frequency feedback control methodology which allows the patches to, in essence, act as stator damping and is thus strictly stabilising.

In general, piezoelectric patches have been shown to be effective at correcting the modal bending of the rotor when passing critical speeds. In addition, their strain-based operation could prove ideal if applied to tackling thermal warping. However, they display certain drawbacks which limit their generalised implementation. Firstly, the patches require surface bonding, which impedes placing any other working component or sensor at the same position as the patch. In addition, piezoelectric materials display low strains (typically 0.1% to

0.3% [69]), which means that patches of practical length posses only limited force capacity. These two characteristics combined imply that a fully active rotor system based on piezoelectric patches would demand long rotors with poor power density. Another drawback is that piezoelectric actuation requires high voltages, which would impose the use of sliprings as the only practical method to supply power. Sliprings can be bulky and require considerable maintenance, making them undesirable in many applications.

Others Other forms of actuation for active or semi-active vibration control systems have been suggested in the past, although none have developed beyond academic research. For instance, Smalley *et al.* [70] proposed the use of metal or ceramic material deposition on a rotor as an on-line balancing technique, and even demonstrated the principle in an experimental rig. Furman [71] introduced a balancing technique in which masses attached to the rotor could be plastically deformed by using pulsed radiant heating, thus enabling the rotor to be rebalanced. Zumbach *et al.* [72] attached heating elements to a spinning rotor, which allowed controlled bending of the rotor to counteract the effects of unbalance. Blanco-Ortega and his colleagues [73] proposed a rotor system with axially translating bearings, which enabled changing the effective length of the rotor and, thus, modify its dynamic behaviour.

Control methods for active vibration control

The performance of an active control system depends strongly on the controller used. Even systems with only a few poorly located sensors and actuators can achieve good vibration control with the appropriate technique.

In general, the basis of all controllers is to establish a relation (transfer function or state space) between a measured phenomenon and controllable actuation parameters, which can enable a desired system state. In the context of rotating machines, the controller typically relates the unbalance-induced vibration measured by the sensors to the source of vibration, so that the rotor may then be re-balanced or control forces applied. Most rotor control methods described in literature require a certain degree of *a priori* knowledge of the transfer function of the system, and can be broadly classified as “estimated” or “modelled”.

Estimation-based a priori control In estimation-based methods the transfer function is approximated through discrete measurements of the rotor response obtained from trial runs under known input conditions. The most prominent

example of this is the Influence Coefficient (IC) method, which was used in all early work involving active mass balancing. For instance, in [74] Van de Vegte used two balancing planes to study linear and quadratic IC-based control schemes. Gosiewski [75, 76], suggested using Van de Vegte's actuator design together with a computer loaded with previously measured influence coefficients, providing improved control compared to the original system. Although Gosiewski's work was purely theoretical, he suggested valuable ideas such as the possibility of using the actuators to generate the influence coefficient table on-line, reducing the number of required trial runs before operation. Lee and Kim's original actuation device was manually controlled, but they presented further work [77] in which a fully automatic control algorithm was developed and tested. An adaptive influence coefficient method was used, with a single initial low speed measurement and subsequent updates being performed on-line. The system was designed to activate when a certain vibration threshold was reached and then the influence coefficients would be updated and the required counter unbalance calculated. This method allowed the first and second critical speeds to be passed without a significant increase in rotor vibration, each needing 4 updates of the balancer position.

On-line coefficient estimation was also used by Dyer and Ni [55] to improve controller performance under changing operating conditions. They explored multi-plane balancing using their electromagnetic actuator and focused on robustness and minimisation of error when estimating influence coefficients. They studied the case where plant dynamics vary due to tool changes in mills, and even considered non-linear stiffening of the spindle due to large vibration amplitudes. The stability of the methods developed by Dyer and Ni was studied by Kim and Lee [78]. Chen *et al.* [79] studied the motion of the balance masses during operation and developed a control algorithm to reduce the rotor vibration during the balancing process. Influence coefficient methods have also been applied to active control with AMBs, for instance in the work of Sahinkaya *et al.* [80].

Controllers that estimate the system transfer function rely on the accuracy of the measurements and on performing sufficient trials to cover the full spectrum of operating conditions. Thus, they are most suitable for machines which typically operate under stable, known conditions. Their great advantages are that they are relatively simple to implement, and, with modern automation methods, can require a minimum of human intervention once the initial trials have been performed. On the other hand, these methods make assumptions about the transfer function between vibration state and the actuation param-

eters. This means that they are typically ill-suited to deal with unexpected vibration, so may be less robust in the face of uncertainty.

Model-based a priori control The transfer function in a control problem may also be modelled based on known system parameters. The most common method of rotor modelling involves the finite element technique, which was analysed thoroughly by Nelson and McVaugh [81, 82]. In model-based control, an accurate model of the system must be first derived and validated. During operation, the controller can compare the currently measured system state to that predicted by the model under the assumed operating conditions. If the model is able to closely simulate the real case, then any discrepancies can be assumed to be caused by disturbances, and hence a control signal can be produced to reduce them. A wide range of model-based techniques have been developed, driven partly by the evolution of computing in recent times, which has enabled ever more detailed models to be constructed at ever lower cost. A detailed review of the various types exceeds the scope of this dissertation, but some examples of model based controllers applied to rotors include adaptive controllers [83], fuzzy logic controllers [84, 85], μ-synthesis techniques [86–88] or sliding mode control [89]. Model-based techniques are prevalent in AMBs, most notably robust H_∞ controllers, which were studied prominently by Japanese researchers around the turn of the 20$^{\text{th}}$ century [90–93].

Model-based controllers enable forms of complex control which are usually not possible with estimation-based techniques. For instance, H_∞ control enables disturbance rejection by modifying the sensitivity of a system over its frequency response, while sliding mode control is able to tackle non-linear problems. A strength of model-based techniques is that they can provide information regarding systems states that would not normally be accessible. When used in this form, models are referred to as "state observers" [94]. The principal drawbacks of controllers that utilize simulated system characteristics is their dependence on the degree of detail adopted in the model and the accuracy of the parameters used. In many instances, obtaining a sufficiently detailed model can be a difficult and time-consuming task, requiring considerable expertise and knowledge of the underlying physical processes. Some physical phenomena, such as mechanical wear, can rarely be measured and accounted for in a practical manner. Consequently, model-based methods may not be a sufficiently flexible tool to allow generalised implementation of active control in rotating machines, despite the powerful control capabilities they offer.

2.3 Discussion and research gaps

The review of current literature on active vibration control of rotating machines leads to a number of observations. Firstly, it becomes apparent that active control systems are not yet widely implemented in rotating machines. Active Magnetic Bearing systems are the most developed and common embodiment of them. Nonetheless, their implementation is mostly limited to a few specific applications. In addition, the main drivers behind their uptake are usually their passive characteristics, such as lubrication- and wear-free operation, rather than their active control capability. Most of the other active control technologies reviewed have been largely confined to academic research. A reason for this is that the additional cost and complexity of these systems may be difficult to justify in many rotating machine applications, unless high degrees of vibration control are essential. However, the literature review also reveals the potential benefits of active control technology. In particular, its capacity to increase machine lifetime through vibration reduction and to improve fault prevention through better condition monitoring would be beneficial in a vast range of applications. It would seem, therefore, that further research into active vibration control system designs which can be more generally implemented would be highly constructive.

A further limitation observed in currently considered active control systems is the reduced number of sensors and actuators that can be installed on conventional machines. The active components are usually stator-mounted and require access to clear portions of the rotor. This precludes their positioning at the same location as working components and thus constrains their numbers. In addition, the layout of the various parts of a rotor are largely determined by the mechanical needs of the system, and so sensors and actuators are placed wherever space is available. These positions may be far from optimal, located far from seals, turbine blades or permanent magnets, for instance. Ultimately, small numbers of sub-optimally located sensors and actuators will provide poor observability and controllability of rotor vibration, curtailing the performance of the active control system. Consequently, further benefits could be derived from exploring topologies which would not only enable the use of an increased number of sensors and actuators, but also grant designers greater freedom to select optimum locations for these devices.

In order to address these gaps in research, the study of a new active control topology is proposed. A design which could provide benefits in terms of implementability and also observability/controllability is found in internally-

mounted active control systems. This “active rotor” topology would exploit the inner volume available in hollow rotors, which could contain large numbers of compact sensors and actuators. By being contained within the rotor, the active control system would become independent of the stator, which simplifies the overall design of the rotating machine. In addition, the density of working components along the rotor could be maximised without sacrificing active control capability, as no space would be required for sensors and actuators in the working volume. With this design, the active devices could also be freely positioned along the length of the rotor, without interfering with working components and enabling placement at critical locations such as seals and turbine blades. Another desirable feature is that the sensors and actuators would be naturally protected from the working environment, improving their robustness to changing operating conditions and increasing their lifetime.

Out of the sensing technologies reviewed, only strain gauges and MEMS accelerometers would have the capacity to provide sensing while being mounted within a hollow rotor. However, as mentioned earlier, strain gauges would need to be affixed to an internal frame, which would only be able to provide an indirect measurement of strain. Thus, MEMS accelerometers emerge as the most promising technology. The evolution of these sensors in recent times, driven by the needs of the consumer electronics industry, has provided compact and easily integratable accelerometers to be available at very low cost. Using large numbers of these within a rotor is therefore feasible from the perspectives of both costing and physical installation. The devices can be mounted within a shaft in a practical manner and also provide a direct measurement of rotor vibration.

In terms of system actuation, the literature review reveals that only two technologies are capable of producing stator-independent control forces, which would make them suitable for active rotors. These are piezoelectric patches and mass-balancers. Internal installation of piezoelectric patches would be a complex task, and the system would have to be provided with a high voltage power supply for their operation. Thus, mass balancing emerges as the best option for active rotors. The actuators can be made small and at low cost, using off-the-shelf components such as stepper motors.

From the perspective of the control method, both estimation- and model-based techniques appear balanced in terms of strengths and weaknesses. The former are typically simple to implement but may struggle to deal with unexpected vibration and uncertainty. The latter, on the other hand, can provide more powerful and robust control solutions, but the construction of accurate models requires a degree of expertise and system knowledge which may not be

generally available. It would seem, therefore, that alternative solutions which are better suited to active control of rotating machines should be developed. As the limitations of existing techniques stem, fundamentally, from constructing the transfer function, it would be beneficial to explore options which do not rely on such a process, that is, *non a priori* control techniques.

Thus, after a review of the state of the art in active vibration control in rotating machines, it is concluded that the study of active rotors should be undertaken to address the scant implementability and layout-related limitations of existing systems. The topology to be investigated consists of a hollow rotor in which MEMS accelerometers and mass-balancer actuators are mounted. If feasible, such a design could provide a cost-effective and flexible solution which would enable a more general implementation of active control technology in rotating machines. In addition, the development of a *non a priori* controller should be undertaken in order to provide a technique which is both simple to implement and robust in the face of uncertainty.

2.4 Aims and objectives

To undertake the proposed research, a series of aims and objectives were identified. These aims are presented in the following, with the objectives set to achieve each of them listed below.

A1 To demonstrate the **feasibility** of internally mounted active control systems

- **O1** Construct a computational model of the system
- **O2** Build a fully functional prototype

A2 To understand the behaviour of **internally mounted accelerometers**

- **O3** Derive an analytical model of sensor output
- **O4** Develop techniques to maximise vibration information extraction
- **O5** Identify and address sources of measurement error

A3 To establish **control techniques** suitable for use with internal topologies

- **O6** Develop a *non a priori* controller for internal topologies

A4 To assess the **application** of active rotors to existing challenges

- **O7** Apply active rotor designs to tackle non-collocation issues in AMBs

2.5 Summary

- The goal of this dissertation is to develop active control systems which can be more generally implemented in rotating machines.
- A review of literature related to vibration management in rotating machine was conducted.
- The identified research gaps may be addressed by exploring a novel "active rotor" topology.
- The proposed concept should consist of a hollow rotor with internally mounted MEMS accelerometers, mass-balancer actuator and a *non a priori* controller.

References

[1] S. Zhou and J. Shi, "Active balancing and vibration control of rotating machinery: a survey," *Shock and Vibration Digest*, vol. 33, no. 5, pp. 361–371, 2001.

[2] V. Wowk, *Machinery Vibration: Balancing*. McGraw-Hill Upper Saddle River, New York, USA, 1995.

[3] L. P. Grobel, "Balancing turbine-generator rotors," *General Electric Review*, vol. 56, no. 5, 1953.

[4] T. P. Goodman, "A least-squares method for computing balance corrections," *Journal of Engineering for Industry*, vol. 86, no. 3, pp. 273–277, 1964. 10.1115/1.3670532.

[5] M. S. Darlow, "Balancing of high-speed machinery: Theory, methods and experimental results," *Mechanical Systems and Signal Processing*, vol. 1, no. 1, pp. 105–134, 1987.

[6] M. Leblanc, "Automatic balancer for rotating bodies." U.S. Patent No. 1209730, 1916.

[7] E. I. Thearle, "A new type of dynamic-balancing machine," *Transactions of the ASME*, vol. 54, pp. 131–141, 1932.

[8] R. Horvath, G. T. Flowers, and J. Fausz, "Passive balancing of rotor systems using pendulum balancers," *Journal of Vibration and Acoustics*, vol. 130, no. 4, p. 041011, 2008.

[9] C. Rajalingham and S. Rakheja, "Whirl suppression in hand-held power tool rotors using guided rolling balancers," *Journal of Sound and Vibration*, vol. 217, no. 3, pp. 453–466, 1998.

[10] W. Kim and J. Chung, "Performance of automatic ball balancers on optical disc drives," *Proceedings of the Institution of Mechanical Engineers, Part C: Journal of Mechanical Engineering Science*, vol. 216, no. 11, pp. 1071–1080, 2002.

[11] N. van de Wouw, M. N. van de Heuvel, H. Nijmeijer, and J. A. van Rooij, "Performance of an automatic ball balancer with dry friction," *I. J. Bifurcation and Chaos*, vol. 15, no. 1, pp. 65–82, 2005.

[12] C. R. Fuller, S. Elliot, and P. A. Nelson, *Active control of vibration*. Academic Press, 1996.

[13] K.-O. Olsson, "Limits for the use of auto-balancing," *International Journal of Rotating Machinery*, vol. 10, no. 3, pp. 221–226, 2004.

[14] M. A. Meraz, C. Jiménez, A. Yánez, and R. Pichardo, "Self balancing system for rotating mechanisms," *Revista Facultad de Ingeniería - Universidad de Tarapacá*, vol. 13, no. 2, pp. 59–64, 2005.

[15] B. K. N. Rao, *Handbook of Condition Monitoring*. Oxford: Elsevier, 1996.

[16] R. Barron, *Engineering condition monitoring : practice, methods and applications*. Harlow: Longman, 1996.

[17] P. Tavner, L. Ran, J. Penman, and H. Sedding, *Condition Monitoring of Rotating Electrical Machines*. Institution of Engineering and Technology, 2008.

[18] J. G. Korvink, *MEMS A Practical Guide to Design, Analysis, and Applications*. Dordrecht: Dordrecht : Springer, 2010.

[19] M. J. Gómez, C. Castejón, J. C. García-Prada, and J. López, "Experimental analysis and validation of a vibration-based technique for crack detection in a shaft," in *Proceedings of the 9th IFToMM International Conference on Rotor Dynamics* (P. Pennacchi, ed.), (Milan, Italy), pp. 373–383, Springer International Publishing, 2014.

[20] C. Shravankumar, R. Tiwari, and A. Mahibalan, "Experimental identification of rotor crack forces," in *Proceedings of the 9th IFToMM International Conference on Rotor Dynamics* (P. Pennacchi, ed.), (Milan, Italy), pp. 361–371, Springer International Publishing, 2014.

[21] A. Muszyńska, *Rotordynamics*. Taylor & Francis, 2005.

[22] J. T. Broch, *Mechanical vibration and shock measurements*. Brüel& Kjær, 1984.

[23] L. Arebi, F. Gu, and A. Ball, "Rotor misalignment detection using a wireless sensor and a shaft encoder," in *Future Technologies in Computing and Engineering. Proceedings of Computing and Engineering Annual Researchers' Conference CEARC'10*, (Huddersfield, UK), pp. 6–13, 2010.

[24] L. Arebi, F. Gu, and A. Ball, "A comparative study of misalignment detection using a novel wireless sensor with conventional wired sensors," in *Journal of Physics: Conference Series*, vol. 364, p. 012049, IOP Publishing, 2012.

[25] L. Baghli, J. F. Pautex, and S. Mezani, "Wireless instantaneous torque measurement, application to induction motors," in *19th International Conference on Electrical Machines, ICEM*, (Rome Italy), 2010.

[26] M. Elnady, J. Sinha, and S. Oyadiji, "Identification of critical speeds of rotating machines using on-shaft wireless vibration measurement," in *Journal of Physics: Conference Series*, vol. 364, p. 012142, IOP Publishing, 2012.

[27] M. Elnady, A. Abdelbary, J. Sinha, and S. Oyadiji, "FE and experimental modeling of on-shaft vibration measurement," in *15th International Conference on Aerospace Sciences & Aviation Technology*, (Cairo, Egypt), pp. 1–18, 2013.

[28] B. Koo, C.-H. Kim, J. S. Lee, T. H. Kim, and K. Sim, "Analysis and experimental test of a 200 kw oil-free micro gas turbine simulator," in *Proceedings of the 9th IFToMM International Conference on Rotor Dynamics* (P. Pennacchi, ed.), (Milan, Italy), pp. 307–319, Springer International Publishing, 2014.

[29] E. H. Maslen and G. Schweitzer, *Magnetic Bearings: Theory, Design, and Application to Rotating Machinery*. Springer, 2009.

[30] T. Pfister, P. Gunther, F. Dreier, and J. Czarske, "Dynamic rotor deformation and vibration monitoring using a non-incremental laser doppler distance sensor," in *AIP Conference Proceedings*, vol. 1253, (Ancona, Italy), p. 361, 2010.

[31] O. Song, L. Librescu, and N. Jeong, "Vibration and stability control of smart composite rotating shaft via structural tailoring and piezoelectric strain actuation," *Journal of Sound and Vibration*, vol. 257, no. 3, pp. 503–525, 2002.

[32] M.-Y. Chang, J.-K. Chen, and C.-Y. Chang, "A simple spinning laminated composite shaft model," *International journal of solids and structures*, vol. 41, no. 3, pp. 637–662, 2004.

[33] D. Knappett and J. Garcia, "Blade tip timing and strain gauge correlation on compressor blades," *Proceedings of the Institution of Mechanical Engineers, Part G: Journal of Aerospace Engineering*, vol. 222, no. 4, pp. 497–506, 2008.

[34] U. Retze and M. Schussler, "Dynamic stress and strain measurement." Polytec Ltd., `http://www.polytec.com/fileadmin/user_uploads/Applications/InFocus/Full_Papers_1_2010/OM_TP_InFocus_Strain_2010_02_E.pdf`, 2010. Online. Accessed 11 - December - 2016.

[35] P. Sloetjes and A. de Boer, "Vibration reduction and power generation with piezoceramic sheets mounted to a flexible shaft," *Journal of Intelligent Material Systems and Structures*, vol. 19, no. 1, pp. 25–34, 2008.

[36] A. von Flotow, M. Mercadal, and P. Tappert, "Health monitoring and prognostics of blades and disks with blade tip sensors," in *IEEE Aerospace Conference Proceedings*, vol. 6, (Big Sky, Montana), pp. 433–440 vol.6, 2000.

[37] J. P. Barranger and M. J. Ford, "Laser-optical blade tip clearance measurement system," *Journal of Engineering for Power*, vol. 103, no. 2, pp. 457–460, 1981. 10.1115/1.3230742.

[38] S. B. Lattime and B. M. Steinetz, "High-pressure-turbine clearance control systems: Current practices and future directions," *Journal of Propulsion and Power*, vol. 20, no. 2, pp. 302–311, 2004.

[39] S. Heath and M. Imregun, "An improved single-parameter tip-timing method for turbomachinery blade vibration measurements using optical laser probes," *International Journal of Mechanical Sciences*, vol. 38, no. 10, pp. 1047–1058, 1996.

[40] M. Zielinski and G. Ziller, "Noncontact vibration measurements on compressor rotor blades," *Measurement Science and Technology*, vol. 11, no. 7, p. 847, 2000.

[41] T. Pfister, L. Büttner, and J. Czarske, "Laser doppler sensor employing a single fan-shaped interference fringe system for distance and shape measurement of laterally moving objects," *Applied Optics*, vol. 48, no. 1, pp. 140–154, 2009.

[42] R. G. Dorsch, G. Häusler, and J. M. Herrmann, "Laser triangulation: fundamental uncertainty in distance measurement," *Applied Optics*, vol. 33, no. 7, pp. 1306–1314, 1994.

[43] E. Shafir and G. Berkovic, "Expanding the realm of fiber optic confocal sensing for probing position, displacement, and velocity," *Applied Optics*, vol. 45, no. 30, pp. 7772–7777, 2006.

[44] P. Palojarvi, K. Maatta, and J. Kostamovaara, "Integrated time-of-flight laser radar," *IEEE Transactions on Instrumentation and Measurement*, vol. 46, no. 4, pp. 996–999, 1997.

[45] H. J. Tiziani, A. Rothe, and N. Maier, "Dual-wavelength heterodyne differential interferometer for high-precision measurements of reflective aspherical surfaces and step heights," *Applied Optics*, vol. 35, no. 19, pp. 3525–3533, 1996.

[46] M. Wojtkowski, V. J. Srinivasan, T. H. Ko, J. G. Fujimoto, A. Kowalczyk, and J. S. Duker, "Ultrahigh-resolution, high-speed, fourier domain optical coherence tomography and methods for dispersion compensation," *Optics Express*, vol. 12, no. 11, pp. 2404–2422, 2004.

[47] T. Pfister, L. Büttner, J. Czarske, H. Krain, and R. Schodl, "Turbo machine tip clearance and vibration measurements using a fibre optic laser doppler position sensor," *Measurement Science and Technology*, vol. 17, no. 7, p. 1693, 2006.

[48] H. E. Albrecht, N. Damaschke, M. Borys, and C. Tropea, *Laser Doppler and phase Doppler measurement techniques*. Springer Science & Business Media, 2013.

[49] M. Arman, K. Lyes, and G. Afshin, "Measurement of fluid velocity development in laminar pipe flow using laser doppler velocimetry," *European Journal of Physics*, vol. 34, no. 5, p. 1127, 2013.

[50] P. Gunther, F. Dreier, T. Pfister, J. Czarske, T. Haupt, and W. Hufenbach, "Measurement of radial expansion and tumbling motion of a high-speed rotor using an optical sensor system," *Mechanical Systems and Signal Processing*, vol. 25, no. 1, pp. 319–330, 2011.

[51] J. van de Vegte, "Continuous automatic balancing of rotating systems," *Journal of Mechanical Engineering Science*, vol. 6, no. 3, pp. 264–269, 1964.

[52] J. van de Vegte and R. T. Lake, "Balancing of rotating systems during operation," *Journal of Sound and Vibration*, vol. 57, no. 2, pp. 225–235, 1978.

[53] C.-W. Lee and Y.-D. Kim, "Modal balancing of flexible rotors during operation: Design and manual operation of balancing head," *Proceedings of the Institution of Mechanical Engineers, Part C: Journal of Mechanical Engineering Science*, vol. 201, no. 5, pp. 349–355, 1987.

[54] S. W. Dyer, B. K. Hackett, and J. Kerlin, "Electromagnetically actuated rotating machine unbalance compensator." U.S. Patent No. 5757662, 1998.

[55] S. W. Dyer and J. Ni, "Adaptive influence coefficient control of single-plane active balancing systems for rotating machinery," *Journal of Manufacturing Science and Engineering*, vol. 123, no. 2, pp. 291–298, 2000.

[56] J.-D. Moon, B.-S. Kim, and S.-H. Lee, "Development of the active balancing device for high-speed spindle system using influence coefficients," *International Journal of Machine Tools and Manufacture*, vol. 46, no. 9, pp. 978–987, 2006.

[57] B. Hredzak and G. Guo, "New electromechanical balancing device for active imbalance compensation," *Journal of Sound and Vibration*, vol. 294, no. 45, pp. 737–751, 2006.

[58] P. Sloetjes, A. de Boer, and P. van der Hoogt, "Dynamics of piezoceramics-based mass and force actuators for rotating machines," in *14th International Congress on Sound & Vibration*, (Cairns, Australia), 2007.

[59] F. Giraud, B. Lemaire-Semail, J. Aragones, J. P. Robineau, and J. T. Audren, "Precise position control of a traveling-wave ultrasonic motor," *IEEE Transactions on Industry Applications*, vol. 43, no. 4, pp. 934–941, 2007.

[60] M. N. Sahinkaya, A. H. G. Abulrub, and C. R. Burrows, "An adaptive multi-objective controller for flexible rotor and magnetic bearing systems," *Journal of Dynamic Systems, Measurement and Control*, vol. 133, no. 3, 2011.

[61] J. W. Beams, "High-speed rotation," *Physics Today*, vol. 12, p. 20, 1959.

[62] M. K. Swann, "Magnetic bearings: Fifty years of progress," in *Magnetic Suspension Technology Workshop*, (NASA Langley Research Centre, Virginia, USA), pp. 19–38, 1993.

[63] T. Mizuno and T. Higuchi, "Design of the control system of totally active magnetic bearings," in *Proceedings of the International Symposium on Design and Synthesis*, (Tokyo, Japan), pp. 534–539, 1984.

[64] Z. Viderman and I. Porat, "An optimal control method for passage of a flexible rotor through resonances," *Journal of dynamic systems, measurement, and control*, vol. 109, no. 3, pp. 216–223, 1987.

[65] Y.-H. Fan, S.-T. Chen, and A.-C. Lee, "Active control of an asymmetrical rigid rotor supported by magnetic bearings," *Journal of the Franklin Institute*, vol. 329, no. 6, pp. 1153–1178, 1992.

[66] G. Schweitzer, "Active magnetic bearings - chances and limitations," in *IFToMM 6th International Conference on Rotor Dynamics*, vol. 1, (Sydney, Australia), pp. 1–14, 2002.

[67] H. G. Horst and H. P. Wölfel, "Active vibration control of a high speed rotor using pzt patches on the shaft surface," *Journal of Intelligent Material Systems and Structures*, vol. 15, no. 9-10, pp. 721–728, 2004.

[68] H. Kunze, M. Riedel, K. Schmidt, and E. Bianchini, "Vibration reduction on automotive shafts using piezoceramics," vol. 5054, pp. 382–386, 2003. 10.1117/12.483891.

[69] G. H. Haertling, "Ferroelectric ceramics: History and technology," *Journal of the American Ceramic Society*, vol. 82, no. 4, pp. 797–818, 1999. Cited By :1888 Export Date: 23 June 2016.

[70] A. J. Smalley, R. M. Baldwin, and W. R. Schick, "Spray automated balancing of rotors: Concept and initial feasibility study," *Journal of Engineering for Gas Turbines and Power*, vol. 111, no. 4, pp. 659–665, 1989. 10.1115/1.3240309.

[71] B. J. Furman, "A new, thermally controlled, non-contact rotor balancing method," *Journal of Mechanical Design*, vol. 116, no. 3, pp. 823–832, 1994. 10.1115/1.2919456.

[72] M. Zumbach, G. Schweitzer, and K. Schoellhorn, "On-line thermal balancing technique for a large turbo-generator," *Journal of Vibration and Acoustics*, vol. 114, no. 1, pp. 60–66, 1992. 10.1115/1.2930235.

[73] A. Blanco-Ortega, F. Beltran-Carbajal, and G. Silva-Navarro, "On-line algebraic identification of eccentricity in active vibration control of rotor-bearing systems," in *Electrical and Electronics Engineering, 2007. ICEEE 2007. 4th International Conference on*, pp. 253–256, 2007.

[74] J. van de Vegte, "Balancing of flexible rotors during operation," *Journal of Mechanical Engineering Science*, vol. 23, no. 5, pp. 257–261, 1981.

[75] Z. Gosiewski, "Automatic balancing of flexible rotors, Part I: Theoretical background," *Journal of Sound and Vibration*, vol. 100, no. 4, pp. 551–567, 1985.

[76] Z. Gosiewski, "Automatic balancing of flexible rotors, Part II: Synthesis of system," *Journal of Sound and Vibration*, vol. 114, no. 1, pp. 103–119, 1987.

[77] C.-W. Lee, Y.-D. Joh, and Y.-D. Kim, "Automatic modal balancing of flexible rotors during operation: Computer controlled balancing head," *Proceedings of the Institution of Mechanical Engineers, Part C: Journal of Mechanical Engineering Science*, vol. 204, no. 1, pp. 19–28, 1990.

[78] J.-S. Kim and S.-H. Lee, "The stability of active balancing control using influence coefficients for a variable rotor system," *The International Journal of Advanced Manufacturing Technology*, vol. 22, no. 7-8, pp. 562–567, 2003.

[79] L.-F. Chen, X. Cao, and J.-J. Gao, "A study on electromagnetic driven bi-disc compensator for rotor auto-balancing and its movement control," *WSEAS Transactions on systems and control*, vol. 5, no. 5, pp. 333–342, 2010.

[80] M. N. Sahinkaya, M. O. T. Cole, and C. R. Burrows, "Fault detection and tolerance in synchronous vibration control of rotor-magnetic bearing systems," *Proceedings of the Institu-*

tion of Mechanical Engineers, Part C: Journal of Mechanical Engineering Science, vol. 215, pp. 1401–1416, December 2001.

[81] H. D. Nelson and J. M. McVaugh, "The dynamics of rotor-bearing systems using finite elements," *Journal of Engineering for Industry*, vol. 98, no. 2, pp. 593–600, 1976. 10.1115/1.3438942.

[82] H. D. Nelson, "A finite rotating shaft element using timoshenko beam theory," *Journal of Mechanical Design*, vol. 102, no. 4, pp. 793–803, 1980. 10.1115/1.3254824.

[83] A. Abulrub, M. Sahinkaya, P. Keogh, and C. R. Burrows, "Adaptive control of active magnetic bearings to prevent rotor-bearing contact," in *ASME International Mechanical Engineering Congress and Exposition, IMECE2006*, (Chicago, Illinois), 2006.

[84] S.-K. Hong and R. Langari, "Robust fuzzy control of a magnetic bearing system subject to harmonic disturbances," *IEEE Transactions on Control Systems Technology*, vol. 8, no. 2, pp. 366–371, 2000.

[85] B. Defoy, T. Alban, and J. Mahfoud, "Assessment of the effectiveness of a polar fuzzy approach for the control of centrifugal compressors," *Journal of Dynamic Systems, Measurement, and Control*, vol. 136, no. 4, 2014. 10.1115/1.4026468.

[86] S. E. Mushi, Z. Lin, and P. E. Allaire, "Design, construction, and modeling of a flexible rotor active magnetic bearing test rig," *IEEE/ASME Transactions on Mechatronics*, vol. 17, no. 6, pp. 1170–1182, 2012.

[87] J. Fang, S. Zheng, and B. Han, "AMB vibration control for structural resonance of double-gimbal control moment gyro with high-speed magnetically suspended rotor," *IEEE/ASME Transactions on Mechatronics*, vol. 18, no. 1, pp. 32–43, 2013.

[88] A. H. Pesch, A. Smirnov, O. Pyrhönen, and J. T. Sawicki, "Magnetic bearing spindle tool tracking through μ-synthesis robust control," *IEEE/ASME Transactions on Mechatronics*, vol. 20, no. 3, pp. 1448–1457, 2015.

[89] S. Sivrioglu and K. Nonami, "Sliding mode control with time-varying hyperplane for AMB systems," *IEEE/ASME Transactions on Mechatronics*, vol. 3, no. 1, pp. 51–59, 1998.

[90] M. Fujita, K. Hatake, and F. Matsumura, "Loop shaping based robust control of a magnetic bearing," *IEEE Control Systems*, vol. 13, no. 4, pp. 57–65, 1993.

[91] W. Cui, K. Nonami, and H. Nishimura, "Experimental study on active vibration control of structures by means of h control and h 2 control," *JSME international journal. Ser. C, Dynamics, control, robotics, design and manufacturing*, vol. 37, no. 3, pp. 462–467, 1994.

[92] K. Nonami, H. Ueyama, and Y. Segawa, "H_∞ control of milling amb spindle," *JSME International Journal Series A Solid Mechanics and Material Engineering*, vol. 39, no. 3, pp. 502–508, 1996.

[93] T. Namerikawa and M. Fujita, "H_∞ control system design of the magnetic suspension system considering initial state uncertainties," *IEEJ Transactions on Electronics, Information and Systems*, vol. 123, no. 6, pp. 1094–1100, 2003.

[94] R. C. Dorf and R. H. Bishop, *Modern control systems*. Harlow: Pearson, 12th ed., 2014.

Chapter 3

Active rotor model

3.1 Introduction

In the first phase of the research, a computational model of an active rotor system was constructed, satisfying objective O1. This served several purposes. Firstly, the model served as an exercise in design visualisation, providing a better understanding of the required characteristics and likely challenges associated with an active rotor system. Secondly, the model results were used to determine the size and characteristics of the rotor prototype components. Thirdly, the model allowed control strategies to be safely tested in a simulated environment before being fully implemented in the rotor. Finally, the model served as a virtual test bed on which to trial designs and configurations which could not be implemented on the final prototype due to physical or logistical constraints.

This chapter describes the techniques used to simulate the active rotor design. The finite element method was used together with a state space formulation as the basis of the model. The rotor behaviour was simulated with a dynamic Simulink model. The model was validated by comparing its predictions against analytical results and against results predicted by an alternative, proven model.

3.2 Finite element model

The finite element method was used to model the elastic characteristics of the assembled rotor shaft. This technique has been demonstrated to be effective and is hence widely used in rotordynamic analysis [1].

A custom implementation was used, coded using Matlab. The model was

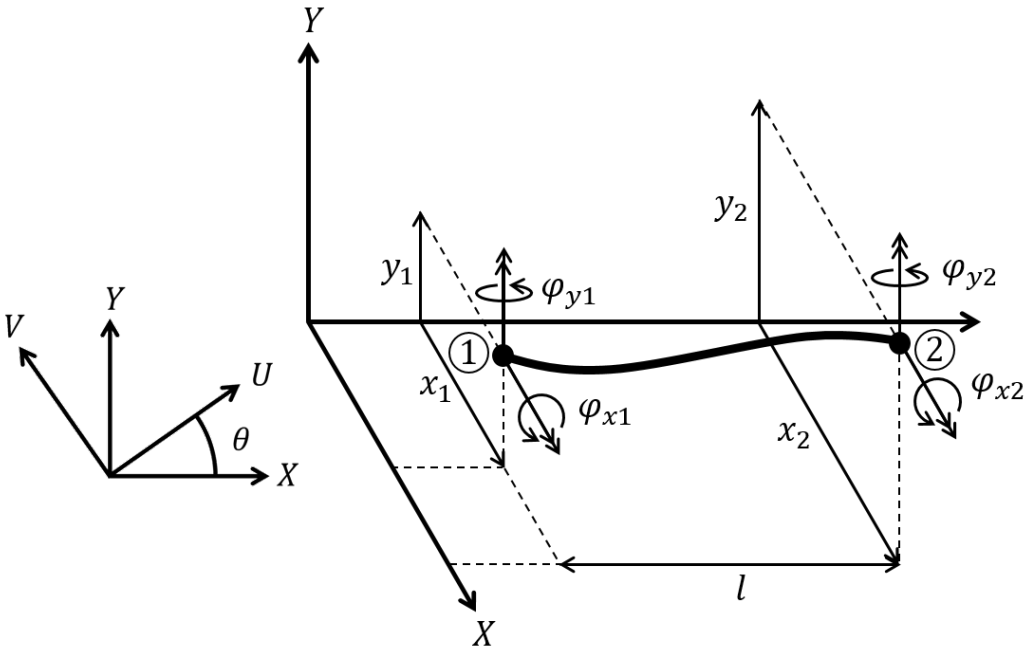

Figure 3.1: Finite element coordinate system.

built with a fundamental requirement of flexibility in mind, so that its capabilities could adapt to the evolving needs of the research. Thus, the code was written in such a way as to allow modification of all model parameters, enabling any configuration of the rotor system to be simulated. These parameters include properties of the finite elements (length, geometry, material, etc.), the bearings (stiffness, damping, location, etc.) and the sensors and actuators (location, mass, sensitivity, etc.).

The rotor was modelled using beam elements with four degrees of freedom per node. These are displacement along (x, y), and rotation around (φ_x, φ_y), the inertial reference frame X and Y axes, as illustrated in Fig. 3.1. The element length is denoted by l. A rotating frame of reference UV is defined as being fixed to the rotor, and rotated with respect to the inertial XY reference frame by an angle θ.

The elastic behaviour of the elements is described with the matrix method of Nelson and McVaugh [2], which includes terms for gyroscopic effects, rotational inertia and shear deformation. To account for the latter, Timoshenko beam elements are used, which expand Euler-Bernoulli beam theory by considering the shear of the material. The difference in deformation between the two beams is illustrated in Fig. 3.2, in which w denotes the displacement of the beam centreline in the vertical Z direction, $2h$ is the beam thickness, Q is the shear force and M is the bending moment.

Each element in the rotor is described by a mass, stiffness and gyroscopic

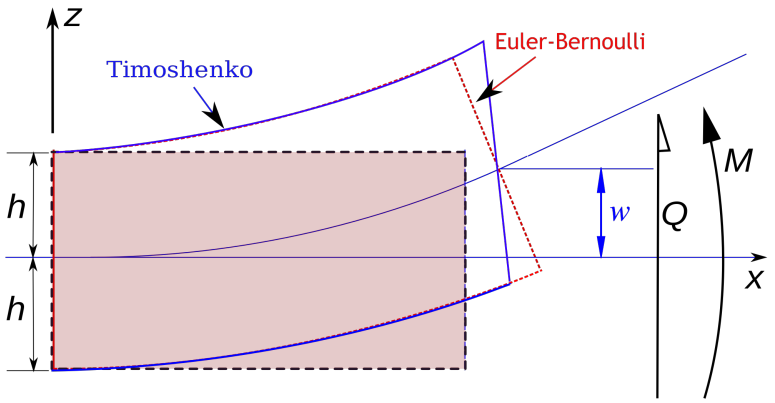

Figure 3.2: Comparison of the deformation of Timoshenko and Euler-Bernoulli beams. Image by Bbanerje and licensed under CC BY-SA 3.0.

element matrix. These are assembled together into system-level matrices which describe the overall behaviour of the rotor. The stiffness and damping afforded by the bearings are then included into these matrices at the node position corresponding to their location. The cross-section of each individual element could be varied, enabling the simulation of rotors with sections of different diameter. The element matrices used can be found in Appendix A.

3.3 Equations of motion

In order to allow prediction of the rotor's vibration response during operation, its dynamic behaviour was described by an equation of motion and then encapsulated in a state space mathematical structure. The matrix-vector equation of motion for a finite element model with n nodes and coordinates defined in the inertial frame of reference, is given by Genta [1] as

$$\mathbf{M}\ddot{\mathbf{q}} + \left[\mathbf{D_B} - \dot{\theta}\mathbf{G}\right]\dot{\mathbf{q}} + \mathbf{K}\mathbf{q} = \mathbf{f} \tag{3.1}$$

where

- $\mathbf{q} = \{x_1, y_1, \varphi_{x1}, \varphi_{y1}, \ldots, x_n, y_n, \varphi_{xn}, \varphi_{yn}\}^{\mathrm{T}}$ is a vector containing the displacement and rotations states of the n nodes of the finite element model
- $\mathbf{M}$ is the mass matrix containing terms for translational and rotational inertia
- $\mathbf{D_B}$ is the damping matrix representing the damping afforded by the bearings

- $\mathbf{G}$ is the skew-symmetric gyroscopic matrix
- $\mathbf{K}$ is the stiffness matrix
- $\dot{\theta}$ is the rotating speed of the rotor
- $\mathbf{f}$ is a vector containing the external forces and moments applied to the rotor

The forces and moments in $\mathbf{f}$ relate to the displacement and rotation of the nodes, respectively. The principal force component considered is unbalance, which is often the most significant source of vibration in rotating machines. The unbalance forces are represented by $2n \times 1$ vector $\mathbf{f_u}$, which contains the unbalance force acting at each node of the finite element model. As no moments are considered to be acting on the rotor, the general forcing term $\mathbf{f}$ becomes:

$$\mathbf{f} = \mathbf{f_u} = \mathbf{TN\Theta}\boldsymbol{\sigma} \tag{3.2}$$

where $2n \times 1$ vector $\boldsymbol{\sigma}$ is a unbalance distribution along the rotor of the form $\boldsymbol{\sigma} = \{\sigma_{u1}, \sigma_{v1}, \ldots, \sigma_{un}, \sigma_{vn}\}^{\mathrm{T}}$, which contains a constant unbalance value in the perpendicular U and V rotating reference frame axes for each node of the finite element model. The matrix $\mathbf{\Theta}$ is a $2n \times 2n$ matrix containing the values of rotor speed and acceleration

$$\mathbf{\Theta} = \begin{bmatrix} \dot{\theta}^2 & \ddot{\theta} & 0 & 0 & \cdots \\ -\ddot{\theta} & \dot{\theta}^2 & 0 & 0 & \cdots \\ 0 & 0 & \dot{\theta}^2 & \ddot{\theta} & \cdots \\ 0 & 0 & -\ddot{\theta} & \dot{\theta}^2 & \cdots \\ \vdots & \vdots & \vdots & \vdots & \ddots \end{bmatrix}, \tag{3.3}$$

while matrix $\mathbf{N}$ is the $4n \times 2n$ linear coefficients matrix

$$\mathbf{N} = \begin{bmatrix} 1 & 0 & 0 & 0 & 0 & 0 & \cdots \\ 0 & 1 & 0 & 0 & 0 & 0 & \cdots \\ 0 & 0 & 0 & 0 & 0 & 0 & \cdots \\ 0 & 0 & 0 & 0 & 0 & 0 & \cdots \\ 0 & 0 & 1 & 0 & 0 & 0 & \cdots \\ 0 & 0 & 0 & 1 & 0 & 0 & \cdots \\ \vdots & \vdots & \vdots & \vdots & \vdots & \vdots & \ddots \end{bmatrix}, \tag{3.4}$$

and matrix $\mathbf{T}$ is a $4n \times 4n$ block diagonal matrix with n basis blocks of the form

$$\mathbf{T}_{nn} = \begin{bmatrix} \cos\theta & -\sin\theta \\ \sin\theta & \cos\theta \end{bmatrix} \tag{3.5}$$

such that

$$\mathbf{T} = \begin{bmatrix} \mathbf{T}_{11} & \mathbf{0} & \mathbf{0} & \cdots \\ \mathbf{0} & \mathbf{T}_{22} & \mathbf{0} & \cdots \\ \mathbf{0} & \mathbf{0} & \mathbf{T}_{33} & \cdots \\ \vdots & \vdots & \vdots & \ddots \end{bmatrix} \tag{3.6}$$

The equation of motion can be expressed in the state space form through $\mathbf{z}_1 = \mathbf{q}$ and $\mathbf{z}_2 = \dot{\mathbf{z}}_1$. For a state vector $\mathbf{z} = [\mathbf{z}_1^{\mathrm{T}}, \mathbf{z}_2^{\mathrm{T}}]^{\mathrm{T}}$,

$$\begin{aligned} \dot{\mathbf{z}} &= \mathbf{A}\mathbf{z} + \mathbf{B}\mathbf{u} \\ \mathbf{y} &= \mathbf{C}\mathbf{z} + \mathbf{D}\mathbf{u} \end{aligned} \tag{3.7}$$

with $\mathbf{u} = \mathbf{f}$ and

$$\mathbf{A} = \begin{bmatrix} \mathbf{0} & \mathbf{I} \\ -\mathbf{M}^{-1}\mathbf{K} & -\mathbf{M}^{-1}\left[\mathbf{D_B} - \dot{\theta}\mathbf{G}\right] \end{bmatrix} \quad , \quad \mathbf{B} = \begin{bmatrix} \mathbf{0} \\ \mathbf{M}^{-1} \end{bmatrix}$$

Both the nodal displacements and accelerations are of interest as outputs, so that $\mathbf{y} = [\mathbf{z}_1^{\mathrm{T}}, \dot{\mathbf{z}}_2^{\mathrm{T}}]^{\mathrm{T}}$ and hence

$$\mathbf{C} = \begin{bmatrix} \mathbf{I} & \mathbf{0} \\ -\mathbf{M}^{-1}\mathbf{K} & -\mathbf{M}^{-1}\left[\mathbf{D_B} - \dot{\theta}\mathbf{G}\right] \end{bmatrix} \quad , \quad \mathbf{D} = \begin{bmatrix} \mathbf{0} \\ \mathbf{M}^{-1} \end{bmatrix}$$

3.3.1 Output in rotating coordinates

As the model can be used to simulate the output of both stator- and rotor-mounted sensors (for instance, representing eddy current sensors and internal accelerometers, respectively), it is desirable to produce the system states in the rotating frame of reference. This can be achieved by transforming the model output between the frames, so that

$$\mathbf{y}_r = \mathbf{E}\mathbf{y} \tag{3.8}$$

where $\mathbf{y}_r$ contains the model output in the rotating frame of reference and $\mathbf{E}$ is a $2n \times 4n$ block diagonal transformation matrix formed by n basis blocks, each

defined as

$$\mathbf{E}_{nn} = \begin{bmatrix} \mathbf{T}^T & \mathbf{0} \end{bmatrix} \tag{3.9}$$

so that

$$\mathbf{E} = \begin{bmatrix} \mathbf{E}_{11} & \mathbf{0} & \mathbf{0} & \cdots \\ \mathbf{0} & \mathbf{E}_{22} & \mathbf{0} & \cdots \\ \mathbf{0} & \mathbf{0} & \mathbf{E}_{33} & \cdots \\ \vdots & \vdots & \vdots & \ddots \end{bmatrix} \tag{3.10}$$

If only rotating frame outputs are required, an alternative approach is to cast the equation of motion (3.1) in rotating coordinates to produce a rotating frame model. This is achieved by performing the coordinate transformation

$$\mathbf{q} = \mathbf{T}\mathbf{p} \tag{3.11}$$

where $\mathbf{p} = \{u_1,\, v_1,\, \varphi_{u1},\, \varphi_{v1},\, \ldots\, ,\, u_n,\, v_n,\, \varphi_{un},\, \varphi_{vn}\}^{\mathrm{T}}$. It can be observed from Eq. (3.5) that

$$\dot{\mathbf{T}}_{nn} = \dot{\theta} \begin{bmatrix} -\sin\theta & -\cos\theta \\ \cos\theta & -\sin\theta \end{bmatrix} = \dot{\theta}\mathbf{T}_{nn}\mathbf{R}_{nn} \tag{3.12}$$

where $\mathbf{R}_{nn}$ is the rotation matrix basis block

$$\mathbf{R}_{nn} = \begin{bmatrix} 0 & -1 \\ 1 & 0 \end{bmatrix} \tag{3.13}$$

with which a $4n \times 4n$ block diagonal matrix $\mathbf{R}$ is constructed:

$$\mathbf{R} = \begin{bmatrix} \mathbf{R}_{11} & \mathbf{0} & \mathbf{0} & \cdots \\ \mathbf{0} & \mathbf{R}_{22} & \mathbf{0} & \cdots \\ \mathbf{0} & \mathbf{0} & \mathbf{R}_{33} & \cdots \\ \vdots & \vdots & \vdots & \ddots \end{bmatrix} \tag{3.14}$$

Consequently, $\dot{\mathbf{T}} = \dot{\theta}\mathbf{T}\mathbf{R}$ and $\ddot{\mathbf{T}} = \ddot{\theta}\mathbf{T}\mathbf{R} - \dot{\theta}^2\mathbf{T}$. Thus, the following expressions can be derived for $\dot{\mathbf{q}}$ and $\ddot{\mathbf{q}}$

$$\dot{\mathbf{q}} = \dot{\mathbf{T}}\mathbf{p} + \mathbf{T}\dot{\mathbf{p}} = \mathbf{T}\left(\dot{\mathbf{p}} + \dot{\theta}\mathbf{R}\mathbf{p}\right) \tag{3.15}$$

$$\ddot{\mathbf{q}} = \mathbf{T}\ddot{\mathbf{p}} + 2\dot{\mathbf{T}}\dot{\mathbf{p}} + \ddot{\mathbf{T}}\mathbf{p} = \mathbf{T}\left(\ddot{\mathbf{p}} + 2\dot{\theta}\mathbf{R}\dot{\mathbf{p}} + (\ddot{\theta}\mathbf{R} - \dot{\theta}^2)\mathbf{p}\right) \tag{3.16}$$

Substituting Eqs. (3.11),(3.15) and (3.16) into (3.1) yields

$$\mathbf{M}\mathbf{T}\left(\ddot{\mathbf{p}} + 2\dot{\theta}\mathbf{R}\dot{\mathbf{p}} + (\ddot{\theta}\mathbf{R} - \dot{\theta}^2)\mathbf{p}\right) + \left[\mathbf{D_B} - \dot{\theta}\mathbf{G}\right]\mathbf{T}\left(\dot{\mathbf{p}} + \dot{\theta}\mathbf{R}\mathbf{p}\right) + \mathbf{K}\mathbf{T}\mathbf{p} = \mathbf{f} \tag{3.17}$$

$$\mathbf{M}\ddot{\mathbf{p}}+\left[\mathbf{D_B}+\dot{\theta}\left(2\mathbf{MR}-\mathbf{G}\right)\right]\dot{\mathbf{p}}+\left[\ddot{\theta}\mathbf{MR}-\dot{\theta}^2\left(\mathbf{M}+\mathbf{GR}\right)+\dot{\theta}\mathbf{D_B}\mathbf{R}+\mathbf{K}\right]\mathbf{p}=\mathbf{T}^{-1}\mathbf{f} \tag{3.18}$$

With the transformed equation, the state space formulation can be rewritten in terms of rotating coordinates state vector $\mathbf{z}_r = [\mathbf{z}_{r1}^{\mathrm{T}}, \mathbf{z}_{r2}^{\mathrm{T}}]^{\mathrm{T}}$, with $\mathbf{z}_{r1} = \mathbf{p}$ and $\mathbf{z}_{r2} = \dot{\mathbf{z}}_{r1}$. Hence,

$$\begin{aligned}\dot{\mathbf{z}}_r &= \mathbf{A}_r\mathbf{z}_r + \mathbf{B}_r\mathbf{u}_r \\ \mathbf{y}_r &= \mathbf{C}_r\mathbf{z}_r + \mathbf{D}_r\mathbf{u}_r\end{aligned} \tag{3.19}$$

with $\mathbf{u}_r = \mathbf{f}$ and

$$\mathbf{A}_r = \begin{bmatrix} \mathbf{0} & \mathbf{I} \\ -\mathbf{M}^{-1}\left[\ddot{\theta}\mathbf{MR}-\dot{\theta}^2\left(\mathbf{M}+\mathbf{GR}\right)+\dot{\theta}\mathbf{D_B}\mathbf{R}+\mathbf{K}\right] & -\mathbf{M}^{-1}\left[\mathbf{D_B}+\dot{\theta}\left(2\mathbf{MR}-\mathbf{G}\right)\right] \end{bmatrix}$$

$$\mathbf{B}_r = \begin{bmatrix} \mathbf{0} \\ \mathbf{M}^{-1}\mathbf{T}^{-1} \end{bmatrix}$$

$$\mathbf{C}_r = \begin{bmatrix} \mathbf{I} & \mathbf{0} \\ -\mathbf{M}^{-1}\left[\ddot{\theta}\mathbf{MR}-\dot{\theta}^2\left(\mathbf{M}+\mathbf{GR}\right)+\dot{\theta}\mathbf{D_B}\mathbf{R}+\mathbf{K}\right] & -\mathbf{M}^{-1}\left[\mathbf{D_B}+\dot{\theta}\left(2\mathbf{MR}-\mathbf{G}\right)\right] \end{bmatrix}$$

$$\mathbf{D}_r = \begin{bmatrix} \mathbf{0} \\ \mathbf{M}^{-1}\mathbf{T}^{-1} \end{bmatrix}$$

In terms of simulating the rotor dynamics, formulations (3.7) and (3.19) are identical. Under non-constant rotational speed conditions both systems become Linear Time Varying and so the computation of the outputs requires updating the state space matrices at each time step with the correct speed, acceleration and transformation terms, $\dot{\theta}$, $\ddot{\theta}$ and $\mathbf{T}^{-1}$, respectively. For the model cast in inertial coordinates, this process requires updating a single submatrix, $-\mathbf{M}^{-1}\left[\mathbf{D_B}-\dot{\theta}\mathbf{G}\right]$. In the case of the rotating frame model, however, more submatrices must be reconstructed. Because of this, performance tests undertaken indicate that the inertial model operates marginally faster (around 3%), and hence was adopted as the preferred method.

3.4 Dynamic model

A dynamic model was constructed in Simulink, with which the operation of the full rotor system could be simulated and its behaviour predicted. The basic arrangement consists of the inertial state space model, an unbalance force input, two plotting options, and the frame transformation blocks, as illustrated in Fig. 3.3. Blocks shaded in blue indicate operations performed in the rotating frame

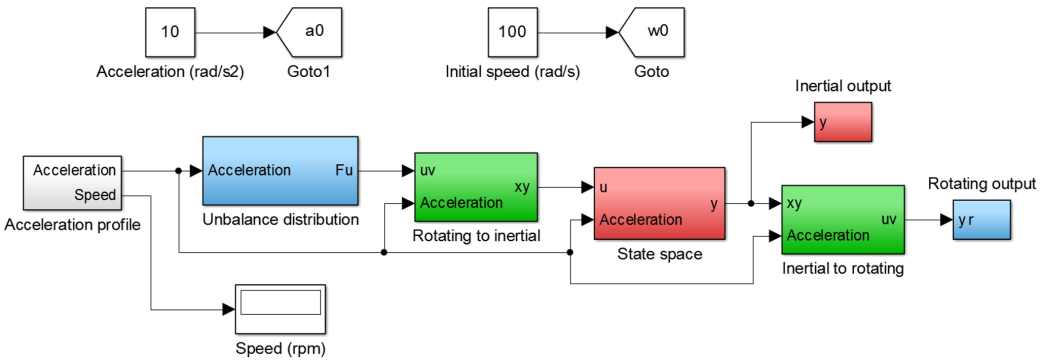

Figure 3.3: Basic Simulink dynamic model.

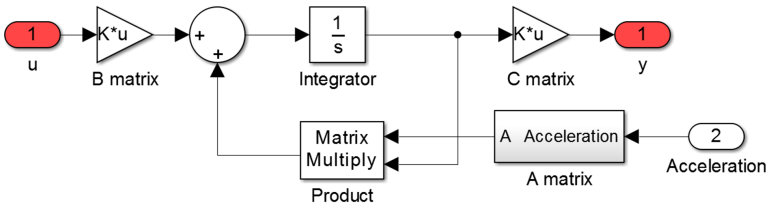

Figure 3.4: Inertial state space block used in the Simulink model.

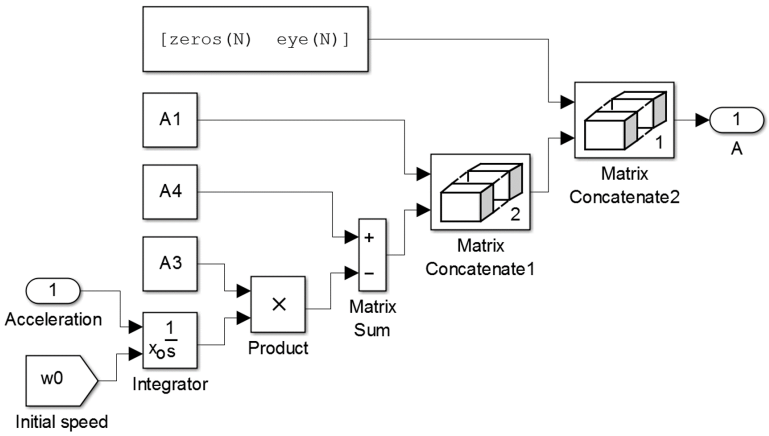

Figure 3.5: Construction of the speed-dependent $\mathbf{A}$ matrix in Simulink.

of reference, while blocks in red are associated with the inertial frame. Green is used to indicate blocks that transform between the frames.

The state space block was custom built to enable updating of the rotating speed parameter in the system $\mathbf{A}$ matrix at each time step. Although computationally more intense, this arrangement allows the same model to be used for speed-varying scenarios, enabling more realistic simulation of the rotor behaviour. Figure 3.4 shows the custom state space block, and Fig. 3.5 shows how the system $\mathbf{A}$ matrix is constructed from parameters defined as:

$$\mathbf{A}_1 = -\mathbf{M}^{-1}\mathbf{K} \qquad \mathbf{A}_2 = -\mathbf{M}^{-1}\mathbf{D}_\mathbf{B} \qquad \mathbf{A}_3 = -\mathbf{M}^{-1}\mathbf{G}$$

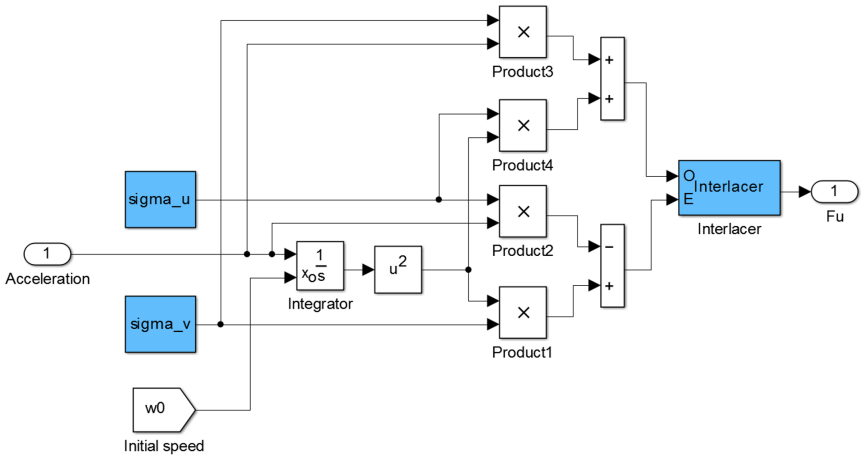

Figure 3.6: Unbalance force block in the Simulink model.

The unbalance force generation is performed by the block depicted in Fig. 3.6. The unbalance distribution is described by parameters `sigma_u` and `sigma_v`, which are produced by a Matlab generator. The code randomly selects masses and eccentricities for each node from a range of values, with the allowable maximum chosen such that the unbalance at each node has a user-defined upper bound. The code then calculates the overall unbalance of the existing distribution and modifies a randomly selected node so that the total rotor unbalance satisfies the requirements of a user-defined ISO unbalance grade [4].

The frame transformation blocks allow conversion of data between the rotating and inertial reference frames, and *vice versa*. The blocks depicted in Figs. 3.7 and 3.8 represent the rotating to inertial (matrix $\mathbf{T}$) and inertial to rotating (matrix $\mathbf{T}^{-1}$) transformations, respectively.

Throughout the research, numerous variations of the base model were developed to simulate a range of operating conditions and rotor configurations. Further details regarding some of these implementations are given in later Chapters where relevant, but examples of the research tasks which were undertaken with the help of models include:

- Validating the assumption of quasi-static accelerometer proof mass behaviour in the prototype operating speed range
- Simulating impacts to understand transient vibration behaviour
- Implementing a model-based controller
- Simulating the behaviour of different controllers with multi-sensor/actuator configurations

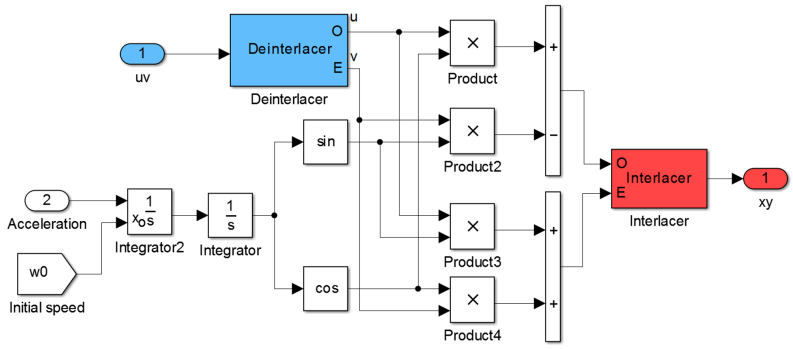

Figure 3.7: Rotating to inertial frame transformation block in the Simulink model.

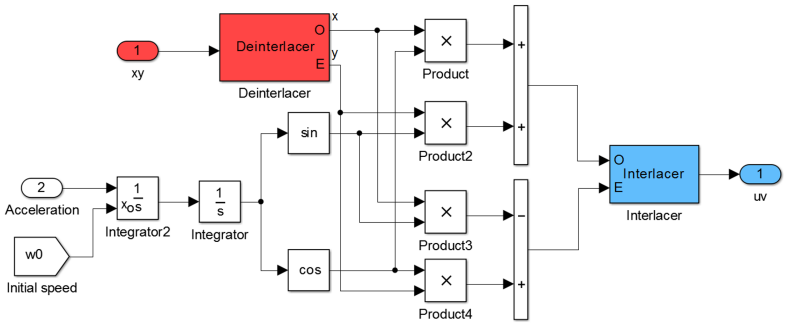

Figure 3.8: Inertial to rotating frame transformation block in the Simulink model.

3.5 Model validation

Validation of the model was undertaken to guarantee the accuracy of the predictions. Firstly, the model was used to predict the critical speeds of a simple uniform steel rotor. These results were compared against those derived analytically by Thomson [5] for a free-free and pinned-pinned uniform beam. The results are given in Table 3.1.

Table 3.1: Critical speed prediction for a uniform steel rotor: analytical vs. constructed model.

	Free-free			**Pinned-pinned**		
Mode	Analytical (Hz)	Model (Hz)	Error	Analytical (Hz)	Model (Hz)	Error
1^{st}	45.57	45.53	-0.08%	103.42	102.90	-0.50%
2^{nd}	182.35	181.67	-0.37%	284.83	282.22	-0.92%
3^{rd}	410.40	407.22	-0.78%	558.58	549.60	-1.61%
4^{th}	728.93	720.32	-1.18%	922.83	901.15	-2.35%

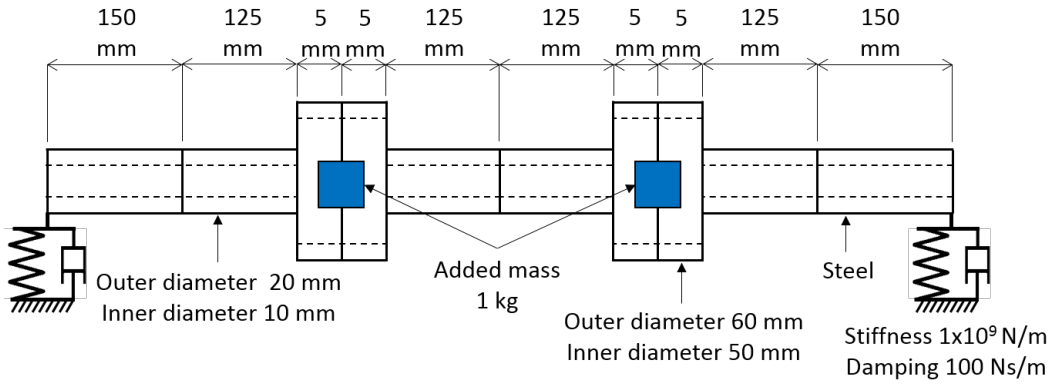

Figure 3.9: Rotor model used for model validation.

Table 3.2: Critical speed prediction for comparison of critical speeds predicted analytically and with the constructed model.

Mode	**Sahinkaya model** (Hz)	**Jiménez model** (Hz)	**Error**
1st	29.83	29.83	0.00%
2nd	124.03	124.05	-0.02%
3rd	392.12	388.18	-1.00%
4th	684.07	675.17	-1.30%

The model was further validated by comparing the results predicted for a more detailed rotor configuration against those obtained using a proven model constructed by Sahinkaya [6–8]. The validation topology consists of a steel rotor with a varying cross-section, as illustrated in Fig. 3.9. The smaller shafts have an outer and inner diameter of 20 mm and 10 mm, respectively. The larger sections are also hollow, with a 60 mm outer diameter and 50 mm inner diameter. The critical speeds predicted with the developed model correlate strongly with those obtained via the Sahinkaya model, as shown in the results presented in Table 3.2.

3.6 Model prototype predictions

The finalised model was used for a number of tasks, including sizing the active rotor prototype. After an iterative design process, final dimensions were established, and the model was used to predict the behaviour of the prototype. The final finite element model is shown in Fig. 3.10, with the assumed bearing model parameters shown in Table 3.3. The first two predicted critical speeds and mode shapes are presented in Fig. 3.11.

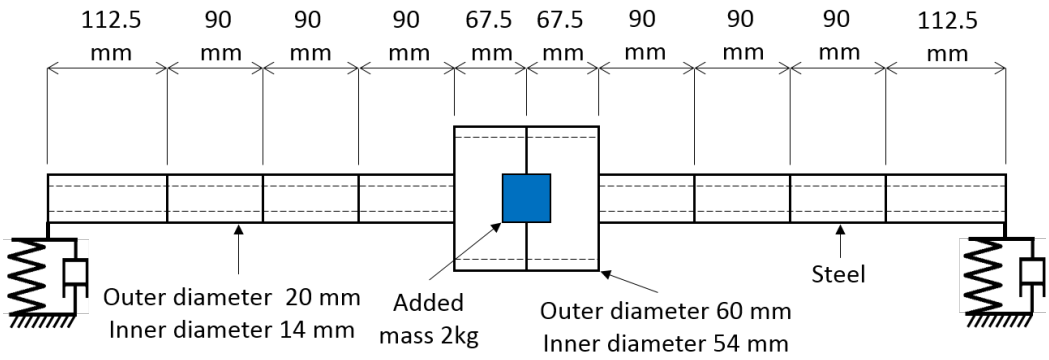

Figure 3.10: Rotor model of active rotor prototype.

Table 3.3: Finite element model parameters for bearing assembly.

Parameter	**Value**	**Unit**
Net linear stiffness - X,Y	1×10^7	N/m
Net torsional stiffness - Φ_Y,Φ_X	2×10^3	Nm/rad
Net damping - X,Y	1×10^2	Ns/m

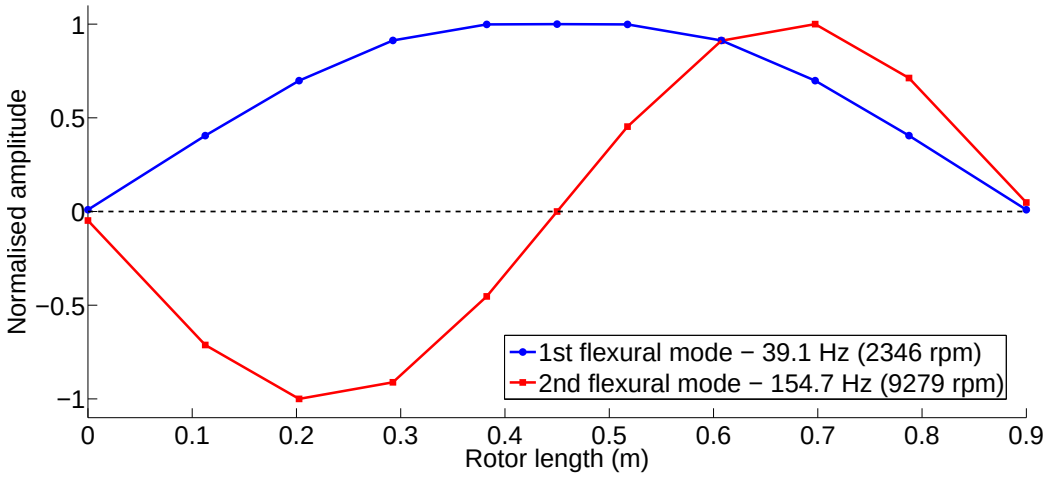

Figure 3.11: First two critical speeds and corresponding mode shapes of the active rotor prototype, as predicted by the model.

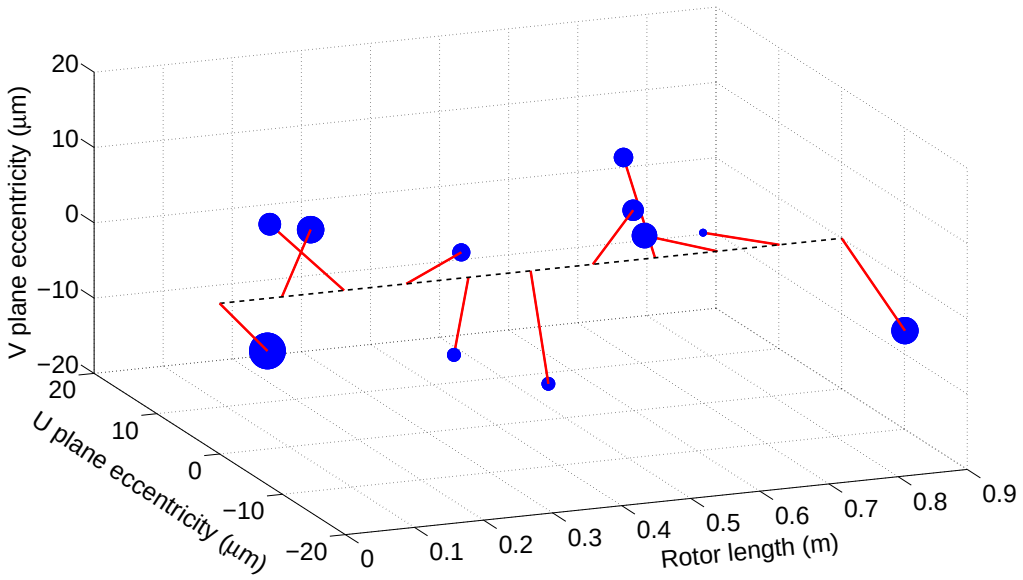

Figure 3.12: Random unbalance distribution for dynamic simulation.

As an example, the rotor was simulated under the effect of a random unbalance distribution which provides an overall unbalance of 180 g.mm. Each node has a unique unbalance, formed by a random mass and eccentricity, as represented schematically in Fig. 3.12. The simulated speed range is 0 to $3,000$ rpm. Figure 3.13 shows the inertial Y plane displacement response of the rotor, while Fig. 3.14 shows the rotating U plane displacement. The first flexural mode shape can be clearly observed between $2,000$ and $2,500$ rpm.

3.7 Conclusions

A computational model suitable for researching active rotor topologies was constructed in the first phase of the research. This was used to size the prototype and to simulate control strategies and rotor configurations.

The rotor was modelled using the finite element technique, implemented through a custom Matlab code. The equations of motion of the rotor were then encapsulated in a state space formulation, which could be used to predict the rotor response in inertial and rotating coordinates. Simulink was used to implement the state space formulation as a dynamic model.

The model was first validated by comparing its critical speed predictions of a simplified rotor against analytical calculations. A further validation was undertaken in which a more complex rotor configuration was simulated using an alternative, proven model used at the University of Bath. In both validation cases, strong correlation between the predicted results was found.

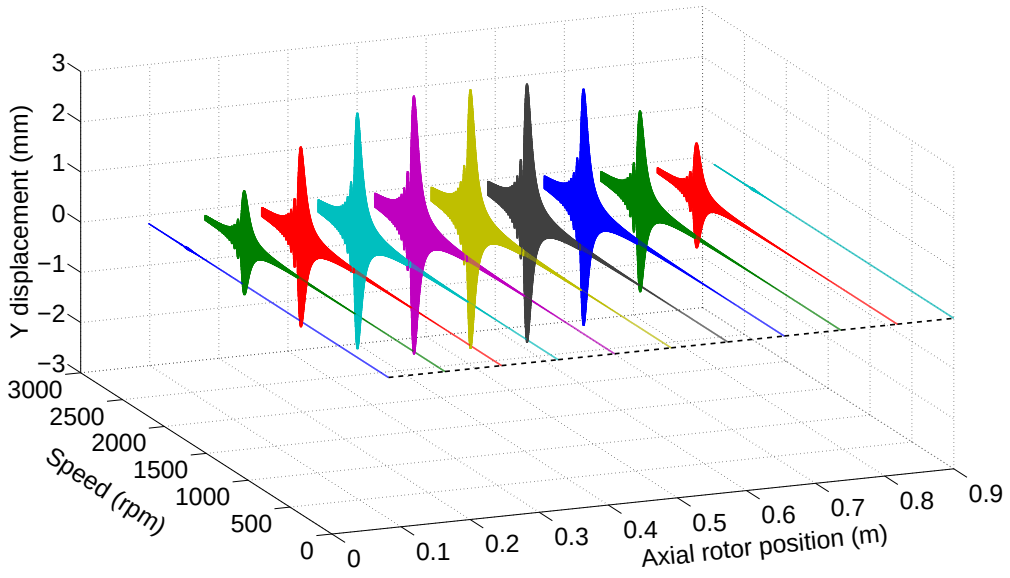

Figure 3.13: Inertial Y plane simulated response between 0 and $3,000$ rpm.

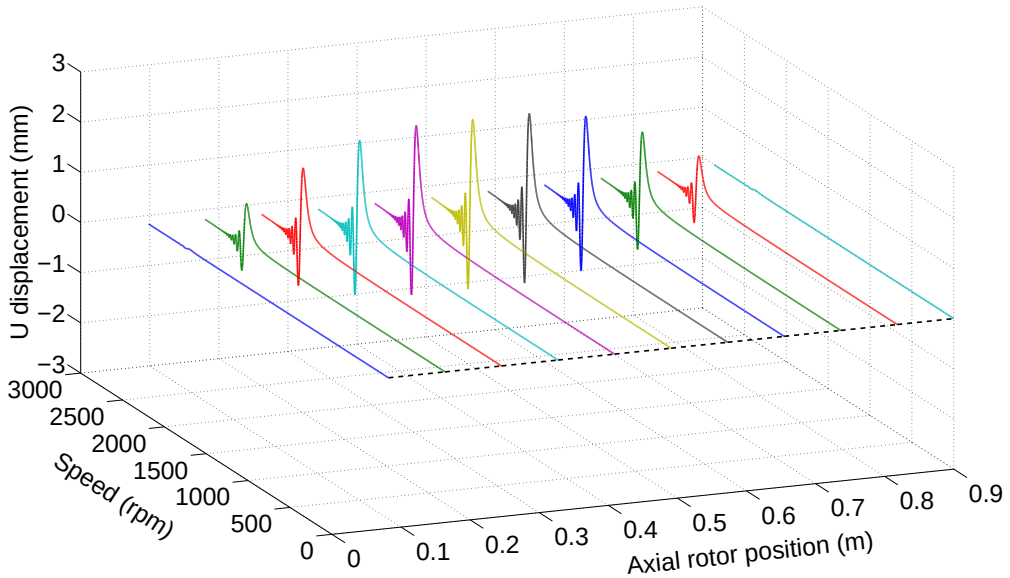

Figure 3.14: Rotating U plane simulated response between 0 and $3,000$ rpm.

3.8 Summary

- The rotor behaviour was modelled with the finite element technique.
- The equations of motion were expressed through a state space formulation.
- Simulink was used to implement a dynamic model of the system.
- The model was validated by comparing its predictions against analytical and simulated results.

References

[1] G. Genta, *Dynamics of Rotating Systems*. Springer, 2009.

[2] H. D. Nelson, "A finite rotating shaft element using timoshenko beam theory," *Journal of Mechanical Design*, vol. 102, no. 4, pp. 793–803, 1980. 10.1115/1.3254824.

[3] G. R. Cowper, "The shear coefficient in timoshenkos beam theory," *Journal of Applied Mechanics*, vol. 33, no. 2, pp. 335–340, 1966. 10.1115/1.3625046.

[4] International Organisation for Standardization, "Mechanical vibration - balance quality requirements for rotors in a constant (rigid) state - Part 1: specification and verification of balance tolerances," Tech. Rep. ISO 1940-1:2003/Cor 1:2005, 2005.

[5] W. T. Thomson, *Theory of vibration with applications*. Taylor & Francis, 1993.

[6] P. S. Keogh, M. O. T. Cole, M. N. Sahinkaya, and C. R. Burrows, "On the control of synchronous vibration in rotor/magnetic bearing systems involving auxiliary bearing contact," *Journal of Engineering for Gas Turbines and Power*, vol. 126, no. 2, pp. 366–372, 2004. 10.1115/1.1689362.

[7] M. N. Sahinkaya, A. H. G. Abulrub, P. S. Keogh, and C. R. Burrows, "Multiple sliding and rolling contact dynamics for a flexible rotor/magnetic bearing system," *IEEE/ASME Transactions on Mechatronics*, vol. 12, no. 2, pp. 179–189, 2007.

[8] M. Sahinkaya, A. Abulrub, P. Keogh, and C. Burrows, "Experiments on the transient performance of an adaptive multi-objective controller for rotating machinery," *Journal of Engineering for Gas Turbines and Power*, vol. 133, no. 2, pp. 022503–1 – 022503–7, 2010.

Chapter 4

Active rotor prototype

4.1 Introduction

The potential benefits of internally mounted active vibration control systems can only be derived if these can be realistically designed, manufactured and assembled. Therefore, objective O2 of the research was to demonstrate that the proposed topology was feasible in practice. Consequently, a prototype active shaft rotor was constructed as a design exercise to better understand the challenges and potential benefits of the technology. The prototype also served a second key purpose as a test bed to undertake experiments in internal sensing and control strategies.

This Chapter describes the design and manufacture of the prototype active shaft rotor. It firstly gives an overview of the design philosophy and objectives. It then details the mechanical design aspect of both the rotor and the stator. This is followed by a description of the electronic component design. Finally, explanation is given regarding the software programmed to control the test rig and its various components.

4.2 Design overview

The rotor is only one of the many components that make up a complete rotating machine. As such, it is reasonable to assume that any hypothetical uptake of active rotor technology in an industrial setting would be conditioned by the degree to which existing rotating machines would have to be redesigned to accommodate an active shaft. Ultimately, the vision for active rotor technology is for it to be fully embeddable within the rotor, in such a manner that any conventional passive rotor could be replaced by an active counterpart on any

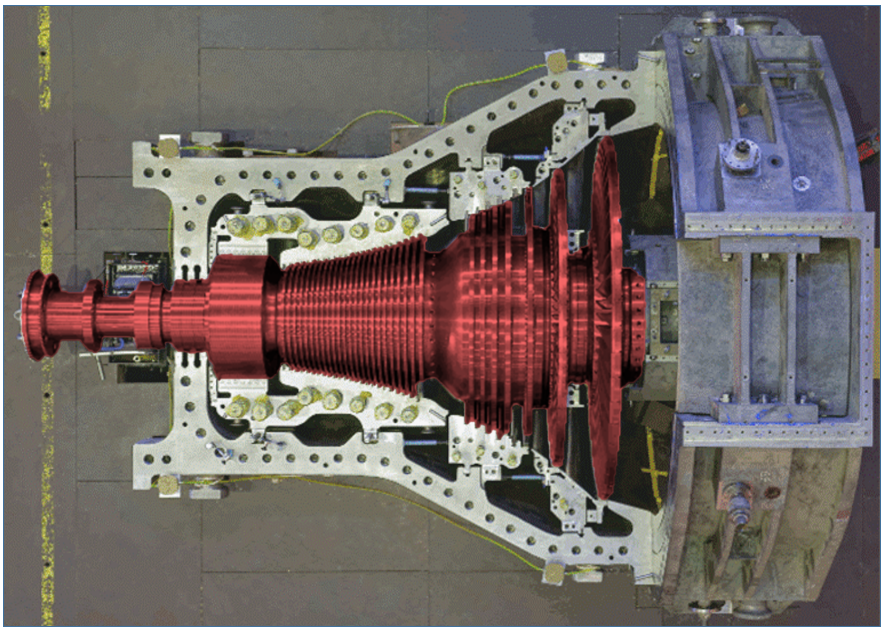

Figure 4.1: Rotor-centred design boundary, delineated on a steam turbine. The available design space is shaded in red. Original image courtesy of Alborz Turbine.

rotating machine. The new active rotor would have an identical outer surface design, but contain a fully functioning active system. This type of technology could provide passive rotor systems with condition monitoring and vibration control capabilities, allowing considerable performance improvements in a vast range of applications.

Thus, the principal objective was to produce a rotor-centred design, one which was as independent as possible from the stator and any external components. The design should also be as non-invasive as possible to the general rotating machine, such that the active system would not interfere with other system-level design considerations such as location of working components (turbine blades, seals, etc.). To satisfy this design philosophy, the device should use internally-mounted sensing and actuation, require a minimum of externally-obtained information to achieve its vibration control goals and, to the degree that it was possible, not depend on an external power supply. Consequently, a design boundary as depicted in Fig. 4.1 was established. The doctrine of rotor-centred design would later be extended beyond the physical design into the fields of sensing and control, for instance leading to the application of rotor-mounted accelerometers as virtual encoders (Chapter 5) or the development of a *non a priori* Algorithmic Direct Search Controller (Chapter 6).

As discussed in Chapter 2, the review of active vibration control literature determined that the most appropriate sensing technology for a generally imple-

mentable active rotor was MEMS accelerometers. In a similar manner, mass-balancers emerged as the ideal actuation method. Thus, the prototype design adopted both technologies from the offset.

4.3 Mechanical design

This section gives details regarding the design of the various mechanical components of the prototype, subdivided into rotor- and stator-related components. Figure 4.2 shows the final prototype iteration.

The rotor is an assembled shaft, and contains the housings for the sensors, microcontroller and radio, as well as the mass-balancer actuators. The slipring and motor-end coupling assemblies are described. The stator is composed of a base, housed bearings and a motor with an encoder. The auxiliary eddy current displacement sensors used are also described here, as are the various safety features included in the design.

4.3.1 Rotor design

Shaft

The rotor was required to display significant vibration within the available speed range of the motor (up to $3,000$ rpm), to provide easily observable and controllable dynamic behaviour. It thus needed to be flexible, demanding a long rotor with small outer diameter. On the other hand, the section of rotor in which the active components would be held was required to be relatively large to ease design and assembly. An assembled rotor design was decided upon, which could satisfy both of these seemingly contradictory requirements.

Aside from providing increased flexibility, the assembled design allows the central section to be detached, which greatly eases assembly of the internal components in the prototype. Not only do these have to be mechanically fastened into place, but electrical connections have to be made between them, which would have proven extremely difficult in a single shaft rotor. For more general rotors, however, an assembled shaft design may not be practical. Thus, alternative arrangements for internally mounting the active components are discussed further in Chapter 8.

The rotor is composed of three hollow shaft sections, as shown colour-coded in Fig. 4.3. The central, shorter section, measures 110 mm in length and has outer and inner diameters of 60 and 54 mm, respectively. This section houses the active components. The remaining shaft sections have an outer

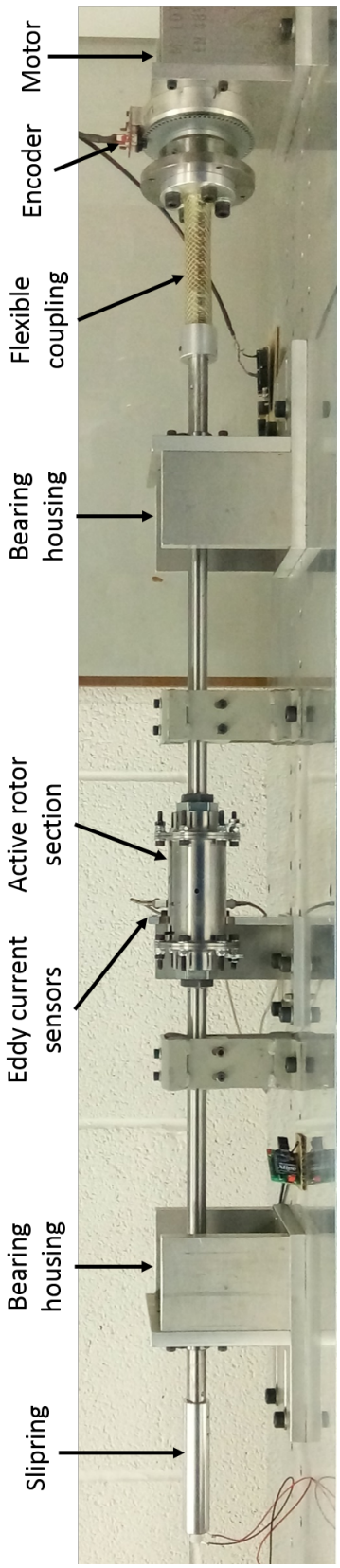

Figure 4.2: Active rotor prototype.

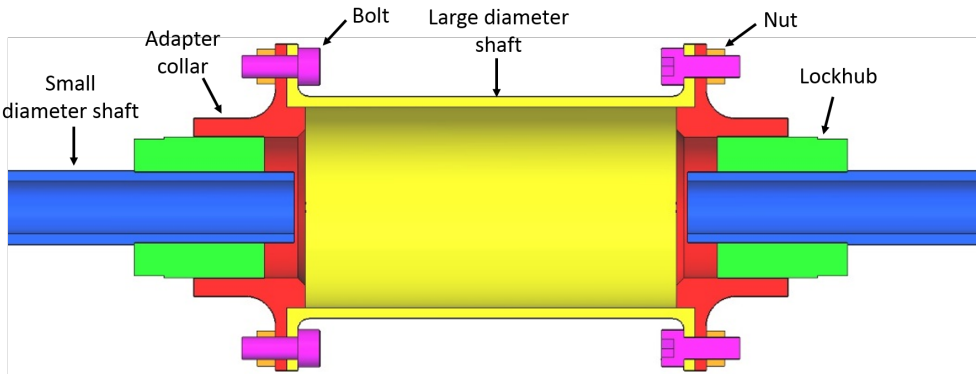

Figure 4.3: Cross-section of central assembly, indicating its constituent parts.

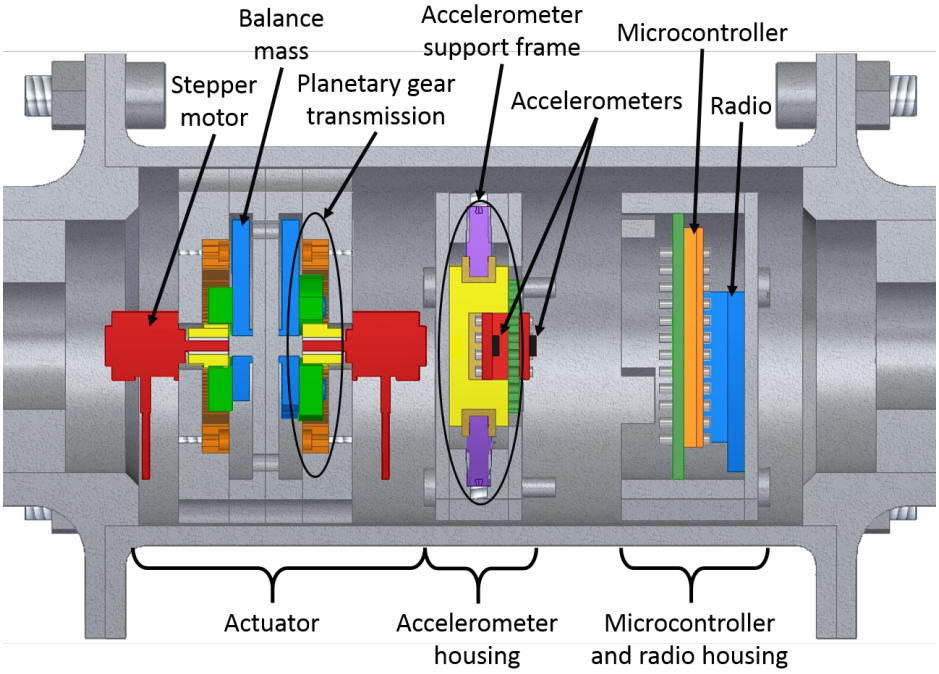

Figure 4.4: Cross section of central assembly, showing the internal components.

diameter of 20 mm, an inner diameter of 14 mm and a length of 500 mm. The overall dimensions of the rotor where determined with the aid of the model described in Chapter 3, aiming to obtain specific rotordynamic characteristics. The shafts are attached together through two flanged adapter collars, which fit the dimensions of two lockhubs. The flanges are bolted together.

The active components were mounted in housings with a circular outer diameter which matched the inner diameter of the central shaft. This ensured they could be securely slid inside the shaft during assembly, remaining perpendicular to the main rotor axis. Their axial position was then fixed by tightening grub screws located at predefined positions. Figure 4.4 shows the central shaft section with the active components inside.

When fully assembled, the rotor's zero speed natural frequency is 38.5 Hz ($2,310$ rpm), established by performing impact tests and using the internal accelerometers to determine the resonance frequency.

Accelerometer support frame

The accelerometers were mounted on a support frame held within the central shaft. If the sensors were not located at the geometric centre of the rotor, they would be subjected to increased centripetal acceleration caused by the eccentricity, aside from the acceleration associated with the dynamic behaviour of the rotor. Although this additional acceleration could be removed from the data by simple signal processing, its presence could also cause the accelerometers to saturate prematurely, limiting the effectiveness of the vibration measurements. Thus, the support was designed to allow varying the accelerometer position within the rotor. This is shown in Fig. 4.5.

The accelerometers were obtained ready-soldered on breakout boards, measuring 12×10 mm. These were then mounted on a piece of solder board, one on top of the other with their "Z" axes aligned. The board was screwed onto a central steel frame. Once fully assembled, the actuator Z axes lie along the main axis of rotation, with their "U" and "V" axes perpendicular to it. The frame is supported on four brass rails, and these in turn are held in position by a dog point screw and a pair of springs. The screws are threaded through the supporting outer frame. By adjusting the screws the position of the whole central frame can be moved in the U and V axes, by up to ± 2 mm. The screws are accessible from the outside of the rotor, through holes drilled in the central shaft section. The springs rest on the outer frame and ensure that the rails remain parallel to the sides of the frame during movement. Adjusting the U axis position by, for example, 1 mm, requires loosening the V axis screws slightly, retracting the +U screw by 1 mm and then pushing the frame with the -U axis screw, after which the V axis screws can be retightened. The screws have a 0.5 mm pitch, allowing the frame to be accurately positioned. The frame and screws are made out of steel to ensure that they do not deform noticeably under the potentially high centrifugal loads experienced during rotation.

Microcontroller and radio module housing

The accelerometer support frame was attached to a control and data transmission module which contained a microcontroller and radio transmitter/receiver. The reduced size of these components (33×18 mm for the microcontroller and

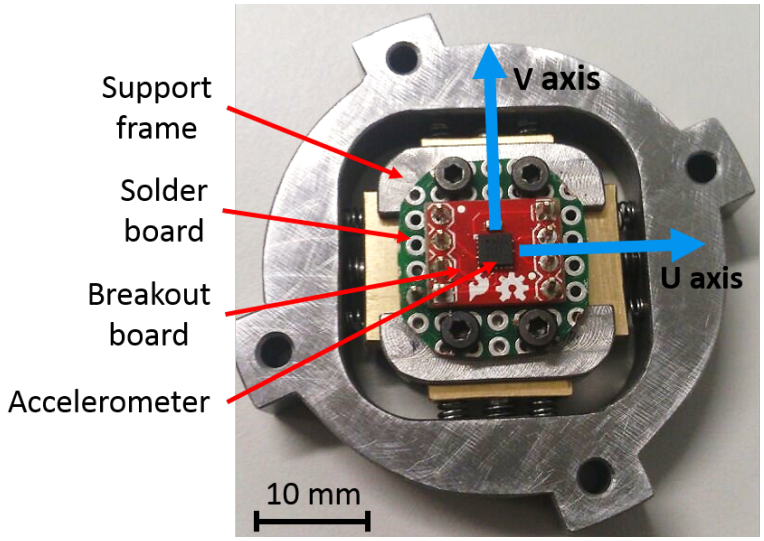

(a) Default position

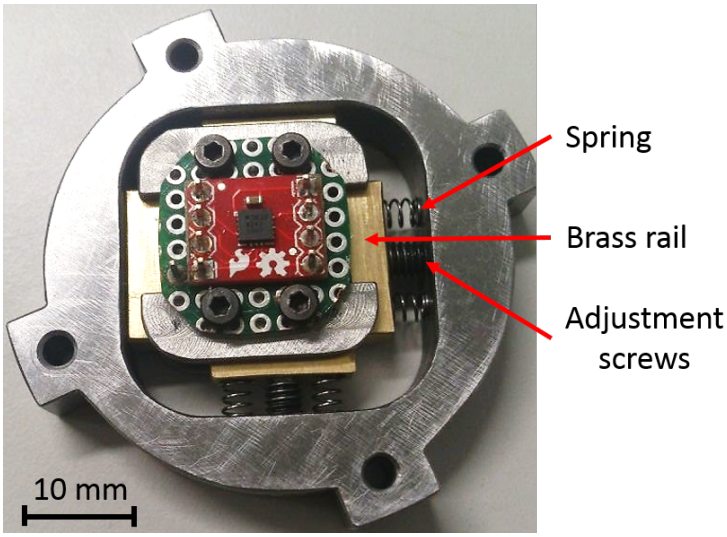

(b) $(-2, +2)$ mm adjustment

Figure 4.5: Photographs of the accelerometer support frame, shown in the default position and also translated by $(-2, +2)$ mm.

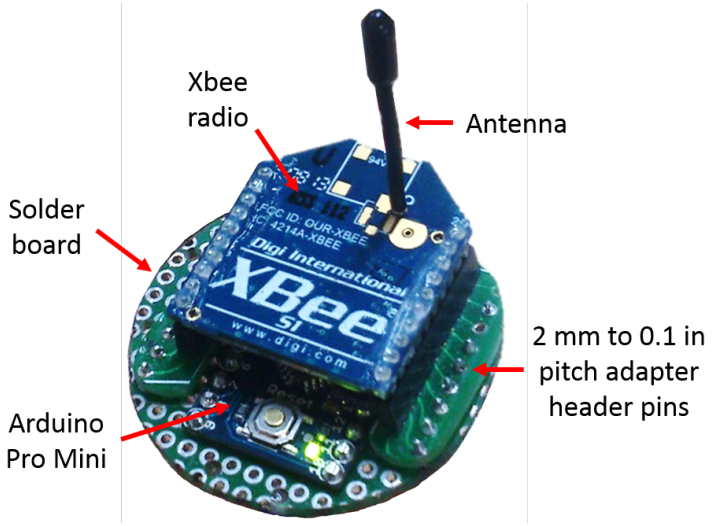

Figure 4.6: Microcontroller and radio module assembly.

28×24 mm for the radio module) allowed them to be fitted on a single modified solder board, stacking one on top of each other. This design considerably reduced the volume taken up by the components, as shown in Fig. 4.6. As the Xbee radio uses 2 mm pin pitch instead of the more conventional 0.1 in of the Arduino, modified adapter header pins were used to connect the devices. The solder board was mechanically attached to a steel housing using nylon screws, with a port drilled to allow the antenna to protrude.

The housing was attached to the accelerometer support frame, creating an integrated sensing unit containing all necessary electronic components to create a wireless accelerometer module. Figure 4.7 shows the module, including the auxiliary battery pack used only during the calibration process described in Chapter 5. The calibration power pack (Fig. 4.8) consists of an aluminium housing which contains a lithium polymer battery, with a nominal voltage of 3.7 V and a capacity of 165 mAh. With the battery pack, the accelerometers, microcontroller and radio can operate as a portable, standalone wireless sensor.

Actuators

The control forces in the active control system are provided by a mass-balancer type actuator. Two eccentric masses, located close together, provide a counter-unbalance which, under rotation, generates a force. If the masses are fixed in position, the force will be synchronous, but if the masses rotate, sub- or super-synchronous control forces can be generated. Controlling the position of the mass allows the magnitude and phase of the counter-unbalance to be

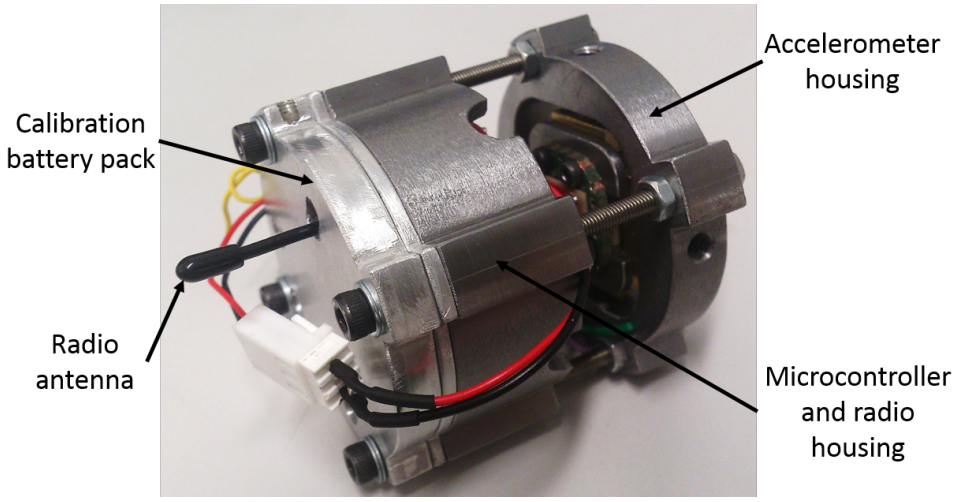

Figure 4.7: Photograph of sensing module with the calibration battery pack mounted.

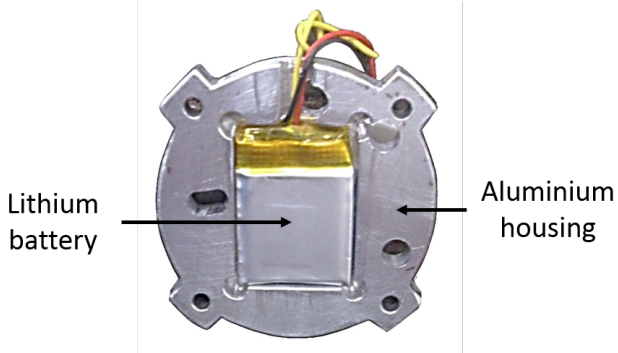

Figure 4.8: Photograph of calibration battery pack showing the lithium polymer battery within.

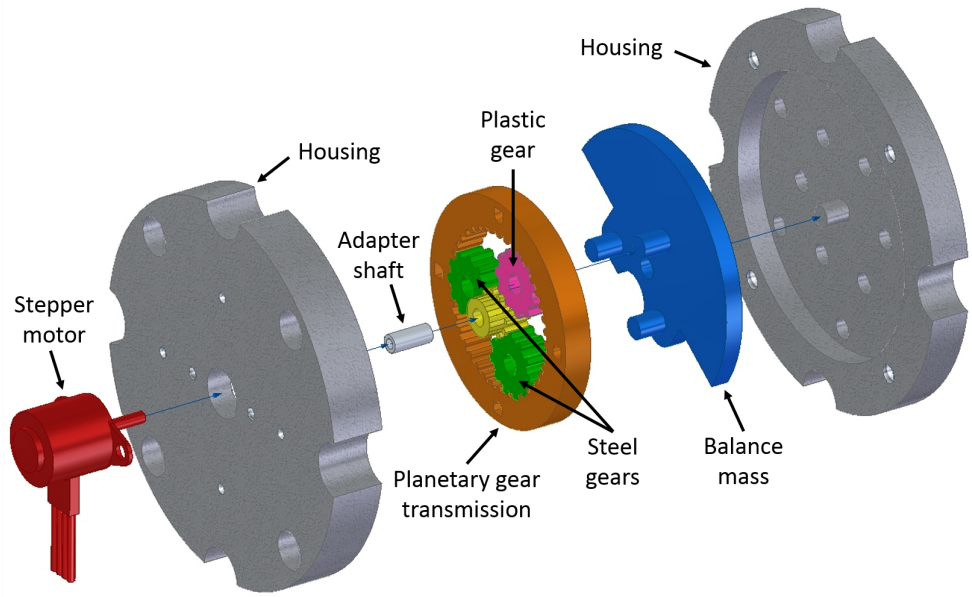

Figure 4.9: Exploded view of the mechanical components in one of the actuation modules. Two modules together form a single actuator.

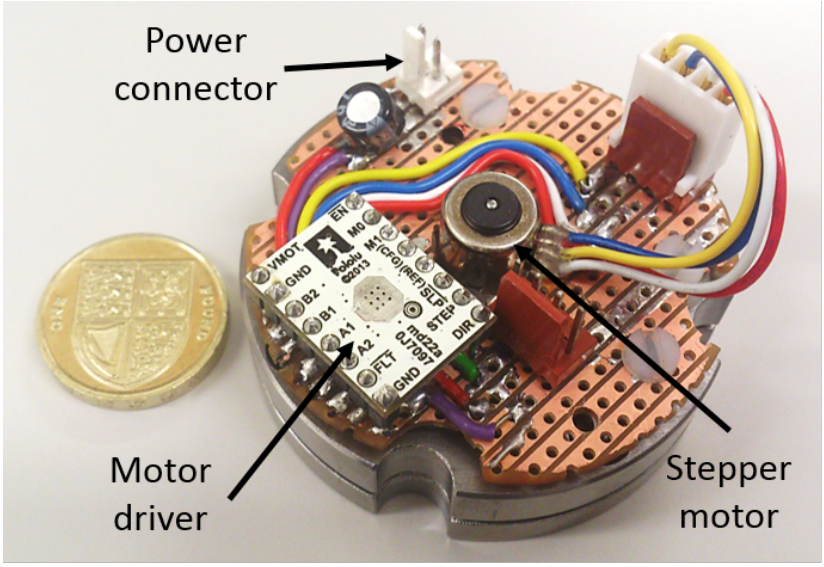

Figure 4.10: Detail of the electronics board mounted on the actuator housing, which contains the motor driver and electrical connectors.

controlled. The actuator is formed by two actuation modules, each of which contains an eccentric mass. The masses are driven by a stepper motor through a planetary gear transmission. Figure 4.9 shows an exploded view of the mechanical components of an actuator module.

The motors are Nanotec SP1018M0204-A stepper motors. They operate at 3.3 V, drawing a current of 440 mA. They were selected due to their very compact size (17.8 mm x 10.5 mm x 11 mm) and their low voltage requirements, which allow them to be powered by lithium ion batteries. This enabled the prototype to consider different power sources, improving its versatility as a test bed. The actuator electronics are all soldered on a single board, cut in the shape of the actuator housing and attached to it using nylon screws. The electronics board mounted on the actuator housing is shown in Fig. 4.10.

The motors provide 20 steps per revolution and a holding torque of 1.6 Nmm. The planetary gear assembly, with a reduction ratio of 5.2:1, converts this to 104 steps per revolution and a holding torque of 8.32 Nmm. The gearing system consists of a sun gear attached to the stepper motor shaft. An annular gear is supported by the housing to which the motor is attached, and which locates the actuation unit within the central shaft. Three planet gears are used, and the carrier which supports them is asymmetric, so that it has an eccentric centre of mass and hence also satisfies the role of balance mass. This provides the actuator with a very compact design, suitable for use in an internal topology. Figure 4.11 shows the gear housing and planet carrier/balance mass.

The sizing of the balance masses was performed by taking into account the

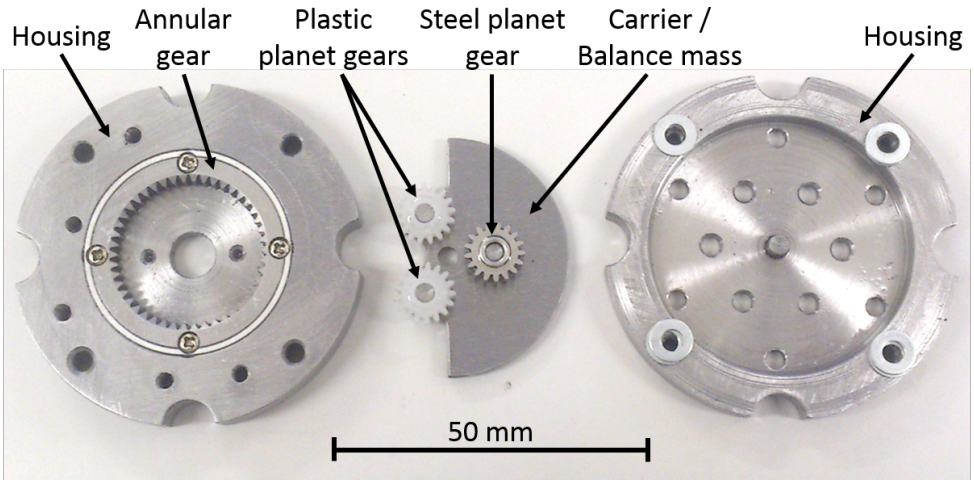

Figure 4.11: Planetary gears and housing, with asymmetric balance mass.

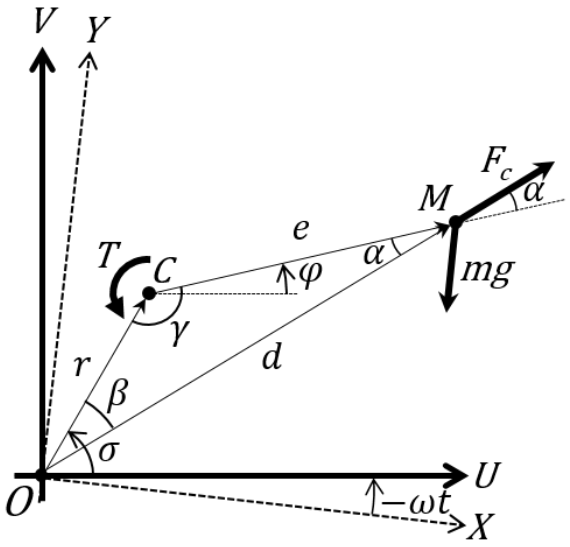

Figure 4.12: Schematic depiction of the balance mass.

maximum holding torque of the motor and transmission as well as the expected limiting operating conditions of the rotor. Figure 4.12 presents a diagram of an active shaft rotor in rotating frame of reference UV, operating at speed ω. Represented also is the inertial reference frame XY, rotated with respect to the rotating frame by an angle $-\omega t$. The rotor geometric centre C is assumed to describe a circular whirl orbit around O with orbit radius r. A single balance mass is located at M. The centrifugal force F_c acts on the centre of the balance mass, creating torque T at the centre of the rotor, where the actuator motor is assumed to be located. The torque is given by

$$T = eF_c \sin\alpha - emg\cos\left(\alpha - \omega t\right) \tag{4.1}$$

where m is the mass of the balancer and g the gravitational acceleration. The centrifugal force acting on M is given by $F_c = md\omega^2$, so Eq. (4.1) becomes

$$T = me(d\omega^2 \sin\alpha - g\cos(\alpha - \omega t)) \tag{4.2}$$

By similar triangles, it can be deduced that $\gamma = \pi + \varphi - \sigma$ and from the sine rule:

$$\sin\alpha = \frac{r}{d}\sin\gamma \tag{4.3}$$

Hence,

$$\sin\alpha = \frac{r}{d}\sin(\pi + \varphi - \sigma) = \frac{r}{d}\sin(\sigma - \varphi) \tag{4.4}$$

and thus the torque at the motor can be expressed as

$$T = em(r\omega^2 \sin(\sigma - \varphi) - g\cos(\alpha - \omega t)) \tag{4.5}$$

The torque will be maximum when $\sin(\sigma - \varphi) = 1$ and $\cos(\alpha - \omega t) = -1$, hence

$$\hat{T} = me(r\omega^2 + g) \tag{4.6}$$

Thus, the maximum counter unbalance that the stepper motors can hold in the worst case scenario is determined by

$$me = \frac{\hat{T}}{s(r\omega^2 + g)} \tag{4.7}$$

where s is a factor of safety. Assuming a maximum whirl orbit of 0.75 mm, a maximum speed of $2,100$ rpm and a safety factor of 2, the limiting unbalance for a holding torque of 8.32 N.mm is 90.3 g.mm.

In order to increase the unbalance provided by the actuator while maintaining a practically sized carrier, one of the planet gears used would be steel and the others would be plastic. This produces an unbalance of 6.3 g.mm. The final carrier design has a mass of 14 g and an eccentricity of 6 mm, producing 84 g.mm unbalance. Thus, the two masses in the actuator can provide a total counter-unbalance which ranges between 0 and 180.6 g.mm. This would be sufficient to correct the unbalance of a rotor with the same mass as the prototype (3.52 kg) and a Balance Quality Grade G6.3 or below, as specified by ISO standard 1940-1:2003/Cor.1:2005 [1]. This grade is suitable for electric motors, flywheels or aircraft gas turbines, for example.

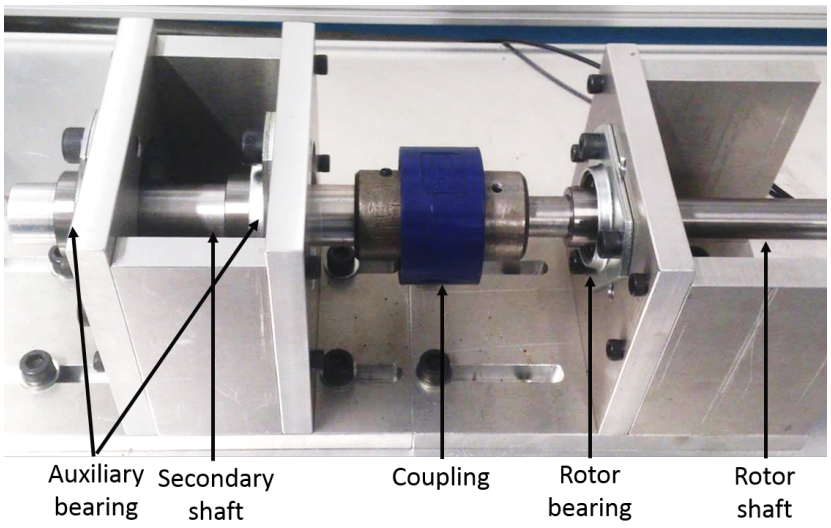

Figure 4.13: Photograph of the battery module used to power the active rotor components in an early design iteration.

Power supply

For a truly stator-independent rotor design, the energy used by the internal components would have to be extracted from the rotational energy of the shaft by energy harvesting. However, the design and implementation of a suitable device was found to be beyond the scope this research project. Therefore, an early iteration of the prototype used on-board batteries to supply power to the internal components. These were mounted inside a secondary shaft, flexibly attached to the main rotor via a barrel gear coupling to ensure that the unbalance vibration associated with the rotating batteries would not affect the dynamic behaviour of the active rotor. The secondary shaft was aluminium, 170 mm in length, with an outer diameter of 30 mm, an inner diameter of 26 mm and mounted on two rolling element bearings, as shown in Fig. 4.13.

The active system requires approximately 1 A current at 3.3 V, and so rechargeable lithium ion batteries were used, which provide a nominal voltage of 3.7 V. Two 18650-size batteries (18.6 mm diameter and 65 mm in length) were used, giving a total capacity of around $4,000$ mAh and up to 4 hours of testing time. This finite duration demanded careful planning of the test schedule to guarantee that fully charged replacement batteries were always available when required, and hence the battery system was eventually replaced by a slipring assembly. Although a compromise on the rotor-centred design philosophy, this enabled the prototype to more easily fulfill its role as a test bed, while keeping the research project within scope. Further considerations regarding the power supply are discussed in Chapter 8.

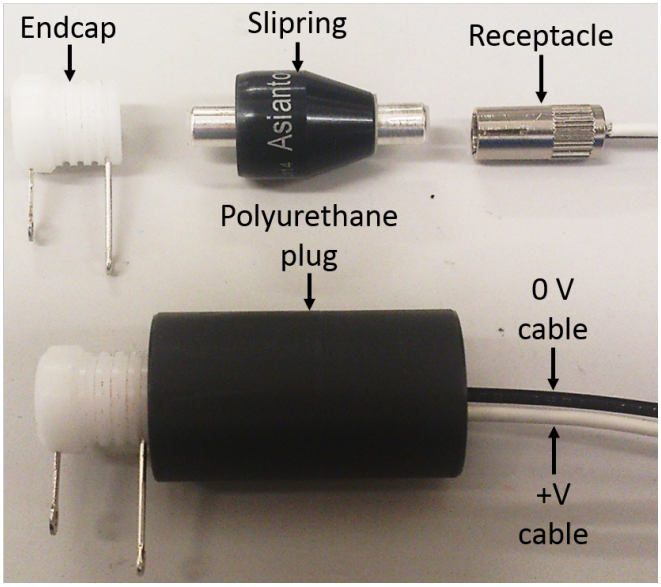

Figure 4.14: Photograph of the slipring components (top) and its appearance once mounted in the polyurethane plug (bottom).

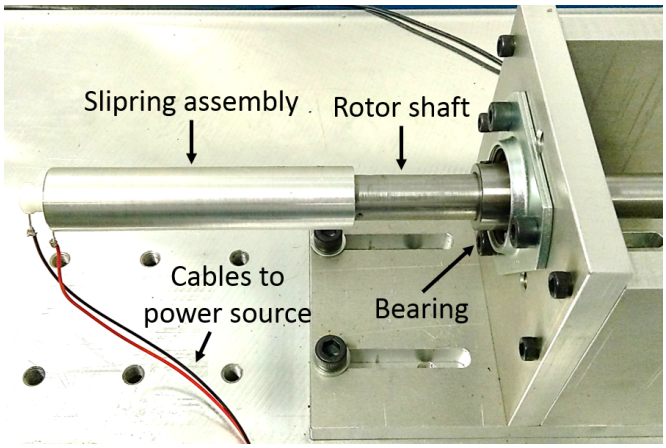

Figure 4.15: Photograph of the slipring assembly mounted on the prototype.

Only mercury-based sliprings were found to be able to withstand the necessary rotating speeds while remaining within a prototyping budget. The Asiantools A2S model was finally selected, as it has two conductor poles: one for + V and one for 0 V. It is a coaxial design and withstands a maximum operating speed of $2,000$ rpm, withstanding voltages of up to 250 V and currents up to 4 A. It has an outer diameter of 14.3 mm and an assembled length of 46 mm. The upper half of Fig. 4.14 shows the slipring with its corresponding end cap and receptacle. Beneath this is shown the assembled slipring located within a protective plug machined out of polyurethane. This plug was inserted within a machined aluminium tube, which was attached to the rotor shaft, as shown in Fig. 4.15.

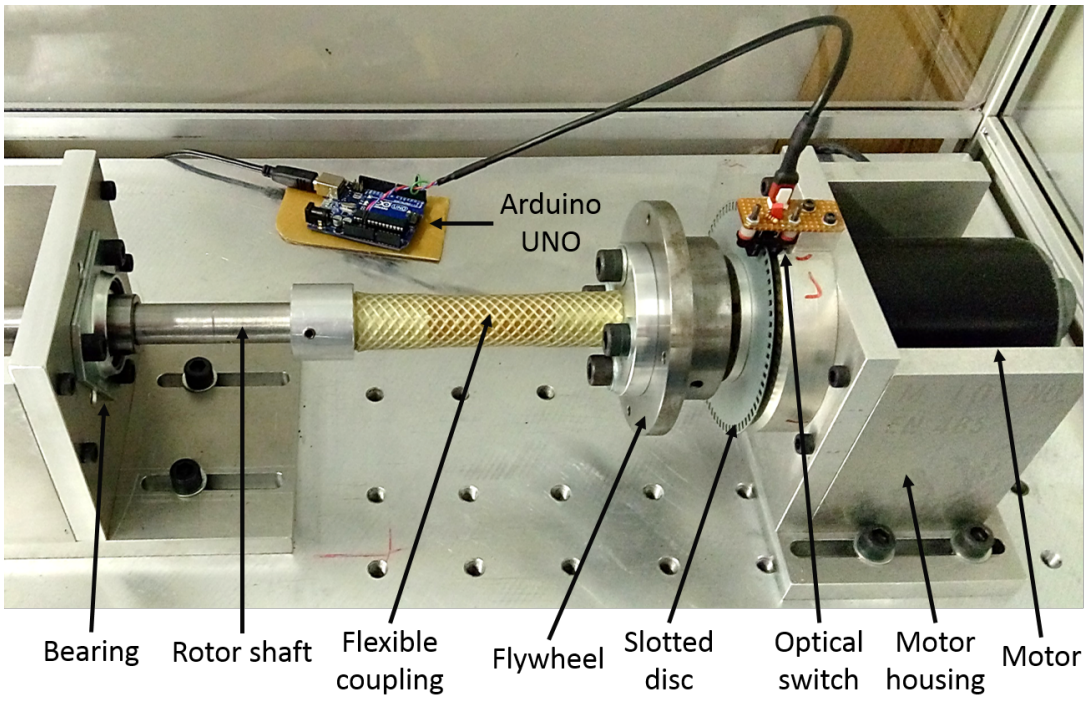

Figure 4.16: Photograph of the motor-side coupling, showing various components.

Motor-side coupling

The motor and shaft are attached via a flexible coupling. Early iterations of the design used a nylon barrel gear coupling. However, it was found that certain dynamic behaviour was excited by the rubbing between the coupling gears and nylon barrel. Due to the very flexible nature of the prototype, this excitation interfered with some of the tests. Thus, the barrel coupling was replaced with a rubber coupling which prevented such behaviour, as shown in Fig. 4.16. It was constructed with a section of rubber tubing, press fitted onto machined aluminium couplings. These could be secured on the rotor and motor shaft via grub screws, which allowed for a simple assembly and disassembly procedure.

4.3.2 Stator design

Stator base

The stator base consists of a tooled aluminium plate measuring $200 \times 50 \times 2$ cm. It was provided with threaded M10 holes along its length, which allowed the stator components to be located at different positions, so that the stator design could adapt to the evolving testing requirements. The base plate was attached to a rigid steel frame via 10 isolating rubber mounts. Figure 4.17 shows the components of the stator base.

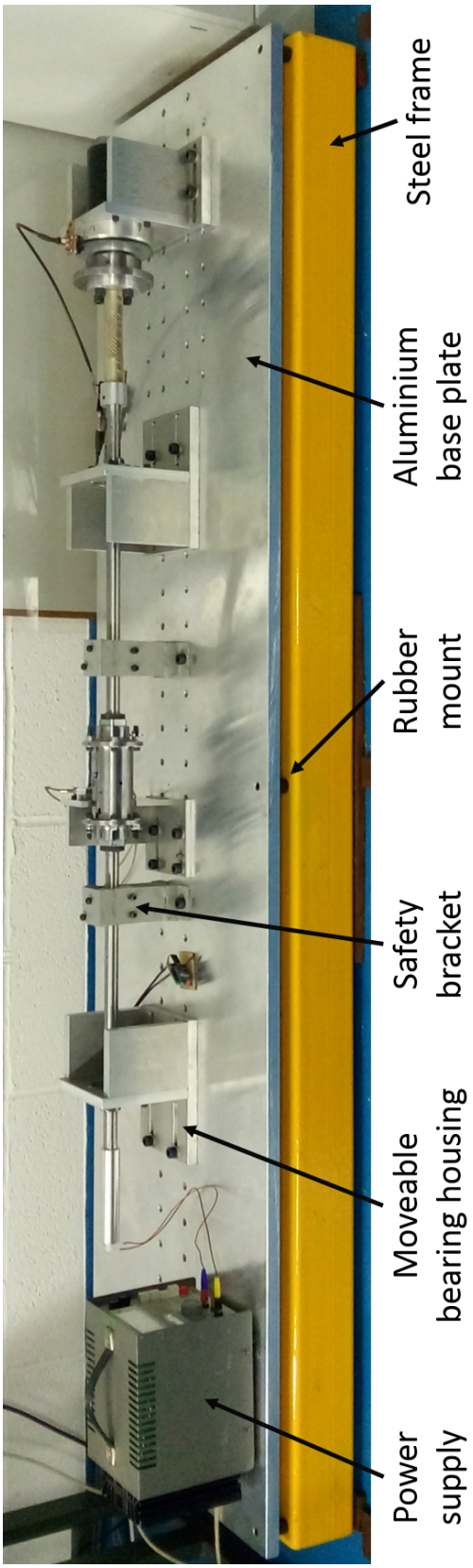

Figure 4.17: Photograph of the stator base, with relevant components labeled.

Bearings

Two rolling element bearings with an inner diameter of 20 mm are used to support the rotor at each end. The bearing housings were manufactured out of 15 mm thick aluminium plate. The design of the base plate allowed the separation between the bearings to be changed, in order to vary the rotor length. In the final design, the bearings were separated by 90 cm.

Motor

The rotor shaft is driven by a DC motor able to operate at $3,000$ rpm. It requires a 11.5 V supply and is rated for a maximum current of 14 A. A steel flywheel is attached to the rotor shaft to provide an inertial load which can smooth the motor output. The motor is supported by an aluminium housing, fabricated from 15 mm thick plate. The motor and housing are indicated in Fig. 4.16. A motor speed controller with a potentiometer, located in the laboratory control room, enables manual control of the motor speed.

Encoder

The rotor speed is measured using a custom-built encoder. It consists of a disc with 72 slots and an optical switch. The switch is connected to an Arduino UNO microcontroller board, which measures the time in between each passing of a slot and calculates the rotational speed. This information is then transmitted via a serial-USB cable to the external PC, where the speed is displayed and recorded. The encoder's components are labeled in Fig. 4.16.

Eddy current sensors

A pair of stator-mounted eddy current displacement sensors was installed on the prototype. This provided a reference vibration measurement obtained with conventional sensing technology, which could be used to validate the results from the rotor-mounted accelerometers. The sensors have a range of 0 to 2.5 mm, and a sensitivity of 8 μV/μm. The output from their 24 V drivers is processed by a dSPACE controller, which uses a Simulink model to configure the measurement settings. The sampling rate is 1 kHz. The probes are mounted on an adjustable aluminium frame, at an angle of $+45^\circ$ and -45° with respect to the inertial X axis, as illustrated in Fig. 4.18. They form a secondary reference frame P_1P_2, and so their output is transformed to the XY frame using the following transformation matrix:

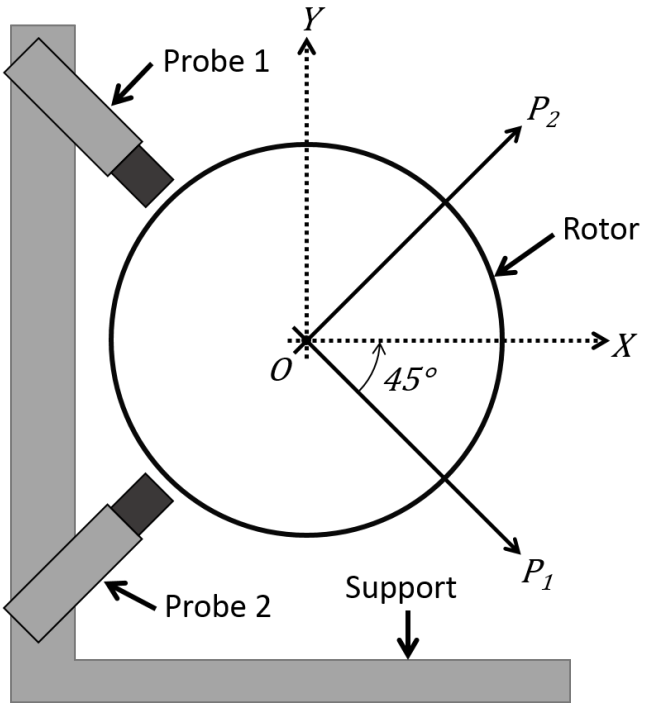

Figure 4.18: Eddy current sensor arrangement.

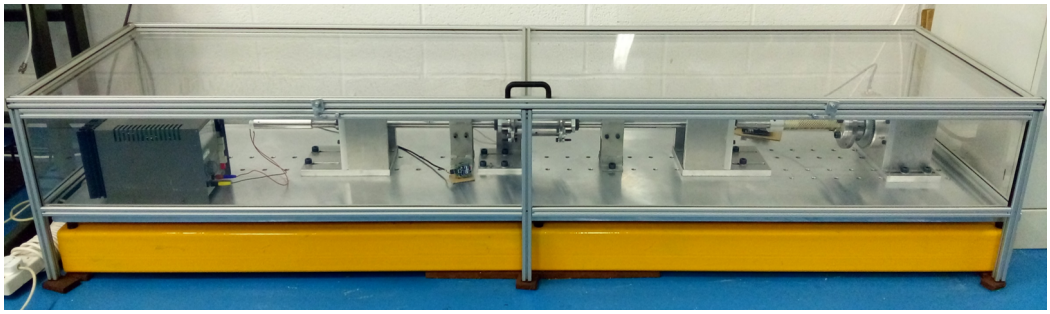

Figure 4.19: Photograph of test rig with safety guard installed.

$$\begin{Bmatrix} x \\ y \end{Bmatrix} = \begin{bmatrix} \cos\frac{\pi}{4} & \sin\frac{\pi}{4} \\ -\sin\frac{\pi}{4} & \cos\frac{\pi}{4} \end{bmatrix} \begin{Bmatrix} p_1 \\ p_2 \end{Bmatrix} \tag{4.8}$$

Safety features

As the prototype rotor is an assembly of parts, it was deemed necessary to install safety guards in the stator to minimise damage in the case of failure. Steel safety brackets, shown in Fig. 4.17, were placed over the rotor shaft. They are lined with machined nylon pads and are designed to contain the smaller diameter shafts in case of a lockhub failure. In addition, an aluminium frame with transparent polycarbonate panels was installed to protect the working environment from possible debris which could be ejected from the rotor in case of failure. This safety guard is shown in Fig. 4.19.

4.4 Electronic design

With regards to electronic components, the prototype contains a microcontroller, a radio, two accelerometers and two actuators, each with a stepper motor and associated driver. The design considerations related to these devices are detailed in this section. A circuit diagram of the various internal electronic devices is provided in Fig. 4.20.

Microcontroller

The microcontroller board used in the prototype is an Arduino Pro Mini (3.3 V model, shown in Fig. 4.21). Arduinos are open-source microcontroller boards, designed to allow non-experts to design and operate electronic circuits. Their low-cost, ease of use and strong user community support make them ideal for use in prototyping and research. The use of open-source technology such as this is firmly established and gaining popularity in research environments, as commented by Pearce [2].

The board contains an Atmel ATmega328 microcontroller, with a clock speed of 8 MHz. There are 14 digital input/output, some with specialised functions such as Serial data transmission, SPI communication or external interrupts. All of these would be utilised to maximise the functionality of the Arduino, thus enabling a single unit to control all the electronic components in the active system. The Arduino operates at 3.3 V, which is produced from an in-built voltage regulator which can take up to 12 V as input. This enables the microcontroller to operate using lithium ion batteries, which usually produce a voltage of around 4.2 V at maximum charge, progressively decreasing to around 3.2 V as the charge is depleted. This regulated supply was used to provide power to the accelerometers and the Xbee radio module.

Radio module

The two radio units are Xbee 802.15.4 modules. These use the Zigbee communication protocol, designed for small personal area networks. A key characteristic is their ease of use, enabling their implementation by non-experts. Their low power consumption makes them ideal for mounting within a rotating shaft. One radio acts as network coordinator, establishing the network and storing related information such as security keys. The other module is mounted on the rotor and acts as an end device. If more than one sensor/actuator pair were used, several end devices could be used with a single coordinator.

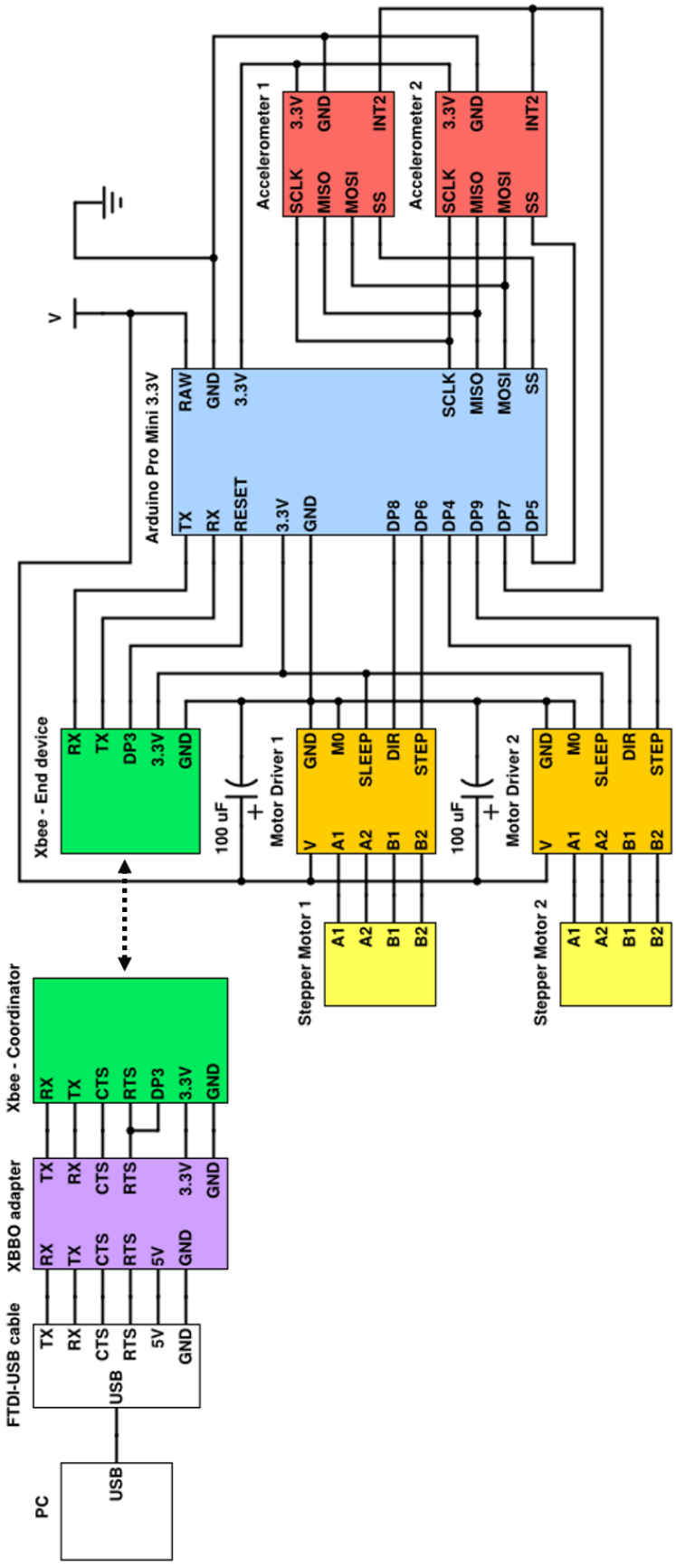

Figure 4.20: Circuit diagram of the prototype active rotor.

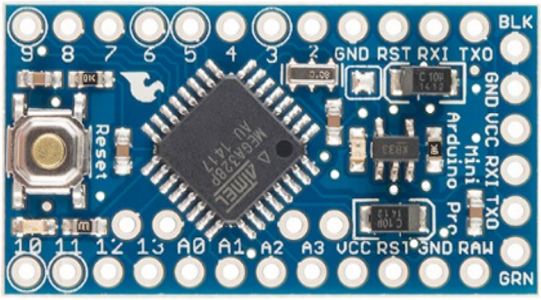

Figure 4.21: Photograph of an Arduino Pro Mini board. Original image from Sparkfun, reproduced under CC BY-NC-SA 3.0 license.

Figure 4.22: Photograph of the coordinator Xbee radio mounted on the XBBO adapter board.

The coordinator is located within the stator safety cage, mounted on a CISECO XBBO adapter board and connected to a PC via a FTDI-USB cable. The XBee model mounted on the rotor uses a whip-type antenna, enabling it to protrude from the central shaft section body to avoid the steel housing from blocking the transmission. Figure 4.22 shows the Xbee mounted on the adapter board, while Fig. 4.23 shows its location within the stator. The short distance between the coordinator and end-device means that the relatively low transmission distance associated with the Zigbee protocol (10 to 100 m) does not affect the operation of the system.

As the transmitted data consists of relatively small packages of sensor and actuator information, the 250 kbit/s data transfer rate is sufficient for a prototype application. Other protocols such as Bluetooth, WiFi or Wireless USB would be suitable alternatives if larger data transfer rates were required.

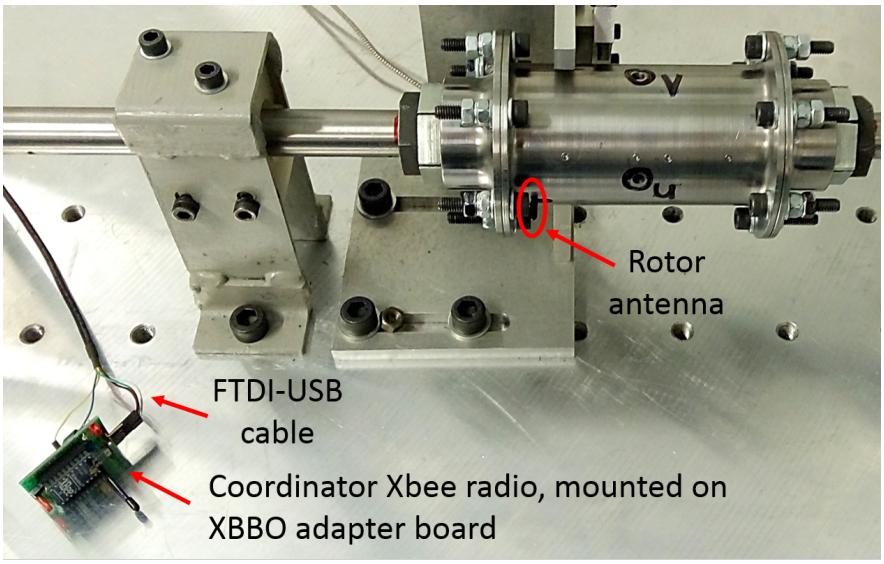

Figure 4.23: Photograph detailing the location of the coordinator Xbee within the rig stator, as well as the rotor antenna.

The Xbees are used in “Transparent” mode (referred to as AT mode), which enables a simpler setup when only two radios are communicating. In this operating mode, the radios act as a virtual serial connection between devices, simply relaying any information that arrives at the Xbee’s serial port.

The Xbees were configured to allow programming of the Arduino and observing the serial monitor over the wireless network, which greatly simplified the task of upgrading the Arduino code as the prototype evolved. Programming an Arduino can only be done after a reset, which is typically triggered automatically by the RTS (Request To Send, used for flow-control) signal, produced by a PC when communicating with the Arduino. However, serial communication between an Xbee and Arduino does not carry the RTS information. To enable wireless programming, a bridge was formed between the RTS status on the PC and the Arduino’s reset pin, using one of the functionalities of Xbee radios: digital line passing. This allows the status of a digital pin on the coordinator to be replicated on the end device without interrupting regular transmission. One of the digital pins on the coordinator Xbee was connected to the RTS pin and a jumper was also soldered between the end device Xbee’s replicated digital pin (DP3) and the reset pin on the Arduino. In this way, the Arduino could be wirelessly reset (and consequently, programmed) following the same process used with conventional wired connection.

Accelerometers

MEMS accelerometers are used in the prototype. Recent developments in the portable electronics industry have lead to the mass-production of MEMS accelerometers, meaning these devices are readily available, and at very low cost. Modern designs strive for miniaturisation and minimal power consumption. Thus, MEMS accelerometers are ideally suited to be used as internally mounted sensors, because large numbers of them can be fitted while maintaining an affordable design with practical power requirements.

Two accelerometers are used, for redundancy. These are Analog Devices ADXL362 digital MEMS accelerometers, which are shown ready-mounted on breakout boards in Fig. 4.24. They measure acceleration in three axes, referred to as "U", "V" and "Z". In addition, they can measure temperature between -40°C and $+85$°C. They have 12-bit resolution, which allows selectable measurement ranges of $\pm$2, 4 or 8 *g* with a corresponding resolution of $\pm$1, 2 or 4 m*g*. The sampling rate can be set to default values of 12.5, 25, 50, 100, 200 or 400 Hz. These rates can be scaled by using an external clock instead of the built-in 51.2 kHz one or, as is done in the prototype, data can be sampled in response to an external trigger. If using the latter approach, the maximum achievable sampling rate is 625 Hz. However, the accelerometers have an in-built anti-aliasing filter, which is set as a fraction ($^1/_2$ or $^1/_4$) of the sampling rate setting. Because of this, the anti-aliasing filter has a maximum cut-off frequency of 200 Hz, so that any vibration components with a higher frequency are attenuated. Given that the maximum operating speed of the rotor was approximately 33.3 Hz (2,000 rpm), the 200 Hz cut-off is sufficient to capture any meaningful rotor vibration behaviour of the prototype. For many industrial applications, sampling rates in the kHz range would be required. MEMS accelerometer technology continues to evolve, and high performance devices with bandwidths up to 14.25 kHz are commercially available [3].

The accelerometers are designed with low power applications in mind. Consequently, they operate on a voltage ranging from 1.6 V to 3.5 V, with current consumption in the μA range. As the power supply has a significant effect on the accelerometer output, it is necessary to use a regulated supply to ensure constant operating conditions are maintained. In this instance, the voltage regulator on the Arduino was used to provide the supply to both the accelerometers.

The devices communicate using a Serial Peripheral Interface (SPI) bus, which involves a master-slave design. In this instance, the microcontroller acts as a master, and the accelerometers are slaves. The bus requires three connections

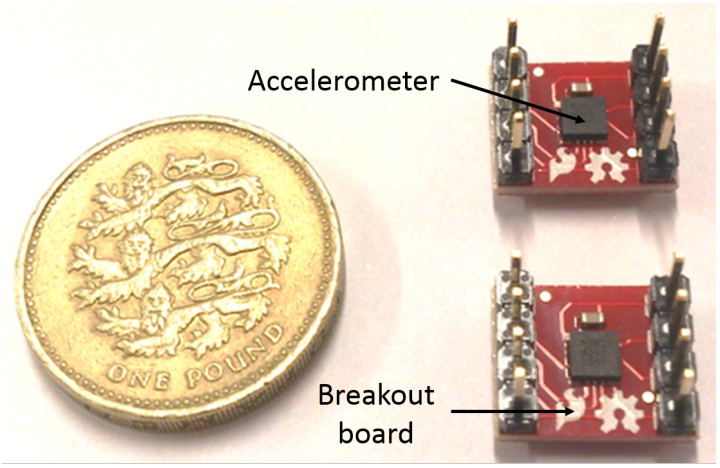

Figure 4.24: Photograph of the MEMS accelerometers used in the prototype, mounted on breakout boards.

which are shared by the microcontroller and the two slaves. These are SCLK (Serial Clock), MOSI (Master Output, Slave Input) and MISO (Master Input, Slave Output). Two further connections called SS (Slave Select) link the microcontroller to each of the slaves individually. The master outputs information to the slave on the MOSI line, while the slave simultaneously outputs information to the master on the MISO line, a technique known as full duplex transmission. The SS lines determine which of the slave devices is communicating with the master at any given time, and are connected to different digital pins on the Arduino.

Two interrupt pins are available on the accelerometers, which can be used as either input or output pins to enable various functions, such as indicating whether or not the accelerometers are in sleep mode (used to reduce power consumption) or saving samples in response to a trigger event. The latter functionality is used in the prototype, together with the Arduino interrupt functions, to produce a more controllable sampling rate. To this end, the INT2 pins of the accelerometers are connected together, and set to input mode for synchronised data sampling. Thus, when the common pin is driven to a logical high, both accelerometers are triggered at the same time and save an acceleration sample in their internal First In First Out (FIFO) buffers. The Arduino drives the INT2 line high after a predefined period of time, maintains it for 36 μs to ensure detection by the accelerometers, and then drives the line low again. This task is performed on the Arduino as an interrupt, meaning that it takes place in the background while the regular program is run. Although this sampling technique requires a more complex setup, it provides a number of key advantages. Firstly, by setting the period between each of these pulses a user can specify a

sampling rate with greater flexibility than if the predefined sampling rates were used. Secondly, by guaranteeing simultaneous sampling of both accelerometers, this architecture prevents the acceleration measurements obtained by each device from desynchronising due to small variations in sampling rate. In addition, having the microcontroller determine the sampling rate helps to ensure that the reading of the accelerometer data happens at the correct time within the Arduino program, so that the accelerometer buffers do not overflow, nor are they read before being sufficiently filled.

Actuators

The stepper motors used were chosen due to their low voltage requirement. In accordance with this consideration, each actuation unit is fitted with a low voltage stepper motor driver, Texas Instruments' DRV8834. These allow controlling the motors by providing only a step and direction demand from the microcontroller. The drivers were obtained ready-mounted on breakout boards, which simplified their installation.

The drivers can use supply voltages in the 2.5V to 10.8 V range, meaning they do not require a regulated voltage supply and can interface directly with the slipring assembly. This is an important consideration, as the current draw of the stepper motors (440 mA each) is considerably higher than the maximum current output of the Arduino regulator (150 mA). A 100 μF capacitor is provided across the motor supply and ground lines to protect the drivers from supply spikes. As the stepper motors are of two-phase bipolar design, they have a single coil per phase. Thus, each phase requires two connections to the driver, four in total. The drivers feature a sleep function which enables them to power off when not in use to minimise power consumption. The driver sleep pin must be kept high for operation. As the balance masses must be held in position at all times for controlled operation, the sleep pin was connected directly to the Arduino regulated supply, ensuring the motors would remained powered throughout.

To control the stepper motors, the drivers require a step number and direction instruction, which was supplied by the Arduino from its digital pins. The drivers feature microstepping modes, whereby the motors can be moved only a fraction of a step, down to 1/32 step resolution. However, microstepping also reduces the effective holding torque and can lead to reduced stepping accuracy. Thus it was decided to use full-step resolution for maximum torque, relying on the gearing to produce a reasonable step resolution (104 steps/revolution). The driver resolution is controlled by the status of two digital pins, M0 and M1, both

of which must be driven low for full-step mode. As the M1 pin has an internal 200 kΩ pull-down resistor, only the M0 pin required a connection directly to the Arduino's ground.

Wiring and connectors

Due to the many components in the design and the reduced space available, consideration had to be given to the assembly process. This had to allow locating each component inside the rotor securely, while also enabling the user to connect all electronic components. Thus, all wiring was fitted with connectors, and space was provided for them. Figure 4.25 shows the wiring diagram of the prototype.

A single cable runs the length of one of the smaller diameter hollow shafts, from the slipring assembly to the central section. To reduce its unbalance contribution and prevent it from exciting dynamic behaviour in the rotor due to its movement within the shaft, the cable was secured. Four polyurethane plugs with holes drilled through the centre were used, with the cable threaded through them. These plugs were then slid inside the shaft section and secured in place with grub screws. The cable was fitted with connectors at each end, so that electrical connections to the slipring assembly and the components within the active section could be easily made, thus simplifying the assembly process.

4.5 Software design

The control of the different electronic components, as well as the interaction between them, required the development of a significant amount of software. This section describes the functionality of the programs written, which provides an explanation of the general operation of the test rig as a whole. The software written for the microcontroller configures and controls the accelerometers, the data transmission, and the actuators. A general description of its operation is first given, followed by details pertaining to each of its aspects. Software was also written to process, store and display information on the external rig PC, and is also described.

4.5.1 Microcontroller software

The Arduino microcontroller can be programmed using the C++ language. The code written follows the prescribed Arduino structure. When booted, the code

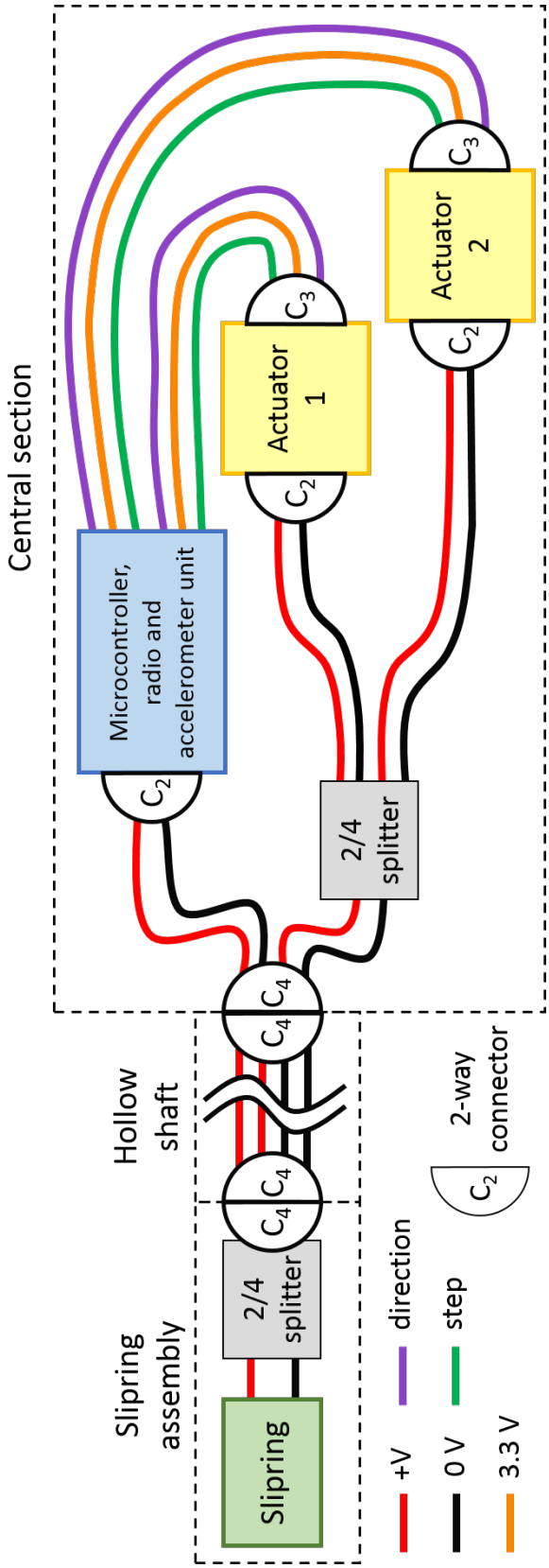

Figure 4.25: Wiring and connector diagram for the active rotor prototype.

first loads any libraries that are to be used and creates the user-defined control variables. A setup loop then runs once, executing all configuration functions required, setting up parameters such as serial communication baud rate or accelerometer measurement mode. The main loop then executes, repeating indefinitely and performing three main tasks: reading the accelerometers, transmitting the data and executing the actuator demands. Throughout, an interrupt function runs in the background, measuring time using an internal clock. After a used-defined time interval, the function sets the interrupt pin high, which causes accelerometers to record a sample.

The main loop, shown as a flow chart in Fig. 4.26(a), first queries the number of samples, n_s, which have been recorded. When the counter shows 12 samples, the accelerometer data is read from the FIFO buffer. The information is then packaged into a specific message structure, and transmitted on the serial connection to the Xbee radio module. Once there, the radio module will transmit the message wirelessly, after having confirmed that the channel is clear. In the meantime, the loop continues by reading the Arduinos' incoming serial buffer, to check if any actuator demand instructions have been received from the PC, via the radio module. If so, a demand processing function is executed, which interprets the number of steps and the direction of motion (clockwise or anti-clockwise) demanded for each actuator. The loop then finalises by executing the actuator steps. To do this, it first checks how many accelerometer 12-sample data packages have been sent. If this number is equal to the user-defined limit, $\hat{n}_m$, it checks how many actuator steps, n_a, have been performed, and whether this satisfies the existing step demand, n_d. If it does not, the actuators are moved a single step in the correct direction, as required. Thus, an actuator step can only take place every $\hat{n}_m$ messages, or $12 \times \hat{n}_m$ samples. The stepping speed is therefore controlled by setting the $\hat{n}_m$ parameter, which is 10 by default. As the sampling rate is high relative to the desired stepping rate, fast actuator speeds can be achieved. The reason for using this configuration is to allow the code to prioritise the Arduino's computing power for sampling data, rather than executing actuator demands. In effect, the stepping takes place in the background, but the user can immediately interrupt the stepping instruction by sending a new demand from the PC, which will reset the number of steps performed.

Accelerometer configuration and data reading

The accelerometers are operated by reading from and writing to 64 hardware registers. This task can be achieved via the microcontroller, taking advantage of

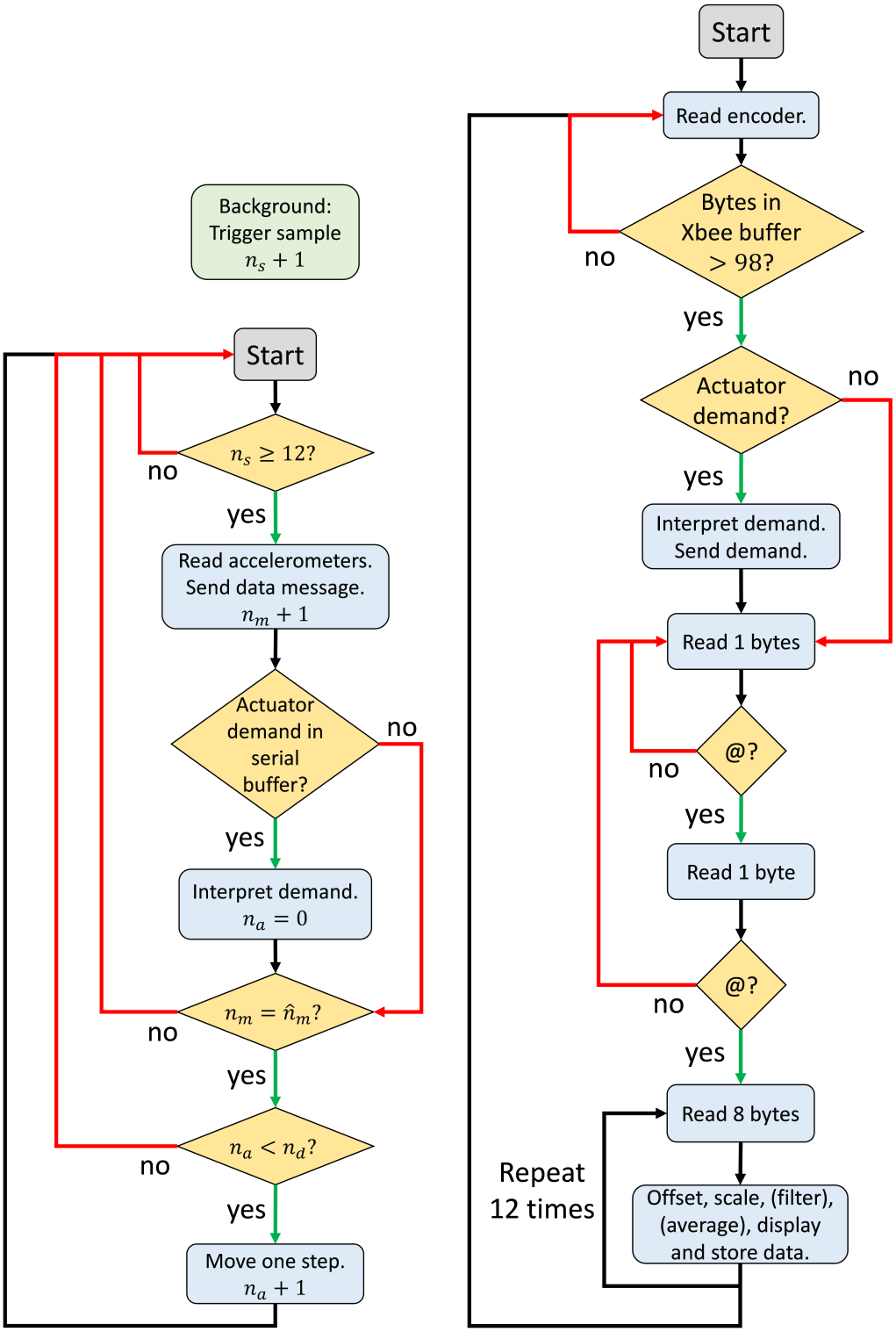

(a) Microcontroller software

(b) Rig control PC software

Figure 4.26: Flow charts for the microcontroller and rig control PC used in the prototype.

Table 4.1: Default accelerometer configuration

Configurable parameter	**Default setting**
Sampling mode	External trigger on interrupt pin
FIFO storage	On, 72 byte buffer size
Anti-aliasing filter frequency	200 Hz
Data reading	From FIFO buffer, UV axis multibyte
Data range	User-defined for each test
Sampling	User-defined for each test

the SPI communication. Thus, an Arduino function library was written which enabled configuring and operating the accelerometers. The library is based on the work by Mahey [4]. The functions can be broadly classified into "sampling modes", "sampling settings" and "data reading" categories.

The first are a group of initialising functions which determine the sampling mode in which the accelerometer is booted. The modes include sampling at fixed frequencies, sampling in response to external triggers, sampling with buffer storage enabled, and combinations thereof.

The "sampling settings" group of functions enable the accelerometer range, sampling rate and anti-aliasing filter frequency to be modified. These can be changed during operation with a soft reset, which reboots the accelerometer, enabling the user to dynamically change the acceleration measurement parameters. This functionality can also enable the microcontroller to automatically adapt to changing operating conditions, for instance increasing the acceleration measurement range setting if sensor saturation is detected.

The final group of functions allow data to be read from the accelerometer. The different functions enable reading the separate U, V and Z axis acceleration data, as well as the temperature data. Data can be read as it becomes available or whenever required by the microcontroller code, reading the samples stored in the accelerometer's FIFO buffer. When reading from the buffers, the code is written to perform multibyte reading, which maximises data throughput. When doing so, the sampling interrupt is disabled so as to prevent the accelerometer from attempting to both read and write to the buffer at the same time, which can compromise the data. The default operating mode and accelerometer settings used when operating the rotor prototype are given in Table 4.1.

Wireless data transmission control

After the accelerometer data is read in the main loop, the information is packaged into a suitable message structure and sent to the Xbee radio module over serial connection. The maximum serial baud rate supported by the Arduino Pro Mini is $57,600$ Bd. The transmission is performed by writing each individual byte in the message to the serial port, which minimises the amount of communication overhead. The radio module stores the packaged data in its incoming serial buffer until it is wirelessly transmitted to the PC.

The Xbee radio module uses the Zigbee standard, which can transmit at up to 250 kbits/s. It does so by sending packets with a 27 byte header and up to 100 bytes of data. Before sending a packet, the Xbee checks whether or not the carrier channel is free. As this requires a finite amount of time per packet, data throughput is maximised if full packets are sent. Thus, it is desirable to contain a set of accelerometer samples within a single Xbee packet. When measuring data from the U and V axes only, each sample will require 4 bytes of information (2 axes and 2 bytes per sample to capture the full 12-bit resolution). As two accelerometers are used for redundancy, a maximum of 12 samples can be transmitted in a single packet (96 bytes of information).

The data structure of the message is $\texttt{@@}\mathtt{A}_1\mathtt{A}_2$. The arrays $\mathtt{A}_1$ and $\mathtt{A}_2$ each contain the 48 data bytes corresponding to 12 samples of the U and V axes of the accelerometers, in the form $\{\mathtt{U}_{\mathtt{l}1}, \mathtt{U}_{\mathtt{h}1}, \mathtt{V}_{\mathtt{l}1}, \mathtt{V}_{\mathtt{h}1}, \ldots, \mathtt{U}_{\mathtt{l}48}, \mathtt{U}_{\mathtt{h}48}, \mathtt{V}_{\mathtt{l}48}, \mathtt{V}_{\mathtt{h}48}\}$. The $\mathtt{l}$ subscript indicates a byte holding the 8 least significant bits (LSBs) of data and the $\mathtt{h}$ subscript denotes a byte with the sign-extended 4 most significant bits (MSBs). The `@@` header is used to identify a new packet, and adds two bytes for a total message length of 98 bytes.

The `@` character is used as a header because it is represented by the binary string `0100 0000`. The first four bits of the high byte ($\mathtt{U}_{\mathtt{h}1}$, for instance) are a sign extension of the MSB, and will hence all be either `0`'s (for a positive number) or `1`'s (for a negative number), following two's complement arithmetic. Thus, the MSB byte can never take the form of the `@` binary string, as the first four bits would not all be the same. Consequently, two consecutive bytes containing accelerometer data may never both be `0100 0000`, and this fact can be used to clearly identify a message header.

When actuator demands are sent from the PC, the coordinator Xbee (in the stator) will wait until no incoming data packets are sensed before transmitting to the end-device Xbee (inside the rotor). The receiving Xbee will then send the actuator demand over the serial port to the Arduino. The demand is stored in the microcontroller's receiving serial buffer until it is read by the main loop.

Actuator demand processing

The actuator step demand is produced by the PC and sent as a string of characters to the Arduino's receiving serial buffer via the radio modules. When the main loop detects data in the buffer, it reads and processes it. The message received will usually be of the form $\texttt{\#N}_1\texttt{*N}_2$. The # and * characters are used to indicate whether the step demand corresponds to the first or second actuator, respectively. The parameters $\texttt{N}_1$ and $\texttt{N}_2$ indicate the number of steps. By convention, a positive number indicates a clockwise step, while a negative number will lead to anti-clockwise motion. As the actuators are positioned with rotational symmetry around the V axis, the code internally changes the sign of the step demands for actuator 2, so that the actuator masses move in the same direction if $\texttt{N}_1$ and $\texttt{N}_2$ have the same sign. A demand of zero steps will stop the actuator from moving any further. The command $\texttt{s}\hat{\texttt{n}}_\texttt{m}$ allows changing the stepping rate by setting a new value of $\hat{n}_m$. Command `z` sets the current actuator position to be the zero reference, and `r` resets the actuator position to this point. This enables returning to a previous known position, a useful feature when troubleshooting.

The step execution is performed with a single function, which firstly drives the direction pin high if the step demand is positive (clockwise) or low if it is negative (anti-clockwise). The Arduino then drives the step pin high for 4 μs. When the stepper motor driver detects the rising edge, it instructs the stepper motor to move one step in the desired direction.

The stepping speed of the actuators, S, depends on the sampling and transmission rates of the system, and can be calculated as:

$$S = \frac{n_{spm}\hat{n}_m}{f_s} \tag{4.9}$$

where n_{spm} is the number of samples contained in a single transmitted package and f_s is the accelerometer sampling rate. For example, with a sampling rate of 240 Hz, 12 samples per message and 10 messages per step, the actuator stepping rate would be 2 steps/s.

4.5.2 Rig control PC software

The overall rig control is performed from an external PC. On it, a LabVIEW program allows the user to read, display and store incoming accelerometer data, apply filters or averaging to the data, set zero-g offsets and send actuator demands. The code is written in LabVIEW's proprietary G graphical programming

language. The program uses two serial connections, one to the Arduino UNO which forms part of the rig speed encoder, and another to the coordinator Xbee located in the stator.

When speed data from the Arduino UNO is received, the program reads it and stores it for use within the main code loop, which is presented in Fig. 4.26(b). The main loop begins when a full 12-sample message is received at the Xbee-connected serial port. The code first reads bytes in the buffer until the characteristic `@@` header is found, indicating a new data set. Immediately after, the actuator demands, if any have been given by the user, are interpreted, packaged and sent to the coordinator Xbee's serial buffer for transmission to the rotor. Sending the actuator demand immediately after a new incoming message is received ensures that the carrier channel is clear, speeding up the transmission process. The accelerometer data is then unpackaged, reconstructed from double 8-bit form to single 16-bit numbers, and converted into m*g*. This processed information is then passed through optional filtering and averaging functions. The user can select from a range of filter types (lowpass, highpass, bandpass and bandstop), change the relevant cutoff frequencies, or adjust the averaging time, all of which can aid in interpreting the sensor output. When applying a low-pass filter, the data is also converted into a displacement signal, via a procedure described further in Chapter 5. The acceleration, displacement and rotor speed information is then displayed in real time and stored for post-processing. Figure 4.27 shows the user interface during a rig test.

4.6 Conclusions

The design and construction of a functional active rotor prototype was undertaken to demonstrate the feasibility of internally-mounted active control systems. The prototype satisfied a dual purpose: its design and manufacture provided a better understanding of the strengths and weaknesses of internal topologies, while its functionality enabled its use as an experimental testing rig for internal sensing and actuation technologies.

An assembled shaft design was adopted to produce a flexible rotor with significant rotor vibration, and also to grant access to the central shaft section where the active components were housed. The rotor shaft measures 90 cm in length and has a mass of 3.5 kg. MEMS accelerometers are used in the design due to their small dimensions, low power requirements and low cost. They are mounted on an adjustable frame which helps prevent premature sensor saturation. They are controlled via an on-board Arduino microcontroller.

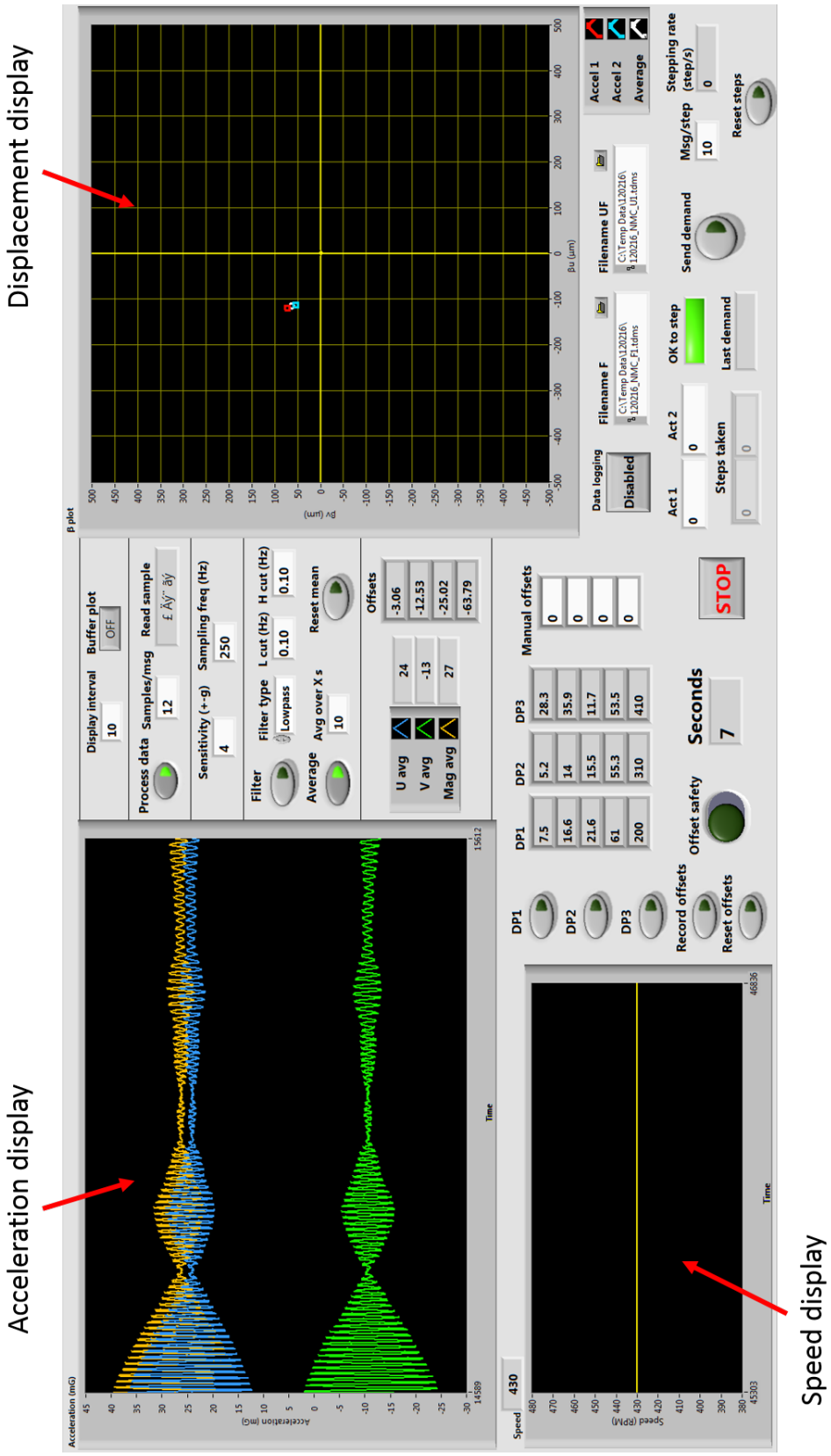

Figure 4.27: Graphical user interface of the rig control PC software.

The accelerometer data is transmitted to an external PC wirelessly thanks to a rotor-mounted Zigbee radio module. Mass-balancers provide internal actuation which is practical to mount and requires a smaller power supply than alternative methods such as piezoelectric patches. The devices used in the prototype consist of an eccentric mass driven by a stepper motor through a planetary gear transmission. The actuator demand is produced by an external PC and transmitted to the rotor wirelessly. The internal components require a stable power supply for operation, and the construction of the prototype highlighted the associated challenges. Due to the additional complexity involved in truly stator-independent designs, a slipring assembly was used. This compromise enabled the prototype to be used as a test bed without exceeding the scope of the research.

The final design closely adheres to a rotor-centred design philosophy, in which the active shaft is mostly independent of the stator. It is a fully-functional embodiment of an active rotor system, and as such demonstrates the feasibility of the concept. In addition, the design provides a robust and versatile testing platform, able to adapt to changing experimental requirements.

4.7 Summary

- A prototype was constructed to demonstrate the feasibility of internally-mounted active rotor systems. A rotor-centred design philosophy was adopted.
- The design and manufacturing process served to better understand the proposed technology. The resulting prototype also serves as a functional test rig for internal sensing and actuation.
- The prototype consists of an assembled shaft, containing MEMS accelerometers and mass-balancer actuators. A slip ring provides power to the internal components.
- The internal components are controlled through an open-source microcontroller, and all data is transmitted to and from the rotor wirelessly. All software is custom-written.

References

[1] International Organisation for Standardization, “Mechanical vibration - balance quality requirements for rotors in a constant (rigid) state - Part 1: specification and verification of balance tolerances,” Tech. Rep. ISO 1940-1:2003/Cor 1:2005, 2005.

[2] J. M. Pearce, “Building research equipment with free, open-source hardware,” *Science*, vol. 337, no. 6100, pp. 1303–1304, 2012.

[3] Analog Devices, *ADIS16223 Digital Tri-Axial Vibration Sensor*, January 2016. Rev. 0.

[4] A. Mahey, “ADXL362.” GitHub repository, `https://github.com/annem/ADXL362`, 2012. Online. Accessed 11 - December - 2016.

Chapter 5

Sensing of rotordynamics with internal MEMS accelerometers

5.1 Introduction

The review of active vibration control literature revealed that MEMS accelerometers are the most suitable form of sensing for active rotor topologies. Their strengths include low cost, compact size, low power consumption and ease of integration in electronic circuits.

As discussed in Chapter 2, MEMS accelerometers have recently been applied as rotor-mounted sensors for misalignment detection [1], measurement of instantaneous torque [2] and condition monitoring [3]. Although previous research has demonstrated the feasibility of mounting MEMS accelerometers on rotors, little attention has been given to understanding the full implications, limits and potential of these devices. Only Elnady [4] has tackled this issue, having produced a simple model to predict the output of accelerometers in a rotating frame of reference. However, in his derivation he wrongly assumed that the centripetal acceleration component could be considered negligible, when, under common operating conditions, it in fact dominates the signal. Therefore, a better understanding of how MEMS accelerometers behave in a rotating reference frame must be developed in order to take full advantage of this sensing technology. This is one of the primary aims of the research (A2) and so this Chapter describes the work conducted to satisfy objectives O3, O4 and O5.

Firstly, an overview of the principle of operation of MEMS accelerometers is provided. The output of internally-mounted accelerometers is then investigated and a model derived. This is applied to the study of rotor whirl orbits, the analysis of impact-related transient vibration and the practical problem of extracting displacement information from the accelerometer signals. Consideration is then

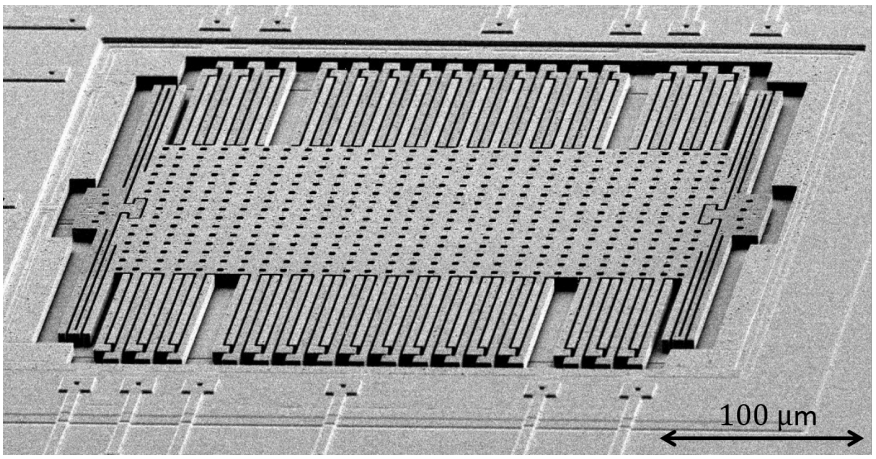

Figure 5.1: Scanning electron microscope image of a MEMS accelerometer proof mass [6].

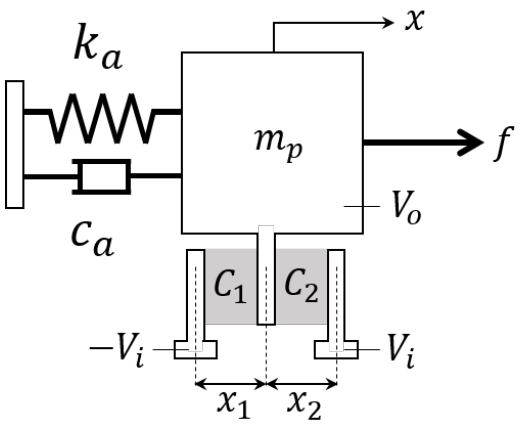

Figure 5.2: Schematic representation of an accelerometer proof mass and surrounding capacitor plates.

given to the principal sources of measurement error in MEMS accelerometers, and techniques developed to mitigate them are discussed. Experimental results of the prototype rotor operating under different unbalance conditions are presented, comparing the results obtained via internal accelerometers and conventional eddy current displacement sensors. Finally, a method is presented with which the operating speed of the rotor can be inferred from the accelerometer signals.

5.2 Operating principles of MEMS accelerometers

MEMS accelerometers consist of a proof mass suspended on spring mounts, and surrounded by capacitor plates, as shown in Fig. 5.1. A schematic diagram of the arrangement for a single axis device is presented in Fig. 5.2, where k_a is

the stiffness of the polysilicon structure, m_p is its mass, and c_a is the fluid film damping produced by the surrounding air [5]. The capacitances of the air gaps between the mass arm and the fixed capacitor plates are denoted by C_1 and C_2:

$$C_1 = \frac{\epsilon A}{x_1} \qquad C_2 = \frac{\epsilon A}{x_2}$$

where ϵ is the permitivity of air and A is the area of the plates. The distances x_1 and x_2 can be expressed in terms of the undeflected distance d and the proof mass displacement x so that

$$C_1 = \frac{\epsilon A}{d + x} \qquad C_2 = \frac{\epsilon A}{d - x} \tag{5.1}$$

As the capacitances are related to the position of the proof mass, they will change as the mass moves under acceleration. The measurement of these changes can be achieved with a C/V converter circuit, which will produce a voltage output proportional to the capacitance change. A wide variety of suitable circuits are available [7]. A common method involves driving the fixed capacitor plates with a square wave voltage of amplitude V_i, with 180° phase difference between the plates. As the overall proof mass charge remains at zero, the following holds

$$(V_o + V_i)C_1 + (V_o - V_i)C_2 = 0 \tag{5.2}$$

$$V_o = \frac{C_2 - C_1}{C_2 + C_1} V_i \tag{5.3}$$

Substituting Eq. (5.1) into (5.3) yields

$$V_o = \frac{x}{d} V_i \tag{5.4}$$

and hence the displacement of the proof mass can be determined by measuring the ratio between the output and input voltages:

$$x = \frac{V_o}{V_i} d \tag{5.5}$$

Under quasi-static conditions, that is, whenever the undamped resonance frequency of the support structure (ω_0) is much larger than the excitation frequency of the measured acceleration (Ω), the motion of the proof mass will be dominated by the stiffness of the spring mounts [7]. This can be shown by considering the response of the proof mass in Fig. 5.2 to a single frequency

harmonic input $f = F \sin \Omega t$:

$$\ddot{x} + 2\zeta\omega_0\dot{x} + \omega_0^2 x = A \sin \Omega t \tag{5.6}$$

where ζ is the damping ratio and $A = F/m_p$. From classical damped harmonic oscillator theory, the steady state displacement of the proof mass can be expressed in terms of an amplitude X and a phase ϕ such that

$$x = X \sin(\Omega t + \phi) \tag{5.7}$$

with

$$\phi = \arctan\left(\frac{2\zeta\eta}{\eta^2 - 1}\right) \tag{5.8}$$

and where η denotes the critical frequency ratio Ω/ω_0. It follows that

$$\dot{x} = X\Omega \cos(\Omega t + \phi) \tag{5.9}$$

$$\ddot{x} = -X\Omega^2 \sin(\Omega t + \phi) \tag{5.10}$$

and hence Eq. (5.6) can be written as

$$X\left[-\Omega^2 \sin(\Omega t + \phi) + 2\zeta\omega_0\Omega \cos(\Omega t + \phi) + \omega_0^2 \sin(\Omega t + \phi)\right] = A \sin \Omega t \tag{5.11}$$

$$\omega_0^2 X\left[-\eta^2 \sin(\Omega t + \phi) + 2\zeta\eta \cos(\Omega t + \phi) + \sin(\Omega t + \phi)\right] = A \sin \Omega t \tag{5.12}$$

$$\omega_0^2 X\left[B_1 \sin(\Omega t + \phi) + B_2 \cos(\Omega t + \phi)\right] = A \sin \Omega t \tag{5.13}$$

where $B_1 = 1 - \eta^2$ and $B_2 = 2\zeta\eta$. The expression for the sum of a sine and a cosine with equal phase angle is given by

$$B_1 \sin(\Omega t + \phi) + B_2 \cos(\Omega t + \phi) = \sqrt{B_1^2 + B_2^2} \cos\left(\Omega t + \arctan\left[\frac{B_2 \sin\phi - B_1 \cos\phi}{B_2 \sin\phi + B_2 \cos\phi}\right]\right) \tag{5.14}$$

The values of B_1 and B_2 imply that $\phi = \arctan(-B_2/B_1)$. Knowing also the following trigonometric identities,

$$\sin(\arctan\alpha) = \frac{\alpha}{\sqrt{1+\alpha^2}} \tag{5.15}$$

$$\cos(\arctan\alpha) = \frac{1}{\sqrt{1+\alpha^2}}, \tag{5.16}$$

it follows that

$$\sin\phi = \frac{\left(\frac{B_2}{-B_1}\right)}{\sqrt{1+\left(\frac{B_2}{-B_1}\right)^2}} \tag{5.17}$$

$$\cos\phi = \frac{1}{\sqrt{1+\left(\frac{B_2}{-B_1}\right)^2}} \tag{5.18}$$

Thus, the right-hand side of Eq. (5.14) becomes

$$\sqrt{B_1^2+B_2^2}\cos\left(\Omega t + \arctan\left[\frac{B_2\left(\frac{B_2}{-B_1}\right)-B_1}{B_1\left(\frac{B_2}{-B_1}\right)+B_2}\right]\right) \tag{5.19}$$

$$\sqrt{B_1^2+B_2^2}\cos\left(\Omega t + \arctan\left[\frac{B_2^2+B_1^2}{0}\right]\right) \tag{5.20}$$

The limit of the arctangent of β when β tends to infinity is

$$\lim_{\beta\to\infty}\arctan\beta = \frac{\pi}{2} \tag{5.21}$$

Substituting these results into Eq. (5.13) yields

$$\omega_0^2 X\sqrt{B_1^2+B_2^2}\cos\left(\Omega t+\frac{\pi}{2}\right) = A\sin\Omega t \tag{5.22}$$

$$-\omega_0^2 X\sqrt{\eta^4+\eta^2(4\zeta^2-2)+1}\sin\Omega t = A\sin\Omega t \tag{5.23}$$

$$-\omega_0^2 X\sqrt{\eta^4+\eta^2(4\zeta^2-2)+1} = A \tag{5.24}$$

The resulting expression describes the amplitude of the proof mass motion in response to an acceleration of amplitude A. Under quasi-static conditions, $\eta \to 0$ and so the square root in Eq. (5.24) tends to 1. This implies that the proof mass motion will be dominated by the term associated with the stiffness of the sprung structure and that the acceleration amplitude can be approximated as

$$A \approx -\omega_0^2 X \tag{5.25}$$

Hence, by measuring the displacement of the proof mass, an approximation of the acceleration of the device can be inferred. The error introduced in this approximation, ρ, can be expressed as a percentage through

$$\rho = 100\left(\frac{1}{\sqrt{\eta^4+\eta^2(4\zeta^2-2)+1}}-1\right) \tag{5.26}$$

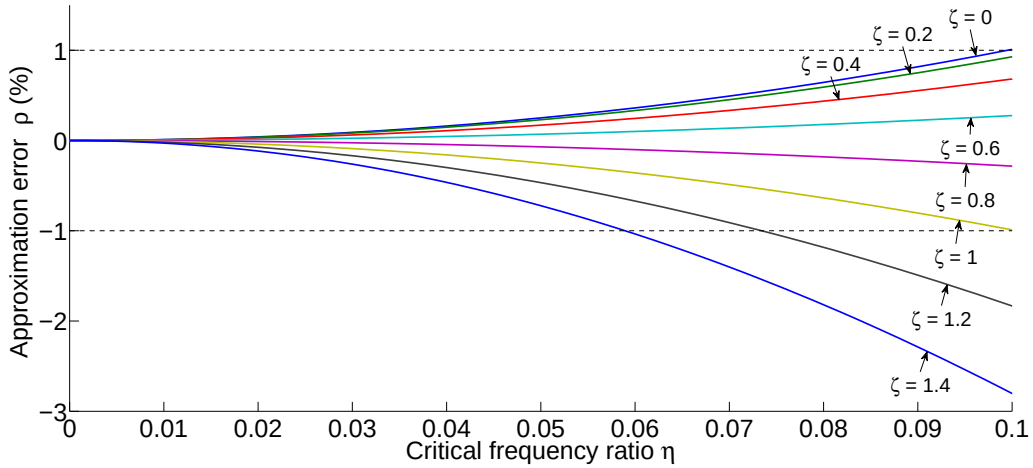

Figure 5.3: Approximation error ρ introduced to the accelerometer measurement as a consequence of assuming quasi-static conditions.

Figure 5.3 plots the values of ρ for a range of damping ratios and critical frequency ratios up to 0.1. The results show that for an underdamped structure ($\zeta < 1$) and a low critical frequency ratio, the error introduced by assuming quasi-static conditions will be less than $\pm 1\%$. For reference, the resonance frequency for the accelerometers used in the prototype described in Chapter 4 is $3,500$ Hz. As the maximum achievable test speed was $3,000$ rpm (50 Hz) the maximum critical frequency ratio for synchronous excitation sources is 0.014, which implies that the assumption of quasi-static conditions will hold for the prototype. However, it is worth noting that, if using internal MEMS accelerometers in high speed applications such as automotive turbochargers (up to $280,000$ rpm [8]), sensors with a high resonance frequency must be used to minimise errors.

5.3 Output of MEMS accelerometers located in a rotating frame

A key objective of the research (O3 in Chapter 2) was to produce a predictive model of the output of internally mounted accelerometers. Not only does this benefit the design process of active rotors, but also allows new signal processing techniques to be developed through which additional useful information may be extracted from the accelerometers. In what follows, the analytical expression of the accelerometer signals in terms of the motion of the rotor is derived.

Figure 5.4 shows the cross-section of a rotor with geometric centre C and an internal accelerometer located at B. The position of the proof mass is denoted

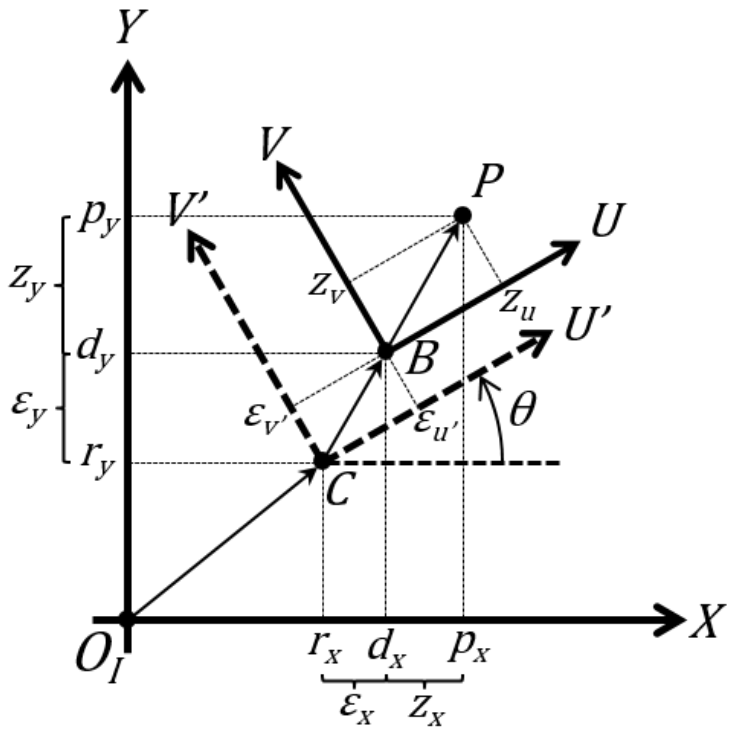

Figure 5.4: Schematic of the rotor cross-section at the measurement plane where the accelerometer is located.

by P. Three distinct reference frames are defined:

(i) XY is the inertial reference frame corresponding to the stator. O_I is the equilibrium point for the rotor geometric centre at zero speed.

(ii) $U'V'$ is a rotating reference frame with origin at C that is rotated together with the rotor by an angle θ.

(iii) UV is a rotating reference frame centered on the accelerometer, which is translated relative to $U'V'$ by an offset displacement $\varepsilon_{u'v'}$.

In the notation adopted in this derivation, if a parameter has components (α_u,α_v) on the U and V planes, its complex form is designated by $\alpha_{uv} = \alpha_u + \mathrm{j}\alpha_v$. Hence, $z_{uv} = (p_u - d_u) + \mathrm{j}(p_v - d_v)$ is the complex representation of the proof mass displacement relative to the accelerometer housing, represented in Fig. 5.5(a). Resolving the total force components into the inertial frame XY (Fig. 5.5(b)), the equation of motion of the proof mass is derived from Newton's Second Law:

$$m_p \ddot{p}_{xy} = F_x + \mathrm{j}F_y = (D_u + \mathrm{j}D_v)\,\mathrm{e}^{\mathrm{j}\theta} - \mathrm{j}m_p g \tag{5.27}$$

The forces associated with the motion of the proof mass are given in the ac-

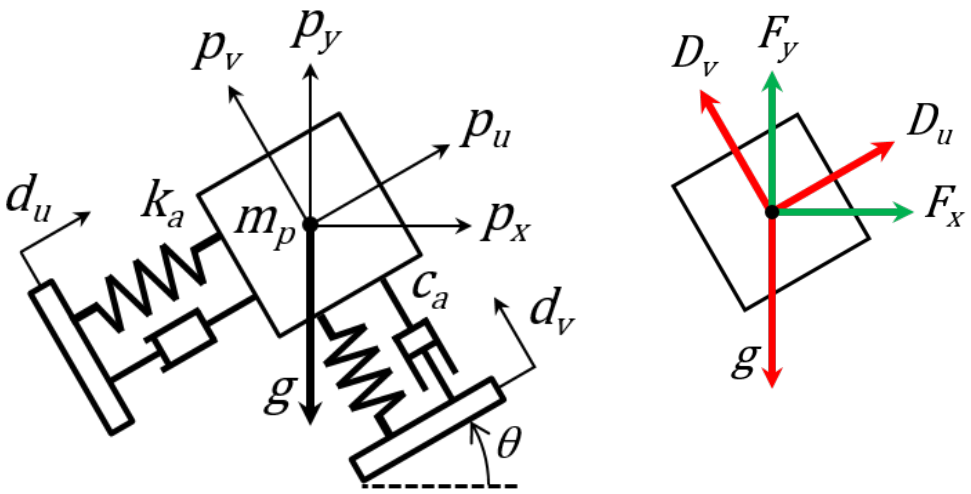

(a) Detail of proof mass (b) Free-body diagram

Figure 5.5: Schematic of the accelerometer proof mass and housing coordinates.

celerometer's UV frame as

$$D_u + \mathrm{j}D_v = -\left(k_a z_{uv} + c_a \dot{z}_{uv}\right) \tag{5.28}$$

and hence

$$m_p \ddot{p}_{xy} = -\left(k_a z_{uv} + c_a \dot{z}_{uv}\right) \mathrm{e}^{\mathrm{j}\theta} - \mathrm{j}m_p g \tag{5.29}$$

Subtracting $m_p \ddot{d}_{xy}$ from each side of the equation yields

$$m_p(\ddot{p}_{xy} - \ddot{d}_{xy}) = -(k_a z_{uv} + c_a \dot{z}_{uv})\mathrm{e}^{\mathrm{j}\theta} - \mathrm{j}m_p g - m_p \ddot{d}_{xy} \tag{5.30}$$

$$m_p \ddot{z}_{xy} = -(k_a z_{uv} + c_a \dot{z}_{uv})\mathrm{e}^{\mathrm{j}\theta} - m_p(\ddot{d}_{xy} + \mathrm{j}g) \tag{5.31}$$

Equation (5.31) can be transformed to the accelerometer-fixed UV frame knowing that

$$z_{xy} = z_{uv}\mathrm{e}^{\mathrm{j}\theta}$$

$$\dot{z}_{xy} = \left[\dot{z}_{uv} + \mathrm{j}\dot{\theta} z_{uv}\right] \mathrm{e}^{\mathrm{j}\theta}$$

$$\ddot{z}_{xy} = \left[\ddot{z}_{uv} + 2\mathrm{j}\dot{\theta}\dot{z}_{uv} + (\mathrm{j}\ddot{\theta} - \dot{\theta}^2) z_{uv}\right] \mathrm{e}^{\mathrm{j}\theta}$$

which results in

$$\left[\ddot{z}_{uv} + 2(\mathrm{j}\dot{\theta} + \zeta\omega_0)\dot{z}_{uv} + (\mathrm{j}\ddot{\theta} - \dot{\theta}^2 + \omega_0^2) z_{uv}\right] \mathrm{e}^{\mathrm{j}\theta} = -(\ddot{d}_{xy} + \mathrm{j}g) \tag{5.32}$$

with $\omega_0 = \sqrt{k_a/m_p}$ and $\zeta = c_a / \left(2\sqrt{k_a m_p}\right)$. For steady speed $\ddot{\theta}$ is zero. Under

the quasi-static conditions assumption, the first two terms in Eq. (5.32) are negligible and $\omega_0^2 \gg \dot{\theta}^2$, and hence

$$\omega_r^2 z_{uv} \mathrm{e}^{\mathrm{j}\theta} \approx -(\ddot{d}_{xy} + \mathrm{j}g) \tag{5.33}$$

From Eq. (5.25), the accelerometer output is defined as $a = -\omega_r^2 z_{uv}$ and so the relationship between the motion of the rotor-mounted accelerometer and its output signal becomes

$$a \approx (\ddot{d}_{xy} + \mathrm{j}g)\mathrm{e}^{-\mathrm{j}\theta} \tag{5.34}$$

In general, the accelerometer may be offset from C, so that

$$d_{xy} = r_{xy} + \varepsilon_{xy} \tag{5.35}$$

where

$$\varepsilon_{xy} = \varepsilon_{u'v'} \mathrm{e}^{\mathrm{j}\theta} \tag{5.36}$$

and $\varepsilon_{u'v'}$ is a constant. However, if $\varepsilon_{u'v'}$ is adjusted to be small (as detailed in Section 5.8.2), $U'V'$ coincides with UV and the displacement of the accelerometer is approximately that of the centre of the rotor, $d_{xy} \approx r_{xy}$. Thus, a can be used to infer $\ddot{r}_{xy}$.

The accelerometer output model expressed in Eq. (5.34) can be validated by studying the prototype data captured at 400, 800 and $2,000$ rpm by both the eddy current sensors (Fig. 5.6) and the internal accelerometers (Fig. 5.7). The displacement data at 400 and 800 rpm (Figs. 5.6(a) and 5.6(b)) shows a similar vibration pattern, with the maximum displacement oscillating between approximately -100 and $+150$ μm. This indicates that the unbalance present in the prototype has little effect at these speeds. The residual vibration is attributable to the shape of the rotor, which is not perfectly straight because it is an assembly of three shafts. If $\ddot{d}_{xy}$ is small, Eq. (5.34) would predict the accelerometer output to be dominated by the gravitational component, oscillating between approximately -1000 and $+1000$ mg and with little variation between the 400 rpm and 800 rpm cases. This behaviour is indeed observed in Figs. 5.7(a) and 5.7(b).

At $2,000$ rpm, however, the unbalance-induced vibration of the rotor is more clearly appreciable. In Fig. 5.6(c), the maximum displacement now varies between -600 and $+600$ μm, indicating that the vibration has increased substantially. The derived model would predict a constant offset in the accelerometer signal produced by the increased centripetal acceleration, and the counterpart data recorded by the accelerometers shows the acceleration varying between 0

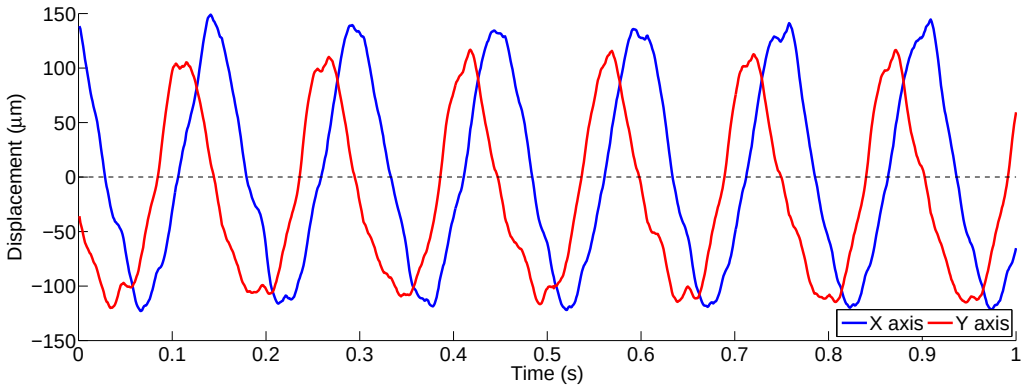

(a) 400 rpm

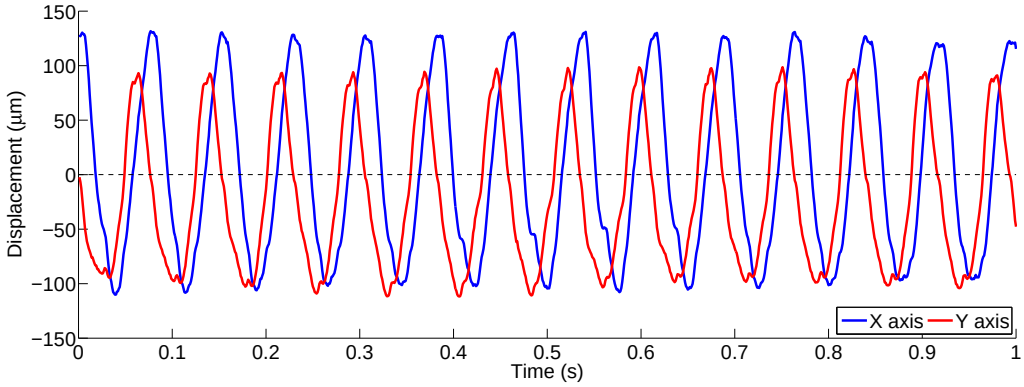

(b) 800 rpm

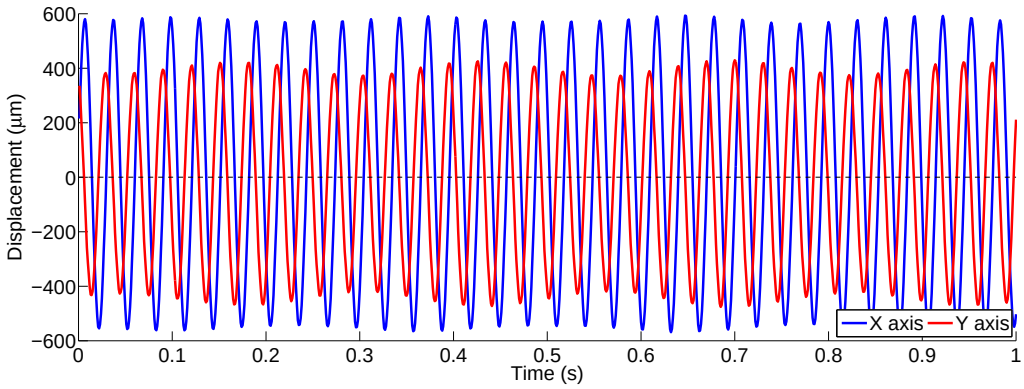

(c) 2,000 rpm

Figure 5.6: Steady state prototype eddy current transducer data measured at different operating speeds.

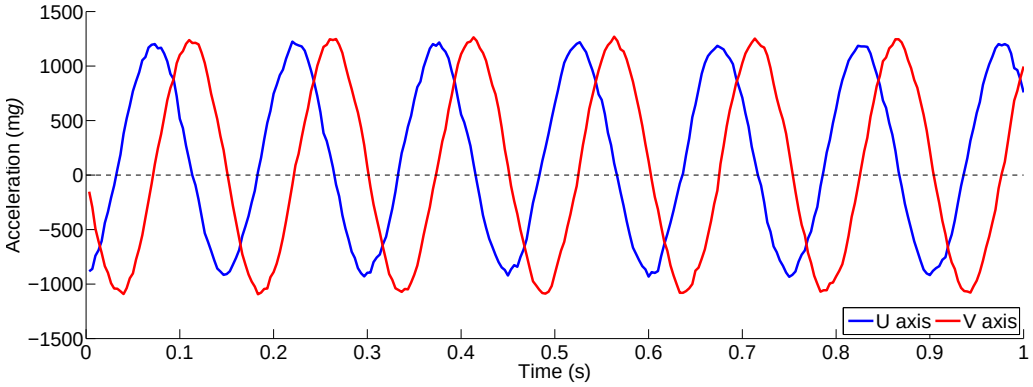

(a) 400 rpm

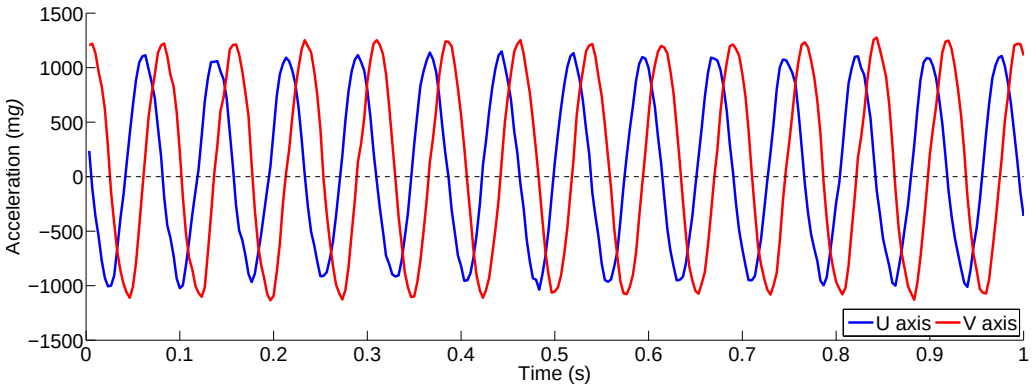

(b) 800 rpm

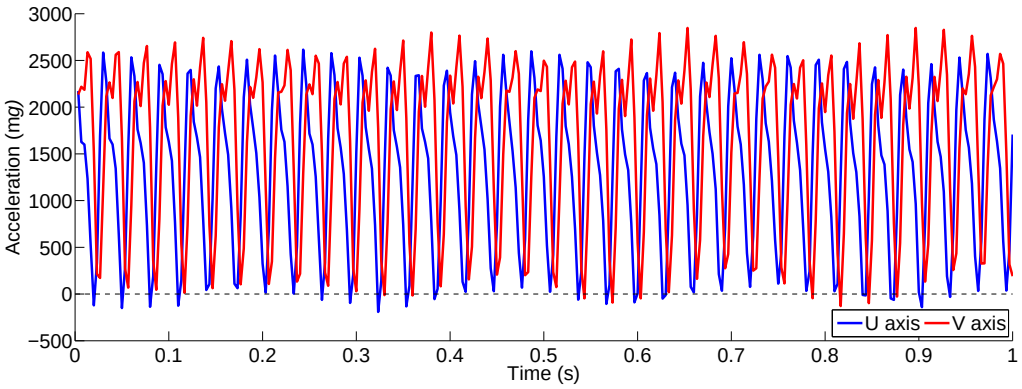

(c) 2,000 rpm

Figure 5.7: Steady state prototype accelerometer data measured at different operating speeds.

and $2,500$ mg. The more pronounced difference between the X and Y axes is indicative of an elliptical whirl orbit, which produces the more complex sinewave pattern in the accelerometer output.

5.4 Orbit characteristics as measured by internal accelerometers

In order to better understand the output of a MEMS accelerometer located inside a rotating shaft, the rotor's whirl orbits can be studied. When rotating at constant speed ($\theta = \omega t$), a rotor will describe an orbit around its equilibrium point (O_I in Fig. 5.4), the size and shape of which will depend on the force inputs to the system. Thus, studying the whirl orbits can often provide insight into the operating state of the rotor, highlighting faults and vibration behaviour. Because of this, it is of interest to understand how the orbiting motion is measured by the accelerometers, particularly because these "acceleration orbits" may not be as intuitive to interpret as the conventional "displacement orbits" obtained via displacement sensors.

Whirl orbits are studied here through the use of a finite element model of the rotor, expressed in state space form as described in Chapter 3. The matrix-vector equation of motion for the finite element model is

$$\mathbf{M}\ddot{\mathbf{q}} + [\mathbf{D_B} - \omega\mathbf{G}]\,\dot{\mathbf{q}} + \mathbf{K}\mathbf{q} = \mathbf{f} \tag{5.37}$$

where $\mathbf{q} = \{x_1,\, y_1,\, \varphi_{x1},\, \varphi_{y1},\, \ldots\,,\, x_n,\, y_n,\, \varphi_{xn},\, \varphi_{yn}\}^{\mathrm{T}}$ is a vector containing the displacement and rotations states of the n nodes of the finite element model, $\mathbf{M}$ is the mass matrix containing terms for translational and rotational inertia, $\mathbf{D_B}$ is the damping matrix representing the bearings, ω is the angular speed of the rotor, $\mathbf{G}$ is the skew-symmetric gyroscopic matrix, $\mathbf{K}$ is the stiffness matrix, and $\mathbf{f}$ is a vector containing the external forces and moments applied to the rotor.

The equation of motion is expressed in state space form through $\mathbf{z}_1 = \mathbf{q}$ and $\mathbf{z}_2 = \dot{\mathbf{z}}_1$. For a state vector $\mathbf{z} = [\mathbf{z}_1^{\mathrm{T}}, \mathbf{z}_2^{\mathrm{T}}]^{\mathrm{T}}$,

$$\begin{aligned} \dot{\mathbf{z}} &= \mathbf{A}\mathbf{z} + \mathbf{B}\mathbf{u} \\ \mathbf{y} &= \mathbf{C}\mathbf{z} + \mathbf{D}\mathbf{u} \end{aligned} \tag{5.38}$$

with $\mathbf{u} = \mathbf{f}$ and

$$\mathbf{A} = \begin{bmatrix} \mathbf{0} & \mathbf{I} \\ -\mathbf{M}^{-1}\mathbf{K} & -\mathbf{M}^{-1}\left[\mathbf{D_B} - \omega\mathbf{G}\right] \end{bmatrix} \quad , \quad \mathbf{B} = \begin{bmatrix} \mathbf{0} \\ \mathbf{M}^{-1} \end{bmatrix}$$

Considering the nodal accelerations as outputs, $\mathbf{y} = \dot{\mathbf{z}}_2$, hence

$$\mathbf{C} = \begin{bmatrix} -\mathbf{M}^{-1}\mathbf{K} & -\mathbf{M}^{-1}\left[\mathbf{D_B} - \omega\mathbf{G}\right] \end{bmatrix} \quad , \quad \mathbf{D} = \mathbf{M}^{-1}$$

The rotor response can be derived from the state space model, which has a general solution

$$\mathbf{z}(t) = \mathrm{e}^{\mathbf{A}t}\mathbf{z}(0) + \int_0^t \mathrm{e}^{\mathbf{A}(t-\tau)}\mathbf{B}\mathbf{u}(\tau)\,\mathrm{d}\tau \tag{5.39}$$

If the eigenvalue/vector problem is solved to yield $\mathbf{AV} = \mathbf{V}\boldsymbol{\Lambda}$ with

$$\mathbf{V} = \begin{bmatrix} \mathbf{v}_1 & \mathbf{v}_{-1} & \dots & \mathbf{v}_{4n} & \mathbf{v}_{-4n} \end{bmatrix}_{(8n\times 8n)}$$

$$\boldsymbol{\Lambda} = \mathrm{diag}\left(\lambda_1, \lambda_{-1}, \dots, \lambda_{4n}, \lambda_{-4n}\right)$$

$$\lambda_{-m} = \lambda_m^*$$

and the state vector is transformed according to $\mathbf{z} = \mathbf{V}\mathbf{p}$, then the state space equation is written in modal coordinates to become

$$\dot{\mathbf{p}} = \boldsymbol{\Lambda}\mathbf{p} + \hat{\mathbf{B}}\mathbf{u} \tag{5.40}$$

where $\hat{\mathbf{B}} = \mathbf{V}^{-1}\mathbf{B}$. Then

$$\mathbf{p}(t) = \mathrm{e}^{\boldsymbol{\Lambda}t}\mathbf{p}(0) + \int_0^t \mathrm{e}^{\boldsymbol{\Lambda}(t-\tau)}\hat{\mathbf{B}}\mathbf{u}(\tau)\,\mathrm{d}\tau \tag{5.41}$$

Since

$$\mathrm{e}^{\boldsymbol{\Lambda}t} = \mathrm{diag}(\mathrm{e}^{\lambda_1 t}, \mathrm{e}^{\lambda_{-1} t}, \dots, \mathrm{e}^{\lambda_{4n} t}, \mathrm{e}^{\lambda_{-4n} t}) \tag{5.42}$$

it follows that the modal states are given by

$$p_m(t) = \mathrm{e}^{\lambda_m t}p_m(0) + \hat{\mathbf{b}}_m^{\mathrm{T}} \int_0^t \mathrm{e}^{\lambda_m(t-\tau)}\mathbf{u}(\tau)\,\mathrm{d}\tau \tag{5.43}$$

where $\hat{\mathbf{b}}_m$ contains the transposed m^{th} row of $\hat{\mathbf{B}}$. The r^{th} state can therefore be expressed as

$$z_r(t) = \sum_{m=-4n}^{4n} v_{rm}\mathrm{e}^{\lambda_m t}p_m(0) + \sum_{m=-4n}^{4n} v_{rm}\hat{\mathbf{b}}_m^{\mathrm{T}} \int_0^t \mathrm{e}^{\lambda_m(t-\tau)}\mathbf{u}(\tau)\,\mathrm{d}\tau \tag{5.44}$$

If every eigenvalue has a negative real part (stable rotor system), the first summation of modal terms arising from initial conditions will decay to zero. The second summation involves a convolution integral of modal terms with each input component. The position of the rotor centre at the point of interest for the accelerometer plane is given in terms of Eq. (5.44) as $d_{xy}(t) = z_r(t) + \mathrm{j}z_s(t)$ for an appropriate choice of r and $s = r+1$. Hence, the displacement and acceleration of the accelerometer in the inertial reference frame will be, respectively,

$$d_{xy}(t) = \sum_{m=-4n}^{4n} (v_{rm} + \mathrm{j}v_{sm})\, p_m(0)\mathrm{e}^{\lambda_m t} + \sum_{m=-4n}^{4n} (v_{rm} + \mathrm{j}v_{sm})\hat{\mathbf{b}}_m^{\mathrm{T}} \int_0^t \mathrm{e}^{\lambda_m(t-\tau)}\mathbf{u}(\tau)\,\mathrm{d}\tau \tag{5.45}$$

$$\begin{aligned}\ddot{d}_{xy}(t) = &\sum_{m=-4n}^{4n} \lambda_m^2\,(v_{rm} + \mathrm{j}v_{sm})\, p_m(0)\mathrm{e}^{\lambda_m t} \\ &+ \sum_{m=-4n}^{4n} (v_{rm} + \mathrm{j}v_{sm})\hat{\mathbf{b}}_m^{\mathrm{T}} \left(\lambda_m^2 \int_0^t \mathrm{e}^{\lambda_m(t-\tau)}\mathbf{u}(\tau)\,\mathrm{d}\tau + \lambda_m\mathbf{u}(t) + \dot{\mathbf{u}}(t)\right)\end{aligned} \tag{5.46}$$

Combining Eqs. (5.34) and (5.46) gives the corresponding accelerometer signal, which depends on the system input vector $\mathbf{u}$

$$\begin{aligned}a(t) = &\sum_{m=-4n}^{4n} \lambda_m^2\,(v_{rm} + \mathrm{j}v_{sm})\, p_m(0)\mathrm{e}^{(\lambda_m - \mathrm{j}\omega)t} \\ &+ \sum_{m=-4n}^{4n} (v_{rm} + \mathrm{j}v_{sm})\hat{\mathbf{b}}_m^{\mathrm{T}} \left(\lambda_m^2 \int_0^t \mathrm{e}^{\lambda_m(t-\tau)}\mathbf{u}(\tau)\,\mathrm{d}\tau + \lambda_m\mathbf{u}(t) + \dot{\mathbf{u}}(t)\right)\mathrm{e}^{-\mathrm{j}\omega t} \\ &+ \mathrm{j}g\mathrm{e}^{-\mathrm{j}\omega t}\end{aligned} \tag{5.47}$$

A single frequency harmonic input has the form

$$\mathbf{u}(t) = \boldsymbol{\mu}\mathrm{e}^{\mathrm{j}\gamma t} + \boldsymbol{\mu}^*\mathrm{e}^{-\mathrm{j}\gamma t}, \tag{5.48}$$

and so the integral term in Eq. (5.45) can be solved as

$$\int_0^t \mathrm{e}^{\lambda_m(t-\tau)}\mathbf{u}(\tau)\,\mathrm{d}\tau = \frac{\boldsymbol{\mu}}{(-\lambda_m + \mathrm{j}\gamma)}\left(\mathrm{e}^{\mathrm{j}\gamma t} - \mathrm{e}^{\lambda_m t}\right) + \frac{\boldsymbol{\mu}^*}{(-\lambda_m - \mathrm{j}\gamma)}\left(\mathrm{e}^{-\mathrm{j}\gamma t} - \mathrm{e}^{\lambda_m t}\right) \tag{5.49}$$

Thus, the rotor "displacement orbit" in response to periodic force inputs, once

all transient terms have decayed away, is given by

$$d_{xy}(t) = \sum_{m=-4n}^{4n} (v_{rm} + \mathrm{j}v_{sm})\hat{\mathbf{b}}_m^{\mathrm{T}} \left(\frac{\boldsymbol{\mu}}{(-\lambda_m + \mathrm{j}\gamma)} \mathrm{e}^{\mathrm{j}\gamma t} + \frac{\boldsymbol{\mu}^*}{(-\lambda_m - \mathrm{j}\gamma)} \mathrm{e}^{-\mathrm{j}\gamma t} \right) \tag{5.50}$$

This expression can be written in the compact form

$$d_{xy}(t) = R_F \mathrm{e}^{\mathrm{j}(\gamma t + \phi_F)} + R_B \mathrm{e}^{\mathrm{j}(-\gamma t + \phi_B)} \tag{5.51}$$

where the rotor orbit is described in terms of forward and backward whirls of radii R_F and R_B and phases ϕ_F and ϕ_B, respectively, given by

$$R_F(\gamma, \boldsymbol{\mu}) = \left| \sum_{m=-4n}^{4n} (v_{rm} + \mathrm{j}v_{sm})\hat{\mathbf{b}}_m^{\mathrm{T}} \frac{\boldsymbol{\mu}}{(-\lambda_m + \mathrm{j}\gamma)} \right| \tag{5.52}$$

$$\phi_F(\gamma, \boldsymbol{\mu}) = \arg \left(\sum_{m=-4n}^{4n} (v_{rm} + \mathrm{j}v_{sm})\hat{\mathbf{b}}_m^{\mathrm{T}} \frac{\boldsymbol{\mu}}{(-\lambda_m + \mathrm{j}\gamma)} \right) \tag{5.53}$$

$$R_B(-\gamma, \boldsymbol{\mu}^*) = \left| \sum_{m=-4n}^{4n} (v_{rm} + \mathrm{j}v_{sm})\hat{\mathbf{b}}_m^{\mathrm{T}} \frac{\boldsymbol{\mu}^*}{(-\lambda_m - \mathrm{j}\gamma)} \right| \tag{5.54}$$

$$\phi_B(-\gamma, \boldsymbol{\mu}^*) = \arg \left(\sum_{m=-4n}^{4n} (v_{rm} + \mathrm{j}v_{sm})\hat{\mathbf{b}}_m^{\mathrm{T}} \frac{\boldsymbol{\mu}^*}{(-\lambda_m - \mathrm{j}\gamma)} \right) \tag{5.55}$$

The same orbit, measured by the internal accelerometers is described by

$$a = -\gamma^2 R_F \mathrm{e}^{\mathrm{j}((\gamma-\omega)t + \phi_F)} - \gamma^2 R_B \mathrm{e}^{\mathrm{j}(-(\gamma+\omega)t + \phi_B)} + \mathrm{j}g\mathrm{e}^{-\mathrm{j}\omega t} \tag{5.56}$$

This result can be applied to a more a general input consisting of unbalance and other sources of vibration,

$$\mathbf{u}(t) = \omega^2 \boldsymbol{\sigma} \mathrm{e}^{\mathrm{j}\omega t} + \omega^2 \boldsymbol{\sigma}^* \mathrm{e}^{-\mathrm{j}\omega t} + \mathbf{u}_{res}(t) \tag{5.57}$$

where $\boldsymbol{\sigma}$ is a complex mass-eccentricity unbalance vector and $\mathbf{u}_{res}$ indicates the residual forcing produced by the remaining input sources. Thus, the displacement in the inertial reference frame and the corresponding accelerometer output for a general rotor will be

$$d_{xy} = R_{F\sigma} \mathrm{e}^{\mathrm{j}(\omega t + \phi_{F\sigma})} + R_{B\sigma} \mathrm{e}^{\mathrm{j}(-\omega t + \phi_{B\sigma})} + \sum_{m=-4n}^{4n} (v_{rm} + \mathrm{j}v_{sm})\hat{\mathbf{b}}_m^{\mathrm{T}} \int_0^t \mathrm{e}^{\lambda_m (t-\tau)} \mathbf{u}_{res}(\tau)\, \mathrm{d}\tau \tag{5.58}$$

$$a = -\omega^2 R_{F\sigma} \mathrm{e}^{\mathrm{j}\phi_{F\sigma}} - \omega^2 R_{B\sigma} \mathrm{e}^{\mathrm{j}(-2\omega t + \phi_{B\sigma})} + \mathrm{j}g\mathrm{e}^{-\mathrm{j}\omega t} + \sum_{m=-4n}^{4n} (v_{rm} + \mathrm{j}v_{sm}) \hat{\mathbf{b}}_m^{\mathrm{T}} \left(\lambda_m^2 \int_0^t \mathrm{e}^{\lambda_m (t-\tau)} \mathbf{u}_{res}(\tau)\, \mathrm{d}\tau + \lambda_m \mathbf{u}_{res}(t) + \dot{\mathbf{u}}_{res}(t) \right) \mathrm{e}^{-\mathrm{j}\omega t} \tag{5.59}$$

with

$$R_{F\sigma} = \omega^2 R_F(\omega, \boldsymbol{\sigma}) \qquad R_{B\sigma} = \omega^2 R_B(\omega, \boldsymbol{\sigma}^*)$$

$$\phi_{F\sigma} = \phi_F(\omega, \omega^2 \boldsymbol{\sigma}) \qquad \phi_{B\sigma} = \phi_B(\omega, \omega^2 \boldsymbol{\sigma}^*)$$

In the inertial frame "displacement orbit", d_{xy} in Eq. (5.58), the first term can be understood to form a base circular orbit of radius $R_{F\sigma}$, with all other signal components being deviations therefrom. Thus, the presence of the second term produces an elliptical orbit and any remaining periodic terms are related to non-synchronous vibration sources, such as bearing race faults or rotor-stator contact. In the "acceleration orbit" measured by the accelerometers, Eq. (5.59), the first term expresses the zero frequency centripetal acceleration. The second term and the gravitational acceleration both produce counter-rotating vectors, with frequencies -2ω and $-\omega$, respectively.

For a rotordynamic system excited only by unbalance, the displacement of the accelerometer in the inertial frame and its output signal are

$$d_{xy} = R_{F\sigma} \mathrm{e}^{\mathrm{j}(\omega t + \phi_{F\sigma})} + R_{B\sigma} \mathrm{e}^{\mathrm{j}(-\omega t + \phi_{B\sigma})} \tag{5.60}$$

$$a = -\omega^2 R_{F\sigma} \mathrm{e}^{\mathrm{j}\phi_{F\sigma}} - \omega^2 R_{B\sigma} \mathrm{e}^{\mathrm{j}(-2\omega t + \phi_{B\sigma})} + \mathrm{j}g\mathrm{e}^{-\mathrm{j}\omega t} \tag{5.61}$$

Equation (5.60) describes an elliptical orbit, in which the semi-major and semi-minor axes are $R_{F\sigma} + R_{B\sigma}$ and $R_{F\sigma} - R_{B\sigma}$, respectively. In the special case where $R_{F\sigma} \gg R_{B\sigma}$, the rotor approximates the idealised circular orbit.

Example plots for two different orbits are presented below. The orbits are shown as a "displacement orbit" viewed from the inertial reference frame (as typically obtained from eddy current displacement sensors) and as an "acceleration orbit", observed by internally mounted accelerometers (i.e. $\mathrm{Im}(a)$ vs. $\mathrm{Re}(a)$). Figures 5.8 and 5.9 show an unbalance-induced elliptical orbit whereas Figs. 5.10 and 5.11 show a multi-frequency case, which includes two additional super-synchronous periodic forcing inputs. In both cases the "acceleration orbits" are not centered at the origin due to the presence of the synchronous component $-\omega^2 R_{F\sigma} \mathrm{e}^{\mathrm{j}\phi_{F\sigma}}$. This component is highlighted in the accelerometer orbit figures, appearing as a single point. The parameters which define each orbit can be found in Table 5.1.

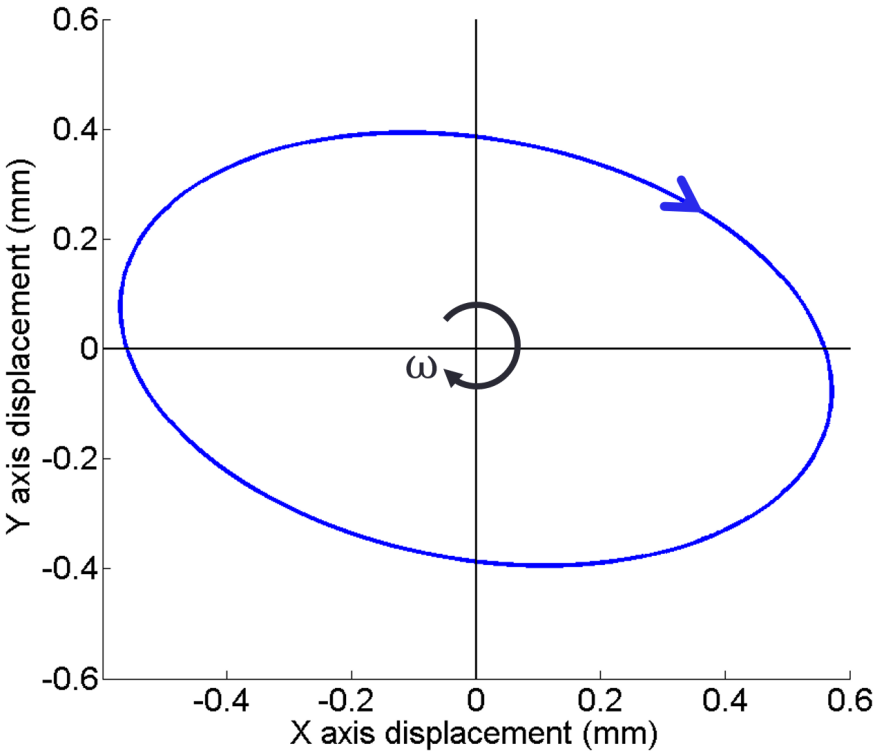

Figure 5.8: Theoretical single-frequency elliptical rotor orbit, as would be measured with stator-mounted displacement sensors.

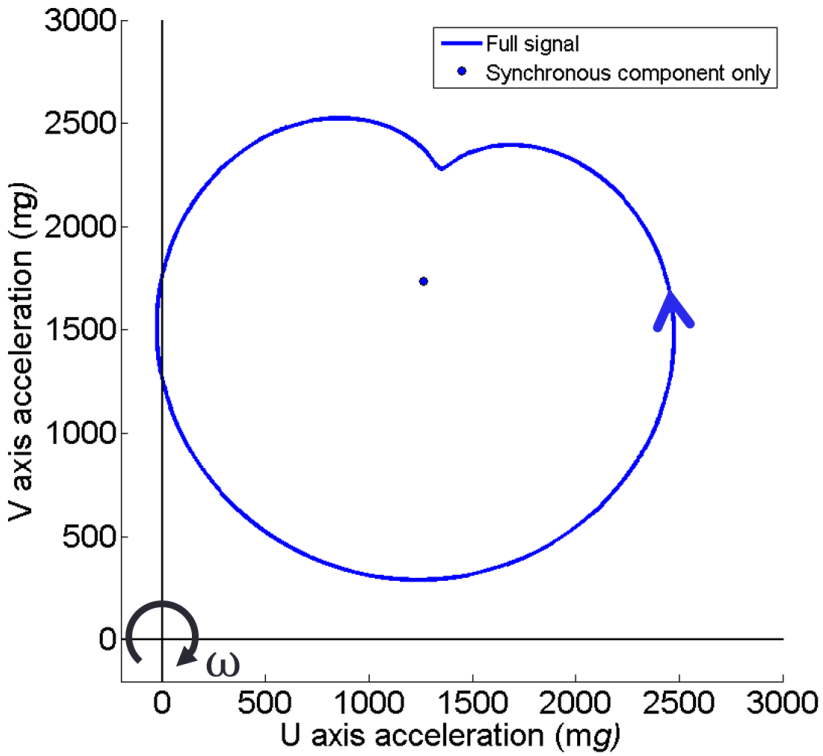

Figure 5.9: Theoretical single-frequency elliptical rotor orbit, as would be measured with rotor-mounted accelerometers.

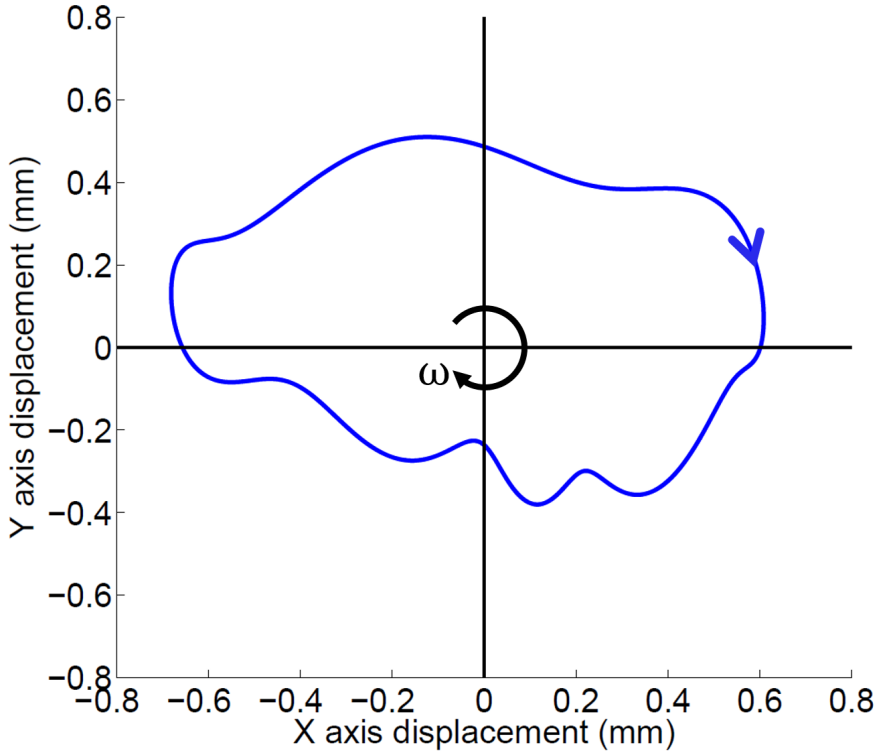

Figure 5.10: Theoretical multi-frequency arbitrary rotor orbit, as would be measured with stator-mounted displacement sensors.

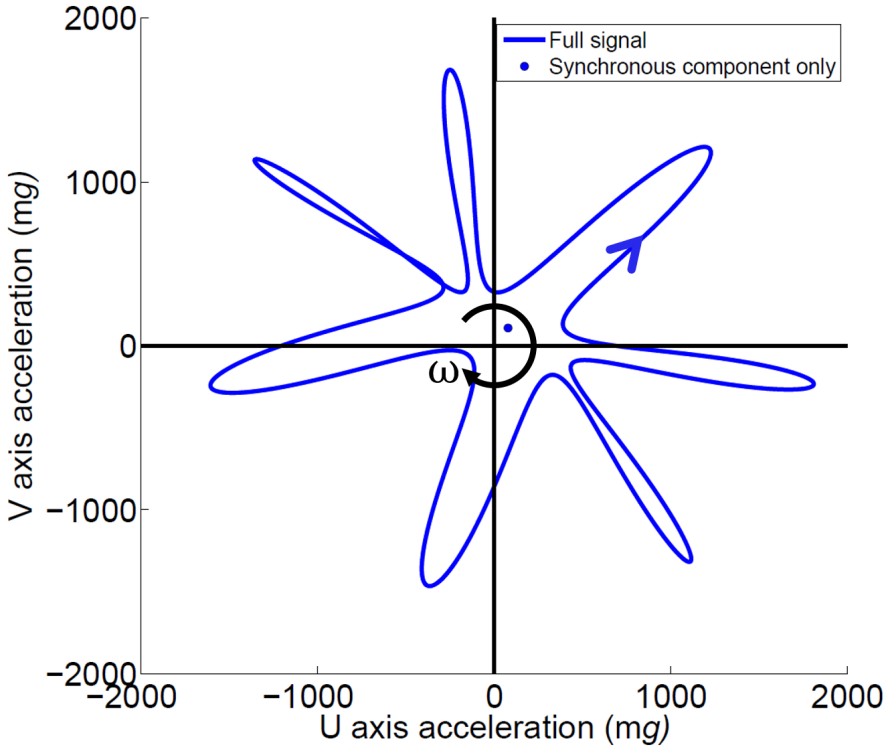

Figure 5.11: Theoretical multi-frequency arbitrary rotor orbit, as would be measured with rotor-mounted accelerometers.

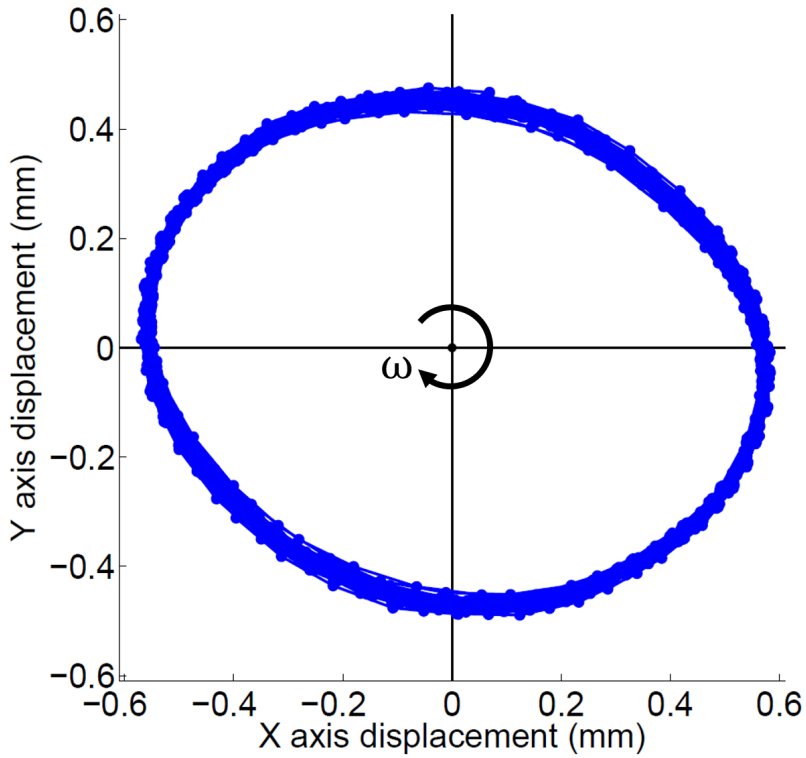

Figure 5.12: Rotor orbit at $2,000$ rpm measured with stator-mounted displacement sensors.

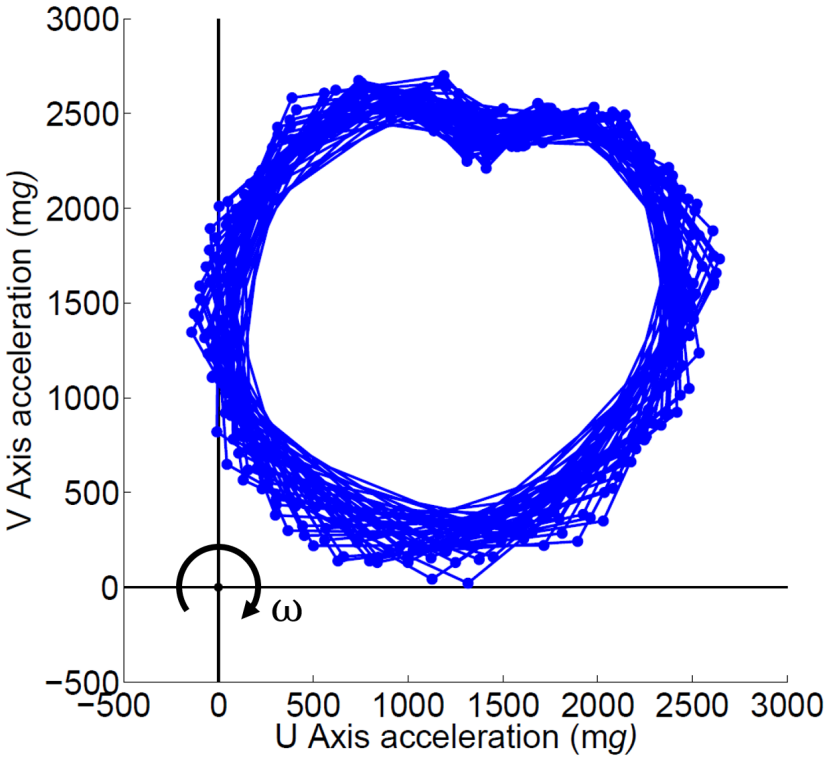

Figure 5.13: Rotor orbit at $2,000$ rpm measured with measured with rotor-mounted accelerometers.

Table 5.1: Parameters of orbits shown in Figs. 5.8 to 5.11.

	Orbit parameters					
	ω (rad/s)	γ_σ (rad/s)	$R_{F\sigma}$ (mm)	$R_{B\sigma}$ (mm)	$\phi_{F\sigma}$ (°)	$\phi_{B\sigma}$ (°)
Elliptical	209.4	ω	0.48	0.1	234	-261
Multi-frequency	52.4	ω, 2ω, 7ω	0.48, 0.12, 0.03	0.1, 0.05, 0.02	234, 20, -47	-261, 15, -136

The analytical results can be validated with experimental data obtained from the prototype test rig. Figure 5.12 presents the X and Y axis eddy current displacement sensor data for steady rotation at $2,000$ rpm, which shows a near elliptical orbit. The counterpart data provided by the accelerometers (Fig. 5.13) shows a limaçon, not centred at the axis origin. The characteristics of these measured rotor orbits correlate with the theoretical orbits shown in Figs. 5.8 and 5.9.

5.5 Transient vibration as measured by internal accelerometers

The study of whirl orbits provides information about the steady state vibration condition of the rotor. However, transient vibration can often also provide a wealth of knowledge, particularly in relation to short duration, high energy events such rotor/stator contact. Thus, the measurement of impact-related transient vibration with internal accelerometers was studied, using the theoretical framework developed for the study of whirl orbits.

The considered case is that of an impulsive force acting on the rotor during operation, which will give rise to non-synchronous transient components in the rotor orbit. It can be modelled as a time-delayed half sine function, such that

$$F_I(t) = \begin{cases} 0 & \text{if } t < T \\ F_0 \sin \omega_p (t - T) & \text{if } T \leq t \leq \frac{\pi}{\omega_p} + T \\ 0 & \text{if } t > \frac{\pi}{\omega_p} + T \end{cases} \tag{5.62}$$

where $\frac{\pi}{\omega_p}$ is the duration of the pulse and F_0 is its amplitude. The force input will be of the form $\mathbf{u} = F_I(t)\boldsymbol{\beta}$, where $\boldsymbol{\beta}$ is a $(2n \times 1)$ vector indicating the

coordinate and angle of incidence β_i of the force:

$$\boldsymbol{\beta} = [0, 0, \ldots, \cos\beta_i, \sin\beta_i, \ldots, 0, 0]^{\mathrm{T}}$$

In this case, the integration in the second term of Eq. (5.44), identified by Ψ for clarity, is expressed in terms of general limits of integration p and q as

$$\Psi(\tau) = \int_p^q \mathrm{e}^{\lambda_m(t-\tau)}\mathbf{u}(\tau)\,\mathrm{d}\tau = F_0\boldsymbol{\beta}\mathrm{e}^{\lambda_m t}\int_p^q \mathrm{e}^{-\lambda_m\tau}\sin\omega_p(\tau - T)\,\mathrm{d}\tau \tag{5.63}$$

The integral $I = \int_p^q \mathrm{e}^{-\lambda_m\tau}\sin\omega_p(\tau - T)\,\mathrm{d}\tau$ can be solved by parts defining

$$u_1 = \sin\omega_p(\tau - T) \qquad \mathrm{d}u_1 = \omega_p\cos\omega_p(\tau - T)$$

$$\mathrm{d}v_1 = \mathrm{e}^{-\lambda_m\tau} \qquad v_1 = \mathrm{e}^{-\lambda_m\tau}\frac{1}{-\lambda_m}$$

such that

$$I = \frac{\mathrm{e}^{-\lambda_m\tau}}{-\lambda_m}\sin\omega_p(\tau - T) + \frac{\omega_p}{\lambda_m}\int_p^q \mathrm{e}^{-\lambda_m\tau}\cos\omega_p(\tau - T)\,\mathrm{d}\tau\Big|_p^q \tag{5.64}$$

The integral containing the cosine can also be solved by parts, this time with

$$u_2 = \cos\omega_p(\tau - T) \qquad \mathrm{d}u_2 = -\omega_p\sin\omega_p(\tau - T) \tag{5.65}$$

$$\mathrm{d}v_2 = \mathrm{e}^{-\lambda_m\tau} \qquad v_2 = \mathrm{e}^{-\lambda_m\tau}\frac{1}{-\lambda_m} \tag{5.66}$$

and hence

$$I = \frac{\mathrm{e}^{-\lambda_m\tau}}{-\lambda_m}\sin\omega_p(\tau - T) + \frac{\omega_p}{\lambda_m}\left(\frac{\mathrm{e}^{-\lambda_m\tau}}{-\lambda_m}\cos\omega_p(\tau - T) + \frac{\omega_p}{-\lambda_m}I\right)\Big|_p^q \tag{5.67}$$

$$I = \frac{\mathrm{e}^{-\lambda_m\tau}}{-\lambda_m}\sin\omega_p(\tau - T) + \frac{\omega_p\mathrm{e}^{-\lambda_m\tau}}{-\lambda_m^2}\cos\omega_p(\tau - T) + \frac{\omega_p^2}{-\lambda_m^2}I\Big|_p^q \tag{5.68}$$

$$-\lambda_m^2 I = \lambda_m\mathrm{e}^{-\lambda_m\tau}\sin\omega_p(\tau - T) + \omega_p\mathrm{e}^{-\lambda_m\tau}\cos\omega_p(\tau - T) + \omega_p^2 I\Big|_p^q \tag{5.69}$$

$$I = \frac{-\mathrm{e}^{-\lambda_m\tau}}{\lambda_m^2 + \omega_p^2}\left(\lambda_m\sin\omega_p(\tau - T) + \omega_p\cos\omega_p(\tau - T)\right)\Big|_p^q \tag{5.70}$$

Thus,

$$\Psi = \frac{-F_0\boldsymbol{\beta}\mathrm{e}^{\lambda_m(t-\tau)}}{\lambda_m^2 + \omega_p^2}\left(\lambda_m\sin\omega_p(\tau - T) + \omega_p\cos\omega_p(\tau - T)\right)\Big|_p^q \tag{5.71}$$

The impulsive force F_I (Eq. (5.62)) will, by definition, be 0 over the intervals $[0, T)$ and $(\frac{\pi}{\omega_p} + T, \infty)$. Thus, the integral is evaluated over the intervals $[T, t]$ and $[t, \frac{\pi}{\omega_p} + T]$. Given that

$$\Psi(T) = \frac{-F_0\boldsymbol{\beta}}{\lambda_m^2 + \omega_p^2}\omega_p \mathrm{e}^{\lambda_m(t-T)}, \tag{5.72}$$

$$\Psi(t) = \frac{-F_0\boldsymbol{\beta}}{\lambda_m^2 + \omega_p^2}\left(\lambda_m \sin\omega_p(t-T) + \omega_p \cos\omega_p(t-T)\right), \tag{5.73}$$

and

$$\Psi(\frac{\pi}{\omega_p} + T) = \frac{F_0\boldsymbol{\beta}}{\lambda_m^2 + \omega_p^2}\omega_p \mathrm{e}^{\lambda_m(t-\frac{\pi}{\omega_p}-T)}, \tag{5.74}$$

it follows that

$$\Psi(t) - \Psi(T) = \frac{-F_0\boldsymbol{\beta}}{\lambda_m^2 + \omega_p^2}\left(\lambda_m \sin\omega_p(t-T) + \omega_p \cos\omega_p(t-T) - \omega_p \mathrm{e}^{\lambda_m(t-T)}\right) \tag{5.75}$$

and

$$\Psi(T) - \Psi(\frac{\pi}{\omega_p} + T) = \frac{-F_0\boldsymbol{\beta}\omega_p}{\lambda_m^2 + \omega_p^2}\left(1 - \mathrm{e}^{-\lambda_m\frac{\pi}{\omega_p}}\right)\mathrm{e}^{\lambda_m(t-T)} \tag{5.76}$$

Hence, the integral term Ψ for an impulsive load F_I as defined in Eq. (5.62) will be

$$\Psi(\tau) = \begin{cases} 0 & \text{if } t < T \\ \frac{-F_0\boldsymbol{\beta}}{\lambda_m^2+\omega_p^2}\left(\lambda_m \sin\omega_p(t-T) + \omega_p\cos\omega_p(t-T) - \omega_p \mathrm{e}^{\lambda_m(t-T)}\right) & \text{if } T \le t \le \frac{\pi}{\omega_p} + T \\ \frac{-F_0\boldsymbol{\beta}\omega_p}{\lambda_m^2+\omega_p^2}\left(1 - \mathrm{e}^{-\lambda_m\frac{\pi}{\omega_p}}\right)\mathrm{e}^{\lambda_m(t-T)} & \text{if } t > \frac{\pi}{\omega_p} + T \end{cases} \tag{5.77}$$

If the pulse duration is assumed to be small, only the response beyond $t = \frac{\pi}{\omega_p} + T$ will be of practical interest. Hence, the rotor displacement in response to an impact occurring at time T is obtained by substituting Eq. (5.77) into (5.45), so that

$$d_{xy}(t) = F_0 \sum_{m=-4n}^{4n} (v_{rm} + \mathrm{j}v_{sm})\hat{\mathbf{b}}_m^{\mathrm{T}}\boldsymbol{\beta}\frac{\omega_p}{(\lambda_m^2 + \omega_p^2)}\left(1 + \mathrm{e}^{-\lambda_m\frac{\pi}{\omega_p}}\right)\mathrm{e}^{\lambda_m(t-T)} \tag{5.78}$$

Consequently, the corresponding accelerometer output will be

$$a(t) = \mathrm{j}g\mathrm{e}^{-\mathrm{j}\omega t} + F_0 \sum_{m=-4n}^{4n} (v_{rm} + \mathrm{j}v_{sm})\hat{\mathbf{b}}_m^{\mathrm{T}}\boldsymbol{\beta}\frac{\lambda_m^2\omega_p}{(\lambda_m^2 + \omega_p^2)}\left(1 + \mathrm{e}^{-\lambda_m\frac{\pi}{\omega_p}}\right)\mathrm{e}^{[(\lambda_m - \mathrm{j}\omega)t - \lambda_m T]} \tag{5.79}$$

The conjugate pair of system eigenvalues associated with a particular vibration

mode will take the form $\lambda_m = -\alpha_m + \mathrm{j}\omega_m$ and $\lambda_{-m} = -\alpha_m - \mathrm{j}\omega_m$, where α_m is the modal decay term and ω_m is the damped natural frequency. Hence, the displacement for an unbalanced rotor after a single impulse applied to the rotor mid-plane, considering only the dominant first modal response, will be

$$d_{xy} = R_{F\sigma}\mathrm{e}^{\mathrm{j}(\omega t+\phi_{F\sigma})} + R_{B\sigma}\mathrm{e}^{\mathrm{j}(-\omega t+\phi_{B\sigma})} + A_1\mathrm{e}^{(-\alpha_1+\mathrm{j}\omega_1)t} + A_{-1}\mathrm{e}^{(-\alpha_1-\mathrm{j}\omega_1)t} \tag{5.80}$$

where, for clarity, the constant amplitude terms are grouped as

$$A_1 = F_0(v_{r1} + \mathrm{j}v_{s1})\hat{\mathbf{b}}_1^{\mathrm{T}}\boldsymbol{\beta}\frac{\omega_p}{(\lambda_1^2+\omega_p^2)}\left(1+\mathrm{e}^{-\lambda_1\frac{\pi}{\omega_p}}\right)\mathrm{e}^{-\lambda_1 T}$$
$$A_{-1} = F_0(v_{r-1} + \mathrm{j}v_{s-1})\hat{\mathbf{b}}_{-1}^{\mathrm{T}}\boldsymbol{\beta}\frac{\omega_p}{(\lambda_{-1}^2+\omega_p^2)}\left(1+\mathrm{e}^{-\lambda_{-1}\frac{\pi}{\omega_p}}\right)\mathrm{e}^{-\lambda_{-1} T}$$

It follows that the accelerometer output will be

$$\begin{aligned} a = &-\omega^2 R_{F\sigma}\mathrm{e}^{\mathrm{j}\phi_{F\sigma}} - \omega^2 R_{B\sigma}\mathrm{e}^{\mathrm{j}(-2\omega t+\phi_{B\sigma})} + \mathrm{j}g\mathrm{e}^{-\mathrm{j}\omega t} \\ &+ \lambda_1^2 A_1\mathrm{e}^{(-\alpha_1+\mathrm{j}(\omega_1-\omega))t} + \lambda_{-1}^2 A_{-1}\mathrm{e}^{(-\alpha_1-\mathrm{j}(\omega_1+\omega))t} \end{aligned} \tag{5.81}$$

The exponentials of the last two terms in Eq. (5.81) indicate components with frequencies $\omega_m - \omega$ and $-(\omega_m + \omega)$. This suggests that the transient vibration components measured by the internal accelerometers will exhibit a frequency split, as the modal excitation frequency is modulated by the rotational speed, $\pm\omega$.

This phenomenon was confirmed experimentally with the prototype test rig by carrying out a series of impact tests at steady rotor speeds of 0, 400, 800, $1,200$ and $1,600$ rpm. At each speed, an impulse was applied to the rotor using an impact hammer while measurements were recorded with both the accelerometers and the eddy current displacement sensors. Figure 5.14 shows rotor acceleration in the U and V axes of the rotating frame of reference, captured by the internal accelerometers, following an impact at 400 rpm. The impact occurs at approximately 14.75 seconds, and the transient vibrations decay within approximately half a second. The accelerometer signals are compared against reference data obtained with the eddy current displacement sensor. To enable this comparison, the displacement data, r_{xy}, is transformed into an acceleration by applying Eq. (5.34). Thus, the displacement is differentiated twice, the gravitational component added and the resulting signal transformed to the rotating frame of reference:

$$a_{EC} = \left(\frac{\mathrm{d}^2 r_{xy}}{\mathrm{d}t^2} + \mathrm{j}g\right)\mathrm{e}^{-\mathrm{j}\theta} \tag{5.82}$$

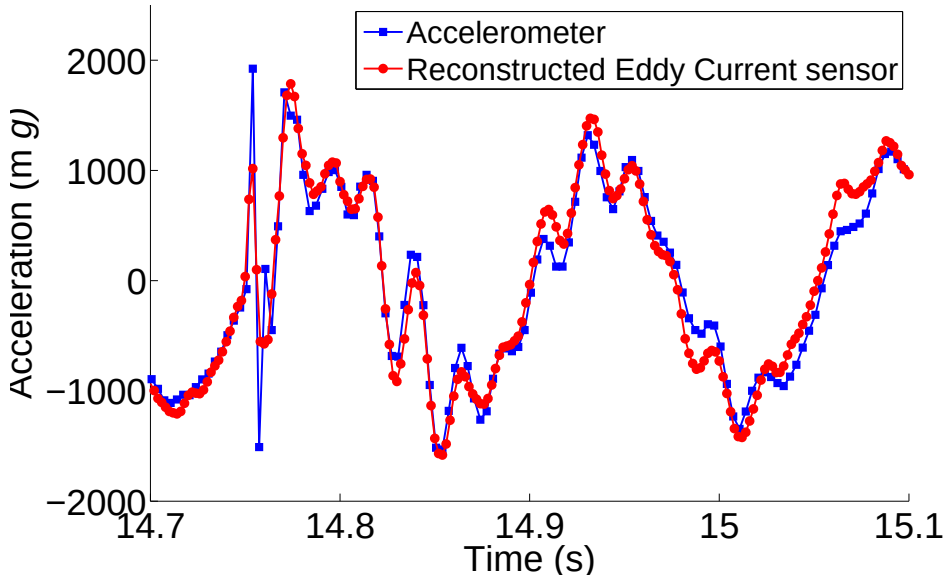

(a) U axis

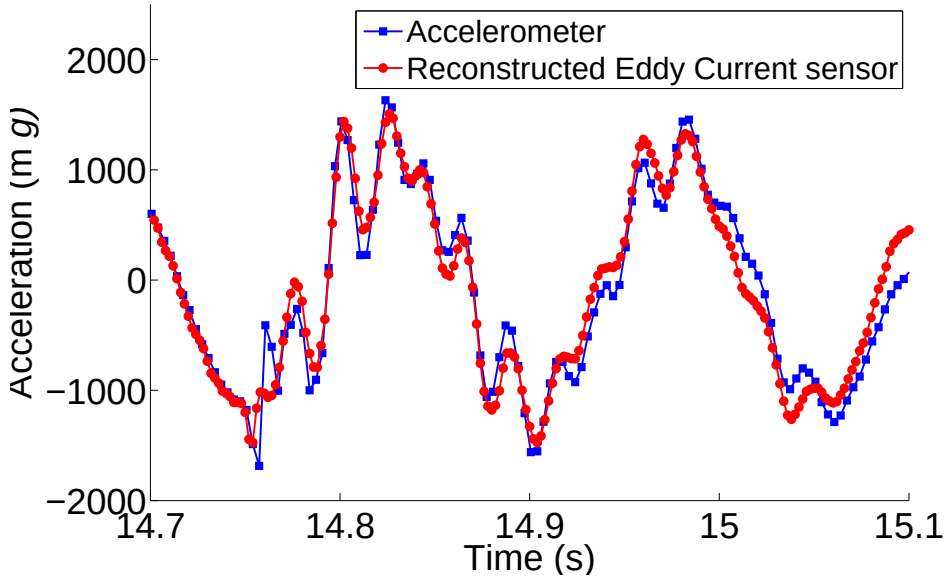

(b) V axis

Figure 5.14: Transient vibration at 400 rpm as measured by accelerometers and reconstructed from eddy current sensor data.

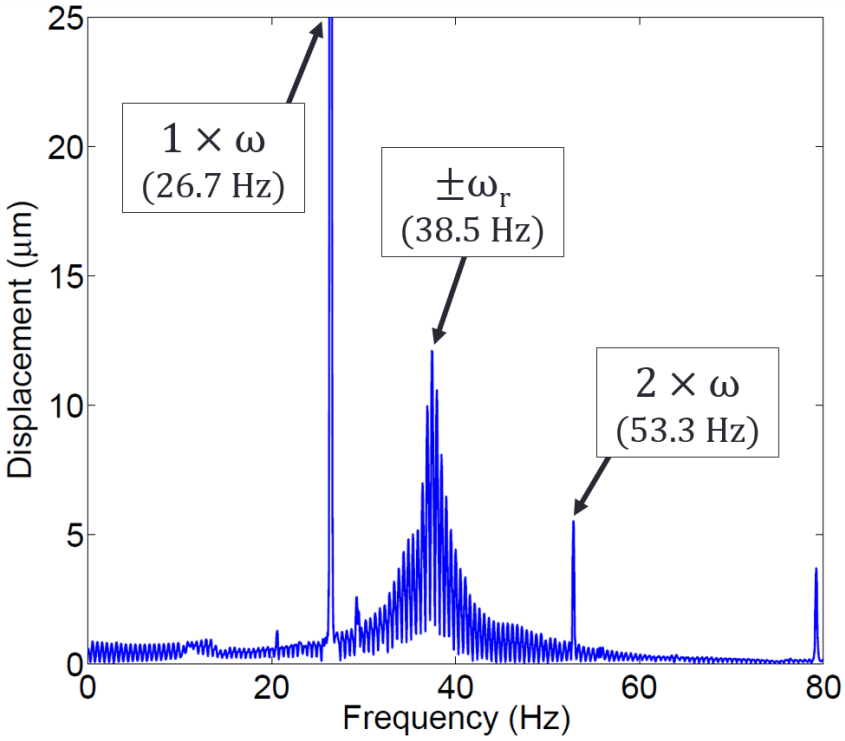

(a) X plane

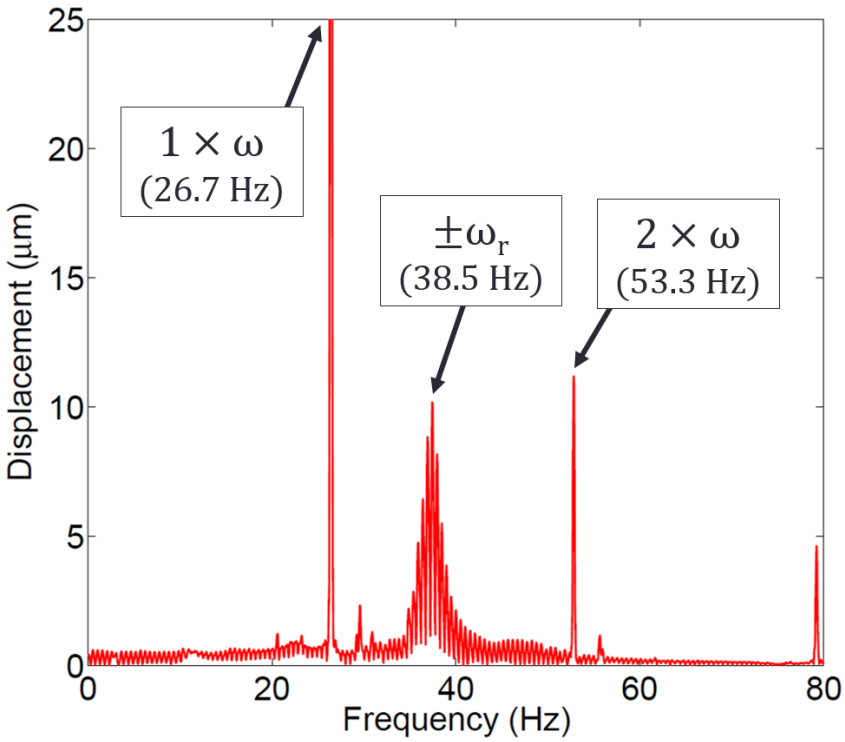

(b) Y plane

Figure 5.15: FFT of sensor data collected with eddy current sensors during impulsive impact tests with rotor operating at 1,600 rpm.

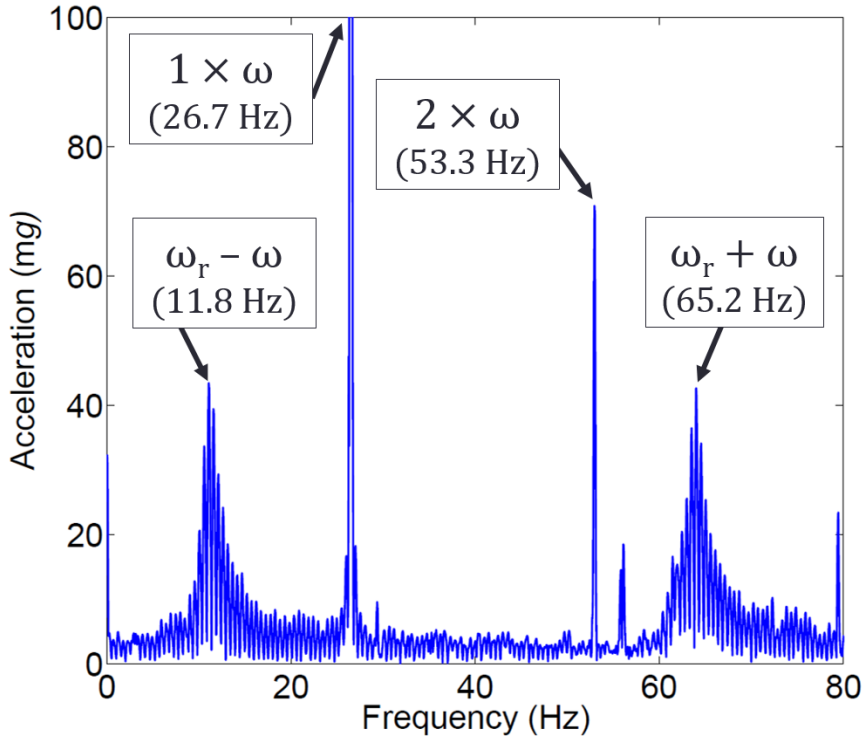

(a) U plane

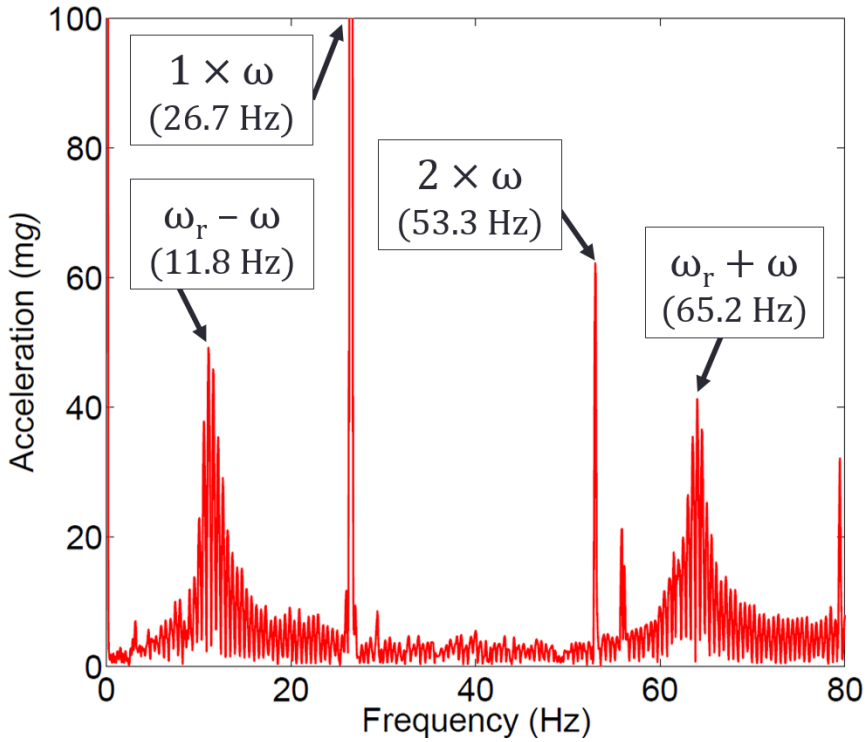

(b) V plane

Figure 5.16: FFT of sensor data collected with the internal accelerometers during impulsive impact tests with rotor operating at 1,600 rpm.

Both data show similar response behaviour, demonstrating that the internal accelerometers can capture transient vibration behaviour in the same way as conventional eddy current displacement sensors. In order to observe the predicted frequency split, Fast Fourier Transforms of the data obtained with each type of sensor at 1,600 rpm were compared, shown in Figs. 5.15 and 5.16. For the stator-mounted displacement sensors the main amplitude peaks correspond to the operating speed ω (26.7 Hz), its higher harmonic 2ω (53.3 Hz) and the resonant frequency ω_r (38.5 Hz). In the case of the internally mounted accelerometers those peaks are found at ω due to the gravitational acceleration term, 2ω due to the non-circular orbit described by the rotor and also at $\omega_r - \omega$ (11.8 Hz) and $\omega_r + \omega$ (65.2 Hz), which are produced by the hammer strike. Thus, the frequency split predicted by the analytical description of Eq. (5.81) is confirmed. These findings further verify the capability of the derived analytical framework to predict the output of accelerometers mounted within a rotating shaft.

5.6 Extracting displacement information from internal accelerometers

Although the internal MEMS accelerometers capture the motion of the rotor during operation, it can often be useful to have knowledge of its displacement. For example, when monitoring clearances between the rotor and stator components or when using PID control schemes for levitation in Active Magnetic Bearings. Because of this, the problem of extracting displacement-related information from the accelerometer signals was studied, satisfying objective O4. Two methods were considered: double integration of acceleration and isolation of the synchronous centripetal acceleration component via low-pass filtering.

Double integration

When dealing with an acceleration signal, an obvious first approach to obtain displacement would be to perform double integration. However, this method is generally regarded to be sensitive to initial conditions and DC offset errors [9], and can therefore be impractical. Nonetheless, it was explored to understand whether its application to rotating accelerometers was at least viable.

The displacement information desired to be extracted by double integration from the accelerometer output (Eq. 5.34) is the accelerometer position d_{xy}. The accelerometer signal must be converted to the inertial XY reference frame and

the gravitational acceleration subtracted before integration can be performed. This requires knowledge of both the gravitational component g and the angular position θ, which may not be known exactly. Thus, the estimated values g_e and θ_e are used, which introduces error terms g_ε and θ_ε:

$$g_\varepsilon = g - g_e \qquad\qquad \theta_\varepsilon = \theta - \theta_e$$

The accelerometer-derived inertial frame acceleration, $\ddot{d}_a$, is therefore give by

$$\ddot{d}_a = a\mathrm{e}^{\mathrm{j}\theta_e} - \mathrm{j}g_e \tag{5.83}$$

$$\ddot{d}_a = \ddot{d}_{xy}\mathrm{e}^{-\mathrm{j}\theta_\varepsilon} + \mathrm{j}\left(g\mathrm{e}^{-\mathrm{j}\theta_\varepsilon} - g_e\right) \tag{5.84}$$

Under constant rotational speed, $\theta = \omega t + \theta(0)$. Assuming a small error in its measurement, $\theta_\varepsilon = \omega_\varepsilon t + \theta_\varepsilon(0)$. The double integration of $\ddot{d}_a$ will then yield

$$\dot{d}_a = \int \ddot{d}_a \,\mathrm{d}t = \int \ddot{d}_{xy}\mathrm{e}^{-\mathrm{j}\theta_\varepsilon}\,\mathrm{d}t - \frac{g}{\omega_\varepsilon}\mathrm{e}^{-\mathrm{j}\theta_\varepsilon} - \mathrm{j}g_e t + k_1 \tag{5.85}$$

$$d_a = \int \dot{d}_a \,\mathrm{d}t = \iint \ddot{d}_{xy}\mathrm{e}^{-\mathrm{j}\theta_\varepsilon}\,\mathrm{d}t\,\mathrm{d}t - \mathrm{j}\frac{g}{\omega_\varepsilon^2}\mathrm{e}^{-\mathrm{j}\theta_\varepsilon} - \mathrm{j}g_e\frac{t^2}{2} + k_1 t + k_2 \tag{5.86}$$

where k_1 and k_2 denote the integration constants, that is, the initial conditions. As neither the displacement or velocity of the rotor are measured by the accelerometer, the initial conditions will not usually be known. Equation (5.86) illustrates the difficulties associated with extracting rotor displacement information from the internal accelerometer signals. Even small uncertainties in the gravitational component, the initial angular position or the initial conditions may lead to exponentially growing errors in the displacement estimation.

The situation is exacerbated when a non-ideal accelerometer is considered. If the accelerometer is not located at the geometric centre of the rotor, such that ε_{xy} in Fig. 5.4 is non-zero, it follows from Eq. (5.36) that

$$\ddot{d}_{xy} = \ddot{r}_{xy} - \varepsilon_{u'v'}\omega^2\mathrm{e}^{\mathrm{j}\theta} \tag{5.87}$$

In addition to this, the accelerometer output will be subject to measurement error sources such as resolution limits and noise (see Section 5.8). The former will introduce errors associated with rounding the accelerometer signals to its resolution limit, represented by an acceleration-dependent discontinuous function $f_r(a)$. The latter introduces a random, time-dependent error term, $f_n(t)$. Even for sensors with good resolution and noise characteristics, the double integration of these error sources can lead to exponential errors in the position

estimation. Equation (5.84) becomes

$$\ddot{d}_a = \ddot{r}_{xy}\mathrm{e}^{-\mathrm{j}\theta_\varepsilon} + \mathrm{j}\left(g\mathrm{e}^{-\mathrm{j}\theta_\varepsilon} - g_e\right) - \varepsilon_{u'v'}\omega^2\mathrm{e}^{\mathrm{j}\theta_e} + f_r(a) + f_n(t) \tag{5.88}$$

and integrating twice will give

$$\begin{aligned} d_a = &\iint \ddot{r}_{xy}\mathrm{e}^{-\mathrm{j}\theta_\varepsilon}\,\mathrm{d}t\,\mathrm{d}t - \mathrm{j}\frac{g}{\omega_\varepsilon^2}\mathrm{e}^{-\mathrm{j}\theta_\varepsilon} - \mathrm{j}g_e\frac{t^2}{2} + p_1 t + p_2 \\ &+ \varepsilon_{u'v'}\frac{\omega^2}{\omega_e^2}\mathrm{e}^{\mathrm{j}\theta_e} + \iint f_r\,\mathrm{d}t\,\mathrm{d}t + \iint f_n\,\mathrm{d}t\,\mathrm{d}t \end{aligned} \tag{5.89}$$

Thus, it is apparent that extracting displacement information from internally-mounted accelerometers presents practical challenges in its implementation, as any small deviation from ideal conditions will lead to the accumulation of integration errors.

Centripetal acceleration

Given the sensitivity of the double integration technique to uncertainty, an alternative method was sought to extract displacement information from the accelerometer signals. In many applications, knowing the instantaneous rotor position is not necessary, as the magnitude of the average displacement gives sufficient indication of the general vibration state. Thus, an integration-free method for obtaining the mean whirl orbit radius was developed.

A low-pass filter may be applied to the accelerometer signal to reduce the gravitational acceleration and high-frequency terms appearing in Eq. (5.59). This filtered acceleration signal will approximate the mean value,

$$\bar{a} = -\omega^2 R_{F\sigma}\mathrm{e}^{\mathrm{j}\phi_{F\sigma}} \tag{5.90}$$

This term constitutes the centripetal acceleration measured by the accelerometers, which is proportional to the rotor's displacement. Hence, a corresponding mean complex radius parameter may be calculated from $\bar{a}$ and ω as

$$d_m = d_{mu} + \mathrm{j}d_{mv} = -\frac{\bar{a}}{\omega^2} = R_{F\sigma}\mathrm{e}^{\mathrm{j}\phi_{F\sigma}} \tag{5.91}$$

The magnitude of this parameter, $|d_m|$, yields the displacement amplitude of the idealised base circular orbit, $R_{F\sigma}$. For the simple case of a circular orbit $|d_{xy}| = R_{F\sigma}$, and therefore the radius of orbit of the rotor can be directly inferred from the accelerometer measurements with the use of a simple low-pass filter. For non-circular orbits, the instantaneous orbit radius $|d_{xy}|$ is not constant, but the

parameter $|d_m|$ provides a good estimate of its mean value for rotors whose behaviour is dominated by unbalance. The mean value of the instantaneous radius over a single revolution is given by

$$\overline{|d_{xy}|} = \frac{\omega}{2\pi} \int_0^{\frac{2\pi}{\omega}} |d_{xy}| \, \mathrm{d}t \tag{5.92}$$

For an elliptical orbit, d_{xy} is given by Eq. (5.60) and so

$$|d_{xy}| = \sqrt{\left(\mathrm{Re}(d_{xy})\right)^2 + \left(\mathrm{Im}(d_{xy})\right)^2} \tag{5.93}$$

$$|d_{xy}| = \sqrt{R_{F\sigma}^2 + R_{B\sigma}^2 + 2R_{F\sigma}R_{B\sigma}\cos(2\omega t + \phi_{F\sigma} - \phi_{B\sigma})} \tag{5.94}$$

therefore,

$$\overline{|d_{xy}|} = \frac{\omega}{2\pi} \int_0^{\frac{2\pi}{\omega}} \sqrt{R_{F\sigma}^2 + R_{B\sigma}^2 + 2R_{F\sigma}R_{B\sigma}\cos(2\omega t + \phi_{F\sigma} - \phi_{B\sigma})} \, \mathrm{d}t \tag{5.95}$$

A term χ can be defined as the deviation ratio between the backward and forward whirl orbit radii as $\chi = \frac{R_{B\sigma}}{R_{F\sigma}}$. The cosine term can be rewritten as $\cos 2\xi$, where $\xi = \omega t + \frac{\phi_{F\sigma}}{2} - \frac{\phi_{B\sigma}}{2}$. Knowing that the double-angle formula is

$$\cos 2\xi = 1 - 2\sin^2 \xi, \tag{5.96}$$

it follows that Eq. (5.95) becomes

$$\overline{|d_{xy}|} = \frac{\omega R_{F\sigma}}{2\pi} \int_0^{\frac{2\pi}{\omega}} \sqrt{1 + \chi^2 + 2\chi(1 - 2\sin^2 \xi)} \, \mathrm{d}t \tag{5.97}$$

$$\overline{|d_{xy}|} = \frac{\omega R_{F\sigma}(1+\chi)}{2\pi} \int_0^{\frac{2\pi}{\omega}} \sqrt{1 - \frac{4\chi}{(1+\chi)^2}\sin^2 \xi} \, \mathrm{d}t \tag{5.98}$$

A change of integration variable from t to ξ can be performed knowing that $\mathrm{d}\xi = \omega \, \mathrm{d}t$, and so

$$\overline{|d_{xy}|} = \frac{R_{F\sigma}(1+\chi)}{2\pi} \int_\alpha^\beta \sqrt{1 - \frac{4\chi}{(1+\chi)^2}\sin^2(\xi)} \, \mathrm{d}\xi \tag{5.99}$$

with limits of integration

$$\alpha = \frac{\phi_{F\sigma} - \phi_{B\sigma}}{2} \qquad\qquad \beta = 2\pi + \frac{\phi_{F\sigma} - \phi_{B\sigma}}{2}$$

In this way, the integral term can be rewritten as the difference between two

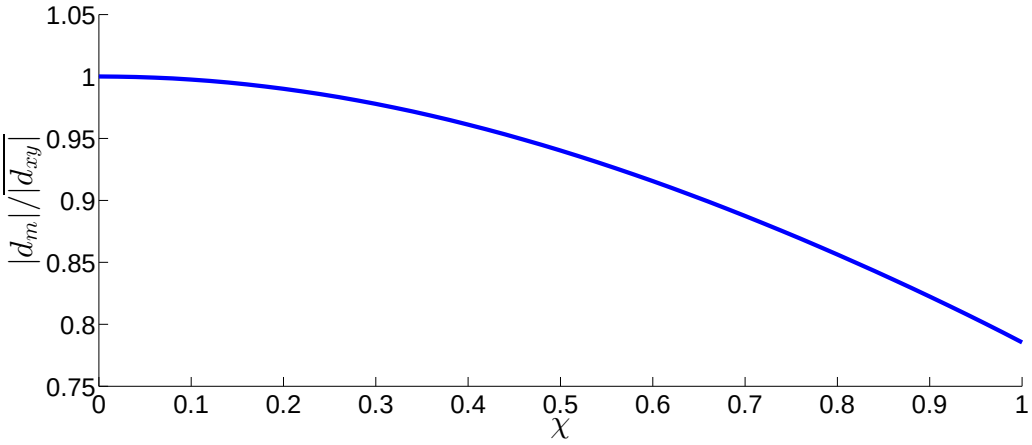

Figure 5.17: Variation of $|d_m|/\overline{|d_{xy}|}$ as a function of the deviation ratio $\chi = R_{B\sigma}/R_{F\sigma}$ for an elliptical orbit.

incomplete elliptic integrals of the second kind in the form

$$E(a|m) = \int_0^a \sqrt{1 - m\sin^2(\xi)}\,\mathrm{d}\xi$$

where

$$m = \frac{4\chi}{(1+\chi)^2}$$

so that

$$\overline{|d_{xy}|} = \frac{R_{F\sigma}(1+\chi)}{2\pi}\left[E(\beta|m) - E(\alpha|m)\right] \tag{5.100}$$

Figure 5.17 presents the ratio $|d_m|/\overline{|d_{xy}|}$ as a function of deviation ratio χ for an elliptical orbit. For small χ, that is, small deviation from the ideal circular orbit, $\overline{|d_{xy}|} \approx |d_m|$. Hence, the parameter $|d_m|$, obtained by applying a simple low-pass filter to an accelerometer signal and dividing by $-\omega^2$, will provide a good estimate of the average radius of orbit of rotors whose behaviour is dominated by unbalance, without the need for complex and time-consuming transformations. As an example, the $|d_m|/\overline{|d_{xy}|}$ ratio for the orbits presented in Figs. 5.9 and 5.11 are 0.989 and 0.974, respectively.

5.7 Estimation of rotational speed with internal accelerometers

Rotational speed measurement is a fundamental sensing capability in any rotating machine. Encoders are used for this purpose, and a wide variety of designs are available. The two principal technologies are electromagnetic and optical,

both of which require a reference to the stator to measure the relative speed of the rotor. Thus, encoders occupy space along the outer surface of the rotor shaft. In accordance with the active rotor design principles, it would be beneficial to develop internally housed encoders which do not require interaction with the stator. The potential of MEMS accelerometers to achieve this was studied, and a method for rotational speed estimation in flexible rotors was developed.

Previously, Cheng *et al.* [10] used a pair of wireless MEMS accelerometers to measure rotational speed. The accelerometers were housed in a plastic case at either side of the centre of rotation, in such a way as to achieve cancellation of the gravitational component when adding their outputs. The device was rotated on a lathe, and acceleration a assumed to be purely centripetal, so that $a = -r\omega^2$. If the accelerometer position r is known, then the rotational speed can be inferred. This method can provide rotational speed measurements for rigid rotors or those dominated by synchronous vibration. However, it is unsuitable under multi-frequency vibration experienced by flexible or more realistic rotor systems. Thus, a new technique for extracting angular speed information from the accelerometer output was required.

The gravity component exhibited in the accelerometer signals acts as a virtual reference to the inertial frame, and, consequently, allows tracking of rotational speed. Crucially, the gravity component is independent of vibration and depends only on the angle of rotation (Eq. (5.34)), and thus can be used in all types of horizontal rotor system. The method developed, therefore, tracks the gravitational component in the accelerometer signal and estimates its frequency to measure the rotational speed of the rotor.

In theory, the spectral analysis of the accelerometer signals should produce a gravity component with a magnitude of 1 *g* at the synchronous frequency. However, sampled data may suffer from spectral leakage, whereby the energy of a particular spectral component is spread between adjacent frequency bins [11]. A FFT-based algorithm was developed to track the 1 *g* amplitude peak such that an accurate value for average rotational speed could be obtained:

1. Perform a FFT over a short time interval of the accelerometer data using a flat top window function.
2. Find local maxima and mark those with a magnitude greater than 900 mg as feasible synchronous frequencies.
3. Identify which of the feasible frequencies corresponds to the rotating speed.
4. Refine the speed estimation by using a frequency domain interpolation method.

Table 5.2: Flat top window coefficients.

Coefficient	q_0	q_1	q_2	q_3	q_4
Value	1	-1.932	1.286	-0.388	0.032

To ensure identification of the 1 *g* amplitude component, a window function is initially used to modify the FFT spectrum of the accelerometer signal. A rectangular window function occurs naturally when sampling and produces the best frequency resolution, but has large amplitude errors [12]. Because of this, a flat top window is used, which is designed to have the lowest amplitude measurement error:

$$w(n) = q_0 + q_1 \cos(2\psi) + q_2 \cos(4\psi) + q_3 \cos(6\psi) + q_4 \cos(8\psi) \tag{5.101}$$

where $\psi = \pi n/(N-1)$, for which N is the number of samples of a used in the FFT and $0 \leq n \leq N-1$. The q_i coefficients are given in Table 5.2 [11].

The identification of the synchronous frequency in step 3 can be achieved by selecting the frequency which is closest to the previous estimated speed or establishing a maximum deviation criteria which eliminates any candidate frequencies falling outside of a feasible speed variation range. For more complex vibration cases the historical FFT data can be used to discard candidate frequencies which appear in prior speed estimations, under the assumption that they must correspond to other types of vibration phenomena.

The frequency resolution of the FFT is directly related to the window size through $R_f = f_s/W$, where R_f is the frequency resolution, f_s is the sampling frequency and W is the window size in number of samples. Larger window sizes will give improved frequency resolution at the expense of increased delay in speed estimation and are more suitable for rotors operating under quasi steady state conditions. In cases where the rotor speed may change rapidly, window sizes must be kept short. However, the resolution of the estimated rotational speed can be improved further through the use of a frequency domain interpolation technique. Andria *et al.* [13] provided an expression for the frequency shift $\Delta\omega$ between the frequency associated with a given peak ω_k (which is a multiple k of the frequency resolution) and the true frequency of the associated spectral component, ω. Thus, the interpolated frequency is given by $\omega = \omega_k + \Delta\omega$, where

$$\Delta\omega = 2\pi(L+0.5)\frac{Z_k(Z_{k+1} - Z_{k-1})}{(Z_k + Z_{k+1})(Z_k + Z_{k-1})} \tag{5.102}$$

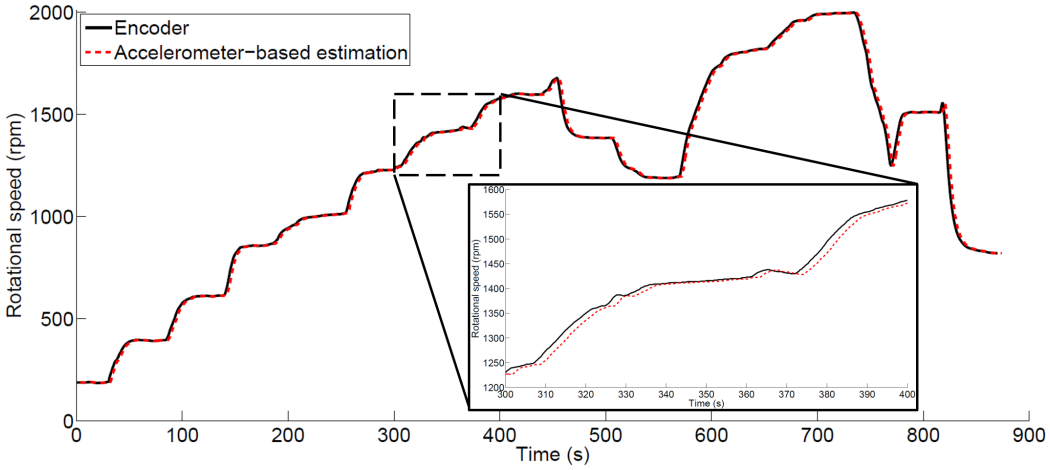

Figure 5.18: Estimated rotor speed using accelerometer-based virtual encoder compared against encoder-measured data.

Parameter L is the order of the employed window function and Z_k denotes the amplitude of the FFT at multiple k of the frequency resolution. Although the work of Andria and his colleagues focused on Rife-Vincent window functions, their method can be applied to flat top windows due to the similarities between the two functions. Rife-Vincent windows comprise three classes of functions formulated as a summation of cosines, taking the general form

$$w_{RV}(n) = 1 + \sum_{l=1}^{L} q_l \cos(2l\psi) \tag{5.103}$$

where L is the order of the window, and q_l are coefficients. The three classes are obtained by optimising the window coefficients to satisfy different desirable properties. The fourth order class I Rife-Vincent window, which is most similar to the flat top, takes coefficients $q_1 = -1.6$, $q_2 = 0.8$, $q_3 = -0.229$, and $q_1 = 0.029$.

The speed estimation algorithm was tested on a rotor operating at a range of speeds between 200 and $2,000$ rpm. The test included constant speed intervals of approximately 30 seconds as well as acceleration and deceleration. A comparison between the speed estimated using the accelerometers and the speed measured by the encoder is presented in Fig. 5.18. The data are shown for a sampling rate of 300 Hz and a window size of $1,200$ samples (4 second window size). The detailed view of the results shows how the estimation is delayed due to the fact that data is recorded over the time interval before processing. The use of the accelerometer signals as a virtual encoder provides good real-time estimation of the true rotor speed even during acceleration and deceleration.

5.8 Sources of measurement error and mitigation techniques

Like any sensing technology, accelerometer measurements are subject to a variety of error sources. The most significant of these were studied in order to better understand the limitations of the sensing capability of internally-mounted MEMS accelerometers, addressing objective O5. Where necessary, techniques were developed to mitigate the errors, and they are also discussed here. The types of error studied are, in order of significance: zero-*g* offsets, accelerometer positioning, limits of range, limits of resolution, and temperature fluctuations.

5.8.1 Zero-*g* offsets

Accelerometers measure proper acceleration, that is, the acceleration relative to an observer in a free-fall state. Therefore, an accelerometer in free-fall should produce a 0 *g* signal. However, due to manufacturing limitations, the signal is typically offset by a value, which differs for each accelerometer and for each measurement axis, and also depends strongly on the power supply. For a rotating accelerometer the zero-*g* offset can be significant, particularly at low speeds for which centripetal acceleration is usually small. It can be most detrimental when estimating the steady state orbit radius, as described in Section 5.6. This is illustrated in Fig. 5.19, which shows the radius of orbit of the rotor over the operating speed range, as measured with the eddy current displacement sensors and estimated with the internal accelerometers. The uncorrected accelerometer-based estimation correlates closely with the reference eddy current measurements at high speed, but produces an obviously incorrect trend at low speeds.

Thus, to reduce the zero-*g* offset error, a complex correction term $k_{uv} = k_u + \mathrm{j}k_v$ is introduced:

$$d_c = d_m - \frac{k_{uv}}{\omega^2} \tag{5.104}$$

The value of k_{uv} is calculated based on the principle that, at low speeds, the effect of unbalance on the rotor response is negligible, and so there should be little variation in the U and V plane components of the rotor orbit over a set of different speeds. Thus, the real and imaginary parts of d_m can be evaluated at different and suitably low speeds, and a least squares formulation used to

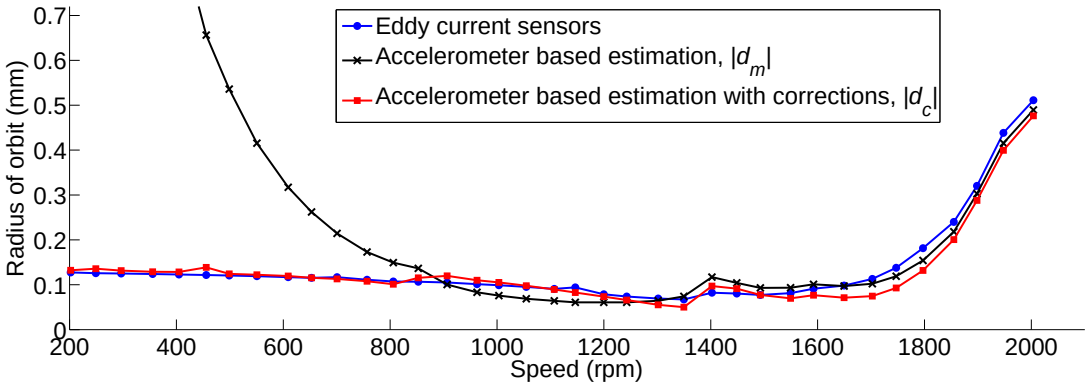

Figure 5.19: Orbit radius estimations derived from internal accelerometer measurements subject to zero-g offsets. Comparison between corrected and uncorrected data, and eddy current sensor measurements.

obtain values of k_u and k_v that minimise S_u and S_v, respectively, with

$$\begin{aligned} Su &= \sum_{i=1}^{l-1} \sum_{j=i+1}^{l} \left[\mathrm{Re}(d_{ci} - d_{cj})\right]^2 \\ Sv &= \sum_{i=1}^{l-1} \sum_{j=i+1}^{l} \left[\mathrm{Im}(d_{ci} - d_{cj})\right]^2 \end{aligned} \tag{5.105}$$

where the values corresponding to each of the l speeds are denoted by subscripts $i = 1, 2, \ldots, l-1$ and $j = i+1, i+2, \ldots, l$. It follows for the U axis data that

$$Su = \sum_{i=1}^{l-1} \sum_{j=i+1}^{l} \left[(d_{ui} - d_{uj}) - k_u \left(\frac{1}{\omega_i^2} - \frac{1}{\omega_j^2}\right)\right]^2 \tag{5.106}$$

and

$$\frac{\partial Su}{\partial k_{uv}} = \sum_{i=1}^{l-1} \sum_{j=i+1}^{l} 2\left(\frac{1}{\omega_i^2} - \frac{1}{\omega_j^2}\right) \left[(d_{ui} - d_{uj}) - k_u \left(\frac{1}{\omega_i^2} - \frac{1}{\omega_j^2}\right)\right] \tag{5.107}$$

Equating Eq. 5.107 to 0 yields

$$\sum_{i=1}^{l-1} \sum_{j=i+1}^{l} k_u \left(\frac{1}{\omega_i^2} - \frac{1}{\omega_j^2}\right)^2 = \sum_{i=1}^{l-1} \sum_{j=i+1}^{l} (d_{ui} - d_{uj}) \left(\frac{1}{\omega_i^2} - \frac{1}{\omega_j^2}\right) \tag{5.108}$$

$$k_u = \frac{\displaystyle\sum_{i=1}^{l-1} \sum_{j=i+1}^{l} (d_{ui} - d_{uj}) \left(\frac{1}{\omega_i^2} - \frac{1}{\omega_j^2}\right)}{\displaystyle\sum_{i=1}^{l-1} \sum_{j=i+1}^{l} \left(\frac{1}{\omega_i^2} - \frac{1}{\omega_j^2}\right)^2} \tag{5.109}$$

The same procedure can be followed for the V axis data, and so k_{uv} can be calculated as

$$k_{uv} = \frac{P}{Q} \tag{5.110}$$

where

$$P = \sum_{i=1}^{l-1} \sum_{j=i+1}^{l} (d_{mi} - d_{mj}) \left(\frac{1}{\omega_i^2} - \frac{1}{\omega_j^2} \right) \tag{5.111}$$

$$Q = \sum_{i=1}^{l-1} \sum_{j=i+1}^{l} \left(\frac{1}{\omega_i^2} - \frac{1}{\omega_j^2} \right)^2 \tag{5.112}$$

To assess the procedure, experimental results were taken from the prototype rotor, with $l = 3$ and d_m measurements taken at 200, 300 and 400 rpm. The corrected orbit radius estimation ($|d_c|$ in Fig. 5.19) displays a clear improvement, since the results align with the eddy current measurements over the complete speed range. As the zero-g offsets of each accelerometer are an intrinsic property, this correction procedure can be performed once and the offset values recorded for future use, provided that no significant changes in power supply or ambient temperature occur.

5.8.2 Accelerometer positioning

The offset ε_{xy} describes the position of the accelerometer relative to the centre of the rotor C (Fig. 5.4). If it is known, it can be compensated numerically when analysing the accelerometer data and hence does not constitute a significant source of measurement error of its own accord. However, the non-centred position of the accelerometer can lead to premature sensor saturation caused by excessive centripetal acceleration. It is therefore desirable to minimise the magnitude of ε_{xy}, and so a procedure to achieve this was developed.

For constant speed ω, it follows from Eqs. (5.35) and (5.36) that

$$\ddot{d}_{xy} = \ddot{r}_{xy} - \omega^2 \varepsilon_{u'v'} \mathrm{e}^{\mathrm{j}\omega t} \tag{5.113}$$

with $\varepsilon_{u'v'}$ being a constant, complex parameter describing the positional offset in the rotor-fixed frame. If the rotor were free of vibration, $r_{xy} = 0$. Hence, the accelerometer output would be

$$a = \left(-\omega^2 \varepsilon_{u'v'} \mathrm{e}^{\mathrm{j}\omega t} + \mathrm{j}g \right) \mathrm{e}^{-\mathrm{j}\omega t} \tag{5.114}$$

$$a = -\omega^2 \varepsilon_{u'v'} + \mathrm{j}g \mathrm{e}^{-\mathrm{j}\omega t} \tag{5.115}$$

The mean radius of orbit parameter d_c can be calculated as described in Section 5.6 by applying a lowpass filter to the accelerometer signal and dividing by $-\omega^2$, which yields $d_c = \varepsilon_{u'v'}$. Thus, the mean radius of orbit would indicate the positional offset. However, as the prototype is a flexible rotor, it will not be free of vibration. To allow measurement of the positional offset, therefore, the central shaft section containing the sensing module was placed on a lathe, which is assumed to be infinitely stiff and thus $r_{xy} = 0$. The lathe was then operated over a range of speeds and the acceleration measured. The parameter d_c was calculated from the measured data and used to adjust the support frame in Fig. 4.5 by $-d_c$ to minimise $|\varepsilon_{xy}|$, using the accessible screw ports. This calibration process was repeated until the positional offset magnitude was suitably small (< 10 μm).

5.8.3 Analogue to Digital conversion

As all sensors, accelerometers have limited measurement range and resolution. In digital MEMS accelerometers, the source of limitation is the Analogue to Digital Converter (ADC), which has a finite number of bits for converting the analog voltage from the capacitance measurements into a digital signal. This translates into a trade-off between range (avoiding saturation) and resolution (maintaining sufficient accuracy).

Saturation

Accelerometers typically display a relatively small measurement range, and this is exacerbated when placed in a rotating frame of reference. The accelerometer output for a rotor subject to unbalance is derived in Eq. (5.59). The magnitudes of the corresponding forward and backward rotor whirl orbits are defined as $R_{F\sigma} = \omega^2 R_F(\omega, \boldsymbol{\sigma})$ and $R_{B\sigma} = \omega^2 R_B(\omega, \boldsymbol{\sigma}^*)$, respectively. Considering only the effect of unbalance then, the accelerometer output can be written as

$$a = -\omega^4 R_F(\omega, \boldsymbol{\sigma}) \mathrm{e}^{\mathrm{j}\phi_{F\sigma}} - \omega^4 R_B(\omega, \boldsymbol{\sigma}^*) \mathrm{e}^{\mathrm{j}(-2\omega t + \phi_{B\sigma})} + \mathrm{j}g\mathrm{e}^{-\mathrm{j}\omega t} \tag{5.116}$$

which shows that the components of the acceleration signal related to the rotor orbits are proportional to the fourth power of the operating speed. Consequently, in order to operate over a large speed range without saturation, a very large range must be available on the accelerometers. The error related to saturation can be considered to be 0 as long as the acceleration remains within the sensor's range, but will become dominant if the range is exceeded.

Resolution

The ADC of the accelerometers used in the prototype has 12-bit resolution. Thus, it divides the total measurement range (4, 8 or 16 *g*) into 4096 parts, and the smallest measurable change in acceleration, $\check{a}$, will be

$$\check{a} = \frac{a_{range}}{4096} \tag{5.117}$$

The error associated with resolution limits will be at most $\check{a}/2$. It follows from equation (5.91) that the resolution of the d_m displacement measurement is therefore

$$\check{d}_m = -\frac{a_{range}}{4096\,\omega^2} \tag{5.118}$$

Whereas the resolution of the acceleration measurements is fixed for a given measurement range, the interpretation of the measurement as a mean displacement is inversely proportional to the square of the operating speed. Thus, the resolution of the device, when used as a displacement sensor, increases with speed. This phenomenon enables internal accelerometers to be used as high accuracy mean position sensors in high speed applications. In addition, it partially mitigates the trade-off between measurement range and resolution, as a threshold speed will exist beyond which sufficient accuracy can be obtained, even if suitable resolution is not available over the complete speed range. Hence, mean displacement measurement systems can be designed so as to ensure minimum impact from limited resolution, which suggests that accelerometers should be selected prioritising measurement range over resolution.

5.8.4 Temperature

MEMS accelerometers can typically operate over wide temperature ranges (-40 to 85 °C for the prototype, for example). However, the measurement sensitivity and 0 *g* offsets are temperature dependent. Because of this, the accelerometers feature an embedded temperature sensor which allows the temperature to be monitored and the sensitivity to be adjusted to ensure linear behaviour even under varying temperature conditions.

The two stepper motors and drivers housed within the rotor can become hot during operation. A test was performed to monitor the temperature rise experienced by the accelerometers and determine the effect on measurement accuracy. The test was performed with a static rotor, representing the worst case scenario in which heat dissipation is minimum due to reduced air flow around the central section. The temperature and acceleration were recorded with the

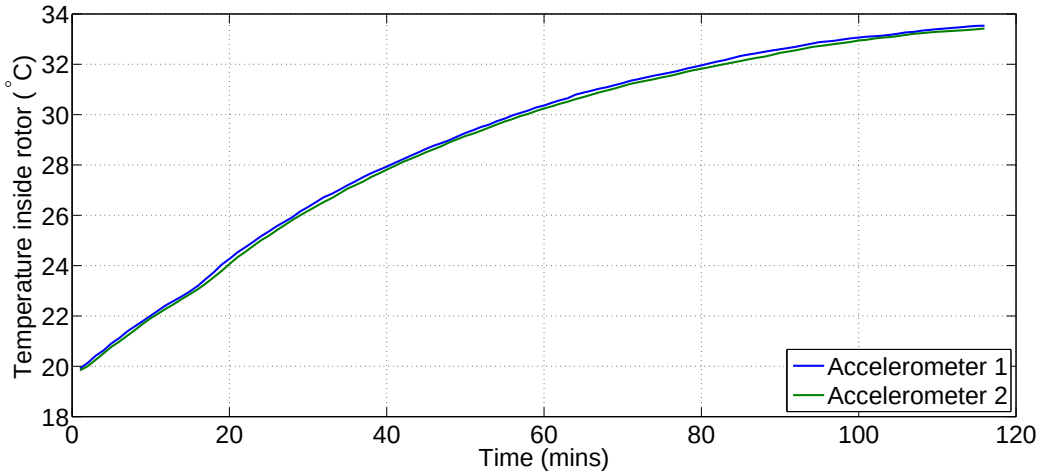

Figure 5.20: Temperature rise inside the rotor over the course of 2 hours, caused by electronic components.

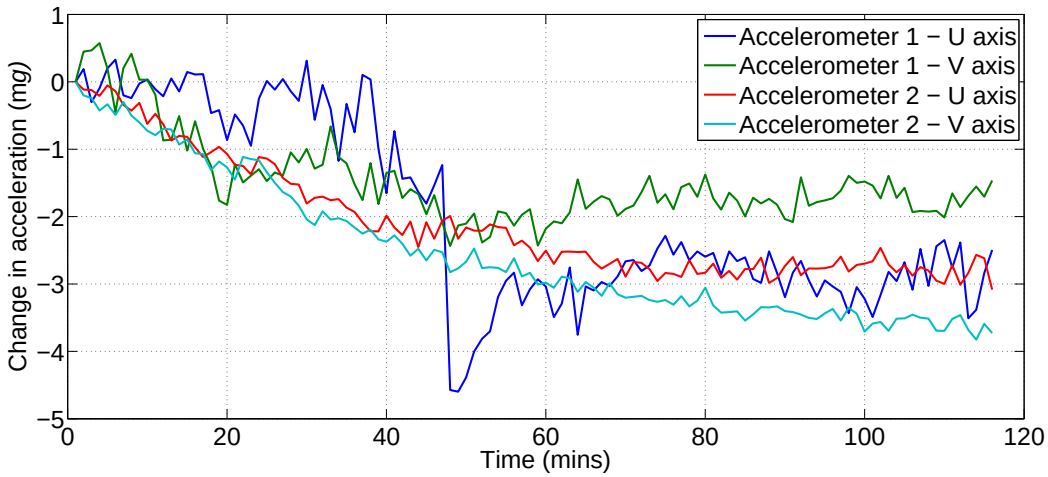

Figure 5.21: Changes in acceleration readings due to the rising temperature inside the rotor.

accelerometers over the course of approximately 2 hours. Figure 5.20 shows a temperature increase of almost 14 °C, which causes a variation in acceleration readings of between -1.5 and -3.5 mg (Figure 5.21). The results indicate that, for the prototype, the measurement error associated with temperature changes between the cold and hot states could be at most ± 4 mg. Nonetheless, this error will be negligible so long as test are conducted under similar temperature conditions.

5.8.5 Other error sources

There exist other sources of error which, however, do not have a significant impact on measurement accuracy under normal operating conditions.

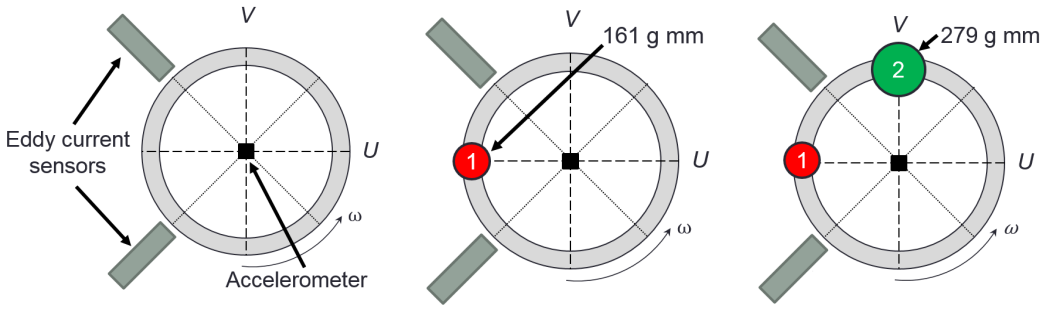

(a) Unbalance condition 1 (b) Unbalance condition 2 (c) Unbalance condition 3

Figure 5.22: Tested unbalance conditions with added masses 1 and 2.

Signal noise is present due to both electrical and thermo-mechanical noise [14]. The latter is a consequence of Brownian motion of the proof-mass, which is displaced by the impacting of air molecules. The circuitry embedded in the accelerometer provides a noise suppression feature, which, combined with an in-built anti-aliasing filter, ensures that noise is kept within manageable bounds.

The power supply to the accelerometers has a substantial effect on zero g offsets, measurement sensitivity and noise. Therefore, a regulated power supply is used to ensure accuracy and measurement repeatability.

The principal damping mechanism in MEMS accelerometers is the squeeze film damping associated with the air surrounding the proof mass, which is proportional to the ambient pressure [15, 16]. Consequently, the motion characteristics of the proof mass will be affected if significant pressure changes are encountered, which may lead to errors in the accelerometer's output. If measuring acceleration in a vacuum, alternative resonant-type MEMS accelerometer designs are available which can overcome these limitations [17].

5.9 Experimental results: effect of rotor unbalance

In order to prove their suitability, the measurement, processing and calibration techniques described in the foregoing sections were applied to a typical rotordynamic problem: the study of the vibration behaviour of the prototype rotor under different unbalance distributions.

Accelerometer and eddy current displacement sensor data were collected under steady state operation at speeds between 200 and $2,000$ rpm (recorded in steps of 50 rpm). The test was repeated for three different unbalance conditions, illustrated in Fig. 5.22.

Figure 5.23 presents the average acceleration for each unbalance case over the tested speed range. The required zero-g offset corrections were calculated

Table 5.3: Zero-*g* offset corrections for each axis of each accelerometer.

Axis	U1	U2	V1	V2
Value (mg)	-174.4	-167.6	-70.0	-102.3

following the procedure described in Section 5.8.1 and are given in Table 5.3, for each axis (U,V) of each of the two accelerometers (1,2). A low-pass filter was applied to the corrected accelerometer output to eliminate the synchronous gravitational acceleration as well as other non-synchronous vibration. The data was then averaged at each speed.

For all unbalance conditions, a clear exponential growth in measured acceleration is evident with increasing speed, corresponding with the increase of unbalance-induced vibration. The addition of mass 1 increases the vibration with respect to the first unbalance condition, indicating that the magnitude of the rotor unbalance has increased. When the second mass is added, the overall acceleration amplitude remains the same, suggesting that unbalance magnitude has not changed. However, the reduction in U axis acceleration and the increase in V demonstrates that the phase of the unbalance has changed. These results illustrate the effects that the variation in unbalance distribution has on the rotor vibration and, most importantly, demonstrate that these are captured by the internal accelerometers.

The results can be validated by comparing the magnitude of the average displacement parameter $|d_c|$ against the mean orbit radius measured by eddy current probes, presented in Fig. 5.24. The accelerometer and eddy current sensor data correlate well, showing an increase in rotor orbit size as the speed approaches the resonant frequency ($2,310$ rpm). The low speed radius of orbit is around 125 μm, as the rotor assembly is not perfectly straight. These results confirm that, for a small positional offset ε_{xy}, the displacement signal d_c gives the mean steady state position of the geometric centre of the rotor in the rotating frame of reference. Thus, the use of internal accelerometers as mean displacement sensors is demonstrated.

The displacement parameter, d_c, indicates how the position of the rotor centre evolves with changes in operating condition. Given that it contains U and V axis information, it can describe both the magnitude and phase of this displacement in the rotating frame of reference, giving further insight into the vibration state of the rotor. As an example, unbalance conditions 2 and 3 produce similar orbit magnitudes, as shown in Fig. 5.24. However, the associated rotor responses have different phases. This is clearly observable in Fig. 5.25, which

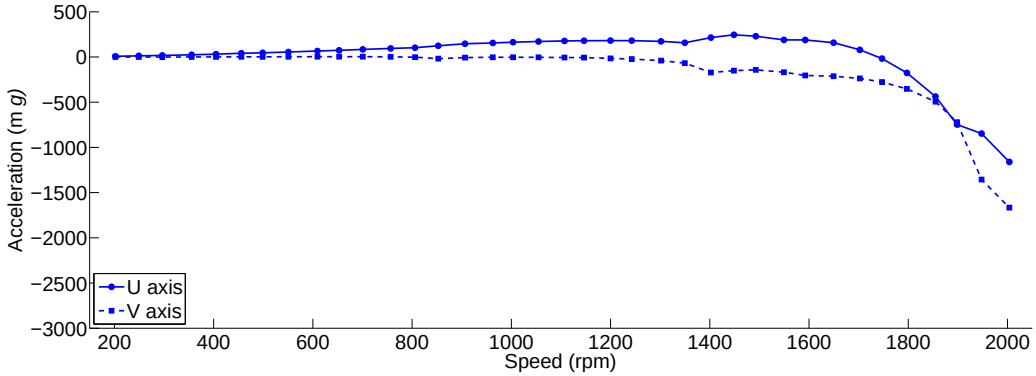

(a) Unbalance condition 1

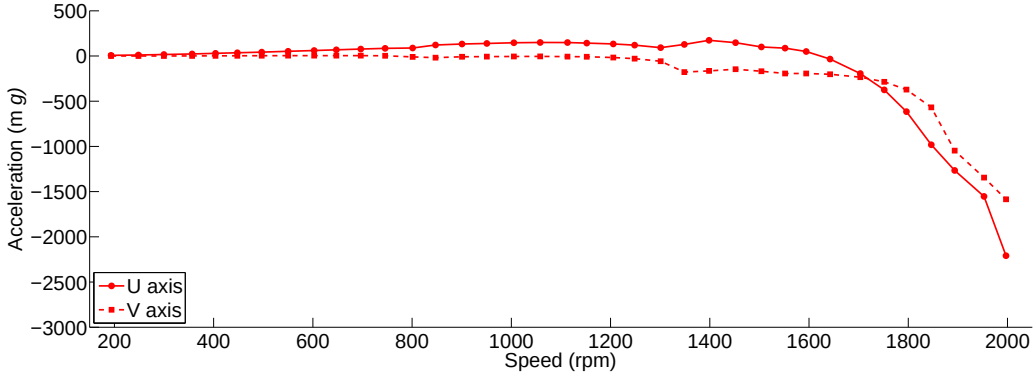

(b) Unbalance condition 2

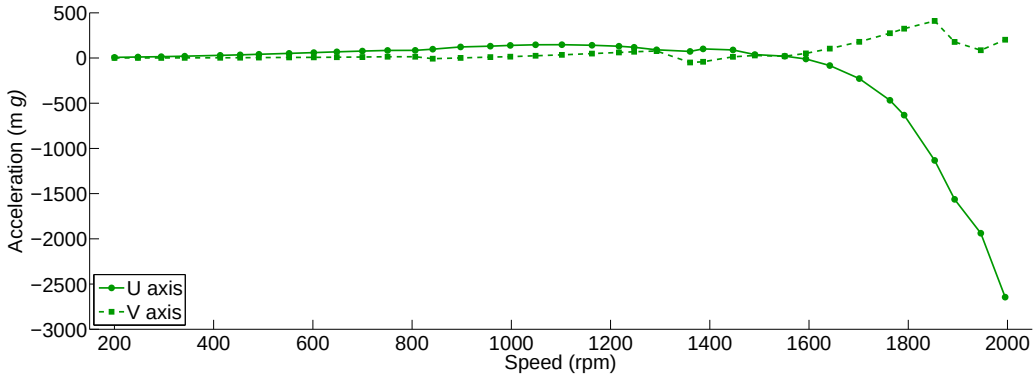

(c) Unbalance condition 3

Figure 5.23: Averaged acceleration measured under different unbalance conditions.

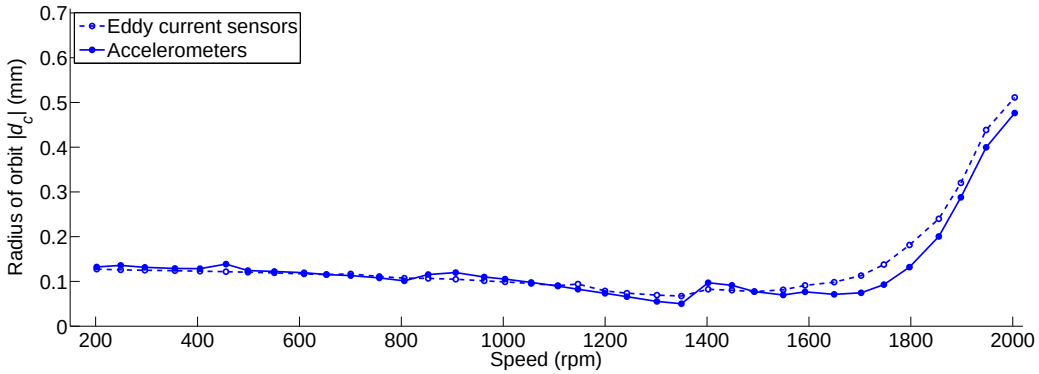

(a) Unbalance condition 1

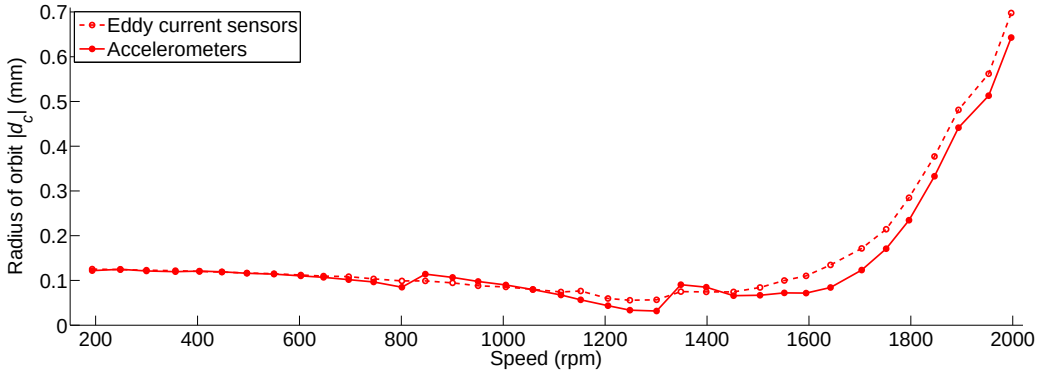

(b) Unbalance condition 2

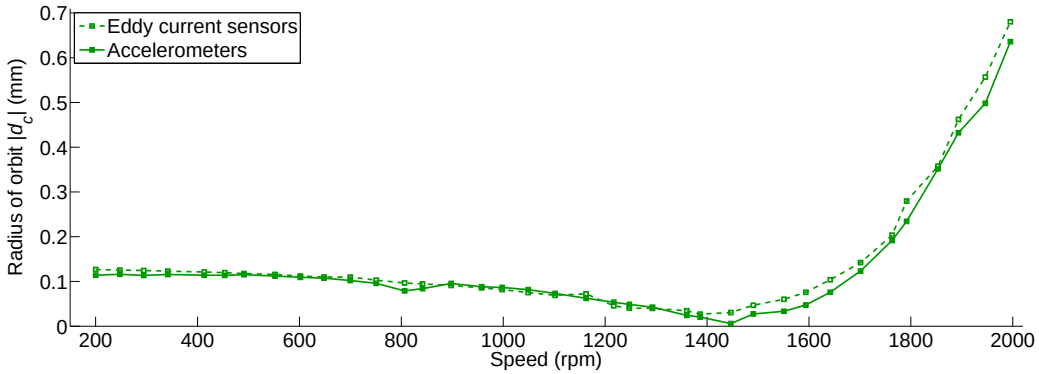

(c) Unbalance condition 3

Figure 5.24: Comparison of accelerometer and eddy current sensor displacement data for the different unbalance conditions.

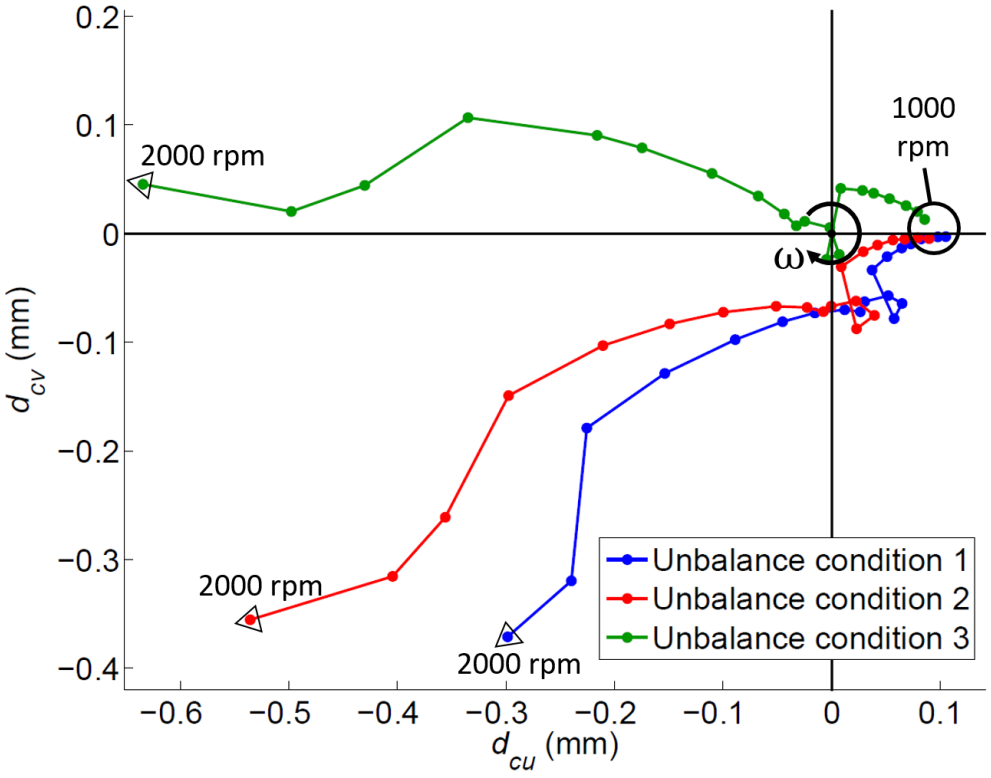

Figure 5.25: Rotor d_c measurements for the three unbalance conditions.

compares the U and V components of d_c for the three unbalance cases, showing data from $1,000$ to $2,000$ rpm. The advantage highlighted here is that phase information has been derived directly, without the need for key phasor sensing.

5.10 Conclusions

One of the principal aims of the research undertaken was to assess the feasibility of using internally-mounted MEMS accelerometers as sensors for active rotor topologies. Various aspects of their implementation, functionality and usage were studied to determine their capabilities and limitations. In general, internally-mounted MEMS accelerometers were found to be reliable, accurate, versatile and cost-effective. Thus, they constitute a promising sensing technology for active rotors.

In accordance with the research objectives established in Chapter 2, a predictive model for the output of MEMS accelerometers located within a rotating shaft was first developed. The derivation was performed beginning with the study of the principles of operation of MEMS accelerometers. The underlying assumption of quasi-static measurement conditions was found to be suitable for

accelerometers operating in a rotating frame of reference.

The derived model was used to investigate how accelerometers measure steady state whirl orbits, and what information can be derived from them. A theoretical framework was developed by which the whirl orbits are expressed as a summation of terms described by a radius, a phase and a whirl frequency. Thus, the orbits of unbalanced rotors are characterised as a base circular orbit, with any deviations from the ideal circle corresponding to non-synchronous components. This work was further applied to the study of impact-induced transient vibration. The analytical prediction of frequency modulation was confirmed via impact tests performed on the active rotor prototype.

The extraction of displacement information from the accelerometer signals via double integration was shown to present practical challenges. Hence, an integration-free method based on isolating the displacement-dependent centripetal acceleration component of the accelerometer signals was developed and validated experimentally. The extraction of angular velocity information was achieved by tracking the gravitational acceleration component in the sensor signals. The experimental results demonstrate the functionality of internal accelerometers as virtual encoders.

An analysis of measurement error sources showed that calibration was required to minimise zero-*g* offset errors and sensor positioning errors. Other error sources can be considered negligible under stable operating conditions in most cases.

The accelerometers were applied to the measurement of the response of the prototype under different unbalance conditions, in order to apply the techniques derived through this research. The internal sensors were successfully used to measure the acceleration and mean displacement of the rotor. A salient result is that both the magnitude and phase of the displacement were measured directly, without the need for key phasor sensing.

5.11 Summary

- Internally-mounted MEMS accelerometers were shown to be a feasible and highly promising sensing technology for active rotor designs.
- The output of internal accelerometers is given in terms of rotor motion by $a \approx (\ddot{d}_{xy} + \mathrm{j}g)\mathrm{e}^{-\mathrm{j}\theta}$.
- The response measured by sensors mounted in the rotating frame of reference will be modulated by the operating speed ω.

- The mean radius of the whirl orbit of unbalanced rotors can be measured with internal accelerometers.
- The rotational speed of a rotor can be measured with internal accelerometers.
- Both zero-*g* offset and sensor positioning errors will typically require minimisation to ensure correct measurement of rotordynamics.
- The phase of the rotor response can be measured directly when utilising a bi-axial internal accelerometer.

References

[1] L. Arebi, F. Gu, and A. Ball, "Rotor misalignment detection using a wireless sensor and a shaft encoder," in *Future Technologies in Computing and Engineering. Proceedings of Computing and Engineering Annual Researchers' Conference CEARC'10*, (Huddersfield, UK), pp. 6–13, 2010.

[2] L. Baghli, J. F. Pautex, and S. Mezani, "Wireless instantaneous torque measurement, application to induction motors," in *19th International Conference on Electrical Machines, ICEM*, (Rome Italy), 2010.

[3] M. Elnady, J. Sinha, and S. Oyadiji, "Identification of critical speeds of rotating machines using on-shaft wireless vibration measurement," in *Journal of Physics: Conference Series*, vol. 364, p. 012142, IOP Publishing, 2012.

[4] M. E. Elnady, *On-shaft vibration measurement using a MEMS accelerometer for faults diagnosis in rotating machines*. PhD thesis, University of Manchester, 2013.

[5] S. E. Lyshevski, *MEMS and NEMS: systems, devices, and structures*. CRC press, 2002.

[6] J. A. Yasaitis, M. Judy, T. Brosnihan, P. M. Garone, N. Pokrovskiy, D. Sniderman, S. Limb, R. T. Howe, B. E. Boser, M. Palaniapan, X. Jiang, and S. Bhave, "A modular process for integrating thick polysilicon mems devices with sub-micron cmos," vol. 4979, pp. 145–154, 2003. 10.1117/12.478294.

[7] J. G. Korvink, *MEMS A Practical Guide to Design, Analysis, and Applications*. Dordrecht: Dordrecht : Springer, 2010.

[8] BorgWarner Turbo Systems GmbH, "Design and function of a turbocharger: Bearing systems." `http://www.turbos.bwauto.com/products/turbochargerBearingSystem.aspx`. Accessed: 23/08/2016.

[9] S. Han, "Measuring displacement signal with an accelerometer," *Journal of Mechanical Science and Technology*, vol. 24, no. 6, pp. 1329–1335, 2010.

[10] P. Cheng, Y. Yang, and B. Oelmann, "Design and implementation of a stator-free rpm sensor prototype based on mems accelerometers," *IEEE Transactions on Instrumentation and Measurement*, vol. 61, no. 3, pp. 775–785, 2012.

[11] G. D'Antona, *Digital Signal Processing for Measurement Systems. Theory and Applications*. New York : Springer-Verlag, 2006.

[12] F. J. Harris, "On the use of windows for harmonic analysis with the discrete fourier transform," *Proceedings of the IEEE*, vol. 66, no. 1, pp. 51–83, 1978.

[13] G. Andria, M. Savino, and A. Trotta, "Windows and interpolation algorithms to improve electrical measurement accuracy," *IEEE Transactions on Instrumentation and Measurement*, vol. 38, no. 4, pp. 856–863, 1989.

[14] Z. Djuric, "Mechanisms of noise sources in microelectromechanical systems," *Microelectronics Reliability*, vol. 40, no. 6, pp. 919–932, 2000.

[15] M. Bao and H. Yang, "Squeeze film air damping in mems," *Sensors and Actuators A: Physical*, vol. 136, no. 1, pp. 3–27, 2007.

[16] S. Hartono, "Squeeze-film damping in the free molecular regime: model validation and measurement on a mems," *Journal of Micromechanics and Microengineering*, vol. 17, no. 11, p. 2231, 2007.

[17] A. A. Seshia, M. Palaniapan, T. A. Roessig, R. T. Howe, R. W. Gooch, T. R. Schimert, and S. Montague, "A vacuum packaged surface micromachined resonant accelerometer," *Journal of Microelectromechanical Systems*, vol. 11, no. 6, pp. 784–793, 2002.

Chapter 6

Vibration control with active rotors

6.1 Introduction

The primary goal of the development of active rotor technology was to enable a generally implementable active vibration control system, which could be applied to a wide range of rotating machines. From the perspective of the controller, this imposes restrictions on the degree to which human operators intervene to achieve the desired control performance. In an ideal scenario, the active rotor would be able to minimise its own vibration without requiring any prior information on the design or condition of the stator or the rotating machine as a whole. This would allow the active rotor to be designed independently and to operate autonomously, facilitating its implementation.

As discussed in Chapter 2, a review of available techniques allowed classification into two broad categories of *a priori* controller: "estimated" and "modelled". The distinction between them corresponds to whether the system transfer function is determined by measuring the response under known input conditions or by constructing a computer model, respectively. On review, neither class of *a priori* controller was deemed suitable to meet the required degree of autonomy. Estimation-based methods require trial runs being performed under known input conditions, requiring a considerable amount of human intervention. In addition, their performance is limited by the spectrum of conditions under which trial runs can be performed, thus reducing their capability in the face of uncertainty. On the other hand, model-based controllers can be designed in such a way as to be robust to unknown disturbances. However, they rely on accurate computer models of the rotor system, which can be time-consuming to develop and require considerable expertise. In some instances, where large uncertainty is present or the physical phenomena being modelled are highly complex, the problem of producing a sufficiently accurate model under timing

and budget constraints may simply be intractable.

The limitations of *a priori* controllers are fundamentally associated with the methods of establishing the transfer function between the measured system state and the actuator inputs. The alternative approach considered was to develop a *non a priori* controller, one in which the transfer function was not constructed.

This chapter therefore reports on the research undertaken to design and implement a *non a priori* control method, referred to as Algorithmic Direct Search Control (ADSC). Firstly, the control problem of reducing vibration in an unbalanced active rotor is posed. As a first step, a conventional model-based controller was applied in simulation, in order to better understand the practicalities of using a rotor-mounted active control system. The development of the ADSC is then reported. The method is based on applying a derivative-free optimisation technique, known as the Nelder-Mead algorithm, directly as a control law. Hence, the original algorithm is introduced and then a detailed description is given of the modifications performed to adapt it for use as a controller. The method was validated both in simulation and experimentally, and results are presented.

6.2 Control problem formulation

The control problem to be addressed is that of reducing unbalance-induced vibration in an active rotor. In general, unbalance is the most prevalent source of unwanted vibration in rotating machinery, and so its reduction is a common rotordynamic problem. In the case of active rotors in particular, the mounting of components in the rotor will inevitably lead to a redistribution of unbalance, which could be significant. Thus, it is essential that an active rotor is capable of managing its own unbalance-related vibration.

The control system is depicted schematically in Fig. 6.1, which shows a cross-section of an active rotor whirling around the zero-speed equilibrium point O. An internal accelerometer is located at the geometric centre of the rotor, and the control force is provided by a mass-balancer type actuator with two masses. A typical rotor will have unbalance distributed along its length. This can be represented as a series of discrete eccentric mass unbalances, contained in complex vector $\boldsymbol{\sigma}_r$. The rotor may have s accelerometers and m mass-balancer pair actuators, with parameter Υ indicating the unbalance magnitude of each mass. These have controllable angular positions α_l and β_l, respectively, with $l = 1, 2, \ldots, m$.

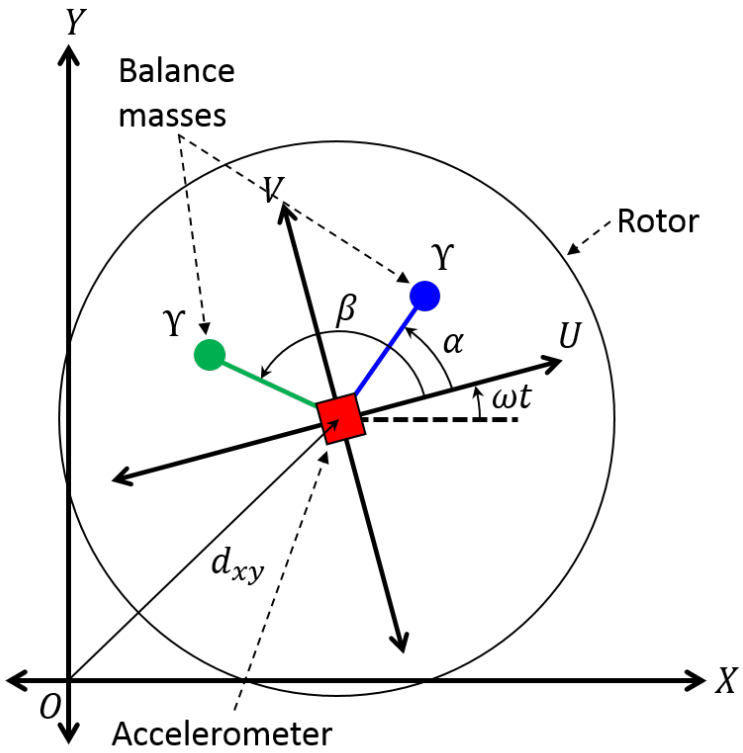

Figure 6.1: Schematic of the rotor cross-section, showing the position of the accelerometer and actuator balance masses.

The output of a single accelerometer located at a given coordinate along the unbalanced rotor is derived from Eq. (5.59) as

$$a = -\omega^2 R_F \mathrm{e}^{\mathrm{j}\phi_F} - \omega^2 R_B \mathrm{e}^{\mathrm{j}(-2\omega t+\phi_B)} + \mathrm{j}g\mathrm{e}^{-\mathrm{j}\omega t} \tag{6.1}$$

where R_F and R_B indicate the forward and backward whirl orbits, respectively. The phases of the orbits are given by terms ϕ_F and ϕ_B. The forward whirl component, which is synchronous in the inertial frame, appears modulated to the zero frequency. It follows from the definition of the forward whirl orbit radius parameter $R_F(\omega, \omega^2\boldsymbol{\sigma}_r)$ in Eq. (5.52) that the minimisation of this zero-frequency component implies a minimisation of term $\hat{\mathrm{b}}_m^{\mathrm{T}}\boldsymbol{\sigma}_r$, which can be understood as the equivalent unbalance at the accelerometer position. Hence, only the first term in Eq. (6.1) needs to be observed to achieve minimisation of the unbalance, and this component can be extracted with the use of a low-pass filter (LP):

$$\tilde{a} = LP(a) = -\omega^2 R_F \mathrm{e}^{\mathrm{j}\phi_F} + \epsilon(\omega) \tag{6.2}$$

where $\epsilon(\omega)$ indicates the residual error associated with filtering and will be negligible below a breakpoint frequency. The matrix-vector equation of motion

for the considered rotor is

$$\mathbf{M}\ddot{\mathbf{d}}_{xy} + (\mathbf{C} - \mathrm{j}\omega\mathbf{G})\dot{\mathbf{d}}_{xy} + \mathbf{K}\mathbf{d}_{xy} = \omega^2 \left(\boldsymbol{\sigma}_r + \boldsymbol{\Psi}\boldsymbol{\sigma}\right) \mathrm{e}^{\mathrm{j}\omega t} \tag{6.3}$$

where $\mathbf{d}_{xy}$ is a $(n \times 1)$ complex displacement vector in the XY inertial frame of reference, $\mathbf{M}$ is the rotor mass matrix, $\mathbf{C}$ is the system damping matrix, $\mathbf{G}$ is the gyroscopic matrix and $\mathbf{K}$ is the stiffness matrix [1]. The $(m \times 1)$ vector $\boldsymbol{\sigma}$ denotes the counter-unbalance provided by the actuators, and takes the form

$$\boldsymbol{\sigma} = \Upsilon \begin{bmatrix} \mathrm{e}^{\mathrm{j}\alpha_1} + \mathrm{e}^{\mathrm{j}\beta_1} \\ \mathrm{e}^{\mathrm{j}\alpha_2} + \mathrm{e}^{\mathrm{j}\beta_2} \\ \vdots \\ \mathrm{e}^{\mathrm{j}\alpha_n} + \mathrm{e}^{\mathrm{j}\beta_n} \end{bmatrix}, \tag{6.4}$$

while $\boldsymbol{\Psi}$ is a $(n \times m)$ matrix indicating the position of the actuators along the rotor. Equation (6.3) can be converted to the UV rotating frame displacement $\mathbf{d}_{uv}$ knowing that $\mathbf{d}_{xy} = \mathbf{d}_{uv}\mathrm{e}^{\mathrm{j}\omega t}$. Hence, (6.3) becomes

$$\begin{aligned} \mathbf{M}\ddot{\mathbf{d}}_{uv} + \left[\mathbf{C} + \mathrm{j}\omega(2\mathbf{M} - \mathbf{G})\right] \dot{\mathbf{d}}_{uv} + \\ \left[\omega^2(\mathbf{G} - \mathbf{M}) + \mathrm{j}\omega\mathbf{C} + \mathbf{K}\right] \mathbf{d}_{uv} = \omega^2 \left(\boldsymbol{\sigma}_r + \boldsymbol{\Psi}\boldsymbol{\sigma}\right) \end{aligned} \tag{6.5}$$

In the simple case of the rotor being dominated by the forward whirl component, the orbit will be quasi-circular. Hence $\ddot{\mathbf{d}}_{uv} \approx \dot{\mathbf{d}}_{uv} \approx \mathbf{0}$ and vector $\mathbf{d}_{uv}$ will take the form $[R_{F1}\mathrm{e}^{\mathrm{j}\phi_{F1}}, R_{F2}\mathrm{e}^{\mathrm{j}\phi_{F2}}, \ldots, R_{Fn}\mathrm{e}^{\mathrm{j}\phi_{Fn}}]^{\mathrm{T}}$. It follows then that

$$\tilde{\mathbf{a}} = -\omega^2 \boldsymbol{\Gamma}\mathbf{d}_{uv} \tag{6.6}$$

where $(s \times 1)$ vector $\tilde{\mathbf{a}}$ contains the filtered acceleration signals, and the $(s \times n)$ matrix $\boldsymbol{\Gamma}$ specifies the position of the sensors along the rotor. Hence,

$$\left[\omega^2(\mathbf{G} - \mathbf{M}) + \mathrm{j}\omega\mathbf{C} + \mathbf{K}\right] \boldsymbol{\Gamma}^{-1} \frac{\tilde{\mathbf{a}}}{-\omega^2} = \omega^2 \left(\boldsymbol{\sigma}_r + \boldsymbol{\Psi}\boldsymbol{\sigma}\right) \tag{6.7}$$

$$\tilde{\mathbf{a}} = \boldsymbol{\Gamma}\mathbf{H} \left(\boldsymbol{\sigma}_r + \boldsymbol{\Psi}\boldsymbol{\sigma}\right) \tag{6.8}$$

where the receptance matrix $\mathbf{H}$ is given by

$$\mathbf{H} = -\omega^4 \left[\omega^2(\mathbf{G} - \mathbf{M}) + \mathrm{j}\omega\mathbf{C} + \mathbf{K}\right]^{-1} \tag{6.9}$$

Equation (6.8) gives the filtered accelerometer output in response to a given unbalance state. The objective of the control is to minimise the overall rotor

vibration by adjusting the angular positions of the mass-balancers. Thus, the parameter to be minimised is the l_2-norm of $\tilde{\mathbf{a}}$:

$$F = \sqrt{\tilde{\mathbf{a}}^{\mathrm{H}}\tilde{\mathbf{a}}} \tag{6.10}$$

where $\tilde{\mathbf{a}}^{\mathrm{H}}$ indicates the conjugate transpose of $\tilde{\mathbf{a}}$.

In order to understand the implications of using rotor-mounted sensors and actuators from a control perspective, the control problem was first addressed using a conventional model-based technique, described in the following section.

6.3 Model-based control

The model-based approach relies on approximating the receptance matrix $\mathbf{H}$ in Eq. (6.9) using a finite element model of the active rotor. Thus, $\mathbf{H}$ was constructed from the assumed mass, stiffness, damping and gyroscopic matrices presented in Chapter 3.

Following the approach in [2], if the steady state actuator output is given by $\tilde{\mathbf{a}}$ then a step change in the counter-unbalance provided by the actuators will produce a new accelerometer output $\tilde{\mathbf{a}}_N$ such that

$$\tilde{\mathbf{a}}_N = \tilde{\mathbf{a}} - \mathbf{Z}\Delta\boldsymbol{\sigma} \tag{6.11}$$

where $\mathbf{Z} = \boldsymbol{\Gamma}\mathbf{H}\boldsymbol{\Psi}$ and $\Delta\boldsymbol{\sigma} = \left[\mathrm{e}^{\mathrm{j}\Delta\alpha_1} + \mathrm{e}^{\mathrm{j}\Delta\beta_1}, \ldots, \mathrm{e}^{\mathrm{j}\Delta\alpha_m} + \mathrm{e}^{\mathrm{j}\Delta\beta_m}\right]$. A least squares formulation can be used to minimise the l_2 norm of $\tilde{\mathbf{a}}_N$. For simplicity, parameter F^2 can be used so that the objective function S to be minimised will be

$$S(\Delta\boldsymbol{\sigma}) = F^2 = \tilde{\mathbf{a}}_N^{\mathrm{H}}\tilde{\mathbf{a}}_N \tag{6.12}$$

$$S(\Delta\boldsymbol{\sigma}) = \left[\tilde{\mathbf{a}} - \mathbf{Z}\Delta\boldsymbol{\sigma}\right]^{\mathrm{H}}\left[\tilde{\mathbf{a}} - \mathbf{Z}\Delta\boldsymbol{\sigma}\right] \tag{6.13}$$

$$S(\Delta\boldsymbol{\sigma}) = \tilde{\mathbf{a}}^{\mathrm{H}}\tilde{\mathbf{a}} - \tilde{\mathbf{a}}^{\mathrm{H}}\mathbf{Z}\Delta\boldsymbol{\sigma} - \Delta\boldsymbol{\sigma}^{\mathrm{H}}\mathbf{Z}^{\mathrm{H}}\tilde{\mathbf{a}} + \Delta\boldsymbol{\sigma}^{\mathrm{H}}\mathbf{Z}^{\mathrm{H}}\mathbf{Z}\Delta\boldsymbol{\sigma} \tag{6.14}$$

The objective function can be rewritten as summations of matrix elements so that

$$S(\Delta\boldsymbol{\sigma}) = \sum_{i=1}^{s}\overline{\tilde{a}}_i\tilde{a}_i - \sum_{l=1}^{m}\Delta\sigma_l\left(\sum_{i=1}^{s}\overline{\tilde{a}}_i Z_{il}\right) - \sum_{i=1}^{s}\tilde{a}_i\left(\sum_{l=1}^{m}\overline{\Delta\sigma}_l\overline{Z}_{il}\right) + \sum_{i=1}^{s}\left(\sum_{l=1}^{m}\overline{\Delta\sigma}_l\overline{Z}_{il}\right)\left(\sum_{l=1}^{m}\Delta\sigma_l Z_{il}\right) \tag{6.15}$$

This function is differentiated with respect to each component $\Delta\sigma_l$ to find its minimum. To this end, the real and imaginary parts are separated to account for the conjugate terms, so that

$$\Delta\sigma_l = R_l + \mathrm{j}I_l \tag{6.16}$$

and so

$$S(\Delta\boldsymbol{\sigma}) = \sum_{i=1}^{s} \overline{\tilde{a}}_i \tilde{a}_i - \sum_{l=1}^{m} (R_l + \mathrm{j}I_l) \left(\sum_{i=1}^{s} \overline{\tilde{a}}_i Z_{il} \right) - \sum_{i=1}^{s} \tilde{a}_i \left(\sum_{l=1}^{m} (R_l - \mathrm{j}I_l) \overline{Z}_{il} \right) + \sum_{i=1}^{s} \left(\sum_{l=1}^{m} (R_l - \mathrm{j}I_l) \overline{Z}_{il} \right) \left(\sum_{l=1}^{m} (R_l + \mathrm{j}I_l) Z_{il} \right) \tag{6.17}$$

The derivative $\partial S / \partial \Delta\sigma_l$ can then be expressed as

$$\frac{\partial S}{\partial \Delta\sigma_l} = \frac{\partial S}{\partial R_l} \frac{\partial R_l}{\partial \Delta\sigma_l} + \frac{\partial S}{\partial I_l} \frac{\partial I_l}{\partial \Delta\sigma_l} \tag{6.18}$$

Given that

$$\frac{\partial R_l}{\partial \Delta\sigma_l} = 1 \qquad \frac{\partial I_l}{\partial \Delta\sigma_l} = -\mathrm{j},$$

the derivative becomes

$$\frac{\partial S}{\partial \Delta\sigma_l} = \frac{\partial S}{\partial R_l} - \mathrm{j} \frac{\partial S}{\partial I_l} \tag{6.19}$$

It follows that

$$\frac{\partial S}{\partial R_l} = -\sum_{i=1}^{s} \left(\tilde{a}_i \overline{Z}_{il} + \overline{\tilde{a}}_i Z_{il} \right) + 2 \sum_{i=1}^{s} \overline{Z}_{il} Z_{il} R_l + \sum_{i=1}^{s} \sum_{k \neq l}^{m} \left(\overline{Z}_{ik} Z_{il} \overline{\Delta\sigma}_k + Z_{ik} \overline{Z}_{il} \Delta\sigma_k \right) \tag{6.20}$$

$$\frac{\partial S}{\partial I_l} = -\mathrm{j} \sum_{i=1}^{s} \left(\tilde{a}_i \overline{Z}_{il} - \overline{\tilde{a}}_i Z_{il} \right) + 2 \sum_{i=1}^{s} \overline{Z}_{il} Z_{il} I_l + \mathrm{j} \sum_{i=1}^{s} \sum_{k \neq l}^{m} \left(\overline{Z}_{ik} Z_{il} \overline{\Delta\sigma}_k - Z_{ik} \overline{Z}_{il} \Delta\sigma_k \right), \tag{6.21}$$

Substituting these derivatives into Eq. (6.19) yields

$$\frac{\partial S}{\partial \Delta\sigma_l} = -2 \sum_{i=1}^{s} \overline{\tilde{a}}_i Z_{il} + 2 \sum_{i=1}^{s} \overline{Z}_{il} Z_{il} \overline{\Delta\sigma}_l + 2 \sum_{i=1}^{s} \sum_{k \neq l}^{m} \overline{Z}_{ik} Z_{il} \overline{\Delta\sigma}_k \tag{6.22}$$

which can be rewritten in terms of the total contribution from all actuators with $k = 1, 2, \ldots, m$:

$$\frac{\partial S}{\partial \Delta\sigma_l} = -2 \sum_{i=1}^{s} \overline{\tilde{a}}_i Z_{il} + 2 \sum_{i=1}^{s} \sum_{k=1}^{m} Z_{il} \overline{Z}_{ik} \overline{\Delta\sigma}_k \tag{6.23}$$

Equating the derivative to zero to minimise $\tilde{\mathbf{a}}_N$ produces

$$\sum_{i=1}^{s}\sum_{k=1}^{m}\overline{Z}_{il}Z_{ik}\Delta\sigma_k = \sum_{i=1}^{s}\tilde{a}_i\overline{Z}_{il}, \tag{6.24}$$

which returned to the matrix form is

$$\mathbf{Z}^{\mathrm{H}}\mathbf{Z}\Delta\boldsymbol{\sigma} = \mathbf{Z}^{\mathrm{H}}\tilde{\mathbf{a}} \tag{6.25}$$

Hence, the change in actuator counter-unbalance which minimises the rotor response is

$$\Delta\boldsymbol{\sigma} = \mathbf{W}\tilde{\mathbf{a}} \tag{6.26}$$

where $\mathbf{W} = \left(\mathbf{Z}^{\mathrm{H}}\mathbf{Z}\right)^{-1}\mathbf{Z}^{\mathrm{H}}$ is the Moore-Penrose pseudoinverse of $\mathbf{Z}$. Integrating this desired step-change in unbalance yields the overall counter-unbalance demand such that

$$\boldsymbol{\sigma} = k_i\int_0^t \Delta\boldsymbol{\sigma}\,\mathrm{d}t \tag{6.27}$$

where the integrator gain k_i allows regulating the speed of the system response. The unbalance demand must be converted into an angular position demand for each of the balance masses in each actuator. Being a complex vector, it will have a magnitude $|\boldsymbol{\sigma}|$ and phase $\angle\boldsymbol{\sigma}$. For the l^{th} actuator,

$$|\sigma_l|\mathrm{e}^{j\angle\sigma_l} = \Upsilon\left(\mathrm{e}^{\mathrm{j}\alpha_l} + \mathrm{e}^{\mathrm{j}\beta_l}\right) \tag{6.28}$$

As the balance masses are assumed to be identical for all actuators, their desired angular positions will be symmetrical around the minimising counter-unbalance phase, and so can be redefined as

$$\alpha_l = \angle\sigma_l + \delta_l \tag{6.29}$$

$$\beta_l = \angle\sigma_l - \delta_l \tag{6.30}$$

Substituting these identities into Eq. (6.28) yields

$$|\sigma_l|\mathrm{e}^{j\angle\sigma_l} = \Upsilon\mathrm{e}^{j\angle\sigma_l}\left(\mathrm{e}^{\mathrm{j}\delta_l} + \mathrm{e}^{-\mathrm{j}\delta_l}\right) \tag{6.31}$$

$$|\sigma_l| = \Upsilon\left(\mathrm{e}^{\mathrm{j}\delta_l} + \mathrm{e}^{-\mathrm{j}\delta_l}\right) \tag{6.32}$$

$$|\sigma_l| = 2\Upsilon\cos\delta_l \tag{6.33}$$

$$\delta_l = \arccos\left(\frac{|\sigma_l|}{2\Upsilon}\right) \tag{6.34}$$

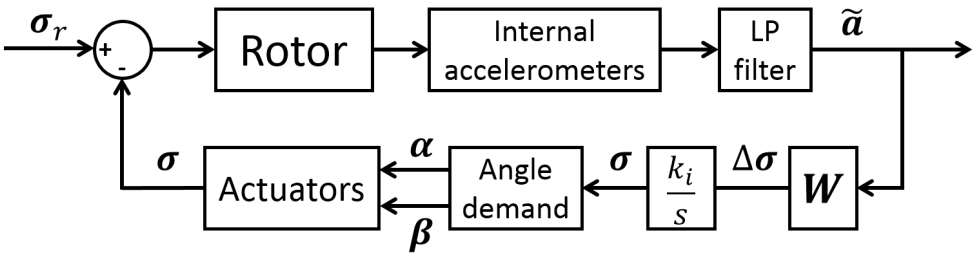

Figure 6.2: Block diagram of the model-based controller.

Thus, the angle demands produced by the controller for the actuators will be

$$\alpha_l = \angle\sigma_l + \arccos\left(\frac{|\sigma_l|}{2\Upsilon}\right) \tag{6.35}$$

$$\beta_l = \angle\sigma_l - \arccos\left(\frac{|\sigma_l|}{2\Upsilon}\right) \tag{6.36}$$

The resulting control scheme is shown in Fig. 6.2. The controller was tested in simulation on the finite element model depicted in Fig. 3.10, which represents the prototype. A single sensor and actuator were assumed to be located at the rotor midspan. Figure 6.3 shows the filtered U and V axis accelerometer signals when operating at $1,500$ rpm, assuming an arbitrary unbalance distribution along the rotor. The controller is activated after 2 s, and successfully reduces the rotor vibration. Figure 6.4 presents the displacement at the sensing plane in the inertial frame, as would be measured by the eddy current displacement sensors on the test rig. Figure 6.5 shows the angular position of the balance masses throughout the control process.

The actuator dynamics are modelled as a first order lag, which is an appropriate simplification because the stepper motors, by their nature, will not overshoot their demanded angular position. As the mass will move continuously until that position is reached, a time constant $\tau = 0.1$ s is selected. With this value, the simulated actuator will move one full step in approximately 5τ s. As the stepping period is 0.5 s (for the default stepping rate of 2 steps/s), the desired continuous motion is achieved.

In addition, the motor resolution is taken into account. The stepper motor and planetary gears are assumed to produce 100 steps per full revolution. This limits the angular position resolution of the masses to $3.6°$, which leads to the small changes in mass position at around 7 and 9 seconds, labelled in Fig. 6.5. The effect of these small steps can be observed in the acceleration and displacement experienced by the rotor. Prior to activating the vibration control, the masses are assumed to be in a neutral position with $\alpha = 90°$ and $\beta = 270°$,

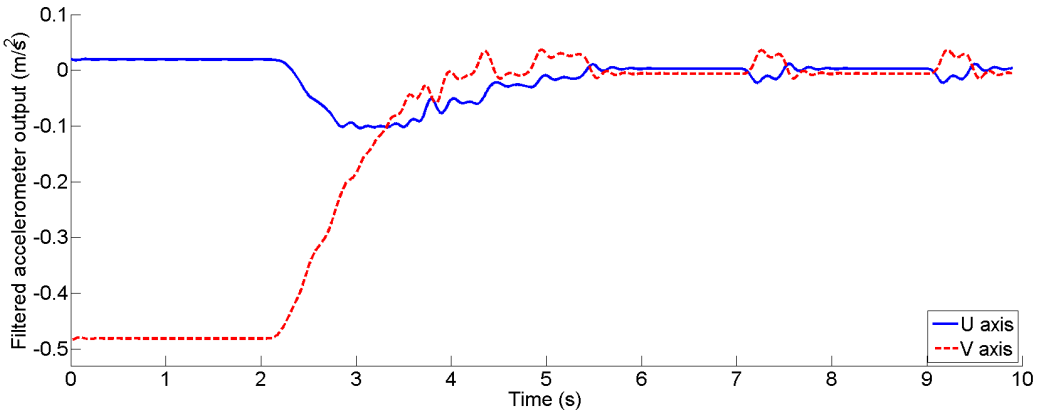

Figure 6.3: Simulated filtered accelerometer output during control.

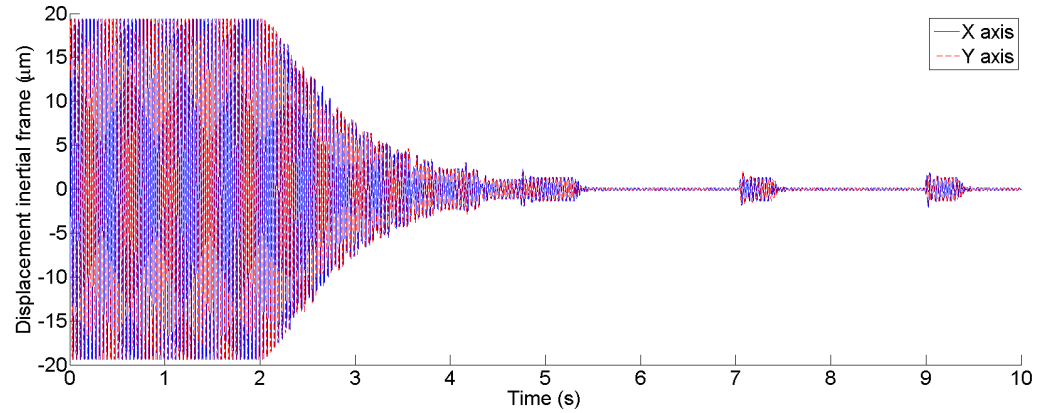

Figure 6.4: Simulated inertial frame displacement during control

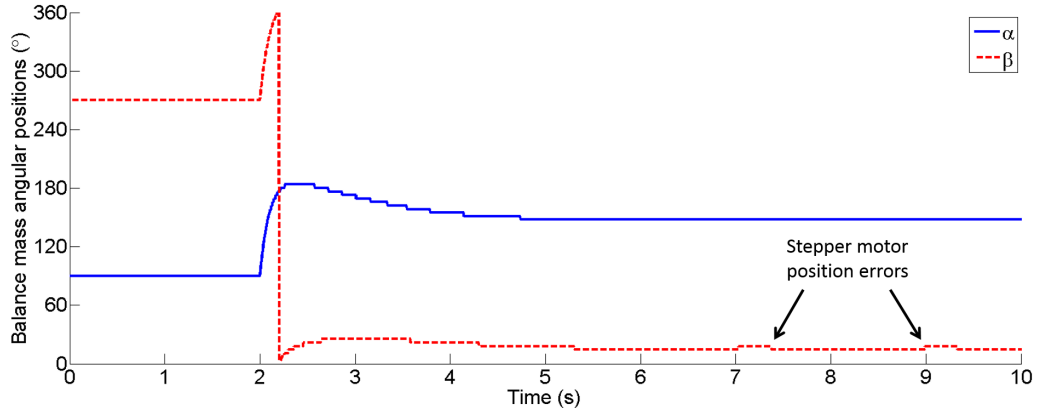

Figure 6.5: Simulated mass-balancer angular position during control.

which ensures the actuator has no effect on the rotor vibration.

The simulation results illustrate some important characteristics of active rotor control, related to the fact that both sensors and actuators are located in the rotating frame of reference. The filtered accelerometer output shown in Fig. 6.3 is non-oscillatory under steady state operation, unlike with stator-mounted sensors. This reduces the computational burden associated with processing the signal. Equally, the control force produced by the actuators is constant in the rotor reference frame. In consequence, the actuator demand (Fig. 6.5) is not required to oscillate synchronously, as is the case for stator-mounted actuators. This reduces the computational complexity and performance characteristics required of the control system, which can be a limiting factor of stator-mounted arrangements. In the case of AMBs, for instance, producing high-frequency control forces requires large, powerful and costly amplifiers, which can often limit the overall system performance. The rotor-mounted nature of the actuators also prevents discrepancies between the controller demand frequency and the angular speed of the rotor, which typically cause issues by introducing phase lag/lead errors.

Hence, the application of the model-based controller shows that active rotors can achieve vibration control with reduced capability requirements being imposed on the control system. This enables smaller, simpler and more cost-effective sensor and actuators to be used, assisting in their implementation within hollow shaft rotors.

6.4 *Non a priori* control

The principal drawbacks of a priori controllers stem from the approximation of the receptance matrix $\mathbf{H}$. Thus, in order to avoid the associated errors, a *non a priori* control method was sought which did not require $\mathbf{H}$ in its computations. The Algorithmic Direct Search Control method developed is based on the Nelder-Mead optimization method.

The Nelder-Mead algorithm (NMA) [3], also referred to as the "Amoeba" or "Simplex" method, provides a means to minimise an objective function by comparing heuristically its values at various test points. It has seen widespread use in a number of fields thanks to its simplicity of implementation and its ability to tackle nonlinear optimization problems. The NMA allows optimization to be carried out without knowledge of the objective function derivatives, and this characteristic is exploited in the ADSC to obtain a heuristic control law for vibration reduction without *a priori* knowledge of the rotor characteristics. A

further desirable property when considering the application of the NMA to rotor control is its relatively low number of function evaluations [4, 5], which ensures that vibration can be minimised within a reasonable time scale. Also, the simplicity of the method allows its implementation on compact, rotor-mounted microcontrollers.

The ADSC, therefore, aims to find the optimum balance mass positions which minimise the objective function F by comparing heuristically its values for different counter-unbalance vectors $\boldsymbol{\sigma}$. This process does not require the rotor characteristics to be estimated or modelled.

The objective function can be analysed for the active rotor prototype case of a single sensor and actuator, assumed to be collocated at the r^{th} rotor node, located at the midspan. Thus, the product $\mathbf{\Gamma H \Psi}$ extracts the rth row and column of $\mathbf{H}$. If the rotor unbalance $\boldsymbol{\sigma}$ is assumed to also be concentrated at the midspan, then Eq. 6.8 yields a complex scalar, which can be written as

$$\tilde{a} = H_{rr}\left(\Upsilon_r \mathrm{e}^{\mathrm{j}\phi} + \Upsilon\left(\mathrm{e}^{\mathrm{j}\alpha} + \mathrm{e}^{\mathrm{j}\beta}\right)\right) \tag{6.37}$$

where Υ_r is the magnitude of the rotor unbalance and ϕ its phase. The objective function P can therefore be considered as the magnitude of the acceleration $|\tilde{a}|$ and so

$$P = Q\left|\left(\Upsilon_r \mathrm{e}^{\mathrm{j}\phi} + \Upsilon\left(\mathrm{e}^{\mathrm{j}\alpha} + \mathrm{e}^{\mathrm{j}\beta}\right)\right)\right| \tag{6.38}$$

with $Q = |H_{rr}|$. The stationary points of the objective function will coincide with those of P^2/Q^2, which are presented in Table 6.1. Their derivation can be found in Appendix B. Figure 6.6 shows a contour plot of the objective function for the arbitrary case $\Upsilon_r = 1.2\Upsilon$ and $\phi = 93.46°$, with the stationary points highlighted.

The ADSC will therefore seek the α and β positions associated with the function minima. In the case where $2\Upsilon < \Upsilon_r$ the actuators cannot provide sufficient counter-unbalance to cancel the effect of rotor unbalance. Hence, the minimum function value is obtained at test point $(\phi + \pi, \phi + \pi)$, where the actuator masses are directly opposite the unbalance, but the function value will be non-zero. The working principle of the Nelder-Mead algorithm which enables these minima to be found is detailed in the following section.

6.4.1 Nelder-Mead algorithm

For an n-dimensional problem, the method requires $n + 1$ initial test points, which form the vertices of a simplex, which is the set $S = \{V_1, V_2, \ldots, V_{n+1}\}$. A

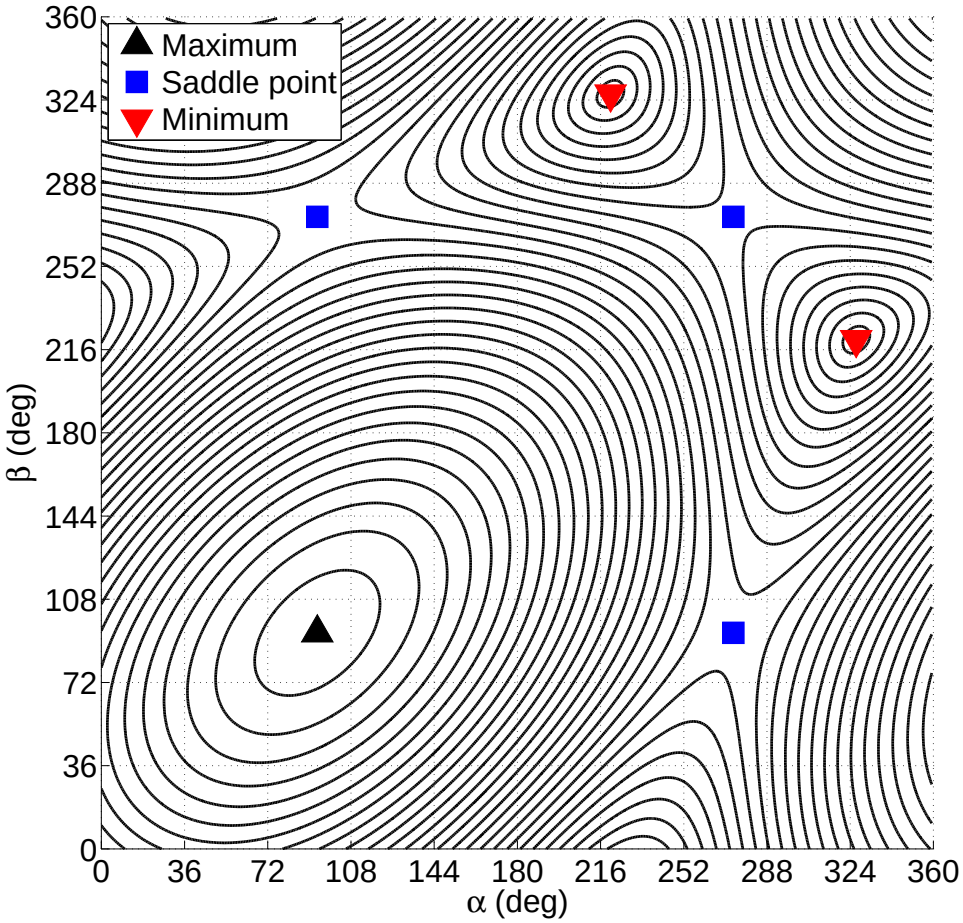

Figure 6.6: Contour plot of P/Q under steady speed conditions.

Table 6.1: Stationary points of the objective function for the single sensor, single actuator case.

$\boldsymbol{\alpha}$	$\boldsymbol{\beta}$	**Stationary point**
ϕ	ϕ	Maximum
$\phi + \pi$	$\phi + \pi$	Saddle point
ϕ	$\phi + \pi$	Saddle point
$\phi + \pi$	ϕ	Saddle point
$\phi + \arccos\left(\frac{\Upsilon_r}{-2\Upsilon}\right)$	$\alpha + \arccos\left(\frac{\Upsilon_r^2}{2\Upsilon^2} - 1\right)$	Minimum
$\phi - \arccos\left(\frac{\Upsilon_r}{-2\Upsilon}\right)$	$\alpha - \arccos\left(\frac{\Upsilon_r^2}{2\Upsilon^2} - 1\right)$	Minimum

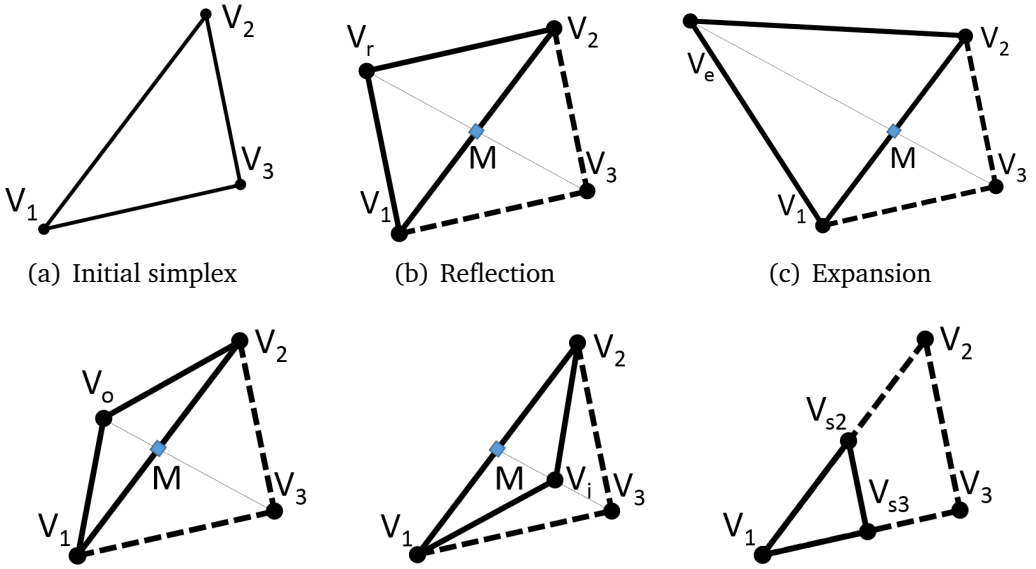

(a) Initial simplex (b) Reflection (c) Expansion

(d) Outer Contraction (e) Inner Contraction (f) Shrink

Figure 6.7: Simplex transformations for a two-dimensional initial simplex with vertices V_1 to V_{n+1}.

simplex is a type of geometric object with flat sides, which can be understood as being a generalization of a triangle extended to n-dimensions, illustrated in Fig. 6.7(a). Formally, it is the convex hull of its $n+1$ points, which forms an n-dimensional polytope. An objective function value $f(V)$ is associated with each test point. As the aim is to find the smallest value of $f(V)$, the symbol V_1 identifies the "best" vertex, V_{n+1} the "worst" and V_n the "second worst", so that $f(V_1) < \cdots < f(V_n) < f(V_{n+1})$.

The algorithm consists of a series of geometric transformations which are applied to the initial simplex to produce new test points. A transformation is accepted or rejected based on whether or not the new test vertex is better than at least one of the existing vertices. If a transformation is rejected, a different one is tested, following the rules described by Nelder and Mead. In general, the transformations aim to move the simplex away from the vertex that produces the largest function value, assuming that the desired minimum lies in this general direction. Thus, the simplex follows a "downhill" path along the objective function, taking steps towards the minimum value. The possible transformations are Reflection, Expansion, Outer Contraction, Inner Contraction and Shrink [6]. The first four are computed as

$$V_k = Z + \gamma_k(Z - T) \tag{6.39}$$

where k is a letter subscript representing each transformation: V_r denotes Re-

flection, V_e Expansion, V_o Outer Contraction, V_i Inner Contraction. The transformed point is denoted by T, and Z is the point which determines the direction of transformation. For these transformations, Z is the centroid M, calculated as the average of all vertices except the worst:

$$M = \frac{1}{n} \sum_{j=1}^{n} V_j \tag{6.40}$$

When performing a Shrink, (6.39) is applied to every vertex except the best, V_1. Thus, T will in turn take values $V_2, V_3, \ldots, V_{n+1}$ and $Z = V_1$. The transformed points are denoted in this instance as V_{s2}, V_{s3}, etc. The transformations are controlled by the γ_k parameter, which typically takes the following values: $\gamma_r = 1$, $\gamma_e = 2$, $\gamma_o = 0.5$, $\gamma_i = -0.5$, and $\gamma_s = -0.5$. The corresponding transformations for the two-dimensional case are shown in Fig. 6.7.

Each iteration of the algorithm consists of three principal steps: ordering the vertices according to their function values; calculating the centroid; and transforming the simplex. The latter is in turn divided into the various transformations, as presented in Algorithm 1. In the case of equal function values when ordering the vertices, the tie-braking rules developed by Lagarias *et al.* [6] are used, which assign higher order numbers to newer vertices.

The NMA algorithm includes termination tests which will stop the algorithm once satisfied. Typically, these are:

- Domain convergence (the simplex is sufficiently small)
- Function value (the function values are sufficiently similar or an acceptable threshold value is reached)
- Number of iterations (the number of iterations exceeds a certain value)

One of the limitations of the NMA is the difficulty of theoretically proving convergence, due to the non-constant shape of the simplex and the simple descent criteria. Few results have been published on the matter [6], prompting some authors to develop modified versions of the NMA, which are provably convergent [7–9]. The NMA has been shown to be susceptible to premature convergence on locally optimum stationary points, such as saddle points, and even on non-stationary points for certain function families [10].

The ADSC incorporates the NMA into a control law. For m actuators, the j^{th} $2m$-dimensional test point V_j consists of the α and β angular positions of the two balance masses in each actuator, so that $V_j = (\alpha_{j1}, \beta_{j1}, \alpha_{j2}, \beta_{j2}, \ldots, \alpha_{jm}, \beta_{jm})$. The parameter P in Eq. (6.10), computed from the filtered sensor output, is

Algorithm 1 NMA iteration

1: **function** NMA ITERATION(f,S)
2: Order Order vertices according to $f(V_j)$
3: Centroid Calculate centroid M
4: Reflection Calculate V_r and evaluate $f(V_r)$
5: **if** $f(V_r) < f(V_1)$ **then**
6: Go to *Expansion* ▷ V_r is best so far.
7: **else if** $f(V_1) \leq f(V_r) < f(V_n)$ **then**
8: Replace V_{n+1} with V_r. Terminate ▷ V_r is better than second worst.
9: **else if** $f(V_n) \leq f(V_r) < f(V_{n+1})$ **then**
10: Go to *Outer Contraction* ▷ V_r is better than worst.
11: **else if** $f(V_{n+1}) \leq f(V_r)$ **then**
12: Go to *Inner Contraction* ▷ V_r is worst so far.
13: Expansion Calculate V_e and evaluate $f(V_e)$
14: **if** $f(V_e) < f(V_r)$ **then**
15: Replace V_{n+1} with V_e. Terminate ▷ V_e is best so far.
16: **else if** $f(V_r) \leq f(V_e)$ **then**
17: Replace V_{n+1} with V_r. Terminate ▷ V_e is not better than V_r.
18: Outer Contraction Calculate V_o and evaluate $f(V_o)$
19: **if** $f(V_o) \leq f(V_r)$ **then**
20: Replace V_{n+1} with V_o. Terminate ▷ V_o is better than V_r.
21: **else if** $f(V_r) < f(V_o)$ **then**
22: Go to *Shrink* ▷ V_o is worse than V_r.
23: Inner Contraction Calculate V_i and evaluate $f(V_i)$
24: **if** $f(V_i) < f(V_{n+1})$ **then**
25: Replace V_{n+1} with V_i. Terminate ▷ V_i is better than worst.
26: **else if** $f(V_{n+1}) \leq f(V_i)$ **then**
27: Go to *Shrink* ▷ V_i is worst so far.
28: Shrink. Calculate V_{sj}. Terminate
29: **return** Transformed simplex S

treated as the function evaluation $f(V)$ at each test point. In the following section, the modifications introduced to the original NMA to adapt it for use in an ADSC are discussed.

6.4.2 Algorithmic Direct Search Controller

Adaptation to discrete problems

The original NMA was intended to be applied to continuous, unbounded problems, where test points can take any rational value between $-\infty$ and ∞. However, the ADSC (Algorithm 2) considers the limitations imposed by stepper motor resolution, which have a discrete number of steps per revolution.

For instance, in the actuators used in the prototype the balance masses may move in $(360/104)^\circ$ steps, producing angular positions 0° to 356.54°, which are labeled as step positions 0 to 103. The ADSC is therefore adapted to solve an integer optimization problem, in which the test points V_j are rounded so that they consist of integer step position coordinates. Thus, the vertices of the simplex in the ADSC are defined in terms of step positions as $V_J = (a_{J1}, b_{J1}, a_{J2}, b_{J2}, \ldots, a_{Jm}, b_{Jm})$, where

$$a_{Jm} = \alpha_{Jm} 104/360 \qquad\qquad b_{Jm} = \beta_{Jm} 104/360,$$

and the uppercase subscript J denotes a vertex with integer coordinates.

A consequence of this discretization is that certain simplex collapse and transformation failure mechanisms may be introduced, which are not present in continuous NMA embodiments. Simplex collapse occurs when the simplex becomes degenerate. For example, when vertices are collinear in the two-dimensional case. If this happens, the simplex can only expand or contract in $n-1$ (or fewer) dimensions. In the continuous NMA, collapse cannot occur unless the initial simplex is itself degenerate [6], although McKinnon [10] identified a case in which repeated contractions can lead to an arbitrarily narrow triangle, which approximates the degenerate case. The introduction of a rounding function in the ADSC means that McKinnon's behavior does not occur, but simplexes can instead collapse prematurely if simple rounding rules are used. This is illustrated for a two-dimensional simplex in Figs. 6.8(a) and 6.8(b), which show how the rounding to integer coordinates of V_o in an Outer Contraction and of V_{s2},V_{s3} in a Shrink, respectively, cause the resulting simplex to collapse.

The collapse of a simplex can be detected by calculating its volume, as this

Algorithm 2 Algorithmic Direct Search Controller iteration - Part 1

function ADSC ITERATION(f,S)
    Order Order vertices according to $f(V_j)$
    Centroid Calculate centroid M
    size Calculate D^2
    Reflection Calculate V_R and evaluate $f(V_R)$
    if $f(V_R) < f(V_1)$ **then**
        Go to *Expansion* ▷ V_R is best so far.
    else if $f(V_1) \leq f(V_R) < f(V_n)$ **then**
        Replace V_{n+1} with V_R. Terminate ▷ V_R is better than second worst.
    else if $f(V_n) \leq f(V_R) < f(V_{n+1})$ **and** $D^2 \geq 4n$ **then**
        Go to *Outer Contraction* ▷ V_R better than worst. Reduction allowed.
    else if $f(V_n) \leq f(V_R) < f(V_{n+1})$ **and** $D^2 < 4n$ **then**
        Replace V_{n+1} with V_R. Go to *Neighbourhood* ▷ Reduction not allowed.
    else if $f(V_{n+1}) \leq f(V_R)$ **and** $D^2 \geq 4n$ **then**
        Go to *Inner Contraction* ▷ V_R is worst so far. Reduction allowed.
    else if $f(V_{n+1}) \leq f(V_R)$**and** $D^2 < 4n$ **then**
        Go to *Neighbourhood* ▷ V_R is worst so far. Reduction not allowed.
    Expansion Calculate V_E and evaluate $f(V_E)$
    if $f(V_E) < f(V_R)$ **then**
        Replace V_{n+1} with V_E. Terminate ▷ V_E is best so far.
    else if $f(V_R) \leq f(V_E)$ **then**
        Replace V_{n+1} with V_R. Terminate ▷ V_E is not better than V_R.
    Outer Contraction Calculate V_O
    if $V_O =$(NaN,NaN) **then**
        Go to *Shrink* ▷ Outer Contraction would collapse simplex.
    else
        Evaluate $f(V_O)$
        if $f(V_O) \leq f(V_R)$ **then**
            Replace V_{n+1} with V_O. Terminate ▷ V_O is better than V_R.
        else if $f(V_R) < f(V_O)$ **then**
            Go to *Shrink* ▷ V_O is not better than V_R.
    Inner Contraction Calculate V_I
    if $V_I =$(NaN,NaN) **then**
        Go to *Shrink* ▷ Inner Contraction would collapse simplex.
    else
        Evaluate $f(V_I)$
        if $f(V_I) < f(V_{n+1})$ **then**
            Replace V_{n+1} with V_I. Terminate ▷ V_I is better than worst.
        else if $f(V_{n+1}) \leq f(V_I)$ **then**
            Go to *Shrink* ▷ V_I is worst so far.
    Shrink Calculate V_{sp*}. Terminate

Algorithm 3 Algorithmic Direct Search Controller iteration - Part 2

Neighbourhood
for $J = n, n-1, \ldots, 2, 1$ **do**
  Calculate V_{NJ} and evaluate $f(V_{NJ})$ ▷ For all vertices except worst.
  if $f(V_{NJ}) < f(V_1)$ **then**
    Go to *Find* ▷ V_{NJ} is best so far.
  else if $f(V_1) \leq f(V_{NJ}) < f(V_{n+1})$ **then**
    Replace V_{n+1} with V_{NJ}. Terminate ▷ V_{NJ} is better than worst.
  else if $f(V_{n+1}) \leq f(V_{NJ})$ **and** $J = 1$ **then**
    Terminate ▷ Neighbourhood transformations do not improve S.
Find Calculate V_{FJ} and evaluate $f(V_{FJ})$
if $f(V_{FJ}) < f(V_{NJ})$ **then**
  Replace V_{n+1} with V_{FJ}. ▷ V_{FJ} is best so far.
else if $f(V_{NJ}) \leq f(V_{FJ})$ **then**
  Replace V_{n+1} with V_{NJ}. Terminate ▷ V_{FJ} is not better than V_{NJ}.
return Transformed simplex S

Algorithm 4 Simplex collapse test

function SCT(S)
  Calculate $X = [(V_2 - V_1), (V_3 - V_1), \ldots, (V_{n+1} - V_1)]$
  if $\frac{1}{n!}|\det X| < C$ **then**
    $Collapse \leftarrow$**true**
  else
    $Collapse \leftarrow$**false**
  return $Collapse$

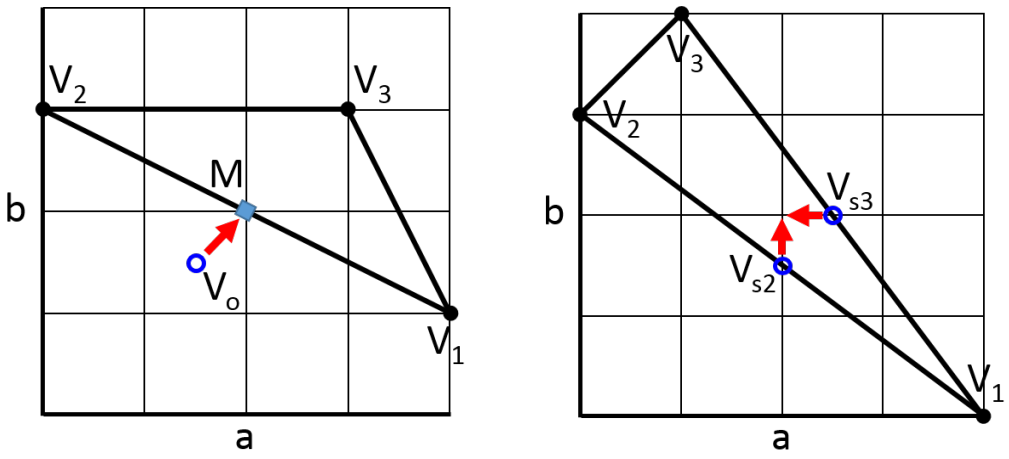

(a) Due to Outer Contraction (b) Due to Shrink

Figure 6.8: Examples of simplex collapse caused by rounding transformation points to integer values during an Outer Contraction and a Shrink. The arrows represent the rounding action while the integer vertex values are represented by the grid lines.

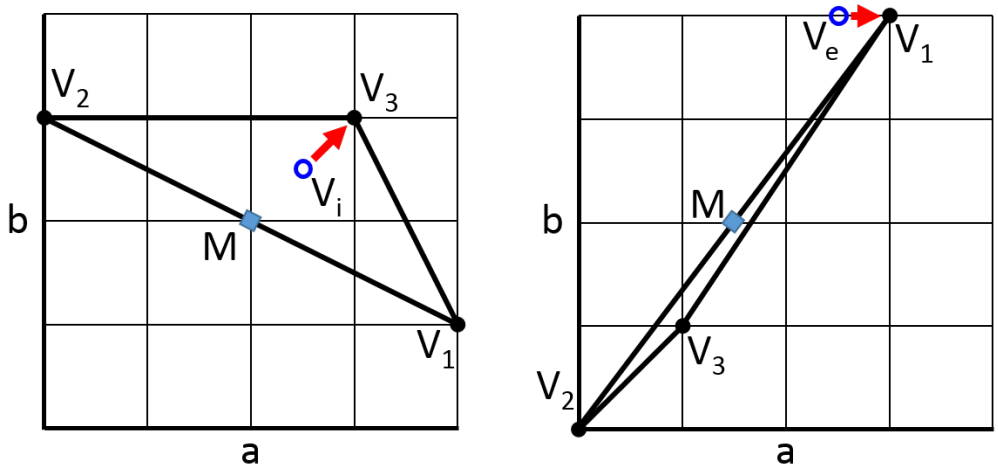

(a) Due to Inner Contraction (b) Due to Expansion

Figure 6.9: Examples of transformation failure caused by rounding transformation points to integer values during an Inner Contraction and an Expansion. The arrows represent the rounding action while the integer vertex values are represented by the grid lines.

will be zero for a degenerate simplex. Thus, collapse occurs if

$$\frac{1}{n!}\,|\det[x_2, x_3, \ldots, x_{n+1}]| < C \tag{6.41}$$

where $x_n = (V_n - V_1)$ denotes the side vector of a simplex and C is a limiting constant associated with floating point arithmetic precision. This test is carried out by Algorithm 4, which is executed after each transformation is calculated, identifying any resulting collapse.

Transformation failure occurs when a new test point is coincident with an existing vertex or another test point previously evaluated in the same iteration. The transformation fails because its execution cannot yield new information. Figs. 6.9(a) and 6.9(b) illustrate transformation failure occurring for Inner Contraction and Expansion of two-dimensional simplexes. The test points resulting from rounding the non-integer vertices, V_i and V_e respectively, coincide with existing points V_3 and V_1.

In order to adapt the ADSC to a discrete problem, Nelder and Mead's original transformation computations from Eq. (6.39) are modified by using a Transformation Point Selection (TPS) algorithm, shown in Algorithm 5. This finds a transformation point with integer coordinates which is as close to the theoretical non-integer point as possible, while avoiding simplex collapse and transformation failure.

The computation of the integer point begins with the corresponding theoret-

Algorithm 5 Transformation point selection

function TPS($Z, T, \gamma, \{S, V_R\}$)
  Compute theoretical point V_k
  Construct O with P_1, P_2, ..., P_{2^n} ▷ Closest points to V_k.
  Construct U with $P_j \notin \{S, V_R\}$ ▷ Non-failing P_j.
  for $j = 1, 2, \ldots, |U|$ **do** ▷ Repeat for each member P_j in U.
    if $SCT(\{V_1, V_2, \ldots, V_n, P_j\}) =$ **false then**
      $P_j \cup NC$ ▷ P_j included in NC if it does not collapse the simplex.
  if $NC = \varnothing$ **then**
    Compute $V_K \leftarrow$ (NaN,NaN) ▷ All P_j collapse the simplex.
  else
    for $l = 1, 2, \ldots, |NC|$ **do** ▷ Repeat for each member P_l in NC.
      Calculate $d_{rl} = ||V_k - P_l||$
    Construct MD with $P_p = \arg\min_{P_l} (d_{rl})$ ▷ Select points with smallest d_{rl}.
    if $|MD| > 1$ **then** ▷ Multiple P_p have smallest d_{rl}.
      for $p = 1, 2, \ldots, |MD|$ **do**
        Calculate $d_{ZP} = ||Z - P_p||$
      Compute $V_K = \arg\min_{P_p} (d_{ZP})$ ▷ Select point with smallest d_{ZP}.
    else ▷ Single P_p has smallest d_{rl}.
      Compute V_K as the only member $P_p \in MD$
  return V_K

ical point, $V_k = (a, b)$, which may have non-integer coordinates. The closest integer points to V_k, at most 2^n, form a set of potential points, $O = \{P_1, P_2, \ldots, P_{2^n}\}$ and are obtained by applying either a floor or ceiling function (denoted by symbols $\lfloor\ \rfloor$ and $\lceil\ \rceil$, respectively) to each of the coordinates in V_k. For example, in the two-dimensional case the potential points are

$$P_1 = (\lfloor a \rfloor, \lfloor b \rfloor), \quad P_2 = (\lfloor a \rfloor, \lceil b \rceil),$$
$$P_3 = (\lceil a \rceil, \lceil b \rceil), \quad P_4 = (\lceil a \rceil, \lfloor b \rfloor)$$

The algorithm then discards any potential point which is coincident with V_R or existing vertices in S, preventing transformation failure. Subset $U = O \setminus \{S, V_R\}$ is defined accordingly. The remaining potential points are tested for collapse by applying Algorithm 4 to each hypothetical simplex resulting from the transformation. A subset, NC, is formed by those potential points, $P_j \in U$, which do not lead to collapse. A final subset, MD, is formed with the potential points, $P_l \in NC$, that minimise the rounding distance, $d_{rl} = ||V_k - P_l||$. These points are closest to the theoretical point, V_k, and hence keep the size of the rounded and theoretical simplexes as similar as possible. The set MD may have

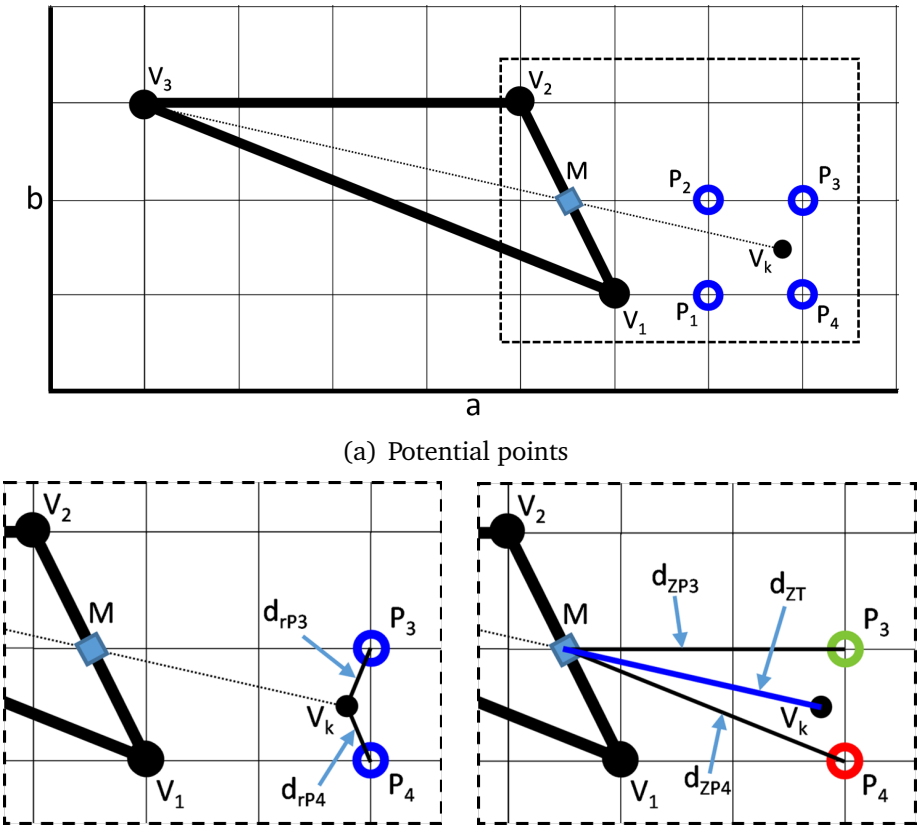

(a) Potential points

(b) Points with smallest rounding distance

(c) Final tie-break

Figure 6.10: Graphical illustration of TPS algorithm for a simplex undergoing an Outer Contraction.

more than one member, in which case a tie-breaking rule is applied. Here, the distances $d_{ZP} = ||Z - P_p||$ between the p remaining potential points and the direction point Z are calculated. The point which minimises $|d_{ZP} - d_{ZT}|$, with $d_{ZT} = ||\gamma_k(Z - T)||$, is chosen as the transformation point, as it ensures that the change in size between the current and new simplexes is also kept as similar as possible to the non-integer case. Figure 6.10 illustrates the application of the TPS algorithm to a two-dimensional simplex undergoing an Outer Contraction. The potential points calculated from V_k are shown in Fig. 6.10(a). As none of these lead to simplex collapse or transformation failure, $U = O$. The rounding distances, d_{rl}, are then calculated, and subset NC is formed with points P_3 and P_4, which share the smallest d_{rl} (Fig. 6.10(b)). The final tie-break, shown in Fig. 6.10(c) selects P_3, as this is the point which minimises $|d_{ZP} - d_{ZT}|$.

The Reflection, Expansion, Outer Contraction and Inner Contraction transformations for the ADSC are therefore defined as

$$V_R = \text{TPS}(M, V_3, \gamma_r, \{S\}) \tag{6.42}$$

$$V_E = \mathrm{TPS}(M, V_3, \gamma_e, \{S, V_R\}) \tag{6.43}$$

$$V_O = \mathrm{TPS}(M, V_3, \gamma_o, \{S, V_R\}) \tag{6.44}$$

$$V_I = \mathrm{TPS}(M, V_3, \gamma_i, \{S, V_R\}) \tag{6.45}$$

with $\gamma_r = 1$, $\gamma_e = 2$, $\gamma_o = 0.5$, and $\gamma_i = -0.5$. When performing certain Contraction transformations it is possible for all the potential points to produce a degenerate simplex. In this case, the test point is computed as $V_K =$(NaN,NaN), where the data type NaN (Not a Number) is used to represent an empty value. Lines 24 and 33 are included in Algorithm 2 so that this scenario is identified and a Shrink is performed instead.

In Shrink transformations, when there is unit separation between a given vertex, say V_n, and the best vertex V_1, it is possible for no acceptable transformation points to be available. To remedy this, a partial shrink transformation is allowed in the ADSC, such that $V_{sn} = V_n$. This option, considered by Zhao *et al.* [11], will yield an acceptable transformation if at least one of the shrunk vertices is transformed to a new test point. It is therefore convenient, when performing a Shrink, to re-order the vertices in terms of their distances from the best vertex (V_1), so that $0 < ||V_{2*} - V_1|| < \cdots < ||V_{(n+1)*} - V_1||$. The asterisk subscript ($_{n*}$) indicates a vertex ordered using this rule. Thus, the shrinking simplex will be $S = \{V_1, V_{2*}, \ldots, V_{(n+1)*}\}$. With this notation, performing the shrink operation will yield transformed simplex $S_s = \{V_1, V_{s2*}, \ldots, V_{s(n+1)*}\}$. The Shrink operation is redefined as

$$V_{sp*} = \mathrm{TPS}(V_1, V_{p*}, \gamma_s, \{W_p, \Omega_p\}), \quad p = 2, \ldots, n, n+1 \tag{6.46}$$

with $\gamma_s = -0.5$. Each shrunk vertex uses a different set of existing vertices $\{W_p, \Omega_p\}$ to test transformation failure and simplex collapse, where

$$W_p = \{V_1, V_{s2*}, \ldots, V_{s(p-1)*}\} \tag{6.47}$$

$$\Omega_p = \{V_{(p+1)*}, V_{(p+2)*}, \ldots, V_{sn*}\} \cup V_{(n+1)*} \tag{6.48}$$

These sets describe the simplex when shrinking each vertex. The union $\cup V_{(n+1)*}$ in Ω_p ensures that the furthest point $V_{(n+1)*}$ must be transformed to a new point which satisfies $V_{s(n+1)*} \neq V_{(n+1)*}$, guaranteeing at least a partial shrink. An example for the four-dimensional case is provided in Table 6.2.

The discrete nature of the optimization problem means that there exists a minimum simplex size. For small simplexes, the rounding error associated with the TPS algorithm may be significant in comparison with the transformation dis-

Table 6.2: Sets of existing vertices for TPS when performing a Shrink on a four-dimensional simplex

$\boldsymbol{p}$	$\boldsymbol{W}_p$	$\boldsymbol{\Omega}_p$
2	V_1	$\{V_{3*}, V_{4*}, V_{5*}\}$
3	$\{V_1, V_{s2*}\}$	$\{V_{4*}, V_{5*}\}$
4	$\{V_1, V_{s2*}, V_{s3*}\}$	V_{5*}
5	$\{V_1, V_{s2*}, V_{s3*}, V_{s4*}\}$	V_{5*}

tance $\gamma_k(Z - T)$ in Eq. (6.39), which limits the similarity between the rounded and theoretical simplexes. In addition, the resolution of sensors and actuators may not be sufficient to clearly distinguish the objective function value of adjacent points, leading to a series of transformations which provide little real reduction of rotor vibration. Thus, a user-defined minimum size restriction is added to the ADSC.

To establish the size of a given simplex, the concept of an axis-aligned minimum bounding box (AAMBB) is used. This is the smallest n-dimensional box which contains all the points in a set and has its edges aligned with the coordinate axes. Multiple different simplexes can be formed on the same AAMBB, but will all enclose a similarly sized region of the search space. Thus, the AAMBB can be used to compare different simplexes based on how disperse their vertices are. A large AAMBB indicates widely dispersed vertices and hence a large search space in which test points are substantially different from each other. A small AAMBB, on the other hand, signifies that the vertices are close together, usually implying that the simplex is close to convergence on a stationary point. An AAMBB is defined by the length of its sides, calculated for each coordinate of V_J as

$$\left.\begin{aligned} \mu_{ai} &= \max_J\ (a_{Ji}) - \min_J\ (a_{Ji}) \\ \mu_{bi} &= \max_J\ (b_{Ji}) - \min_J\ (b_{Ji}) \end{aligned}\right\}, \quad \begin{aligned} J &= 1, \ldots, n, n+1 \\ i &= 1, \ldots, m \end{aligned} \tag{6.49}$$

The square of the axial diagonal of an AAMBB, D^2, can be used as a single-valued metric of its size, and is given by

$$D^2 = \sum_{i=1}^{m} \left(\mu_{ai}^2 + \mu_{bi}^2\right) \tag{6.50}$$

For example, a simplex with coordinates $(6, 2)$, $(3, 7)$, and $(4, 3)$ is contained within a 3×5 AAMBB with $D^2 = 34$. In the prototype, size-reducing trans-

formations (Outer Contraction, Inner Contraction and Shrink) are banned on simplexes with $D^2 < 4n$. This defines a limiting box with side length of 2, which is adequate to prevent inefficient function evaluations being carried out on small simplexes.

Premature convergence may occur at saddle points. This is because the NMA's underlying assumption that the function minimum lies away from the worst point, along the line formed by V_{n+1} and the centroid M, does not necessarily hold at saddle points. In the two-dimensional case, if V_1 and V_2 are approximately aligned with the concave region of the saddle point, then V_3 will be reflected from one side of the convex "valley" to the other with no improvement of the function value. Consequently, the simplex enters a repeating pattern of contractions, eventually leading to collapse or premature convergence. This is illustrated in Fig. 6.11(a), which shows a detailed view of the objective function of Fig. 6.6, with a starting simplex $S = \{V_1, V_2, V_3\}$ which is close to saddle point $(\phi, \phi + \pi)$. The diameter of the vertex markers indicates qualitatively the function value at each test point. The starting simplex undergoes two Inner Contraction transformations ($V_I(1)$ and $V_I(2)$) and reaches the minimum simplex size. If the algorithm were to terminate here, it would have converged to a saddle point.

Prevention of premature convergence at saddle points

To prevent this, two new transformations are introduced, namely Neighbourhood and Find. These are used to explore the Neighbourhood of a stationary point once the minimum size limit is reached. The Neighbourhood transformation consists of the sequential application of the ADSC Reflection on vertices which are not the worst. The transformation iterates following a descending order from second-worst to best vertices, until a better test point is found or until it has been applied to every vertex. If a better test point is found, the Find transformation is applied, which is simply the Expansion transformation applied to the relevant vertex. Thus, the Neighbourhood and Find transformations are defined as

$$V_{NJ} = \mathrm{TPS}(M_J, V_J, \gamma_r, \{S\}), \quad J = n, n-1, \ldots, 1 \tag{6.51}$$

$$V_{FJ} = \mathrm{TPS}(M_J, V_J, \gamma_e, \{S, V_{NJ}\}) \tag{6.52}$$

with

$$M_J = \frac{1}{n}\left(\sum_{I}^{n+1}(V_I) - V_J\right)$$

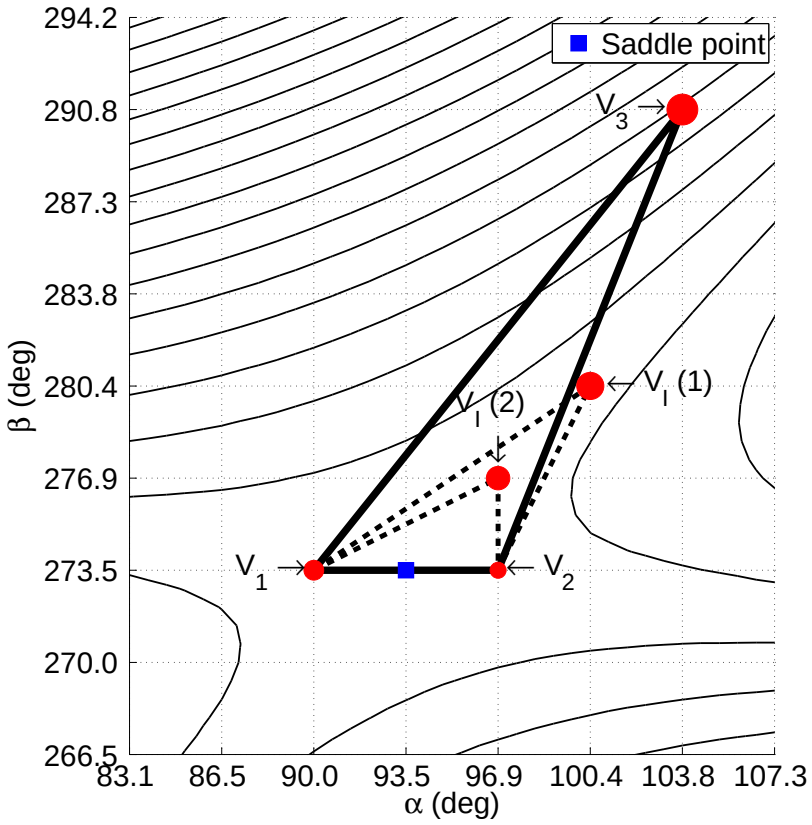

(a) Premature convergence mechanism

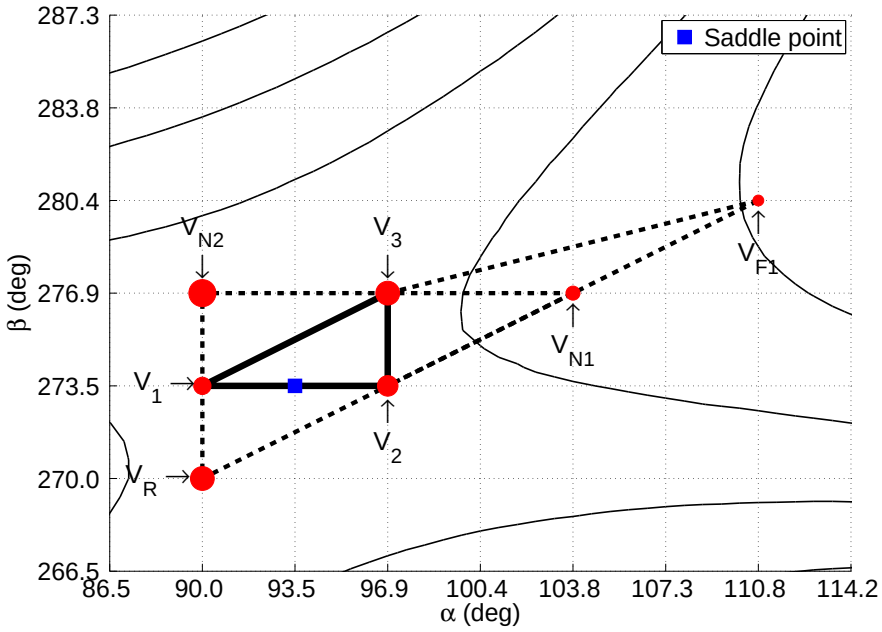

(b) Preventing premature convergence

Figure 6.11: Typical saddle point premature convergence mechanism, and its prevention using Neighbourhood and Find transformations.

Figure 6.11(b) illustrates how these transformations prevent premature convergence at a saddle point. As $f(V_R) \geq f(V_3)$, the Reflection would be rejected, with no further transformations permitted. However, the Neighbourhood transformation allows V_{N2} and V_{N1} to be tested. As the latter yields a better test point, the Find transformation is applied to explore V_{F1}, continuing the search towards the global minimum.

The Neighbourhood and Find transformations are only applied if the simplex has reached the minimum allowable size, and hence act as a domain convergence termination test. They will necessarily be applied last if a stationary point is reached. If it is a saddle point, premature convergence will be avoided, and, if it is a minimum, the Neighbourhood transformation will not yield an improving test point and the algorithm will terminate.

Actuator control

The original NMA is intended to be applied on unbounded problems, where test points can take values between $-\infty$ and ∞. Although the mass-balancers can rotate indefinitely, step demands in excess of a full revolution (104 steps) may lead to undesirable vibration during the position change. One option to prevent this is to consider the objective function as bounded. However, this can introduce undesirable simplex behavior, particularly if optima are located at the boundary [4]. A better solution is to treat the objective function as unbounded, but bound the allowable motion of the actuator masses to a single revolution. This can be achieved by interpreting the new actuator position demand V_w from the ADSC output, V_{ADSC}:

$$V_w = \mathrm{sgn}(V_{ADSC})(|V_{ADSC}| \bmod 103) \tag{6.53}$$

To further minimise rotor vibration during the movement of the mass balancers, the step demand s given to the actuators is calculated from V_w and the current position V_α to ensure minimum motion, hence

$$s = \begin{cases} V_w - V_\alpha & \text{if } |(V_w - V_\alpha)| \leq 52 \\ V_w - V_\alpha - \mathrm{sgn}(V_{wa} - V_\alpha)103 & \text{if } |(V_w - V_\alpha)| > 52 \end{cases} \tag{6.54}$$

With this technique, the spirit of the original, unbounded transformations proposed by Nelder and Mead can be maintained when calculating a new simplex, without detriment to the performance of the controller. The resulting block diagram for the ADSC controller is given in Fig. 6.12.

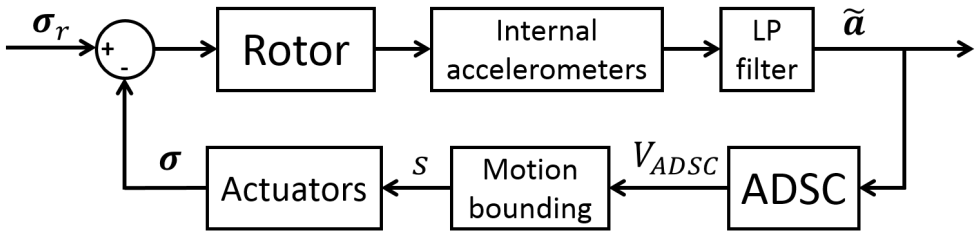

Figure 6.12: Block diagram of ADSC-based active vibration control system.

6.4.3 Simulated application of ADSC

The application of the ADSC to rotor vibration control was firstly simulated for the two-dimensional, single accelerometer, single mass-balancer case. The accelerometer output was modelled as in Eq. (6.38), with arbitrary values of Υ_r and ϕ and assuming $Q = 1$ for simplicity. The ADSC algorithm was then applied to an arbitrary starting simplex to find the position of the actuator masses which minimises F. Figure 6.13 shows the evolution of the simplexes, starting from step positions $S = \{(94, 42), (89, 42), (89, 47)\}$, which correspond to angular positions $(325.4°, 145.4°)$, $(308.1°, 145.4°)$, and $(308.1°, 162.7°)$, respectively. The controller finds the function minimum at $(94, 64)$, that is, $(325.4°, 221.5°)$. Figure 6.14 shows the acceleration of the rotor center throughout the iterations. It is normalised with respect to the neutral position acceleration, for which the actuator has coordinates $(\alpha, \alpha + 180°)$, with arbitrary α. As the counter-unbalance contribution is 0 in this case, the uncontrolled reference acceleration is obtained. The first three acceleration values correspond to the initial simplex vertices. A substantial reduction in acceleration is achieved within the first few iterations of the ADSC algorithm. Beyond that point, a relatively large number of steps are taken which only provide small improvements in the vibration state. The nature of the heuristic method requires the actuator to test positions which may produce increased vibration with respect to the best known case, as observed at test points 14, 17 or 19. Despite none of these points being accepted, the rotor will nonetheless not reach a steady, minimised vibration state until the algorithm terminates. The last three tested points correspond to Neighbourhood transformations being performed, and as no new points are accepted, the algorithm terminates.

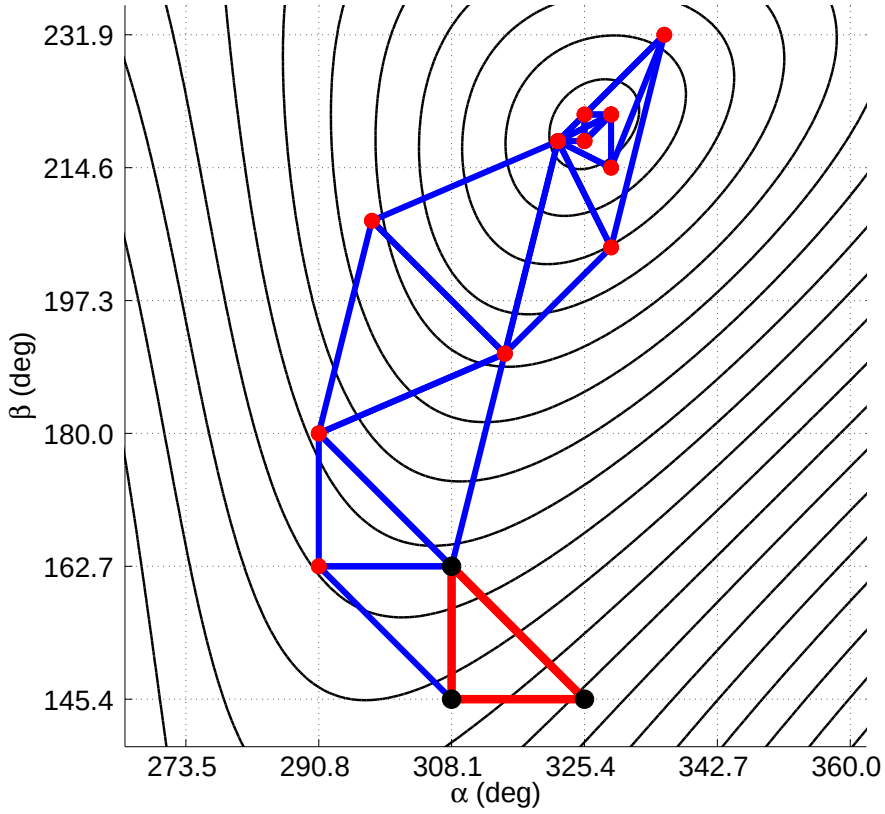

Figure 6.13: Simulation of ADSC control showing the transformations from starting simplex $(325.4°, 145.4°), (308.1°, 145.4°), (308.1°, 162.7°)$

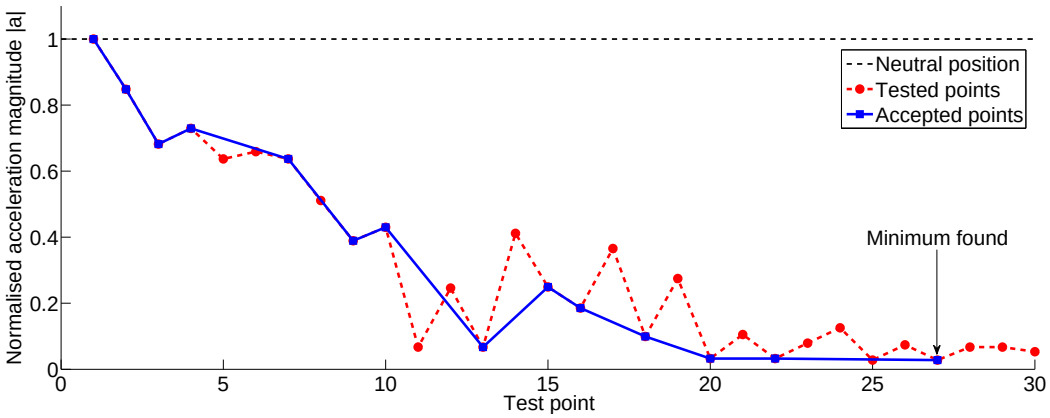

Figure 6.14: Simulated acceleration measurements during ADSC control, normalised with respect to the neutral position acceleration.

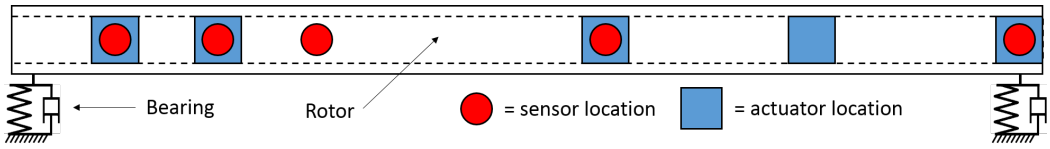

Figure 6.15: Arrangement of sensors and actuators in the multi-component simulation.

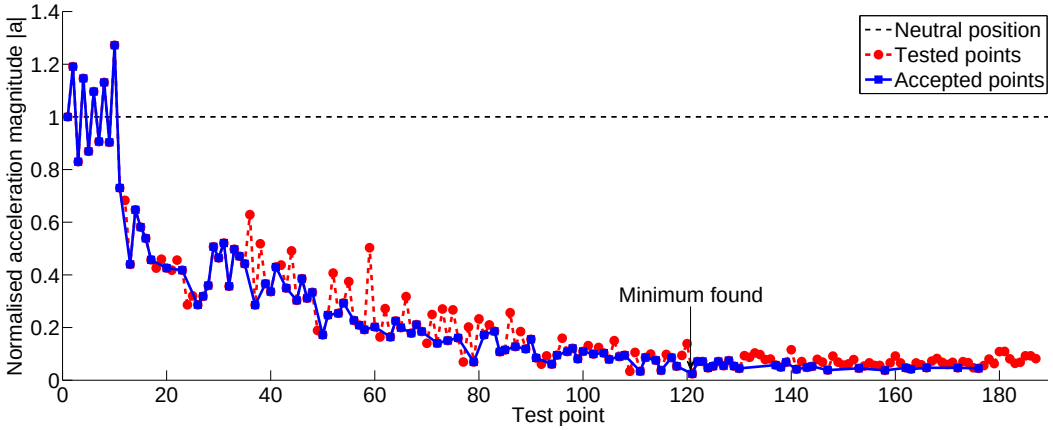

Figure 6.16: Simulated application of ADSC to a rotor with five non-collocated sensors and actuators.

The ADSC algorithm was also applied in simulation to the multi-actuator, multi-sensor case. In this instance, five actuators and sensors were assumed, arranged as in Fig. 6.15. Not all sensors and actuators are collocated. Figure 6.16 presents the corresponding simulated rotor acceleration. As before, the first $n+1$ points define the starting simplex and a considerable vibration reduction is achieved within the first few iterations. However, the multi-sensor/actuator case requires a larger number of test points to terminate the algorithm. This is characteristic of the NMA, which becomes less efficient at higher dimensions [12]. As the evaluation of a test point requires a finite amount of time, a large number of ADSC iterations may translate into an undesirably large convergence time. To alleviate this, Gao and Han [13] have suggested the use of adaptive transformation coefficients, which are conditioned by the dimension of the problem. The extension of this concept to the discrete problem addressed by the ADSC is left for future research.

6.4.4 Experimental implementation of the ADSC

The ADSC was applied to the control of the prototype system, constituting a two-dimensional problem, while operating at a steady speed of $1,700$ rpm. The initial simplex was formed starting from an arbitrary actuator position and eval-

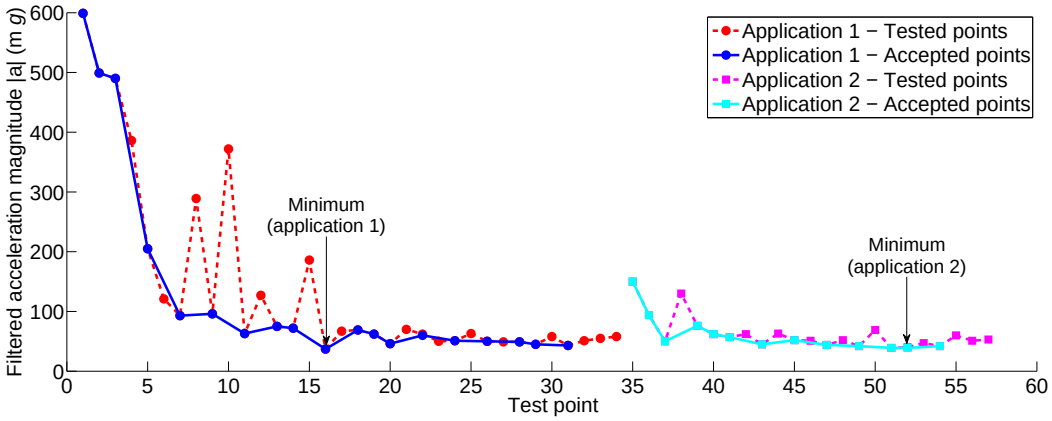

Figure 6.17: Measured rotor acceleration during two applications of ADSC control.

uating vertices (a_0, b_0), $(a_0 + 10, b_0 - 10)$ and $(a_0 + 10, b_0 - 20)$. Two applications of the ADSC were performed sequentially to test the repeatability of the control under constant operating conditions. The starting simplex for the second application was formed from the final actuator position obtained from the first, with vertices $(a_{f1} + 10, b_{f1} - 20)$, $(a_{f1} + 10, b_{f1} - 10)$ and (a_{f1}, b_{f1}). The measured rotor acceleration is presented in Fig. 6.17. The improvement in the rotor vibration state achieved through the first ADSC application is confirmed by the frequency response data recorded by the stator-mounted eddy current displacement sensors, Fig. 6.18. Further detail can be inferred from the diminishing whirl orbits observed when X and Y plane data are plotted together. Fig. 6.19 shows the orbits for the first seven test points, measured over 2 seconds.

In both applications the ADSC reaches similarly reduced acceleration, demonstrating that each cycle of the controller can find a minimising actuator position irrespective of the starting point. The implication is that repeated applications of ADSC can be used to maintain a minimised vibration state, even in systems with changing operating conditions, as each new application of ADSC is treated as an independent optimization problem.

Once the rotor acceleration signals are reduced beyond approximately 100 mg, measurement uncertainty begins to limit the performance of the controller. Small fluctuations in the operating speed (approximately $\pm 1\%$) affect the measured acceleration, and the resulting uncertainty may be larger than the acceleration change produced by an actuator step. In addition, the finite resolution of the accelerometers limits the smallest acceleration difference that can be measured between two test points. These combined effects mean that a test point worse than the existing simplex vertices may be evaluated as being better, preventing the simplex from advancing towards the function minimium. As

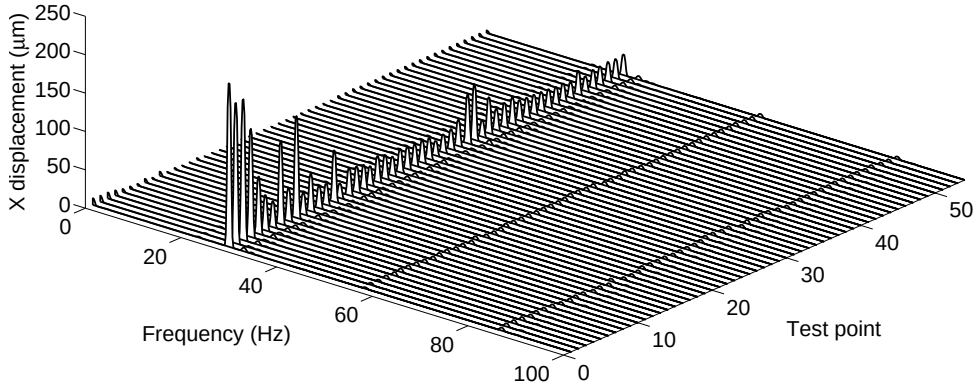

(a) X plane

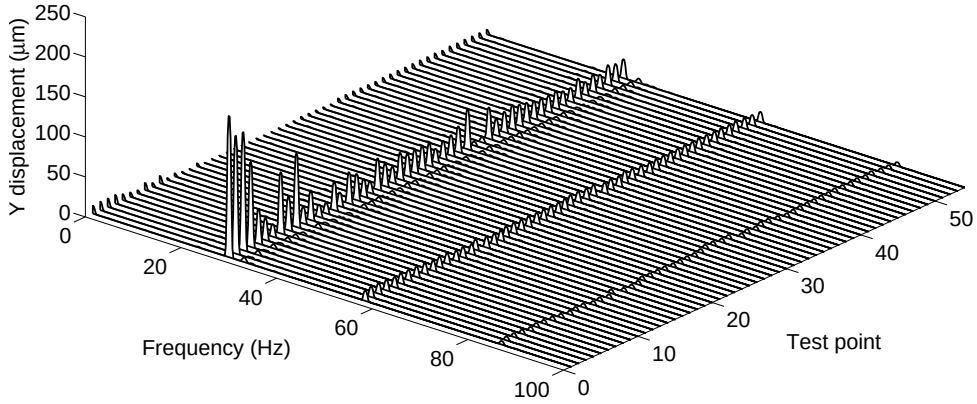

(b) Y plane

Figure 6.18: Frequency response of the rotor in the inertial reference frame as measured by eddy current displacement sensors during the first ADSC application.

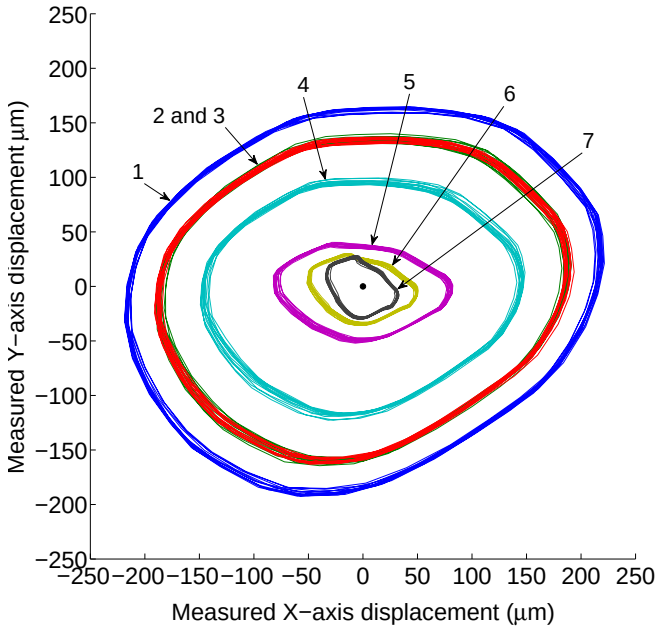

Figure 6.19: Rotor whirl orbits measured by eddy current displacement sensors for the first seven test points evaluated by the ADSC.

this behavior is significant only when close to stationary points, it does not affect the overall capability of the ADSC to improve the rotor's vibration state, but does impose a lower bound on the minimum achievable acceleration [14]. Although some techniques to alleviate the effect of noise and uncertainty have been suggested [4, 15], the nature of the control problem does not require a highly accurate solution, and hence the additional computational effort associated with the techniques is not justified here. However, an analysis of the sensitivity of $\boldsymbol{a}$ to fluctuations in ω can be conducted to determine under what conditions the effect may be most detrimental. The accelerometer signal given by Eq. (6.37) can be linearised around an operating speed ω_o, yielding

$$a = \left[H_{rr}(\omega_o) + \left. \frac{\partial H_{rr}(\omega)}{\partial \omega} \right|_{\omega_o} (\omega - \omega_o) \right] \left(\Upsilon_r \mathrm{e}^{\mathrm{j}\phi} + \Upsilon \left(\mathrm{e}^{\mathrm{j}\alpha} + \mathrm{e}^{\mathrm{j}\beta} \right) \right) \tag{6.55}$$

From Eq. (6.9),

$$H_{rr} = \frac{-\omega^4}{\omega^2 (G_{rr} - M_{rr}) + \mathrm{j}\omega C_{rr} + K_{rr}} \tag{6.56}$$

A qualitative understanding of the phenomenon can be derived by considering the simplified case of a lightly damped rotor with negligible gyroscopic moments. Hence, disregarding terms C_{rr} and G_{rr},

$$H_{rr}(\omega_o) = \frac{-\omega_o^4}{-\omega_o^2 M_{rr} + K_{rr}} \tag{6.57}$$

and

$$\left. \frac{\partial H_{rr}(\omega)}{\partial \omega} \right|_{\omega_o} = \frac{2H_{rr}(\omega_o)}{\omega_o} \left[1 + \frac{K_{rr}}{-\omega_o^2 M_{rr} + K_{rr}} \right] \tag{6.58}$$

If $\chi_o = \omega_o / \omega_c$ denotes the critical speed ratio with $\omega_c = \sqrt{K_{rr}/M_{rr}}$,

$$\left. \frac{\partial H_{rr}(\omega)}{\partial \omega} \right|_{\omega_o} = \frac{2H_{rr}(\omega_o)}{\omega_o} \left[1 + \frac{1}{1 - \chi_o^2} \right] \tag{6.59}$$

It follows that

$$a = \left[H_{rr}(\omega_o) + \frac{2H_{rr}(\omega_o)}{\omega_o} \left[1 + \frac{1}{1 - \chi_o^2} \right] (\omega - \omega_o) \right] \left(\Upsilon_r \mathrm{e}^{\mathrm{j}\phi} + \Upsilon \left(\mathrm{e}^{\mathrm{j}\alpha} + \mathrm{e}^{\mathrm{j}\beta} \right) \right) \tag{6.60}$$

Using the notation a_o to indicate the acceleration at the operating point speed ω_o, Eq. (6.55) becomes

$$a = \left[1 + 2 \left[1 + \frac{1}{1 - \chi_o^2} \right] \left(\frac{\omega}{\omega_o} - 1 \right) \right] a_o \tag{6.61}$$

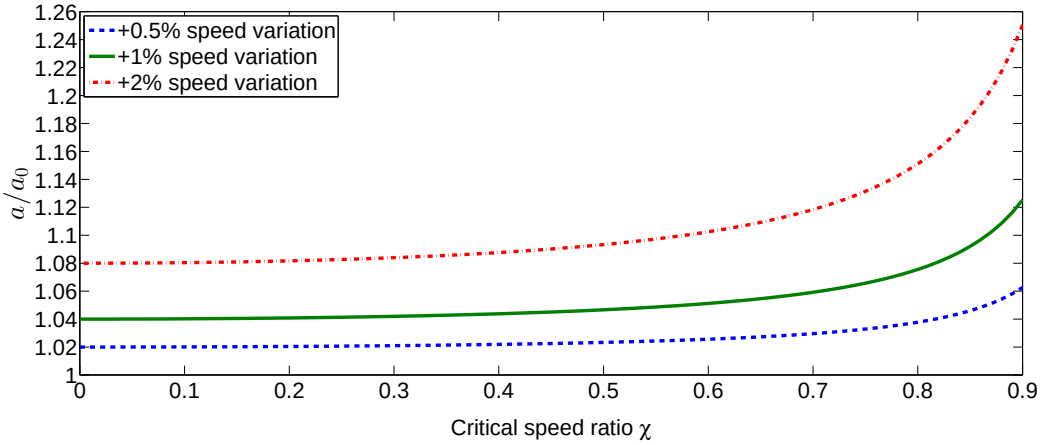

Figure 6.20: Estimated variation in rotor acceleration as a result of operating speed fluctuations in a simplified rotor model.

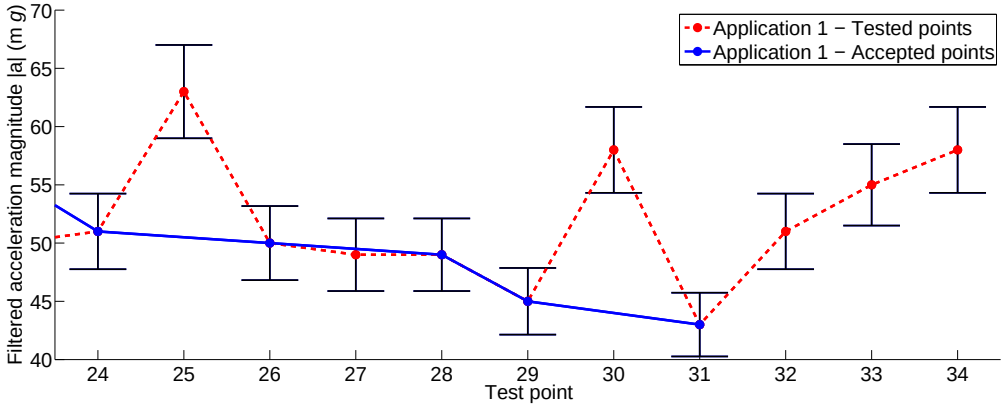

Figure 6.21: Detailed view of measured rotor acceleration from test points 24 to 34, including error bars associated with a $\pm 1\%$ rotational speed fluctuation.

The function a/a_o is presented in Fig. 6.20, and shows the increase in measured acceleration when the true rotational speed is 0.5%, 1% and 2% greater than the intended operating point. It becomes evident that the acceleration measurement can be especially sensitive to operating speed fluctuations when operating close to the critical frequency.

For the prototype operating at $1,700$ rpm, $\chi_o \approx 0.74$. If the speed fluctuations are $\pm 1\%$, then $a/a_o = 1 \pm 0.0636$ and so the acceleration error will be $\pm 6.36\%$. This uncertainty is represented as error bars in Fig. 6.21, which shows a detailed view of the experimental results for test points 24 to 34. The difference in acceleration between test points 24 and 25 is larger than the error, and so the algorithm can establish that the latter produces a worse vibration state. However, the differences between points 26 and 28 are smaller than the uncertainty, and hence the algorithm may perform incorrect transformations, which ultimately limits the attainable vibration reduction.

6.5 Conclusions

A review of existing control methods suitable for use in active rotors was undertaken. It was concluded that the approximation of the system transfer function, via either estimation or modelling, necessarily requires *a priori* knowledge of the controlled system. This implies a degree of human interaction which would be impractical in many rotating machine applications. Thus, the use of these control techniques would limit the general implementability of the active control system. Therefore, a non a priori controller was developed in order to maximise the versatility of active rotor topologies.

The chosen control objective was the minimisation of unbalance-induced vibration. A model-based controller was first applied in order to obtain a better understanding of the effect of using rotor-mounted sensors and actuators in a control system. The method relies on a finite element model of the rotor, and was validated in simulation. A key finding is that the rotor-mounted nature of the control system enables vibration reduction to be achieved without high-frequency control signals, reducing the computational complexity of the system and the design requirements imposed on its constituent devices.

The *non a priori* controller designed, referred to as Algorithmic Direct Search Controller, is based on the derivative-free Nelder-Mead optimisation technique. This enables it to perform a structured and heuristic search of the function space, seeking an optimum actuator position which minimises the rotor vibration. In order to adapt the original algorithm for use as a control law, it was extensively modified to solve an integer optimisation technique. Further, functionality was added to prevent premature convergence at non-minimising stationary points and to minimise the actuator motion for enhanced vibration during demand execution. The method was tested in simulation for the single and multiple sensor/actuator cases. The ADSC was also successfully applied to the active rotor prototype, achieving substantial vibration reduction.

All in all, the use of the ADSC enables control to take place without *a priori* knowledge of the rotor system. This provides active rotors with improved robustness in the face of uncertainty. Further, it allows the control to be fully stator-independent, which introduces the enticing possibility of retrofitting active shaft rotors into a wide array of existing rotating machines. In this manner, performance improvements could be gained without having to adapt and validate computer models for each machine, and without extensive modification of the stator design. Thus, the *non a priori* controller developed contributes towards making active rotors a more generally implementable technology.

6.6 Summary

- Existing *a priori* control methods may limit the general implementability of active vibration control technology.
- Model-based control was applied in simulation to study the implications of using rotor-mounted control systems.
- The Algorithmic Direct Search Controller (ADSC), a *non a priori* method, was developed to improve the autonomy of active rotors.
- The ADSC is based on the Nelder-Mead derivative-free optimisation algorithm, which was extensively modified for use as a control law.
- The ADSC was successfully applied in simulation and experimentally, achieving significant vibration reduction without *a priori* system knowledge.

References

[1] C.-W. Lee, *Vibration analysis of rotors*, vol. 21. Springer Science & Business Media, 1993.

[2] A. Abulrub, M. Sahinkaya, P. Keogh, and C. R. Burrows, "Adaptive control of active magnetic bearings to prevent rotor-bearing contact," in *ASME International Mechanical Engineering Congress and Exposition, IMECE2006*, (Chicago, Illinois), 2006.

[3] J. A. Nelder and R. Mead, "A simplex method for function minimization," *The Computer Journal*, vol. 7, no. 4, pp. 308–313, 1965.

[4] C. H. Brooks, "An introduction to amoeba." `www.cs.usfca.edu/~brooks/papers/amoeba.pdf`. Online. Accessed 11 - December - 2015.

[5] S. Singer and J. Nelder, "Nelder-Mead algorithm," *Scholarpedia*, vol. 4, no. 7, p. 2928, 2009.

[6] J. C. Lagarias, J. A. Reeds, M. H. Wright, and P. E. Wright, "Convergence properties of the Nelder-Mead simplex method in low dimensions," *SIAM J. on Optimization*, vol. 9, no. 1, pp. 112–147, 1998.

[7] A. Burmen, J. Puhan, and T. Tuma, "Grid restrained Nelder-Mead algorithm," *Computational Optimization and Applications*, vol. 34, no. 3, pp. 359–375, 2006.

[8] C. J. Price, I. D. Coope, and D. Byatt, "A convergent variant of the Nelder-Mead algorithm," *Journal of Optimization Theory and Applications*, vol. 113, no. 1, pp. 5–19, 2002.

[9] P. Tseng, "Fortified-descent simplicial search method: a general approach," *SIAM Journal on Optimization*, vol. 10, no. 1, pp. 269–288, 1999.

[10] K. I. M. McKinnon, "Convergence of the Nelder-Mead simplex method to a nonstationary point," *SIAM Journal on Optimization*, vol. 9, no. 1, pp. 148–158, 1998.

[11] Q. H. Zhao, D. Urosevi, N. Mladenovi, and P. Hansen, "A restarted and modified simplex search for unconstrained optimization," *Computers & Operations Research*, vol. 36, no. 12, pp. 3263–3271, 2009.

[12] L. Han and M. Neumann, “Effect of dimensionality on the Nelder-Mead simplex method,” *Optimization Methods & Software*, vol. 21, no. 1, pp. 1–16, 2006.

[13] F. Gao and L. Han, “Implementing the Nelder-Mead simplex algorithm with adaptive parameters,” *Computational Optimization and Applications*, vol. 51, no. 1, pp. 259–277, 2010.

[14] K. Vugrin, *On the Effects of Noise on Parameter Identification Optimization Problems*. PhD thesis, Virginia Polytechnic Institute and State University, 2005.

[15] F. H. Walters, R. Lloyd Jr, S. Morgan, and S. Deming, *Sequential Simplex optimization: a technique for improving quality and productivity in research, development, and manufacturing*. Chemometrics, CRC Press, 1991.

Chapter 7

Active rotors combined with AMBs

7.1 Introduction

In accordance with objective O7, consideration was given to the usage of active rotor designs in applications where they could provide advantages over existing technology. In particular, active rotors were studied as a means to prevent sensor/actuator non-collocation in Active Magnetic Bearings (AMBs).

This was chosen as an example application for three distinct reasons. Firstly, the inherent freedom of selecting sensor/actuator locations afforded by active rotor designs allows sensors to be collocated with the AMBs in a practical manner, eliminating the root cause of the problem. Secondly, active rotors could be implemented in conjunction with AMBs without interference between the systems, making the design feasible. As both display certain strengths and weakness with regards to active vibration control, such a design would also enable the control systems to complement each other, providing improved overall performance. Thirdly, AMB systems are used in high-performance applications where their high cost is an accepted consequence of the advantages they offer, such as flywheel energy storage [4] or reaction wheels in satellites [5]. These types of applications may be the most amenable to accommodating the increased cost associated with using an active, rather than passive, rotor. Hence, they may constitute a logical family of applications in which active rotor technology could first be introduced.

This chapter explores the implications of combining active rotors and AMBs to tackle issues arising from non-collocation. An overview of the non-collocation problem is first given, and the design proposed to overcome it is introduced. Then, the control problem associated with levitating a rotor on AMBs using only internal accelerometers is posed. Finally, the research undertaken to achieve a viable solution is reported, focusing in particular on the techniques used to mit-

igate reference frame transformation errors during the double integration of the accelerometer signals.

7.2 Tackling non-collocation with active rotors

As introduced in Chapter 2, non-collocation occurs when sensors and actuators are not located at the same plane. This generally leads to problems when high-frequency excitation of the rotor is present. In this scenario, a mode shape node may be located between the sensor and actuator, introducing a 180° phase shift between the measured and actuated plane, which negatively affects the control. Due to the bulk of conventional sensors (usually eddy current transducers) and actuators (the AMBs), and also their electromagnetic interference, it is not possible to collocate the devices. The issues associated with non-collocation are well documented, although few definitive solutions have been proposed. Genta and Carabelli [1] presented a control strategy suitable only for rigid rotors. Maslen [2] suggested the use of H_∞ and μ-synthesis control to ensure stability of the system, at the cost of performance. Kulesza [3] discussed the use of virtual collocation via a state observer, which relies on producing a sufficiently accurate computer model of the rotor. Hence, it would be beneficial to develop a system which could provide a more robust solution, suitable for a variety of rotating machines.

The proposed design is presented in Fig. 7.1, which shows a section of hollow rotor with an accelerometer mounted within and suspended on an AMB. Crucially, the sensor is collocated with the bearing. The control force produced by AMBs depends on both the electrical current in the coils and the distance between the bearing and the rotor. Hence, conventional controllers achieve system stabilisation by measuring the rotor/stator gap and controlling the electrical current. As direct displacement measurements are not available with the accelerometers, alternative approaches must be developed.

Three potential solutions are envisioned. Firstly, the existing PID control methods, widely used in AMB applications, could be exploited if displacement information could be extracted from the accelerometer signals. Secondly, new controllers could be developed which use the acceleration signal, rather than displacement, to achieve stable levitation. Finally, designs in which several sensors were combined in a single fusion scheme could also provide robust solutions. The research undertaken considered the first of these potential solutions. The others are proposed as further work in Chapter 8.

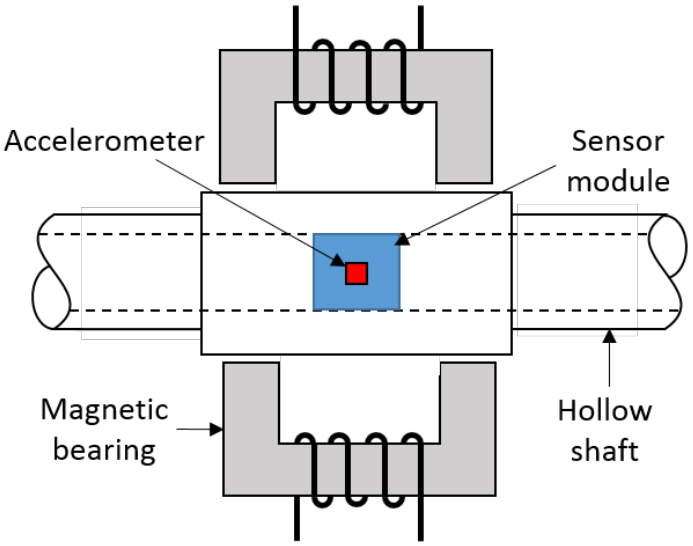

Figure 7.1: Schematic of a sensor supported on AMBs, with collocated internal sensor.

7.3 AMB control by accelerometer-derived position

In first instance, the use of internal accelerometers as the standalone sensor in the AMB system was considered. In order to take advantage of the well-defined PID control structures, it was proposed to attempt to extract the necessary displacement information from the accelerometer signals. The research therefore focused on the feasibility of obtaining displacement information sufficiently quickly and accurately to ensure system stability.

The system under study was simplified by considering a two-dimensional disc mass suspended on a single eight-pole AMB, depicted in Fig. 7.2. The disc has mass M, eccentricity e, unbalance phase φ and has a wireless bi-axial MEMS accelerometer located at its geometric centre O. The magnetic gap is h, and the clearance between the disc and touchdown bearing is c. The displacement of the disc is given by complex parameter d_{xy}. It is assumed that the bearing forces in the X and Y inertial axes are decoupled, so that $F_{xy} = F_x + \mathrm{j}F_y$. The forces depend on the bias and control currents, $i_{bxy} = i_{bx} + \mathrm{j}i_{by}$ and $i_{cxy} = i_{cx} + \mathrm{j}i_{cy}$, respectively, and are given by Maslen and Schweitzer [2] as

$$F_{xy} = k_b \left[\left(\frac{(i_{bx} + i_{cx})^2}{(h-x)^2} - \frac{(i_{bx} - i_{cx})^2}{(h+x)^2} \right) + \mathrm{j} \left(\frac{(i_{by} + i_{cy})^2}{(h-y)^2} - \frac{(i_{by} - i_{cy})^2}{(h+y)^2} \right) \right] \quad (7.1)$$

The parameter k_b is a bearing constant such that

$$k_b = \frac{\mu_0 N^2 A_h}{4} \quad (7.2)$$

where μ_0 is the permeability of free space, N is the number of coils in the magnetic winding, and A_h is the area of the magnetic gap. The control currents satisfy $i_{cx} < i_{bx}$ and $i_{cy} < i_b$.

For the system to remain stable, the force applied by the magnetic bearings must be of the correct amplitude and phase. Figure 7.3 shows an arbitrary trajectory of the disc centre as it whirls around the equilibrium position. The first accelerometer sample is assumed to be taken at a time t_0, at which point an ideal sensing system would instantaneously produce the correct disc position. The magnetic bearing is assumed to be ideal, so that the stabilising force F_0 is also applied instantaneously, once the disc position is known. In a realistic case, the processing of the accelerometer information will require a finite amount of time, so that the force F_1 will be applied at a time $t_1 > t_0$. This necessarily implies a phase lag, which, if kept within the phase margin of the system, may still produce a stable result. If the processing of the sensor information requires excessive time, however, the force F_2 will be applied at $t_2 > t_1$, which may prove to be destabilising. The maximum allowable time for processing the sensor signal, assuming no gain errors from the sensors or actuators, is therefore given by

$$\hat{t}_s = \frac{\phi_{margin}}{\omega} \tag{7.3}$$

In practice, the presence of additional, unavoidable phase and gain errors introduced in both sensors and actuators will further reduce $\hat{t}_s$. This simple example illustrates the timing limitations imposed on the signal processing applied to extract the displacement information from the acceleration data. Given the unstable nature of AMB levitation, it is evident that this conversion must be very fast in order to maintain stability. This precludes the use of frequency domain conversion techniques, such as that discussed by Han [6]. It relies on taking the Fourier transform of the signal, extracting the significant frequency components with a curve-fitting method, scaling by $-\omega^2$ and then taking the inverse Fourier transform. These procedures require a relatively large number of samples to obtain accurate results, and so the technique is best suited for post-processing recorded data, rather than real-time displacement information extraction.

An alternative technique to obtain displacement data is the double integration of the acceleration, as discussed in Chapter 5. Although the method is sensitive to error accumulation, which can rapidly lead to instability, it is also much faster and requires fewer sampling points, making it viable to perform the necessary signal processing within $\hat{t}_s$. Hence, its application to the control problem was considered, which required understanding how the various

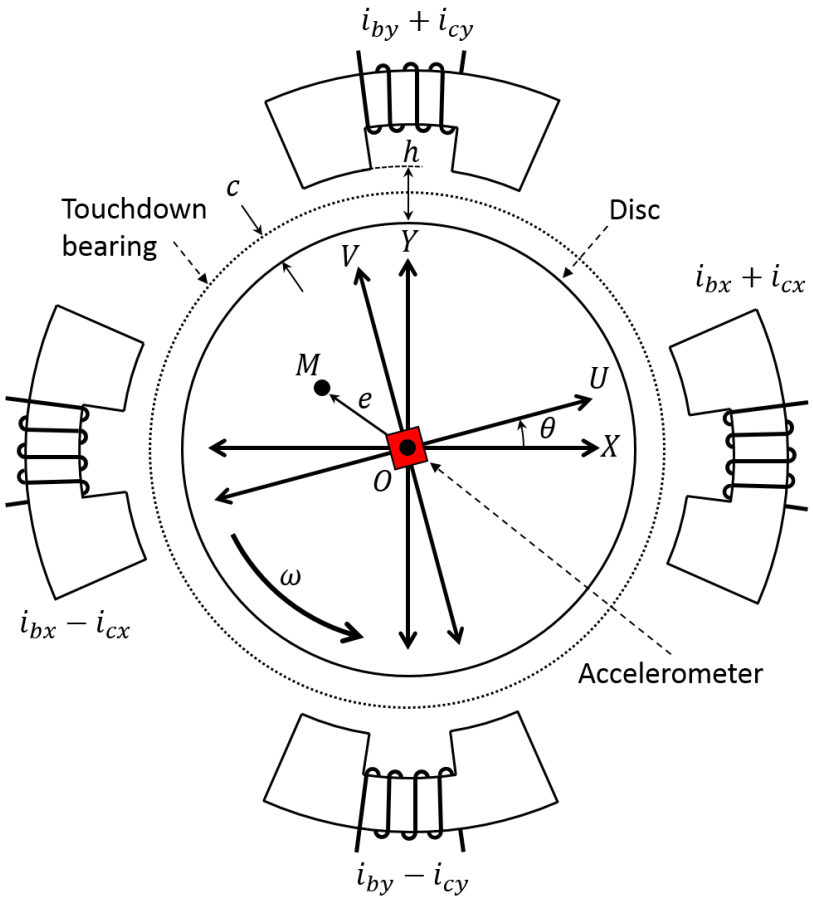

Figure 7.2: Diagram of the measurement plane, indicating the position of the disc within the AMB. The accelerometer is assumed to be located at the exact geometric centre of the disc

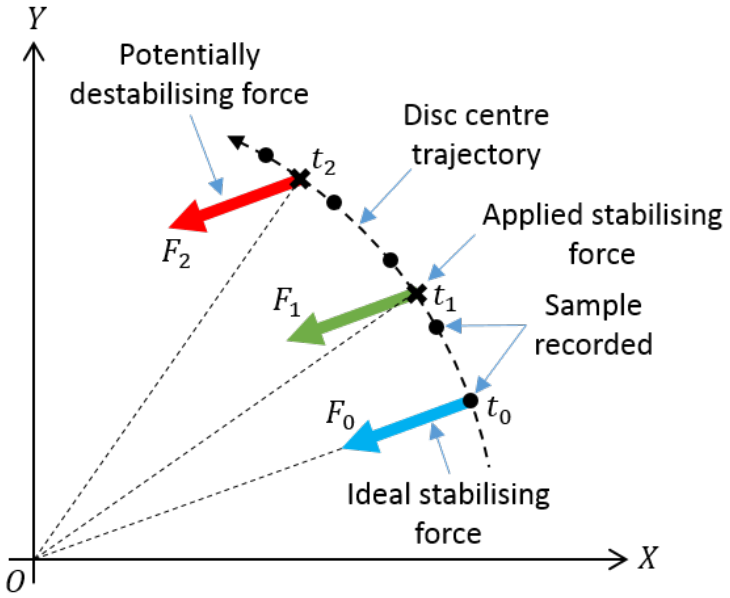

Figure 7.3: Diagram of the measurement plane, indicating the position of the disc within the AMB. The accelerometer is assumed to be located at the geometric centre of the disc

error sources can be minimised. In the following, only the errors of particular relevance to active rotors, that is, those associated with the transformation between the accelerometer's rotating frame and the AMB's inertial frame, are considered. Thus, the accelerometer is assumed to be ideal, with no limits of resolution or signal noise, and located at the exact geometric centre of the disc.

7.4 Mitigation of frame conversion errors

Recalling Eqs. (5.34) and (5.83), the accelerometer-derived inertial frame acceleration, $\ddot{d}_a$, is given by

$$\ddot{d}_a = \left((\ddot{d}_{xy} + \mathrm{j}g)\mathrm{e}^{-\mathrm{j}\theta}\right)\mathrm{e}^{\mathrm{j}\theta_e} - \mathrm{j}g_e \tag{7.4}$$

where $\theta = \omega t + \theta(0)$. It can be assumed that the rotational speed is constant and known, in which case $\theta_e = \omega t + \theta_e(0)$ and hence

$$\ddot{d}_a = \ddot{d}_{xy}\mathrm{e}^{-\mathrm{j}\theta_\varepsilon(0)} + \mathrm{j}\left(g\mathrm{e}^{-\mathrm{j}\theta_\varepsilon(0)} - g_e\right) \tag{7.5}$$

The second term in Eq. (7.5) is related to the errors in the estimation of the initial angle $\theta(0)$ and the gravity component g. If integrated, it will grow rapidly, leading to an erroneous position measurement and, consequently, destabilisation. However, the term is independent of the motion of the disc, and hence, $\ddot{d}_a(0) = \mathrm{j}\left(g\mathrm{e}^{-\mathrm{j}\theta_\varepsilon(0)} - g_e\right)$ can be obtained from converting the accelerometer signals of a stationary disc, for which $\ddot{d}_{xy} = 0$. The signal can then be integrated twice to obtain the accelerometer-derived displacement d_a, considering the initial condition $\ddot{d}_a(0)$:

$$d_a = \iint \left(\ddot{d}_a - \ddot{d}_a(0)\right)\,\mathrm{d}t\,\mathrm{d}t = d_{xy}\mathrm{e}^{-\mathrm{j}\theta_\varepsilon(0)} \tag{7.6}$$

The true position of the disc within the bearings, p_{xy}, will take into account the initial velocity and position conditions, so that $p_{xy} = d_{xy} + \dot{d}_{xy}(0)t + d_{xy}(0)$. Although these parameters cannot be measured with the accelerometer alone, they can be known under certain conditions. Thus, the integration is assumed to begin with the disc resting on the touchdown bearing with zero rotational speed, and hence $\dot{d}_{xy}(0) = 0$ and $d_{xy}(0) = -\mathrm{j}c$, where c is the radial clearance. The practical implication of this assumption is that the position estimation process must begin prior to levitation. Thus, the accelerometer-derived disc position p_a is given by:

$$p_a = d_{xy}\mathrm{e}^{-\mathrm{j}\theta_\varepsilon(0)} - \mathrm{j}c \tag{7.7}$$

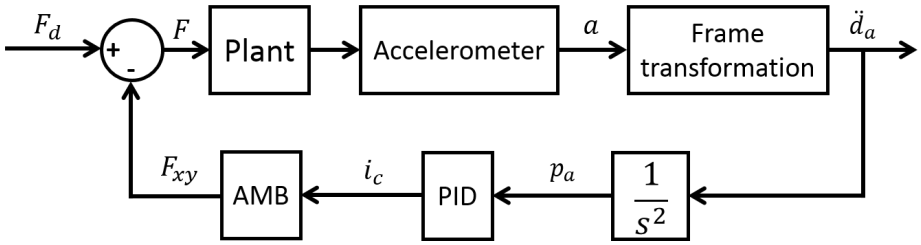

Figure 7.4: Block diagram of AMB control system using accelerometer-derived rotor position information.

It follows that

$$p_{xy} = p_a \mathrm{e}^{\mathrm{j}\theta_\varepsilon(0)} + \mathrm{j}c\left(\mathrm{e}^{\mathrm{j}\theta_\varepsilon(0)} - 1\right) \tag{7.8}$$

Hence, the true disc position will be given by p_a, but subject to a phase error and a steady state error. Conventional PID control can be applied to the derived position to produce the stabilising control currents which enable levitation, so that the system can be represented by the block diagram in Fig. 7.4, in which F_d denotes the system forces that the AMB opposes, such as the disc weight and the unbalance forces.

As the control will aim to minimise p_a, the effect of the phase error for small $\theta_\varepsilon(0)$ does not have a significant effect on the disc position. The second term in Eq. (7.8), on the other hand, can be significant, as it constitutes a steady-state position error which depends on the size of the radial clearance c. This position error cannot be measured by the accelerometer directly and so a high-frequency current injection method was developed to minimise it.

The technique relies on the position dependence of the AMB force output. If a harmonic force is applied with the AMB, the amplitude of the disc response will be proportional to its position within the bearings. The phase of the response will indicate whether the position is positive or negative. Hence, a low-amplitude, high-frequency harmonic current is injected once p_a is minimised with the control. The resulting force output produces a disc response with small displacement but, crucially, large acceleration, which is easily detected by the accelerometer but has negligible effect on the disc dynamics. The force output when current $i_q = i_{qx} + \mathrm{j}i_{qy}$ is injected is given by

$$\begin{aligned} F_{xy} = k_b \Bigg[&\left(\frac{(i_{bx} + i_{cx} + i_{qx})^2}{(h-x)^2} - \frac{(i_{bx} - i_{cx} + i_{qx})^2}{(h+x)^2} \right) \\ &+\mathrm{j}\left(\frac{(i_{by} + i_{cy} + i_{qy})^2}{(h-y)^2} - \frac{(i_{by} - i_{cy} + i_{qy})^2}{(h+y)^2} \right) \Bigg] \end{aligned} \tag{7.9}$$

Separating the terms relating to the injection current i_q yields $F_{xy} = F_l + F_q$,

where $F_l = F_{lx} + \mathrm{j}F_{ly}$ and $F_q = F_{qx} + \mathrm{j}F_{qy}$. The term F_l represents the AMB forces which produce stable levitation, and will coincide with the expression in Eq. (7.1). The forces associated with the current injection, F_q, will be

$$F_q = k_b \left[\left(\frac{i_{qx}^2 + 2i_{qx}(i_{bx} + i_{cx})}{(h-x)^2} - \frac{i_{qx}^2 + 2i_{qx}(i_{bx} - i_{cx})}{(h+x)^2} \right) + \mathrm{j} \left(\frac{i_{qy}^2 + 2i_{qy}(i_{by} + i_{cy})}{(h-y)^2} - \frac{i_{qy}^2 + 2i_{qy}(i_{by} - i_{cy})}{(h+y)^2} \right) \right] \tag{7.10}$$

$$F_q = 2k_b \left[\left(\frac{2i_{qx}^2 hx + 2i_{qx}(2i_{bx}hx + i_{cx}(h^2 + x^2))}{(h^2 - x^2)^2} \right) + \mathrm{j} \left(\frac{2i_{qy}^2 hy + 2i_{qy}(2i_{by}hy + i_{cy}(h^2 + y^2))}{(h^2 - y^2)^2} \right) \right] \tag{7.11}$$

The injected current will be of the form $i_{qx} = i_{qy} = Q \sin \omega_q t$, with $Q \ll i_c < i_b$ and frequency $\omega_q \gg \omega$. Knowing that $2i_{qx}^2 = 2i_{qy}^2 = Q^2(1 - \cos 2\omega_q t)$, it follows that

$$F_q = 2k_b \left[\left(\frac{Q^2 hx(1 - \cos 2\omega_q t) + 2Q(2i_{bx}hx + i_{cx}(h^2 + x^2)) \sin \omega_q t}{(h^2 - x^2)^2} \right) + \mathrm{j} \left(\frac{Q^2 hy(1 - \cos 2\omega_q t) + 2Q(2i_{by}hy + i_{cy}(h^2 + y^2)) \sin \omega_q t}{(h^2 - y^2)^2} \right) \right] \tag{7.12}$$

The terms in Eq. (7.12) associated with $\cos 2\omega_q t$ are of particular relevance because they are proportional to the disc positions in each axis, x and y, and independent of the control and bias currents. In addition, the distinct frequency component at $2\omega_q$ enables the associated disc response to be isolated using a bandpass filter. In general, the equation of motion for the disc will be $M\ddot{p}_{xy} = F_d + F_l + F_q$. Considering only the components of the forces related to the $2\omega_q$ frequency, the general response of the disc can be expressed as

$$M\ddot{p}_q = B \cos 2\omega_q t \tag{7.13}$$

where $\ddot{p}_q$ is the bandpass-filtered acceleration. The amplitude term B will be

$$B = -2k_b hQ^2 \left(\frac{x}{(h^2 - x^2)^2} + \mathrm{j} \frac{y}{(h^2 - y^2)^2} \right) \tag{7.14}$$

and can be linearised around the desired operating point, $x_0 = y_0 = 0$, so

$$B = B(x_0, y_0) + \left. \frac{\partial B(x,y)}{\partial x} \right|_{x_0} (x - x_0) + \left. \frac{\partial B(x,y)}{\partial y} \right|_{y_0} (y - y_0) \tag{7.15}$$

with

$$\left.\frac{\partial B(x,y)}{\partial x}\right|_{x_0} = -2k_b hQ^2 \frac{h^2+3x_0^2}{(h^2-x_0^2)^3} \tag{7.16}$$

and

$$\left.\frac{\partial B(x,y)}{\partial y}\right|_{y_0} = -\mathrm{j}2k_b hQ^2 \frac{h^2+3y_0^2}{(h^2-y_0^2)^3} \tag{7.17}$$

In this case,

$$B = -2k_b hQ^2 \left(\frac{h^2}{h^6}x + \mathrm{j}\frac{h^2}{h^6}y\right) \tag{7.18}$$

$$B = -\frac{2k_b Q^2}{h^3} p_{xy} \tag{7.19}$$

and hence

$$\ddot{p}_q = -\frac{2k_b Q^2}{Mh^3} p_{xy} \cos 2\omega_q t \tag{7.20}$$

For simplicity, it can be assumed that the overall disc motion with and without the injected current is approximately the same and so the contribution of p_q in p_{xy} is negligible, making these variables independent. If the disc is not rotating during the levitation process then p_{xy} will be constant, so the injection-induced displacement p_q will be

$$p_q = \frac{k_b Q^2}{2\omega_q^2 Mh^3} p_{xy} \cos 2\omega_q t \tag{7.21}$$

Equation (7.21) shows that, for a high-frequency injected current, the associated displacement will be inversely proportional to ω_q^2, implying that the disc will be subjected to negligible displacement. However, the related acceleration response (Eq. (7.20)) will remain measurable, with an amplitude controlled by Q^2, and, crucially, proportional to the disc position p_{xy}. The disc response $\ddot{p}_q$ can be derived from the accelerometer-inferred disc acceleration signal $\ddot{d}_a$ (Eq. (7.5)), having accounted for the initial condition $\ddot{d}_a(0)$, by applying a bandpass filter, to yield

$$BP\left(\ddot{d}_a - \ddot{d}_a(0)\right) = \ddot{p}_q \mathrm{e}^{-\mathrm{j}\theta_\varepsilon(0)} \tag{7.22}$$

A Fast Fourier Transform (FFT) can then be used to obtain the response amplitude and phase of the filtered signal, defined as

$$D_f = \left|BP\left(\ddot{d}_a - \ddot{d}_a(0)\right)\right| = \frac{2k_b Q^2}{Mh^3}|p_{xy}| \tag{7.23}$$

$$\phi_f = \arg\left[BP\left(\ddot{d}_a - \ddot{d}_a(0)\right)\right] = \arg p_{xy} - \theta_\varepsilon(0) + \pi \tag{7.24}$$

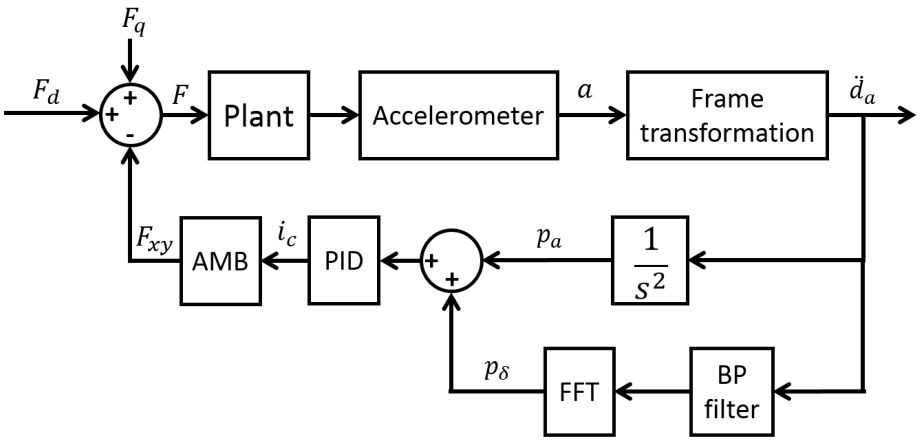

Figure 7.5: Block diagram of AMB control system using accelerometer-derived rotor position information together with high-frequency current injection for steady state error correction.

It follows that

$$-D_f \mathrm{e}^{\mathrm{j}(\phi_f)} \frac{Mh^3}{2k_b Q^2} = p_{xy} \mathrm{e}^{-\mathrm{j}\theta_\varepsilon(0)} \tag{7.25}$$

which combined with Eq. (7.8) yields

$$-D_f \mathrm{e}^{\mathrm{j}(\phi_f)} \frac{Mh^3}{2k_b Q^2} = p_a + \mathrm{j}c\left(1 - \mathrm{e}^{-\mathrm{j}\theta_\varepsilon(0)}\right) \tag{7.26}$$

Therefore, as $p_a \to 0$, having been minimised through the control action,

$$-D_f \mathrm{e}^{\mathrm{j}(\phi_f)} \frac{Mh^3}{2k_b Q^2} \to \mathrm{j}c\left(1 - \mathrm{e}^{-\mathrm{j}\theta_\varepsilon(0)}\right) \tag{7.27}$$

This is the change in p_a required to minimise $p_{xy}\mathrm{e}^{-\mathrm{j}\theta_\varepsilon(0)}$, and so the disturbance p_δ can be added to the accelerometer-derived position, where

$$p_\delta = K_q \frac{Mh^3}{2k_b Q^2} \int D_f \mathrm{e}^{\mathrm{j}(\phi_f)} \,\mathrm{d}t \tag{7.28}$$

and parameter K_q dictates the response time of the integral action. The new system block diagram is given in Fig. 7.5.

The control will now act on both the estimated disc position and disturbance term together, $p_a + p_\delta$, to minimise $p_{xy}\mathrm{e}^{-\mathrm{j}\theta_\varepsilon(0)}$. Thus the steady state error appearing in Eq. (7.7) can be reduced and the true disc position will be controlled, despite no direct measurement of it being available. Once $p_a + p_\delta$ has been minimised, $p_a = \mathrm{j}c\left(\mathrm{e}^{-\mathrm{j}\theta_\varepsilon(0)} - 1\right)$, from which the initial angle error can be obtained as

$$\theta_\varepsilon(0) = \mathrm{j}\ln\left(1 - \mathrm{j}\frac{p_a}{c}\right) \tag{7.29}$$

Table 7.1: Simulation parameters

Parameter	Symbol	Value	Units
Disc mass	M	2	kg
Disc eccentricity	e	1	mm
Unbalance phase	φ	80	deg
Air gap	h	1	mm
Touchdown bearing clearance	c	0.5	mm
Bearing constant	k_b	6.28×10^{-7}	Nm^2/A^2
Bias currents	i_{bx},i_{by}	3	A
PID gain - Proportional	K_P	3.6×10^4	-
PID gain - Derivative	K_D	5.4×10^2	-
PID gain - Integral	K_I	2.2×10^5	-
Initial angular position	$\theta(0)$	150	deg
Initial angular position error	$\theta_\varepsilon(0)$	10	deg
Measured gravity component	g_a	9.5	m/s^2
Estimated gravity component	g_e	9.81	m/s^2
Injected current amplitude	Q	0.1	A
Injected current frequency	ω_q	500	Hz

7.5 Simulated levitation

The levitation of the disc using the control scheme in Fig. 7.5 was tested in simulation. The model parameters are given in Table 7.1. The simulation assumes the disc begins resting on the touchdown bearing with zero rotational speed, and so the initial conditions are known. The gravity-related errors are minimised by offsetting the data with $\ddot{d}_a$ before integrating, as per Eq. (7.6). A controlled levitation from $-\text{j}c$ to the centre of the bearings over 5 s is then performed. PID control is applied throughout, using the accelerometer-derived position p_a for feedback. The discrepancy between p_a and the true disc position p_{xy} is clearly observed in Figs. 7.6 and 7.7, which show the position of the disc in the Y and X axes, respectively. Despite the fact that the motion of the rotor should take place only in the vertical Y direction, the error manifests itself most prominently in the X axis position, with an error equivalent to approximately 17% of the clearance. In order to minimise this steady state error, a high frequency current is injected into the bearings at 7.5 s. This has a negligible effect on the rotor position, but can be clearly identified in the accelerometer signal, presented in Fig. 7.8. The correction signal p_δ is added to the accelerometer-derived position after 10 s, and so the position error is eliminated. At 20 s the injected current is removed and between 25 and 35 s the rotor speed is ramped up from 0 to $1,000$ rpm.

The simulation demonstrates how the position estimation errors associated

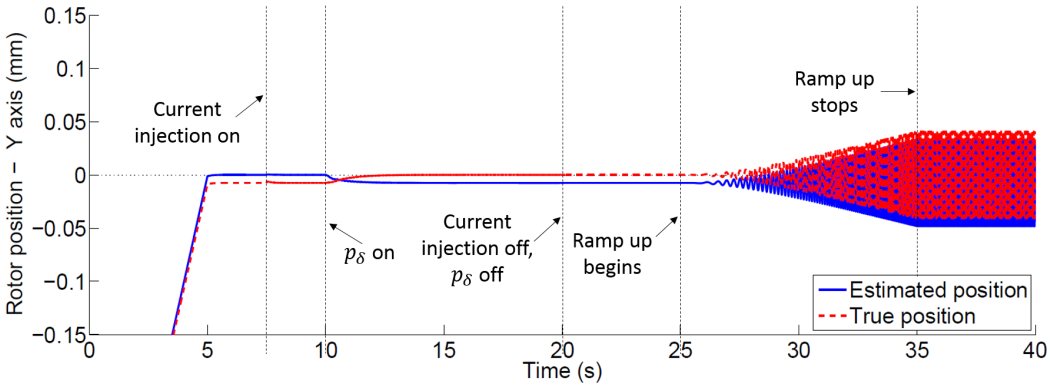

Figure 7.6: Y axis rotor position during simulation of stable levitation of a disc with an ideal accelerometer.

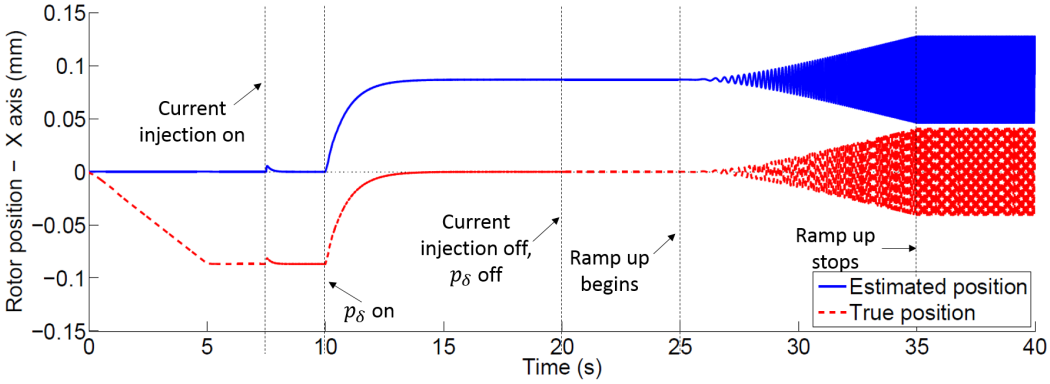

Figure 7.7: X axis rotor position during simulation of stable levitation of a disc with an ideal accelerometer.

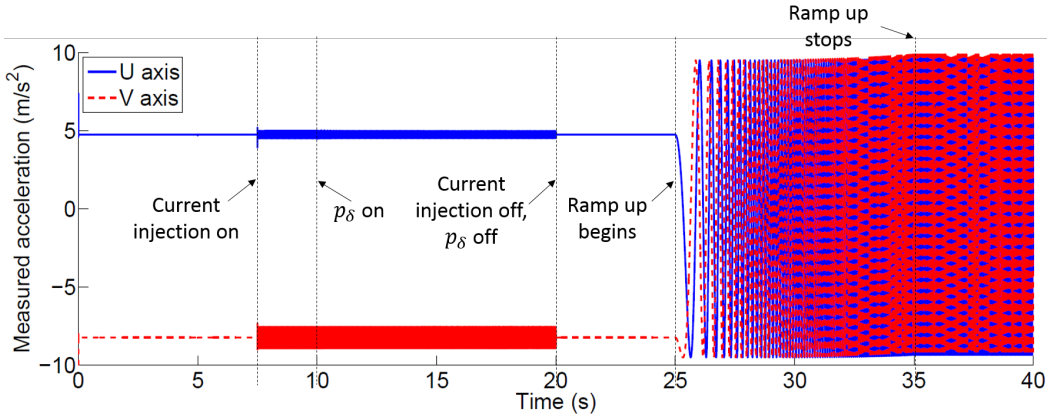

Figure 7.8: Accelerometer output during simulation of stable levitation of a disc with an ideal accelerometer.

with the conversion between the rotating and inertial frames can be addressed. However, other sources of measurement error such as resolution limits and noise would be present in a non-ideal accelerometer, and would lead to exponentially growing position estimation errors, as detailed in Eq. (5.89). This suggests that control of AMB-levitated rotors using displacement information extracted from standalone internally-mounted accelerometers may not be feasible in practice. However, the combination of the accelerometers with ancillary sensors could enable the integration to be reset to avoid accumulation of errors. This idea is discussed in Further Work (Chapter 8).

7.6 Conclusions

Active rotors were considered as a means to prevent the control limitations associated with sensor/actuator non-collocation in AMB systems. The freedom of locating sensors afforded by active rotor designs could enable the root cause of the problem to be eliminated. The combination of active rotors with AMBs is considered a promising development, as both systems can be integrated without interference. Further, the typically high-performance, high-cost applications in which AMBs are used may be suitable for introducing active rotor technology, as increased costs may not pose a significant barrier to implementation.

As a first approach, internal accelerometers were considered as standalone sensors in AMB systems. In order to utilise conventional AMB PID control techniques, the extraction of displacement information from the accelerometers via double integration was studied. Various methods were explored to mitigate the integration errors associated with reference frame conversion. In particular, a high-frequency current injection technique was developed to reduce steady-state position errors, exploiting the position-dependent nature of AMB force outputs. The methods were successfully applied in simulation.

However, when considering non-ideal sensors, the presence of error sources such as limits of resolution or noise must be accounted for. In practice, the effect of these during the integration process would lead to accumulation of position estimation errors, which would destabilise the rotor levitation. Ultimately, therefore, the techniques explored to achieve stable rotor levitation on AMBs using only accelerometer-derived position feedback did not yield a fully feasible solution. Nonetheless, the inherent characteristics of active rotors should allow non-collocation to be overcome, and hence further work is suggested in Chapter 8.

7.7 Summary

- The combination of active rotors and AMBs was considered as a means to overcome the difficulties associated sensor/actuator non-collocation.
- The studied method used accelerometer-derived position feedback together with conventional PID control.
- Techniques to mitigate integration errors stemming from the conversion of the accelerometer signals between the rotating and inertial frames were explored.
- A high-frequency current injection technique was developed to minimise steady-state position error, and validated in simulation.
- The presence of error sources such as noise and resolution limits make the considered method of achieving stable rotor levitation with internal accelerometers unfeasible in practice.

References

[1] G. Genta and S. Carabelli, "Noncolocation effects on the rigid body rotordynamics of rotors on amb," in *7th International Symposium on Magnetic Bearings*, (Zurich, Switzerland), 2000.

[2] E. H. Maslen and G. Schweitzer, *Magnetic Bearings: Theory, Design, and Application to Rotating Machinery*. Springer, 2009.

[3] Z. Kulesza, "Virtual collocation method for a flexible rotor supported by active magnetic bearings," *Journal of Vibration and Control*, vol. 21, no. 8, pp. 1522–1538, 2015.

[4] J. G. Bai, X. Z. Zhang, and L. M. Wang, "A flywheel energy storage system with active magnetic bearings," *Energy Procedia*, vol. 16, pp. 1124–1128, 2012.

[5] C. Zwyssig, T. Baumgartner, and J. W. Kolar, "High-speed magnetically levitated reaction wheel demonstrator," in *International Power Electronics Conference*, (Hiroshima, Japan), pp. 1707–1714, 2014.

[6] S. Han, "Measuring displacement signal with an accelerometer," *Journal of Mechanical Science and Technology*, vol. 24, no. 6, pp. 1329–1335, 2010.

Chapter 8

Conclusions and further work

8.1 Conclusions

Active vibration control constitutes the state of the art in rotating machinery, and holds the key to future developments towards smart rotor technology. However, its implementation is limited to only a few high-cost applications, typically through the use of Active Magnetic Bearing (AMB) systems. Thus, the principal goal of the research discussed here was to study a new rotor topology which could ease the implementability of active control technology in rotating machines, by providing a versatile and cost-effective design which would be easily transferable to a wide range of applications. The "active rotor" design introduced achieves this goal by exploiting the inner volume of hollow rotors to mount larger numbers of sensors and actuators at optimum locations.

From the design perspective, the construction of a fully operational prototype demonstrates the feasibility of mounting an active control system within a hollow rotor. The evolution of electronics and computing technology of recent years enables the use of powerful, robust, and highly integratable sensors, microcontrollers and wireless transmission at very low cost. The analysis of available sensing technology suggests that internal accelerometers can provide a practical and fully stator-independent sensing system. MEMS accelerometers in particular have proven to be accurate, versatile and highly cost-effective. In terms of actuation, mass balancer designs display the required scope for miniaturisation, as demonstrated via the active rotor prototype. Active rotors can house a large number of actuators, and this characteristic can be exploited to utilise a distributed network of mass-balancer. In this case, each actuator needs to only produce a small control force, reducing the physical demands imposed on the individual devices.

Internal accelerometers can be used to monitor rotor vibration by measuring

steady state and transient acceleration at any point along the rotor. An important finding, and major strength, is their diverse functionality, which allows them to be used in a number of different ways. The research has demonstrated their use as mean displacement sensors, which can be achieved by isolating the synchronous centripetal acceleration component of the signal. They have also been applied to directly measure both the magnitude and the phase of the response of an unbalanced rotor. The accelerometers have been used as virtual encoders, using an algorithm which tracks the gravitational acceleration component in the frequency domain to serve as a reference to the inertial frame. During an analysis of sources of measurement error, the accelerometers were even shown to serve as temperature sensors.

From the point of view of control capability, the research has shown that the location of sensors and actuators within the rotating frame of reference enables active rotors to control unbalance-induced vibration without high-frequency sensing and control signals. This reduces both the computational burden and the performance requirements associated with control, enabling smaller, simpler and more cost effective components to be used. Existing *a priori* control methods can be implemented in active rotors, but may limit their widespread implementability, as these techniques require good knowledge of the controlled system, which in turn demands substantial human interaction and supervision. To overcome this barrier, a *non a priori* method, the Algorithmic Direct Search Controller (ADSC), has been developed. This technique is based on the Nelder-Mead optimisation algorithm, which enables the controller to heuristically search for an actuator setting which minimises the rotor vibration, without requiring any knowledge of the system characteristics. The validity of the ADSC has been demonstrated both in simulation and experimentally.

As an example of usage, the active rotor concept was applied to solve the issues associated with non-collocation of sensors and actuators in AMB systems. The problem of levitating a rotor on AMBs using only the internal accelerometers was approached via integration-based displacement information extraction, and applying the PID control typically used with AMBs. Although the proposed method did not yield a fully feasible solution, the techniques developed during the research, such as the high-frequency injection used to reduce steady state position error, demonstrate how active rotors and AMBs can complement each other and illustrate some of the potential capabilities of the combined design.

The research reported here has made substantial headway into the problem of the scant implementability of active control system in rotating machines. This has been achieved by developing an active rotor design and considering its fea-

sibility, the effectiveness of its sensing, its control capabilities and its application within AMBs. A substantial body of work still remains before this technology is ready for industrial deployment. The following section discusses some of these challenges, subdivided in accordance with the four research themes

8.2 Further work

8.2.1 Feasibility

Component mounting

The active rotor design used in the prototype uses an assembled shaft. However, in many industrial applications such a design may not be practical. Thus, further research should be conducted into alternative ways of mounting the active control system within a rotor which could be easier to adopt in an industrial setting. An example of this could be using an internal frame which houses all necessary components and can be assembled outside the rotor. The frame could then be slid inside the hollow shaft and secured, perhaps using a tapered design, such as is commonly used to assemble concentric shafts in milling machines.

An aspect of this research could also be to explore how to produce active rotors with non-hollow shafts. A primary consideration would be the use of composite rotors, which could be built up around a central supporting structure containing the sensors and actuators. In very large rotors, such as those used in the power generation industry, it may be feasible to drill spaces into the rotor body, in which sensors and actuators could be placed. Alternatively, the active devices may be housed within large working components, such as turbine blades, lockhubs, flywheels, etc.

Internal power supply

In the prototype, a slipring was finally used to provide power to the active components. However, this is not an optimal solution for active rotors, as sliprings introduce maintenance requirements and speed limitations. Also, sliprings necessarily interact with the stator, thus compromising the rotor-centred design philosophy. Thus, further work is necessary to design supply systems which can provide the required electrical power within the rotor while having minimal impact on the stator design. Possible solutions can be classified in terms of where the electrical power is generated:

External Here, the power is generated in the stator (electrical generator design) or outside of the rotating machine (power supply installed in the building). This type of power source can easily provide very large voltages, which could be necessary if using piezoelectric materials for actuation. The main drawback is that the power must be wirelessly transmitted to the rotor. Contactless power transmission is an ongoing field of research, with various different technologies being investigated, such as electromagnetic induction, microwave transmission or even light waves [1].

Internal This would constitute an ideal, completely stator-independent system in which the electrical power is generated in the rotor. The energy would be harvested from the rotational or vibrational energy. Again, energy harvesting is an active field of research, but some potential devices have been presented in literature, for instance those by Toh *et al.* [2] or Manla *et al.* [3]. A possible drawback would be the need for the rotor to be operational before energy was supplied to the active system.

Mixed In this case, the power could be generated in the rotor, but would require some interaction with the stator. For example, an inverted electrical generator could be used, in which the electrical power was produced in coils located in the rotor. The main advantages of this technology are that it is readily available and could provide substantial amounts of power. On the other hand, at least a portion of the stator design would be dependent on the rotor. However, even in this case the active rotor design would provide advantages over conventional stator-mounted systems, as the power generator unit could be located at any convenient location along the rotor length.

Sampling rates

The wireless transmission protocol selected for use in the prototype, ZigBee, is ideal for low-power applications but has a limited data throughput rate. The use of active rotors in an industrial setting could require higher sampling rates than those achievable in the prototype. In general, existing wireless transmission protocols are designed to transmit relatively small numbers of large packets of information to many users, which is a typical usage scenario for WiFi networks, for instance. However, achieving large sampling rates with wireless sensors requires transmitting many small packets of information, typically to only a few network users. Thus, new wireless communication protocols may be required in order to achieve high sampling rates with active rotors. A possible solution

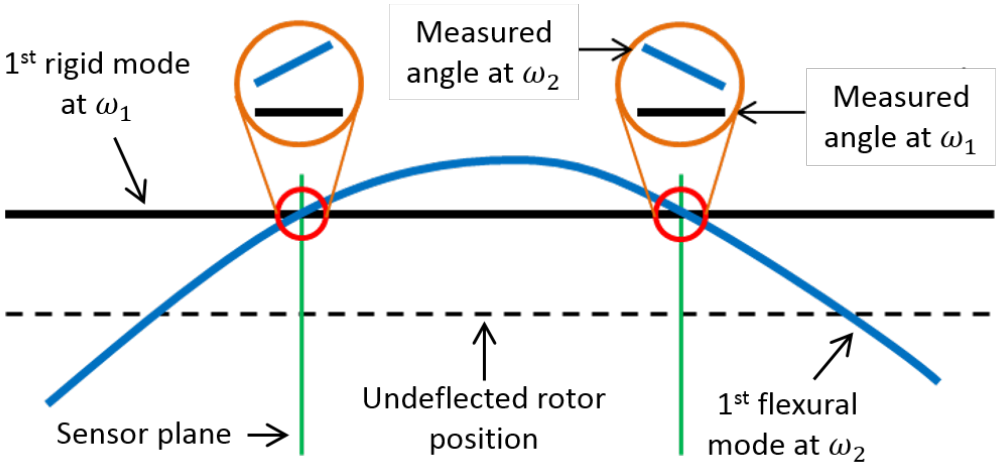

Figure 8.1: Schematic of the use of additional angular information to distinguish between the first rigid vibration mode and the first flexural mode.

to be considered could be RT-WiFi, recently developed by Wei *et al.* [4], which can enable sampling rates of up to 6 kHz.

8.2.2 Sensing

Z axis information

The accelerometers used in the prototype are tri-axial, being able to measure acceleration along the shaft axis in the Z plane as well as the two perpendicular planes U and V. Further research could be undertaken in studying how best to utilise this additional information. One possibility is to use the gravitational component measured in the Z axis to estimate angular position at the measurement location. This additional information could be used, for instance, to distinguish between two vibration modes which display the same displacement at the sensor positions, as illustrated in Fig. 8.1.

Torsional vibration

Torsional vibration is a common fault in multi-stage rotating machines, and is typically difficult to monitor. Internal accelerometers could provide a solution to this, as tangential acceleration could be easily measured by locating a sensor away from the geometric centre of the rotor. Further work would need to be conducted in order to demonstrate the validity of this concept, to develop methods of managing the gravitational component which would appear in the signals, and to understand whether saturation in the radial direction due to large centripetal acceleration may affect the measurements of tangential ac-

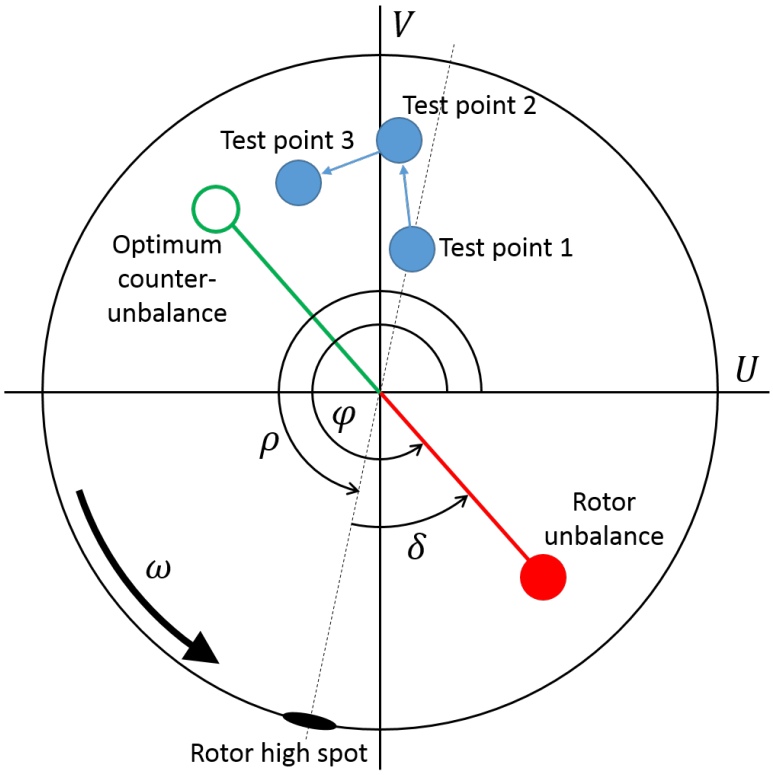

Figure 8.2: Schematic showing how the ADSC starting simplex can be selected to ensure lower vibration and faster convergence.

celeration. Some research into measurement of tangential acceleration with MEMS accelerometers has been undertaken by Baghli *et al.* [5] and Feng *et al.* [6], which could serve as a starting point for this work.

8.2.3 Control

Starting simplex

The Algorithmic Direct Search Control requires an initial simplex with $n + 1$ vertices, where n is the dimension of the problem. In the research undertaken, this simplex was chosen arbitrarily, to represent a worst case vibration scenario. However, it could be possible to inform the selection of the starting test points to ensure that less vibration is encountered in the initial stages of the algorithm execution and also to minimise the number of test points that are evaluated.

An example can be given by considering the simple case of a rotor with its unbalance concentrated at the midspan, where a single sensor and actuator are also located. This is illustrated in Fig. 8.2, which shows the rotor in the rotating frame of reference. If the rotor is operating below its first critical speed, the high point of the rotor will display a phase ρ which will lag the rotor unbalance

phase ϕ by an angle $\delta < \frac{\pi}{2}$. Thus, it can be deduced that the optimum counter-unbalance position will lie at a phase $\rho - \pi + \delta$. Although the phase lag will generally be unknown, the phase of the high point can be measured by the accelerometers, as demonstrated in Chapter 5. Thus, a first test point which locates the resultant actuator counter-unbalance phase at $\rho - \pi$ will have a phase error of at most δ. Subsequent test points can be placed at increasing phases in the direction of rotation, guaranteeing an approximation towards the optimum actuator setting.

These observations may not be applicable in more complex vibration scenarios involving multiple sensors and actuators and a distributed rotor unbalance, and hence further research is required to develop a more robust methodology to determine suitable starting simplexes for the ADSC.

Theoretical proof of saddle point identification

The Neighbourhood and Find transformations were included in the ADSC to prevent premature convergence at saddle points. Although the technique proved successful under the particular test conditions, it would be of interest to expand it for general embodiments of the Nelder-Mead Algorithm.

This could be achieved in part by demonstrating theoretically whether or not the evaluation of the $n + 1$ possible Reflections of an arbitrary, non-degenerate simplex enclosing a given stationary point can provide sufficient information to be able to distinguish between a function minimum and a saddle point. An assumption which may have to be considered is that the resolution of the function evaluation is sufficient to be able to distinguish adjoining test points. This would imply that the test of whether or not a stationary point is a saddle point would have to be performed with a simplex of minimum size.

Adaptive ADSC

The results obtained with the ADSC show that, although the method is successful, the lack of *a prior* knowledge of the objective function may lead to a large number of evaluations which do not produce substantial reduction in vibration. As shown in Chapter 6, this issue is exacerbated for high-dimensional problems, and so it would be of interest to develop methods which can allow the algorithm to converge faster.

Gao and Han [7] have suggested using transformation coefficients which adapt to the size of the simplex, and further work would be required to adapt this idea to the ADSC. Alternative methods could also be developed following

an in-depth analysis of transformation sequences for arbitrary problems. For instance, this approach may identify patterns of repeating transformations which give indication that the simplex is sufficiently close to the minimum to be acceptable, thus enabling early termination.

Hybrid knowledge controllers

The strength of the ADSC lies in its ability to achieve vibration reduction without knowledge of the system. However, the information which it obtains via function evaluations is used only once before being discarded. A powerful approach would be to use the ADSC in conjunction with other techniques which could exploit this information in order to develop a certain amount of predictive power. For instance, machine learning techniques might be used to suggest if a particular simplex transformation may or may not yield an improved result based on previous algorithm iterations, which could ultimately reduce the total number of evaluated test points. In this manner the algorithm could transition between "fully *non a priori*" and "semi *non a priori*" modes. Further research would have to be conducted to determine viable techniques to accomplish this.

8.2.4 Applications

AMBs - Acceleration based control

Three approaches were identified as potential solutions to the problem of levitating a rotor on Active Magnetic Bearings using only internally mounted accelerometers as sensors. The approach discussed in Chapter 7, extracting displacement information via double integration and using existing PID control structures, did not provide a fully feasible solution.

An alternative method would be to develop new control schemes for AMBs which did not rely on the magnetic gap information to achieve stabilisation, instead using the accelerometer signals. The challenge of finding a stabilising control matrix could be posed as an optimisation problem involving linear matrix inequalities (LMI). Ultimately, the motion of the rotor is described by the measured acceleration, so it could be possible to identify patterns in the sensor signals which indicated unstable behaviour, and this information could be used to developed appropriate constraints for the LMI problem. Once stable levitation was achieved, the high-frequency current injection technique developed for steady state position error minimisation could be applied to ensure the rotor was located at the magnetic centre of the bearings. Further work would need

to be conducted to determine if this approach would be able to yield suitable solutions.

AMBs - Sensor fusion schemes

The combination of various types of sensors in a single system was also identified as a route to tackle stable levitation of active rotors in AMBs. A distinction is made based on whether or not the internal accelerometers act as primary sensors (responsible for maintaining stability) or secondary sensors (improve performance).

Accelerometers as primary sensors In a system in which the internal accelerometers act as the primary sensor, the integration-based displacement approach considered in Chapter 7 could be applied, using the information obtained from a secondary sensor to reset the integral, and thus avoiding an accumulation of errors. The secondary sensor need not display high performance, and could be placed at a practical location. Thus, low cost inductive transducers or Hall effect sensors could be utilised. The practical embodiment of this concept would require further research.

Accelerometers as secondary sensors In this scenario, the task of stabilising the levitation of the rotor would be accomplished using an alternative type of sensor, perhaps conventional eddy current transducers. The internal accelerometer could be used to improve performance under specific operation conditions. For instance, the accelerometers could contribute to the control system when high-frequency excitation was present, which is when issues related to the non-collocation of the AMBs and the eddy current sensors would be most significant. Cole, Jiménez and Keogh [8] have presented work in which a complimentary filtering scheme was designed for this purpose, but further work would be required to validate the technique experimentally.

Thermal warping

Thermal warping can constitute a serious source of vibration in rotating machines. In general, rotors affected by this will display slowly increasing synchronous vibration, which is associated with growing unbalance caused by thermal bending of the rotor shaft. This phenomenon is typically referred to as the Morton or Newkirk effect, the latter in the specific case where the heating of

the shaft is caused by light rubbing between the rotor and the stator. In industrial settings, once identified, the unstable growth of vibration can only usually be addressed by shutting down the machine. Given the very specific operating conditions required for the effect to develop and the associated uncertainty, it is often difficult to introduce corrective measures without extensive machine redesign or using active control systems.

The ADSC algorithm has been developed to reduce synchronous vibration, even if stemming from an unknown source. It is therefore well equipped to tackle changing unbalance conditions, such as those introduced by the Morton and Newkirk effects. Hence, further research has been planned in which the ADSC will be applied to identify, manage and reduce the synchronous excitation produced by thermal warping of the active rotor shaft.

References

[1] S. S. Valtchev, E. N. Baikova, and L. R. Jorge, "Electromagnetic field as the wireless transporter of energy," *Facta Universitatis Series: Electronics and Energetics*, vol. 25, no. 3, pp. 171–181, 2012.

[2] T. Toh, P. Mitcheson, A. Holmes, and E. Yeatman, "A continuously rotating energy harvester with maximum power point tracking," *Journal of Micromechanics and Microengineering*, vol. 18, no. 10, 2008.

[3] G. Manla, N. M. White, and M. J. Tudor, "Numerical model of a non-contact piezoelectric energy harvester for rotating objects," *Sensors Journal, IEEE*, vol. 12, no. 6, pp. 1785–1793, 2012.

[4] Y.-H. Wei, Q. Leng, S. Han, A. K. Mok, W. Zhang, and M. Tomizuka, "Rt-wifi: Real-time high-speed communication protocol for wireless cyber-physical control applications," in *Real-Time Systems Symposium (RTSS), 2013 IEEE 34th*, pp. 140–149, IEEE, 2013.

[5] L. Baghli, J. F. Pautex, and S. Mezani, "Wireless instantaneous torque measurement, application to induction motors," in *19th International Conference on Electrical Machines, ICEM*, (Rome Italy), 2010.

[6] G. Feng, N. Hu, Z. Mones, F. Gu, and A. D. Ball, "An investigation of the orthogonal outputs from an on-rotor mems accelerometer for reciprocating compressor condition monitoring," *Mechanical Systems and Signal Processing*, vol. 7677, pp. 228–241, 2016.

[7] F. Gao and L. Han, "Implementing the Nelder-Mead simplex algorithm with adaptive parameters," *Computational Optimization and Applications*, vol. 51, no. 1, pp. 259–277, 2010.

[8] M. Cole, S. Jiménez, and P. S. Keogh, "Feedback control of a magnetic bearing using fusion of rotor acceleration and position measurements," in *14th International Symposium on Magnetic Bearings*, (Linz, Austria), 2014.

Appendix A

Element matrices

The element matrices used in the finite element model are presented below, to which end the following parameters are defined:

- r_o is the outer diameter of the element
- r_i is the inner diameter of the element
- I is the second moment of area $I = \frac{\pi}{4}(r_o^4 - r_i^4)$
- ρ is the density of the beam material
- m_l is mass per unit length $m_l = \pi(r_o^2 - r_i^2)\rho$
- E is the elastic modulus
- G is the shear modulus
- ν is Poisson's ratio
- κ is the transverse shear form factor. For a thick walled tube, Cowper [1] defines
$$\kappa = \frac{6(1+\nu)(1+(r_i/r_o)^2)^2}{(7+6\nu)(1+(r_i/r_o)^2)^2 + (20+12\nu)(r_i/r_o)^2}$$
- Φ is the transverse shear effect
$$\Phi = \frac{12EI}{\kappa G l^2 \pi (r_o^2 - r_i^2)}$$

A.1 Element stiffness matrix

The elemental stiffness matrix is given by

$$\mathbf{K} = \frac{EI}{l^3(1+\Phi)} \begin{bmatrix} 12 & & & & & & & \\ 0 & 12 & & & & & & \\ 0 & -6l & (4+\Phi)l^2 & & & & & \\ 6l & 0 & 0 & (4+\Phi)l^2 & & & & \\ -12 & 0 & 0 & -6l & 12 & & & \\ 0 & -12 & 6l & 0 & 0 & 12 & & \\ 0 & -6l & (2-\Phi)l^2 & 0 & 0 & 6l & (4+\Phi)l^2 & \\ 6l & 0 & 0 & (2-\Phi)l^2 & -6l & 0 & 0 & (4+\Phi)l^2 \end{bmatrix}$$

A.2 Element mass matrix

The elemental mass matrix is given by

$$\mathbf{M} = \mathbf{M_1} + \Phi\mathbf{M_2} + \Phi^2\mathbf{M_3} + \mathbf{N_1} + \Phi\mathbf{N_2} + \Phi^2\mathbf{N_3} \tag{A.1}$$

where $\mathbf{M_1}$, $\mathbf{M_2}$, $\mathbf{M_3}$ are associated with the translational mass, and $\mathbf{N_1}$, $\mathbf{N_2}$, $\mathbf{N_3}$ with the rotational inertia. Nelson and McVaugh's model included large discs on the rotor, and they assumed that these would be the principal contributors to the rotational inertia of the system. As this assumption does not hold for the considered active rotor geometries, the inertia of a thick walled cylinder ($m(3(r_o^2 + r_i^2) + l^2)/12$) was used instead of that of a solid disc ($mr^2/4$). The resulting symmetric matrices are

$$\mathbf{M_1} = \frac{m_l l}{420(1+\Phi)^2} \begin{bmatrix} 156 & & & & & & & \\ 0 & 156 & & & & & & \\ 0 & -22l & 4l^2 & & & & & \\ 22l & 0 & 0 & 4l^2 & & & & \\ 54 & 0 & 0 & 13l & 156 & & & \\ 0 & 54 & -13l & 0 & 0 & 156 & & \\ 0 & 13l & -3l^2 & 0 & 0 & 22l & 4l^2 & \\ -13l & 0 & 0 & -3l^2 & -22l & 0 & 0 & 4l^2 \end{bmatrix}$$

$$\mathbf{M_2} = \frac{m_l l}{420(1+\Phi)^2}\begin{bmatrix} 294 & & & & & & & \\ 0 & 294 & & & & & & \\ 0 & -38.5l & 7l^2 & & & & & \\ 38.5l & 0 & 0 & 7l^2 & & & & \\ 126 & 0 & 0 & 31.5l & 294 & & & \\ 0 & 126 & -31.5l & 0 & 0 & 294 & & \\ 0 & 31.5l & -7l^2 & 0 & 0 & 38.5l & 7l^2 & \\ -31.5l & 0 & 0 & -7l^2 & -38.5l & 0 & 0 & 7l^2 \end{bmatrix}$$

$$\mathbf{M_3} = \frac{m_l l}{420(1+\Phi)^2}\begin{bmatrix} 140 & & & & & & & \\ 0 & 140 & & & & & & \\ 0 & -17.5l & 3.5l^2 & & & & & \\ 17.5l & 0 & 0 & 3.5l^2 & & & & \\ 70 & 0 & 0 & 17.5l & 140 & & & \\ 0 & 70 & -17.5l & 0 & 0 & 140 & & \\ 0 & 17.5l & -3.5l^2 & 0 & 0 & 17.5l & 3.5l^2 & \\ -17.5l & 0 & 0 & -3.5l^2 & -17.5l & 0 & 0 & 3.5l^2 \end{bmatrix}$$

$$\mathbf{N_1} = \frac{m_l(3(r_o^2+r_i^2)+l^2)}{720l(1+\Phi)^2}\begin{bmatrix} 36 & & & & & & & \\ 0 & 36 & & & & & & \\ 0 & -3l & 4l^2 & & & & & \\ 3l & 0 & 0 & 4l^2 & & & & \\ -36 & 0 & 0 & -3l & 36 & & & \\ 0 & -36 & 3l & 0 & 0 & 36 & & \\ 0 & -3l & -l^2 & 0 & 0 & 3l & 4l^2 & \\ 3l & 0 & 0 & -l^2 & -3l & 0 & 0 & 4l^2 \end{bmatrix}$$

$$\mathbf{N_2} = \frac{m_l(3(r_o^2+r_i^2)+l^2)}{720l(1+\Phi)^2}\begin{bmatrix} 0 & & & & & & & \\ 0 & 0 & & & & & & \\ 0 & 15l & 5l^2 & & & & & \\ -15l & 0 & 0 & 5l^2 & & & & \\ 0 & 0 & 0 & 15l & 0 & & & \\ 0 & 0 & -15l & 0 & 0 & 0 & & \\ 0 & 15l & -5l^2 & 0 & 0 & -15l & 5l^2 & \\ -15l & 0 & 0 & -5l^2 & 15l & 0 & 0 & 5l^2 \end{bmatrix}$$

$$\mathbf{N_3} = \frac{m_l(3(r_o^2+r_i^2)+l^2)}{720l(1+\Phi)^2}\begin{bmatrix} 0 & & & & & & & \\ 0 & 0 & & & & & & \\ 0 & 0 & 10l^2 & & & & & \\ 0 & 0 & 0 & 10l^2 & & & & \\ 0 & 0 & 0 & 0 & 0 & & & \\ 0 & 0 & 0 & 0 & 0 & 0 & & \\ 0 & 0 & 5l^2 & 0 & 0 & 0 & 10l^2 & \\ 0 & 0 & 0 & 5l^2 & 0 & 0 & 0 & 10l^2 \end{bmatrix}$$

A.3 Element gyroscopic matrix

The elemental gyroscopic matrix is given by

$$\mathbf{G} = \mathbf{G_1} + \Phi\mathbf{G_2} + \Phi^2\mathbf{G_3} \tag{A.2}$$

where $\mathbf{G_1}$, $\mathbf{G_2}$, $\mathbf{G_3}$ are skew-symmetric matrices, defined as

$$\mathbf{G_1} = \frac{m_l(r_o^2 + r_i^2)}{60l}\begin{bmatrix} 0 & & & & & & & \\ 36 & 0 & & & & & & \\ -3l & 0 & 0 & & & & & \\ 0 & -3l & 4l^2 & 0 & & & & \\ 0 & 36 & -3l & 0 & 0 & & & \\ -36 & 0 & 0 & -3l & 36 & 0 & & \\ -3l & 0 & 0 & l^2 & 3l & 0 & 0 & \\ 0 & -3l & -l^2 & 0 & 0 & 3l & 4l^2 & 0 \end{bmatrix}$$

$$\mathbf{G_2} = \frac{m_l(r_o^2 + r_i^2)}{60l}\begin{bmatrix} 0 & & & & & & & \\ 0 & 0 & & & & & & \\ 15l & 0 & 0 & & & & & \\ 0 & 15l & 5l^2 & 0 & & & & \\ 0 & 0 & 15l & 0 & 0 & & & \\ 0 & 0 & 0 & 15l & 0 & 0 & & \\ 15l & 0 & 0 & 5l^2 & -15l & 0 & 0 & \\ 0 & 15l & -5l^2 & 0 & 0 & -15l & 5l^2 & 0 \end{bmatrix}$$

$$\mathbf{G_3} = \frac{m_l(r_o^2 + r_i^2)}{60l}\begin{bmatrix} 0 & & & & & & & \\ 0 & 0 & & & & & & \\ 0 & 0 & 0 & & & & & \\ 0 & 0 & 10l^2 & 0 & & & & \\ 0 & 0 & 0 & 0 & 0 & & & \\ 0 & 0 & 0 & 0 & 0 & 0 & & \\ 0 & 0 & 0 & -5l^2 & 0 & 0 & 0 & \\ 0 & 0 & 5l^2 & 0 & 0 & 0 & 10l^2 & 0 \end{bmatrix}$$

References

[1] G. R. Cowper, "The shear coefficient in timoshenkos beam theory," *Journal of Applied Mechanics*, vol. 33, no. 2, pp. 335–340, 1966. 10.1115/1.3625046.

Appendix B

Stationary points of the objective function

The stationary points of the objective function will coincide with those of P^2/Q^2:

$$\frac{P^2}{Q^2} = \left(\Upsilon_r \cos\phi + \Upsilon(\cos\alpha + \cos\beta)\right)^2 + \left(\Upsilon_r \sin\phi + \Upsilon(\sin\alpha + \sin\beta)\right)^2 \tag{B.1}$$

$$\begin{aligned}\frac{P^2}{Q^2} =& \Upsilon_r^2 \cos^2\phi + \Upsilon^2(\cos\alpha + \cos\beta)^2 + 2\Upsilon_r\Upsilon\cos\phi(\cos\alpha + \cos\beta) + \\ & \Upsilon_r^2 \sin^2\phi + \Upsilon^2(\sin\alpha + \sin\beta)^2 + 2\Upsilon_r\Upsilon\sin\phi(\sin\alpha + \sin\beta)\end{aligned} \tag{B.2}$$

$$\frac{P^2}{Q^2} = \Upsilon_r^2 + 2\Upsilon^2(1 + \cos(\alpha - \beta)) + 2\Upsilon_r\Upsilon\left(\cos(\phi - \alpha) + \cos(\phi - \beta)\right) \tag{B.3}$$

The stationary points will be located at (α, β) coordinates which satisfy

$$\frac{\partial P^2/Q^2}{\partial\alpha} = \frac{\partial P^2/Q^2}{\partial\beta} = 0 \tag{B.4}$$

Taking the derivatives of Eq. (B.3) with respect to α and β yields

$$\frac{\partial P^2/Q^2}{\partial\alpha} = -2\Upsilon^2\sin(\alpha - \beta) + 2\Upsilon_r\Upsilon\sin(\phi - \alpha) \tag{B.5}$$

$$\frac{\partial P^2/Q^2}{\partial\beta} = 2\Upsilon^2\sin(\alpha - \beta) + 2\Upsilon_r\Upsilon\sin(\phi - \beta) \tag{B.6}$$

Equating these expressions to zero and rearranging produces

$$\sin(\alpha - \beta) = \frac{\Upsilon_r}{\Upsilon}\sin(\phi - \alpha) \tag{B.7}$$

$$\sin(\alpha-\beta) = -\frac{\Upsilon_r}{\Upsilon}\sin(\phi-\beta) \tag{B.8}$$

and so

$$\sin(\phi-\alpha) + \sin(\phi-\beta) = 0 \tag{B.9}$$

Four solutions can be found for the cases where the sine terms are both 0, with angles 0 or π. These correspond to the maximum function value and three saddle points, as detailed in Table 6.1. The function minima will be given in the case where neither sine term is 0. Letting $\phi-\beta = (\phi-\alpha)+(\alpha-\beta)$

$$\sin(\phi-\alpha) + \sin((\phi-\alpha)+(\alpha-\beta)) = 0 \tag{B.10}$$

$$\sin(\phi-\alpha) + \sin(\phi-\alpha)\cos(\alpha-\beta) + \cos(\phi-\alpha)\sin(\alpha-\beta) = 0 \tag{B.11}$$

Substituting the last term with Eq. (B.7) gives

$$\sin(\phi-\alpha) + \sin(\phi-\alpha)\cos(\alpha-\beta) + \cos(\phi-\alpha)\frac{\Upsilon_r}{\Upsilon}\sin(\phi-\alpha) = 0, \tag{B.12}$$

and eliminating the $\sin(\phi-\alpha)$ terms

$$1 + \cos(\alpha-\beta) + \frac{\Upsilon_r}{\Upsilon}\cos(\phi-\alpha) = 0 \tag{B.13}$$

Knowing, from Eq. (B.7), that

$$\alpha-\beta = \arcsin\left(\frac{\Upsilon_r}{\Upsilon}\sin(\phi-\alpha)\right) \tag{B.14}$$

and substituting into Eq. (B.13)

$$1 + \cos\left(\arcsin\left(\frac{\Upsilon_r}{\Upsilon}\sin(\phi-\alpha)\right)\right) + \frac{\Upsilon_r}{\Upsilon}\cos(\phi-\alpha) = 0 \tag{B.15}$$

$$\sqrt{1-\left(\frac{\Upsilon_r}{\Upsilon}\sin(\phi-\alpha)\right)^2} = -\left(1+\frac{\Upsilon_r}{\Upsilon}\cos(\phi-\alpha)\right) \tag{B.16}$$

$$1-\left(\frac{\Upsilon_r}{\Upsilon}\sin(\phi-\alpha)\right)^2 = 1+\left(\frac{\Upsilon_r}{\Upsilon}\cos(\phi-\alpha)\right)^2 + 2\frac{\Upsilon_r}{\Upsilon}\cos(\phi-\alpha) \tag{B.17}$$

$$-\frac{\Upsilon_r}{\Upsilon}\sin^2(\phi-\alpha) = \frac{\Upsilon_r}{\Upsilon}\cos^2(\phi-\alpha) + 2\cos(\phi-\alpha) \tag{B.18}$$

$$2\cos(\phi-\alpha) = -\frac{\Upsilon_r}{\Upsilon} \tag{B.19}$$

$$\phi-\alpha = \pm\arccos\left(\frac{\Upsilon_r}{-2\Upsilon}\right) \tag{B.20}$$

Substituting Eq. (B.20) into (B.13) gives

$$1 + \cos(\alpha - \beta) - \frac{\Upsilon_r^2}{2\Upsilon^2} = 0 \tag{B.21}$$

and so

$$\alpha - \beta = \pm \arccos\left(\frac{\Upsilon_r^2}{2\Upsilon^2} - 1\right) \tag{B.22}$$

Combining Eqs. (B.20) and (B.22) yields the minimising values of α and β:

$$\alpha = \phi \pm \arccos\left(\frac{\Upsilon_r}{-2\Upsilon}\right) \tag{B.23}$$

$$\beta = \phi \pm \arccos\left(\frac{\Upsilon_r}{-2\Upsilon}\right) \pm \arccos\left(\frac{\Upsilon_r^2}{2\Upsilon^2} - 1\right) \tag{B.24}$$